UNIVERSITÉ DE LILLE

Ecole Doctorale des **Sciences de la Matière, du Rayonnement et de l'Environnement**

Unité de recherche **UMET**

Thèse présentée par **Devadas BHAT PANEMANGALORE**

Soutenue le **24 janvier 2019**

En vue de l'obtention du grade de docteur de l'Université de Lille

Discipline **Physique et Science des matériaux**

Development of magnesium-based alloys for biomedical applications

Développement d'alliages à base de magnésium pour applications biomédicales

Composition du jury

Rapporteurs	Caroline RICHARD	Professeur Université de Tours
	Olivier HARDOUIN DUPARC	Chargé de recherché CNRS École Polytechnique Palaiseau
President	Claude ESTOURNES	Directeur de recherché CNRS CIRIMAT -Université Toulouse 3 - Paul Sabatier
Examinateur	David BALLOY	Professeur UMET UMR 8207 - Université de Lille
Directeurs	Rajashekhara SHABADI	Maître de Conférences UMET UMR 8207 - Université de Lille
	Gang JI	Chargé de recherché CNRS UMET UMR 8207 - Université de Lille

Acknowledgements:

I am very grateful to University of Lille for giving me the opportunity to pursue my doctoral studies. My journey at University of Lille has been of continuous learning and it is the support and guidance of the people mentioned below that has helped me climb this steep slope of learning in France.

Firstly, I express my indebtedness to my advisor Dr. Rajashekhara Shabadi for providing an invaluable opportunity to work at University of Lille. I thank him for the long discussion hours spent together related to my Ph.D and life, including weekends. He has taught me to not limit myself and challenge myself that has made my Ph.D journey very clear. It is my immeasurable appreciation for his continuous guidance, untiring support and encouragement in completing my thesis and develop my career.

Dr. Gang Ji is also greatly acknowledged for co-refereeing this work. I thank him for his advice and suggestions throughout my research project.

I am grateful to College Doctoral Lille Nord de France for providing 'Aides a la mobilite internationale des doctorants' that supported my stay at National University of Singapore (NUS).

I would like to express my heartfelt thanks and gratitude to the following personnel who have rendered their support and provided invaluable advice during the duration of my stay at University of Lille and NUS.

Prof. Alexandre Legris for his time and aura. The moments spent with him in the lab are memorable.

Associate Prof. Manoj Gupta (NUS, Singapore), for providing me an opportunity to work in his group. His encouragement and advice have served me well throughout this internship.

Chief of UMET Prof. Patrice Woisel, Dr. Franck Béclin, Prof. Charlotte Becquart, Dr. Marie-Noëlle Avettand-Fénoël, Dr. Rémy Besson, Dr. Jérémie Bouquerel, Dr. Catherine Cordier, Prof. Jacques Foct, Dr. Ingrid Proriol Serre, Dr. Ludovic Thuinet, Dr. Matthieu Touzin, Prof. Jean-Bernard Vogt, Prof. David Balloy, Jean-François Dhenin, Prof. Pascal Roussel, Dr. Myriam Moreau, Dr. Pardis Simon for different interactions in the pursuit of knowledge.

Dr. Amit, Mr. Gururaj, Mr. Vyasraj and Ms. Sravya for their technical guidance and help during synthesis and mechanical characterization at NUS.

Mr. Hong Wei, Mr. Abdul Khalim Bin Abdul, Mr. Juraimi Bin Madon, Ms. Raina of NUS Materials Science Laboratory; Mr. Jocelyn Golek, Mr. Ahmed Addad, Ms. Anne-Marie Blanchenet, Ms. Séverine Bellayer, Ms. Maïa, Mr. Damien Creton, Mr. Laurent d'Apolito, Dr. Florent Blanchard, Dr. Ludovic Lesven, Ms. Aurélie Malfait, Jean-Noël Staelens of UMET, UCCS, and LASIR of University Lille for their effort and technical assistance rendered.

Sincere appreciations to Ms. Fong Yee and Ms. Isabelle Samain and Ms. Corinne Henry, Ms. Carmen Delval for assisting me with all the administrative work at NUS and University Lille respectively.

I am grateful for my colleagues Mr. Romain, Mr. Gabriel, Dr. Jérôme, Mr. Yu, Mr. Rudy, Dr. Marc-Antoine, Ms. Kaoutar, Ms. Sabrina of my office 226; Dr. Maxime, Dr. Gulzar, Ms. Julie, Ms. Isadora, Ms. Amina, Dr. Rebecca, Dr. Raphaël, Dr. Saadia, Mr. Billy, Dr. Yvan of UMET for being with me in this amazing journey.

My friends Tanu, Inder, Shilpa, Piyush, Ragini, Richa, Ankita, Naina, Arun, Rahul, Manharsh, Sumit, Spurthi, Ismail for being with me and rendering emotional support.

Finally, I am grateful to my beloved parents, my wife Dr. Vishakha, my sister Varalaxmi and I am greatly indebted to my family, wellwishers and everyone who rendered their support and co-operation in completing this work.

Abstract:

With the ability to bio-degrade and thereby reducing the stress-shielding effect, biodegradable implants are of great importance in medical research. Among all the materials, magnesium is the one which shows promising results being bio-degradable and with the properties comparable with its young's modulus to that of bones. It also is an essential mineral for the human body. However, pure magnesium corrodes very quickly and it is essential to develop certain alloying additions or coatings to enhance its corrosion resistance and control its degradability. Although a great deal of research is going on in this field for over two decades, there are only a few commercially available Mg-based degradable implants. Hence, in the present study, the approaches adopted to improve the mechanical and corrosion behaviors of pure magnesium using carefully chosen:

(a) Alloying elements like zinc, calcium and erbium (Mg-2Zn-2Er, Mg-2Zn-0.6Ca-1Er, etc.) to control the degradation behavior

(b) Secondary processes like extrusion to alter and improve the microstructure

(c) Surface treatments like fluoride coatings to further protect the surface to resist the rapid dissolution

Alloying additions and choice of coating have been given utmost care in order to minimize the toxicity, cost and while keeping beneficial properties intact. In this study, the synthesis of pure Mg and alloys were carried out using disintegrated melt deposition technique (DMD), followed by hot-extrusion. The first part of this thesis focuses on the microstructural characterization of as-DMDed and as-extruded alloys. Equiaxed fine grained microstructures have been achieved for as-extruded pure magnesium and its alloys as compared to the coarse grained as-DMDed microstructures. The secondary phases are uniformly distributed and they are broken down in the as-extruded microstructures of the alloys. The microstructural characterization (XRD and TEM) reveals the presence of $MgZn_2$, W-phase ($Mg_3Zn_3Er_2$) and i-phases (Mg_3Zn_6Er) in different alloys.

The mechanical property assessment revealed an increment in the tensile and compressive properties of ternary and quaternary alloys as compared to pure Mg and Mg-2Zn binary alloy. These values are attributed to a reduction in grain size, presence of solute atoms and secondary phases. Fractography studies for the alloys reveal the dimples that are an indication of enhanced ductility behavior, along with the presence of twins in the area close to the fractured region as seen in EBSD analysis. The damping behavior studies have indicated that the elastic modulus of the alloys has retained their values as that of pure magnesium, which is beneficial for its biomedical applications.

The corrosion behavior of these alloys in a simulated body fluid at 37 ^{o}C was studied using several techniques like hydrogen evolution, potentiodynamic polarization studies etc. As-DMDed alloys showed an excessive corrosive rate due to a coarse grain sized microstructure, heterogeneities including porosities and segregation of elements. Whereas as-extruded alloys showed enhanced corrosion resistance due to the fine grain sized microstructure and an uniform distribution of secondary phases. Rare-earth element erbium has been introduced in small amounts below the solubility level of the element and it has enhanced the corrosion resistance of Mg-alloys.

A compact fluoride coating was introduced to magnesium alloys using a simple and cost-effective technique of chemical conversion method to minimize degradation rates and provide sufficient corrosion resistance to the alloys tested in phosphate buffer saline (PBS) solution at 37 ^{o}C. The corrosion behavior was determined for coated samples and it was found that the samples exhibited enhanced corrosion resistance with fluoride coatings. These coatings are biocompatible and they can be tailored to provide further protection to the surfaces. The initial studies of biocompatibility assessment using cytotoxicity analysis of these biodegradable alloys has been performed. The cell viability values were enhanced with increased coating time and in turn the coating thickness, it was found that these alloys could serve as potential candidates for further in-vivo tests to establish their applicability.

Résumé :

Étant donné leur capacité de se dégrader à l'intérieur du corps, les implants biodégradables ont fait l'objet de nombreuses recherches médicales. Parmi tous les matériaux, c'est le magnésium, un élément indispensable du corps humain, qui conduit aux résultats les plus favorables car son module d'Young est similaire à celui de l'os. Comme le magnésium pur se corrode relativement rapidement, il est indispensable de lui ajouter certains éléments d'alliage ou de le revêtir afin d'augmenter sa résistance à la corrosion. Bien que de nombreuses recherches soient menées dans ce domaine depuis plus de deux décennies, seuls quelques implants dégradables à base de Mg sont disponibles dans le commerce. De ce fait, les méthodes adoptées afin d'améliorer le comportement du magnésium pur vis-à-vis de la corrosion sont les suivantes:

a) Ajout d'éléments d'alliage comme le zinc, le calcium et l'erbium (Mg-2Zn-2Er, Mg-2Zn-0.6Ca-1Er, etc.) pour contrôler le comportement de dégradation

b) Procédés secondaires tels que l'extrusion pour modifier sa microstructure

c) Revêtements de surface à base de fluorure pour mieux protéger la surface

Les éléments d'alliage et les revêtements, doivent être choisir afin de minimiser la toxicité et les coûts, et de ne pas altérer les propriétés bénéfiques du magnésium. Dans cette étude, la synthèse de Mg pur et d'alliages a été réalisée en utilisant la technique de « Disintegrated melt deposition » (DMD), suivie d'une extrusion à chaud. La première partie de cette thèse porte sur la caractérisation microstructurale d'alliages. Des microstructures à grains fins équiaxes ont été obtenues pour le magnésium pur et ses alliages extrudés alors que des microstructures à grains grossiers ont été développées pour les matériaux DMDed. Les phases secondaires sont uniformément réparties dans les microstructures extrudées des alliages. La caractérisation microstructurale (DRX et TEM) révèle la présence de $MgZn_2$, de phases W ($Mg_3Zn_3Er_2$) et de phases i (Mg_3Zn_6Er) dans différents alliages.

L'évaluation des propriétés mécaniques a révélé une augmentation des propriétés de traction et de compression des alliages ternaires et quaternaires par rapport aux alliages de Mg et de Mg-2Zn. Ces propriétés mécaniques améliorées sont attribuées à une réduction de la taille des grains, à la présence d'atomes de soluté et à des phases secondaires. Les analyses des facies de rupture des alliages révèlent des cupules qui indiquent une amélioration du comportement en matière de ductilité, ainsi que la présence de macles dans la zone proche de la région fracturée, comme le montre l'analyse par EBSD. Les études sur le comportement d'amortissement ont montré que le module d'élasticité des alliages correspond à celui du magnésium pur, ce qui est bénéfique pour les applications biomédicales.

Le comportement à la corrosion de ces alliages dans un fluide corporel simulé à 37 °C a été étudié à l'aide de plusieurs techniques telles que les études d'évolution de l'hydrogène, polarisation

potentiodynamique, etc. Les alliages As-DMDed ont présenté un taux de corrosion excessif en raison d'une microstructure à taille de grains grossière, d'hétérogénéités notamment de porosités et de ségrégation d'éléments tandis que les alliages extrudés présentaient une résistance à la corrosion améliorée en raison de la microstructure à granulométrie fine et d'une répartition uniforme des phases secondaires. L'introduction de l'erbium petites quantités a un taux inférieur à son sous niveau de solubilité dans le magnésium a amélioré la résistance à la corrosion des alliages de Mg.

Un revêtement de fluorure compact a été développe sur les alliages de magnésium par la couche de conversion chimique pour minimiser les taux de dégradation initiaux et fournir une résistance à la corrosion suffisante dans une solution de phosphate buffer saline (PBS) à 37 °C. Le comportement à la corrosion a été déterminé pour les échantillons revêtus et il a été constaté que les échantillons présentaient une résistance accrue à la corrosion avec des revêtements à base de fluorure. Ces revêtements sont biocompatibles et peuvent être encore personnalisés pour offrir une protection accrue à la surface. La première évaluation de la biocompatibilité à l'aide d'une analyse de cytotoxicité de ces alliages biodégradables a été réalisée. Les valeurs de viabilité cellulaire ont été améliorées avec l'épaisseur du temps de revêtement et ces alliages pourraient servir de candidats potentiels pour d'autres tests in vivo.

Contents

List of figures:

List of tables:

CHAPTER 1

INTRODUCTION

1. Introduction

1.1. Background

The history of magnesium began when Sir Humphrey Davy discovered elemental Mg in 1808 and Michael Faraday started the production of Mg by electrolysis of magnesium chloride in 1833 [1]. Its commercial production was made by Robert Bunsen in 1852 and in those days it was only used for pyrotechnical use. It was not so late that in 1878, Edward C. Huse used Mg wires who understood the degradable properties of magnesium and used as ligatures to arrest blood bleeding [1]. Other than UK, physicians in several parts of Europe were studying the applications of magnesium in surgical areas; Payr in Graz and Lambotte in Antwerp who extended the clinical studies and animal experiments [1]. But the problem of corrosion *in-vivo* could not be solved at that stage and due to the emergence of other corrosion resistant materials like steels, the research on magnesium based biomaterials took a step back.

But in the last two decades, there is tremendous ongoing research of using magnesium as an orthopedic and cardiovascular biomaterial. This is because its density and elastic modulus are akin to natural bone. It is advantageous as compared to implants made of titanium and stainless steel. This is because they do not have similar physical and mechanical properties as compared to human bone. Also, these implants require a second surgery to remove from the body as they do not degrade. Hence magnesium is not only biocompatible but biodegradable in bodily fluids and the degraded magnesium furnishes a dietary requirement.

The need for using magnesium alloys for biomedical applications revolves over three points:

1) *In-vivo* biodegradability
2) Abundance in body
3) Strength higher than polymers

Magnesium is highly electrochemically active and corrosive in harsh environments. Alloying additions into magnesium can improve their physical, mechanical and corrosion behavior, which is determined by their quantity, distribution and processing methodologies. Among several alloying additions, commercially produced magnesium alloys include manganese (Mn), aluminum (Al), zinc (Zn), calcium (Ca), zirconium (Zr) and rare earths (RE).

Hence, basic groups of alloy systems are Mg-Mn [2], Mg-Ca [3], Mg-Al-Mn [4], Mg-Al-Zn-Mn [5], Mg-Zr [6], Mg-Zn-Zr [7], Mg-RE-Zr [8], Mg-Ag-RE-Zr [9] and Mg-Y-RE-Zr [10]. Aluminum is the principal alloying element and the most commonly used alloy is AZ91 [11], which has enhanced mechanical strength and corrosion properties. AM series were introduced by reducing aluminum content and adding manganese, as there is a gradual reduction in ductility with increase in aluminum. AS series contain silicon or RE for high temperature applications. Different mechanisms including solid-solution strengthening, precipitation hardening and grain-boundary strengthening etc. play a vital role in enhancing the mechanical properties of magnesium, which depends on the quantity and the type of alloying additions. For engineering applications, one of the reasons these alloying additions are tailored is to minimize the cost of the final product.

However, for biomedical applications, apart from providing a low-cost material, alloying additions should not be harmful and their quantity has to be within the limits of recommended daily allowance (RDA) of human body. Aluminum as an alloying element to magnesium may induce neurotoxicity that might lead to Alzheimer's and hence it is not beneficial as an alloying element [12]. Therefore, several commercial alloys like AZ31, AZ91 and LAE442 which have excellent mechanical properties and corrosion resistance could not be used as an implant material [11,12]. Hence there is a need for selecting an alloying element that enhances the properties but not harmful.

Zinc as an alloying element for magnesium in only second best to aluminum in terms of its effectiveness. Addition of zinc leads to enhancement of ductility and deformability. It increases strength via age hardening and solid solution strengthening effect. It enhances the corrosion resistance by elevating the corrosion potential of magnesium alloy. For human body, it is very essential for the immune system. It acts as a co-factor for specific enzymes in bone and cartilage. Several studies have been made on Mg-Zn alloys but an optimum amount of alloying addition to enhance the material's behavior was not been done before. In bones, the element calcium is the major component. With a density of 1.55 g/cm^3 which is similar to that of low dense Mg, it can help in maintaining its specific properties. It is essential in chemical signaling with cells [13]. Erbium is relatively new as an alloying element to magnesium. Several rare-earth elements have been tested and they are found to be less corrosive than aluminum and zinc alloys. It was found that Mg-RE alloys have four times higher corrosion resistance than AZ91D by Nakatsugawa et al [14]. Erbium was used before as a mischmetal along with other rare-earths but its effects have not been discussed in detail in the literature.

1.2. Scope of work

For validating magnesium based alloys for biomedical applications, the material should possess similar young’s modulus to that of human bone, high yield strength, moderate ductility, and minimal degradation behavior and enhanced biocompatibility. And therefore, the mechanical property assessment, electrochemical behavior, surface modification and biocompatibility studies are necessary. In this thesis, these aspects will be addressed.

The main aims of this thesis are as follows:

Aim 1: To synthesize new Mg-based alloys with minor additions of zinc, calcium and erbium using disintegrated melt deposition method followed by hot extrusion and carry out the mechanical property assessment.

Expected outcome: The synthesized new alloys after hot-extrusion will be dense and exhibit enhanced tensile, compressive and damping behavior as compared to pure magnesium.

Aim 2: To study the electrochemical behavior of these new alloys in general corrosive media (NaCl at 25 ^{o}C) and in bio-corrosive media (phosphate buffer saline, PBS at 37 ^{o}C).

Expected outcome: It is expected that these new alloys exhibit a controlled degradation rate for biomedical applications and exhibit lower corrosion rate as compared to pure Mg.

Aim 3: To study the surface modification of these new alloys using fluoride coatings and study their degradation rates.

Expected outcome: It is expected that the coated alloys exhibit better degradation rates as compared to the uncoated alloys.

Aim 4: To perform the biocompatibility studies of these Mg-Zn-Ca-Er alloys using *in-vitro* cellular studies to validate as an orthopedic implant material.

Expected outcome: It is expected that the new alloys will exhibit minimum cell-toxicity and within the ISO standards.

1.3. Organization of Thesis

The following will be described in the forthcoming chapters:

Chapter 2 introduces the literature survey, which could be broadly classified into four sections. The first section comprises of elaborating magnesium and its necessity as a biomaterial. The second section is composed of different mechanisms of deformation and corrosion. This is followed by the recent developments in biodegradable magnesium materials. Later, ongoing research in coatings is discussed.

Chapter 3 describes the experimental procedure adapted in synthesis, processing and characterization of the developed Mg based materials.

Chapter 4 is about the detailed investigation of the microstructure and mechanical properties of the newly synthesized alloys.

Chapter 5 presents the electrochemical study of these materials conducted using a series of immersion tests, H_2 evolution tests and potentiodynamic polarization studies in two different electrolytes.

Chapter 6 is about the fluoride coating methodology adopted, its characterization and the biocompatibility studies showing the improvement in degradation performance.

Chapter 7 lists the overall conclusions and it is followed by a proposed set of recommendations for the future work in chapter 8.

A schematic representation of the research methodology is shown in Figure 1.1.

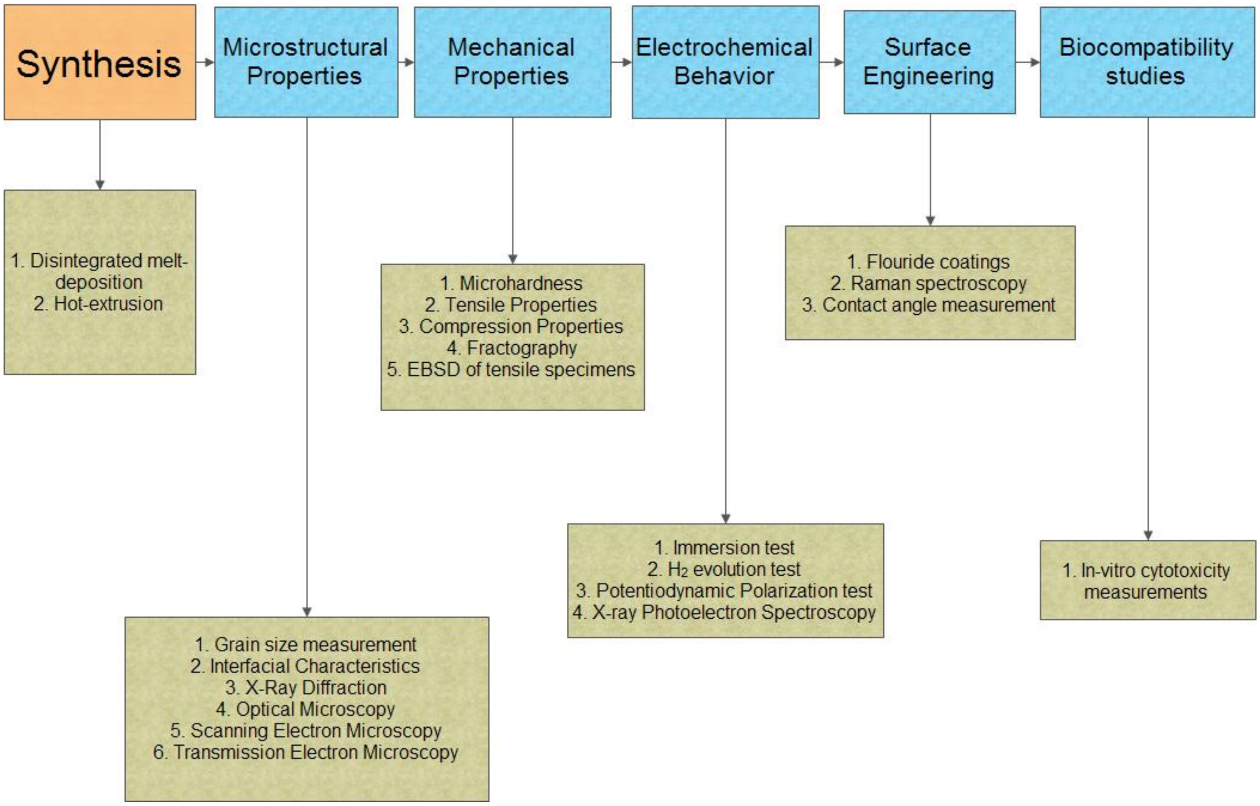

Figure 1.1: Schematic representation of the research methodology

CHAPTER 2

LITERATURE SURVEY

2. Literature Survey

2.1. Introduction to magnesium

An element with atomic number 12 in the alkaline earth metals group (II) in the periodic table, Magnesium (Mg) is the sixth rich element in the earth's surface and the lightest practicable structural metal discovered in 1755 by a Scottish chemist after the ancient city Magnesia. Since it belongs to group of alkaline earth metals, these are not found in elemental form in nature, but only in chemical combinations. Boasting its lightness among all the engineering metals, it is 34% lighter than aluminum and 50% lighter than titanium. Therefore, with a higher specific strength, it allows using thinner sections and achieving an even lower weight for a component. It stands third after iron and aluminum as a structural metal that is most commonly used. The popularity of this element is from the fact that it can be easily machined, cast, forged and welded. Also the popularity rose post world war in the field of military applications, as magnesium was used extensively for weapon manufacturing in World War 1 [15].

Mg is the seventh abundant element in the earth crust by mass. The natural ores of magnesium are: $MgCO_3.CaCO_3$ (dolomite) and $MgCO_3$ (magnesite). Magnesium is industrially manufactured via two processes namely, electrolysis and thermal reduction. Although magnesium was discovered by Sir H. Davy in 1808, their significant industrial production began in the early 20th century. Magnesium production has witnessed fluctuations, from a total of only ~ 10 ty^{-1} at the beginning of the century, peak production during WWII (228 kt) to recession afterwards. After 1945, the price for magnesium increased suddenly because it was stored by many European countries after WWII and hence it was given prime importance. Magnesium is largely used for alloying in aluminum and this was the main reason for its increased production volume and its growth mirroring that of structural aluminum alloys and particularly aluminum beverage cans.

Since late 90s, there has been a renewed interest to use magnesium alloys in the automotive and aviation industries; in the year 2000, magnesium production reached close to 400 kt. Chemically, Mg alloys are relatively unstable and are susceptible to corrosion. Mg alloys have excellent stiffness and specific strength, low density, very good machinability, high damping capacity, dimensional stability and good weldability under a controlled atmosphere. Alloying additions has dual effect, it enhances both the mechanical properties of Mg and also impart considerable effects on its corrosion resistance and biocompatibility. Uniform and controlled corrosion rate is very important for bioresorbable materials. If not, it could lead to a rapid release of dissolved metal ions and biological medical complications. Alloying additions of calcium, zinc and erbium were incorporated in to pure magnesium and they are explained in the following sections.

2.1.1. Physical metallurgy

With a crystal structure hexagonal close packed (HCP), magnesium is derived from sources that occur widely and in immense quantities. Hence this metal which has HCP crystal structure with limited room temperature ductility is not subjected to cold forming. Basal plane slipping $\{0001\}$ $\langle 11\bar{2}0\rangle$ and pyramidal $\{10\bar{1}2\}$ $\langle 10\bar{1}1\rangle$ twinning is possible below 225^{o}C.

Also these materials exhibit a tendency for brittleness due to intercrystalline failure and local transcrystalline fracture at twin zones or {0001} basal planes. Extensive deformation only occurs at higher temperatures due to new {1011} basal planes. The commercial production is by the thermal reduction of calcined dolomite or by the electrolysis of either hydrous or anhydrous magnesium chloride. It is brightly-colored, ductile and a chemically active metal. The lattice parameters of pure Mg are a=0.32092 nm and c=0.52105 nm, thus the c/a ratio is 1.6236. The actual value of c/a is very close to that of the ideal HCP crystal structure (1.633). The atomic positions, principal planes and directions are illustrated in Figure 2.1.

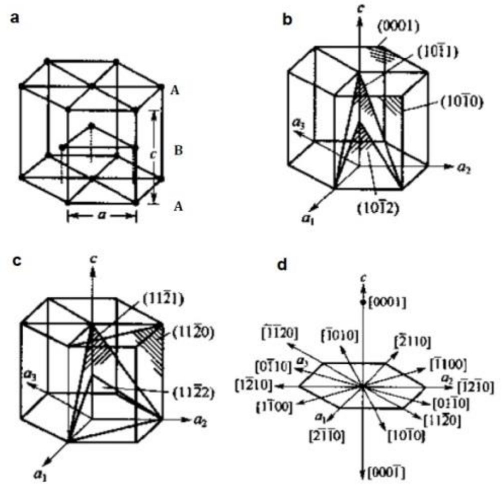

Figure 2.1: The magnesium crystal: (a) atomic positions; (b) principal planes of the $[1\ \bar{2}\ 1\ 0]$; (c) principal planes of the $[1\ \bar{1}\ 0\ 0]$ zone; (d) principal directions [16]

2.1.2. Solid solution hardening

Solid solution hardening is an alloying methodology used to enhance the strength of pure metal. A solid solution can be formed by introducing atoms of an element to the crystalline lattice of another element. Due to this nonuniformity, the dislocation motion is impeded and makes plastic deformation more difficult. This is because with the addition of solute atoms, the local stress fields are created. There is an interaction of the stress field with those of the dislocations. In polycrystalline magnesium alloys, the plastic deformation is anisotropic. It starts with slip on the basal planes and then prismatic slip gets activated with high strain hardening rate.

2.1.3. Physical and chemical properties

Magnesium metal is shiny and the color is silver or gray. It is most commonly used in pyrotechnics, aircraft and automobiles. In the field of medicine, citrate, chloride, hydroxide and sulfates (Epsom salts) are used. Magnesium citrates and sulfates are used for relieving from constipation. To treat low amounts of magnesium in the blood, magnesium supplements are taken which is nothing but magnesium chloride. These are in tablet form and is consumed orally. Magnesium hydroxides, also known as milk of magnesia are sold as antacids to neutralize the acids in the stomach. The properties of pure magnesium are listed in Table 2.1 [17–19].

Table 2.1: Properties of pure magnesium [17–19]

No	Property	Value
1	Crystal structure	hcp
2	Density	1.738 g/cm^3 at RT
3	Young's modulus	45 GPa
4	Ultimate Tensile Strength	10-100 MPa
5	Fracture Elongation	1-12%
6	Melting Point	650±0.5 ^{o}C
7	Boiling Point	1090 ^{o}C
8	Specific Heat Capacity	1.05 kJ/ (kg K)
9	Fusion Heat	195 kJ/kg
10	Heat Conductivity	156 W/ (m.K) (RT)
11	Linear Expansion Coefficient	26* 10^{-6} K^{-1} (RT)
12	Shrinkage (solid-liquid)	4.2%
13	Shrinkage (T_s-RT)	approx. 5%
14	Specific Electrical Conductivity	22.4 m / (ohm mm^{-2}) (RT)
15	Normal Potential	-2.37 V

2.1.4.Alloying nomenclature

To identify different conventional and commercial magnesium based alloys, it is important to standardize in ASTM norms for easy identification. The following Table 2.2 shows the key letters for each alloying element.

Table 2.2: ASTM codes for alloying elements in magnesium

Abbreviation	Alloying element	Effect
A	Aluminum	Strengthens
B	Bismuth	Grain refiner
C	Copper	Reduces corrosion resistance
D	Cadmium	Toxic
E	Rare earths	Strengthens and improves creep resistance
F	Iron	Enhances corrosion
H	Thorium	Age hardening
K	Zirconium	Grain refiner
L	Lithium	Increases ductility
M	Manganese	Increases corrosion resistance
N	Nickel	Catalysis
P	Lead	Dielectric properties
Q	Silver	Strengthens
S	Silicon	Strengthens and improves corrosion resistance
T	Tin	Increases thermoelectric properties
W	Yttrium	Strengthens and improves creep resistance
Y	Antimony	Energy storage
Z	Zinc	Strengthens

2.1.5. Alloying elements

For the enhancement of mechanical properties of pure magnesium, alloying additions provide precipitation hardening and/or solid-solution hardening. Among all the alloying additions, aluminum has the most favorable effect and it significantly increases the tensile strength by the formation of $Mg_{17}Al_{12}$ intermetallic phase. It also provides sufficient castability, ductility and resistance to corrosion. The conventional Mg-Al alloys used belong to the series AZ and AM (AZ91D, AM50A and AM60B). Zinc, manganese and rare-earth additions also lead to precipitation hardening.

Minor additions of zirconium can aid as an excellent grain refiner, which provides favorable sites for heterogeneous nucleation sites for magnesium grains [20]. High temperature strength could be achieved by the addition of silver. But elements like iron and nickel could be very harmful for the corrosion resistance of magnesium even with 0.005 wt%. Recently, it was found out that the addition of lithium helps in reducing the density further and improves the specific strength better. The nominal compositions of commercially available magnesium alloys are listed in Table 2.3.

Table 2.3: Summary of commercially available magnesium alloys [18,21–26]

Sl.No	Designation	Nominal composition (wt.%)							
		Al	Zn	Mn	Si	Zr	RE	Y	Th
1	AZ91	9	1	0.5					
2	AZ31	2.5-3.5	0.6-1.4	0.2-1					
3	AZ61	5.8-7.2	0.4-1.5	0.15-0.5					
4	AZ80	8.5	0.5	0.12					
5	AM50	5		0.3					
6	AM20	2	0.2	0.5					
7	AS21	2		0.5	0.5				
8	ZK40		3.5-4.5			0.45 min			
9	ZK60		6			0.5			
10	ZM21		2	1					
11	ZW3		3			0.6			
12	HM21			0.8					2
13	HM31			0.8					3
14	WE43					0.5	3.25	4	
15	WE54					0.5	3.5 (Nd)	5.25	

2.2. Introduction to biomaterials

2.2.1. General concepts

There are several definitions to define a biomaterial. In short, it is a non-living material that is designed to mimic an existing material of the body and delivers the application when integrated with the biological system. Metallic biomaterials can endure tensile stresses as compared to that of ceramics and polymers. These materials are widely used for skeletal reconstruction. They are also used for functional devices like valves and heart pacemakers etc. ISO 10993 developed by the International Standards Organization describes a series of standards for determining the biocompatibility of devices for medical applications. Other standard organizations like American Society for Testing and Materials (ASTM), International Conference on harmonization (ICH), Organization for Economic Co-operation and Development (OECD), U.S Food and Drug Administration (FDA), U.S Pharmacopeia Convention (USP) have also devised relevant biocompatibility standards.

2.2.2. Application of Biomaterials

Integration of several types of materials like metals, ceramics, polymers have varied applications as biomaterials. The following are some of the materials that are either natural or synthetic (man-made mineral or organic) and applications in various parts of human body.

2.2.2.1. Oral/dental applications

As a denture, PMMA is mostly used which is economical, convenient, light weight and has low water absorption. Others include PVC, Bakelite, vulcanite, celluloid etc. For tissue engineering and regenerating dental structures, there has been repeated usage of poly (lactic-co-glycolic acid). Dental restorations like crowns and bridges are mostly made of biocompatible porcelain which has high toughness. Dental sciences have been developed to be metal-free, because it can ionize and release valence electrons. But noble metals like gold and platinum have found a myriad of applications as crown, bridge, orthodontic wires and implants. These metals and their alloys have excellent resistance to bending and thermal expansion. Facial surface of the teeth, its color and contour could be modified by the used of composite resins to rebuild the tooth structure. These resins include dimethacrylate (Bis-GMA), urethane di-methacrylate oligomers (UDMA).

2.2.2.2. Orthopedic applications

A wide range of materials are used for orthopedic applications. Biodegradable polymers are used in knee meniscus (cartilage where two bones meet), spine surgery, intervertebral disc, bone grafts. Hydroxyapatite, zirconia, carbon fibers are used for hip prosthesis. Among metals, aluminum, titanium and stainless steel have been used as bone implants. Several polymer based ceramic composites have been used for bone defects filler.

2.2.2.3. Cardiovascular applications

Stents, catheters, vascular grafts are some of the examples for polymers like polyester, polyurethane and polyamides as implant materials for cardiovascular applications. Metals are used mainly for stents, which is explained in detail in the subsequent sections.

2.2.3. Metallic implants in orthopedics

From USD 21.7 billion in 2007, today the global market for orthopedic implants has reached USD 47.2 billion. It is also estimated that this will reach USD 74.7 billion by 2023. During the period 2016-2023, the highest CAGR of 9.7% is expected in the Asia-Pacific region. It is necessary for greater innovation in this area with the increase in demand. Different key players in the orthopedic market are listed below:

1) 3M Health Care

2) Abbott Laboratories

3) Aesculap Implant Systems, LLC

4) Arthrocare Corporation

5) Baxter International Inc.

6) Boston Scientific Corporation

7) Conmed Corporation

8) DePuy Synthes

9) Johnson and Johnson

10) Medtronic Plc

11) NuVasice, Inc.

12) Phillips Precision Inc.

13) Smith and Nephew Plc

14) Stryker Corporation

15) Synthes Inc.

16) Wright Medical Technology, Inc.

17) Zimmer Biomet Holdings, Inc.

2.2.3.1. Stainless steel

Since 1900s, stainless steels are commonly used for surgical practices. Stainless steels are ideal implants due to the absence of inclusion, which contains sulfur that encourages corrosion. Among them, austenitic stainless steel grades such as 316, 316L and 302 are widely used orthopedic implant materials due to its low cost, high strength and formability. The most widely used is 316L that has good strength and ductility, work hardenability, fatigue properties, resistant to stress corrosion cracking (SCC) in the body and has little tensile notch sensitivity. They are used as plate fixations for tibial fractures and in the form of wires and screws in oral, maxillofacial and other allied areas of surgery. Ferrite phase should not be introduced, as it is magnetic and could interfere with Magnetic Resonance Imaging (MRI) equipment. They are susceptible to heating and it is possible to alter the shape of such implant materials.

2.2.3.2. Titanium and its alloys

During 1960s, titanium became a popular choice of material for orthopedic implants. They are lighter than stainless steel, have lower modulus of elasticity and are less prone to induce adverse reactions with human body. Ti-6Al-4V (R56400, TC4) is the most famous α-β titanium alloy with alloying additions of 6 wt.% aluminum and 4 wt.% vanadium. They have been extensively used for biomechanical applications as implants and prostheses (an implant that completely replaces a body part).

2.2.4. Problems associated with existing biomaterials

Two key issues in using a biomaterial are its ability of host response and the ability of microbes to colonize its surface. The definition of biocompatibility evolved from understanding these concepts and it led to the development of functional materials.

Over the years in the field of biomaterials, non-degradable titanium, Ti-6Al-4V and SS316L have been extensively used for bone fixation implants in orthopedic division. The orthopedic industry have been widely using these materials for medical procedures since decades. However, the major disadvantage of these materials is that they have high elastic moduli. This leads to serious stress-shielding problem as the implant material which has greater elastic moduli bears greater load for the same amount of strain imposed on the bone-implant. Also, the non-degradability of these permanent fixtures necessitates a second intervention for implant removal. Several problems like additional cost, pain and risk of infection arises with the removal of implant. Also there is a possibility of the release of toxic ions such as titanium particles through corrosion or wear process that may lead to inflammatory osteolysis. Therefore, it is very urgent and important to develop next-generation implant biomaterials.

2.2.5. A new class of controlled degradable biomaterials

Biodegradable metals (BMs) are a new class of metals which is required to biodegrade gradually inside the human body *in-vivo*. It should bio-degrade in such a way as to elicit an appropriate host response by released products without causing any adverse effect. After healing, these implants should dissolve completely. They should not leave any implant residues and should ensure complete tissue healing. Biodegradation in medical field is already known after the introduction of biodegradable sutures made of polymers [27]. The implant materials earlier known to be corrosion resistant are currently challenged after the introduction of biodegradable metals.

2.2.6. Desired properties of biodegradable materials

To synthesize an ideal implant, it has to meet certain requirements which are classified into three categories.

- Material
- Mechanical properties
- Manufacturing

2.2.6.1. Material

Biodegradability is defined as the ability of a material to be degraded by enzymes and other bio-based reactions when placed within a biological system [28]. Bio-inertness is defined as the property of a material to retain its chemical structure and remain unreactive with the host while performing its intended functions [29]. Biocompatibility is defined as the material's ability to perform its desired function for a certain application with an appropriate host response [30].The elements that are introduced in an implant should not undergo any adverse reaction with the human body. Bioactivity is defined as a specific effect or reaction of a biological tissue upon exposure to a substance.

2.2.6.2. Mechanical properties

With regard to bio functionality, the implant should have adequate mechanical properties, especially Young's modulus and fatigue strength as close to that of the bone as possible [31]. A comparison of the mechanical properties of implant materials and cortical bone is presented in Table 2.4. It could be seen that the traditional implant materials like stainless steel and Ti6Al4V have elastic modulus 20 times greater than that of bone. But, pure Mg and cortical bone have similar density, strength values and Young’s modulus.

Table 2.4: Mechanical properties of cortical bone, magnesium and conventional implants

Material	**Density (g/cm^3)**	**Strength**		**Young’s modulus (GPa)**	**Ductility (%)**
		Compressive (MPa)	**Tensile (MPa)**		
Cortical bone	1.7-2.0	164-240	80-150	3-30	3-4
Stainless steels	7.9-8.1	170-310	480-620	165-200	30-40
Ti6Al4V	4.43	758-1117	930-1140	100-110	8-15
Co-Cr alloy	8.3-9.2	450-1000	-	230	-
Co-Cr-Mo alloy	-	-	908-1282	-	8-41
Magnesium	1.74-2.0	65-100	170	41-42	6.1

2.2.6.3. Manufacturing

The final product should be available to the market at the right time and it has to be economical after utilizing high-quality raw materials and attain better surface finish. These elements used for manufacturing a product should have a definite host response and therefore it is expected to have extremely pure raw materials during synthesis [32]. The synthesis technique must be adapted in such a way that it is expected to exhibit repeatability of properties [33].

2.2.7. Magnesium in body

Among one of the essential six minerals which has to be supplied in the diet, magnesium is one among them. It can be called as a vital regulator of basic health due to its numerous functions. About 25g of magnesium is contained in an average human body. The magnesium supplements get broken down into divalent cations and they function as a part of the body structure. These act as a co-factor, which are like switches that regulate the activity of enzymes. Enzymes perform several chemical reactions in our body, which include digestion, production of proteins, breakdown of fats and etc. Magnesium is one element that powers enzymes. More than 300 enzyme-driven biochemical reactions need magnesium. Their role is considered as important as hormones, except that magnesium is not present in our body on its own, it has to be introduced. Adenosine triphosphate (ATP), which is the main source of energy in cells, is magnesium complexed ATP or MgATP. Mg ion has to be bound to ATP to make it biologically active. Magnesium also protects our DNA. Insufficient magnesium causes destabilization of DNA structures and can negatively impact cellular function.

2.2.8. Magnesium in bone

Bone has the capability to remodel itself throughout a human's lifespan. It has the ability to heal majority of fractures internally. Magnesium is equally important as calcium in the bone. Deficiency of one element could actually affect the metabolism of the other. It could possibly result in loss of magnesium, if there is an increase in calcium supplement intake into our body. This might result in excess calcium deposition in soft tissues and can lead to arthritis.

2.2.9. Magnesium as a biomaterial

Magnesium is biodegradable [34–36] and has high specific strength, and this is the only material to possess both of these properties. Mg alloys can reduce the stress shielding effect in orthopedic applications as their Young’s Modulus is similar to that of bone. It is unique due to its extremely high damping capacity (ability to absorb energy), the highest of any metal. Due to its poor corrosion behavior of Mg alloys, it forbids their applications in numerous areas. But the property of biodegradability allows magnesium to be used as a temporary implant. With the rapid advancement in technology, it is possible to develop high-purity magnesium materials by designing optimum degradation rates as per human body requirements. This is a booming area in research and the following representation in Figure 2.2 gives an idea of the number of researchers working on this field over the past two decades.

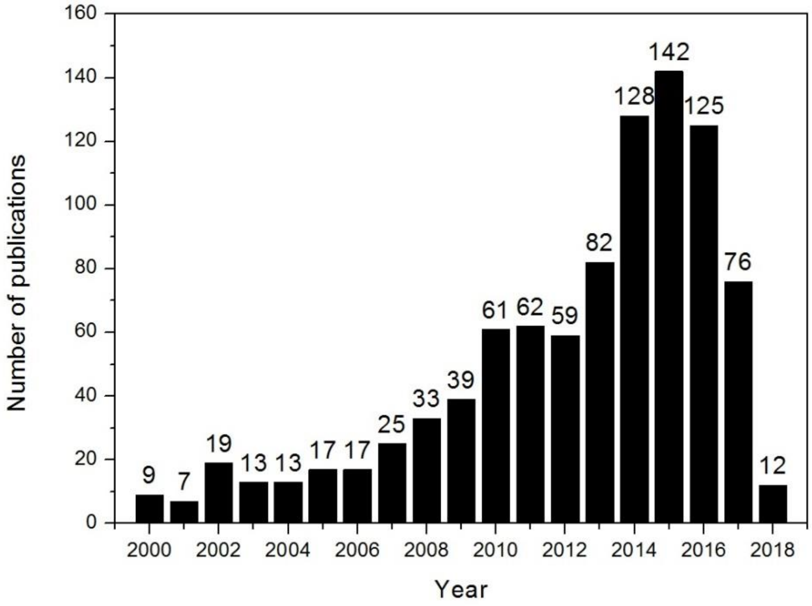

Figure 2.2: Publications and conference proceedings on the subject of biological applications of magnesium alloys and its composites against the year of print (adapted from Scopus)

2.2.10. Recent developments

2.2.10.1. Stents

For the treatment of coronary artery disease, a coronary stent is an artificial temporary support device that is placed to keep the vessel open. The forms of such stents are usually mesh-shaped and they are available in different sizes to open the blockage. Predominantly SS316 is the material used by nearly 3 million patients worldwide.

These stents are divided into three categories:

(a) Bare-metal stents (BMS)

These stents are made of cobalt-chromium alloy or stainless steel. But there were several problems due to this, which include blood clotting. Hence this led to the development of more advanced stents.

(b) Drug-eluting stents (DES)

This class of stent materials includes several coated polymer layers which consists of antiproliferative drugs on the metal stents. Different Drug-eluting stents that are under development are listed in Table 2.5.

Table 2.5: Various DES under development

Manufacturer	**Trade name**	**Stent**	**Polymer**	**Drug**
Abbot	ZoMaxx	Tantalum/SS	Durable	Zotarolimus
Boston Scientific	Taxus	SS	Durable	TAxus
Cordis (J and J)	Cypher	SS	Bio-absorbable	Everolimus
Terumo	Nobori	SS	Bio-absorbable	Biolimus-A9

(c) Bioabsorbable stents (BS)

The previously explained stents are permanent and are of no use after the vessel healing takes place. Therefore, a new class of biodegradable stents, which gets fully absorbed after fulfilling their mission leaving no residual prosthesis, is developed. Magnesium alloy is one among the materials used to overcome the limitations of non-degradable permanent stents [37]. A typical example shown in Figure 2.3 is a balloon shaped stent in its tubular form derived from a magnesium alloy using laser. These stents are developed by BIOTRONIK AG, Switzerland.

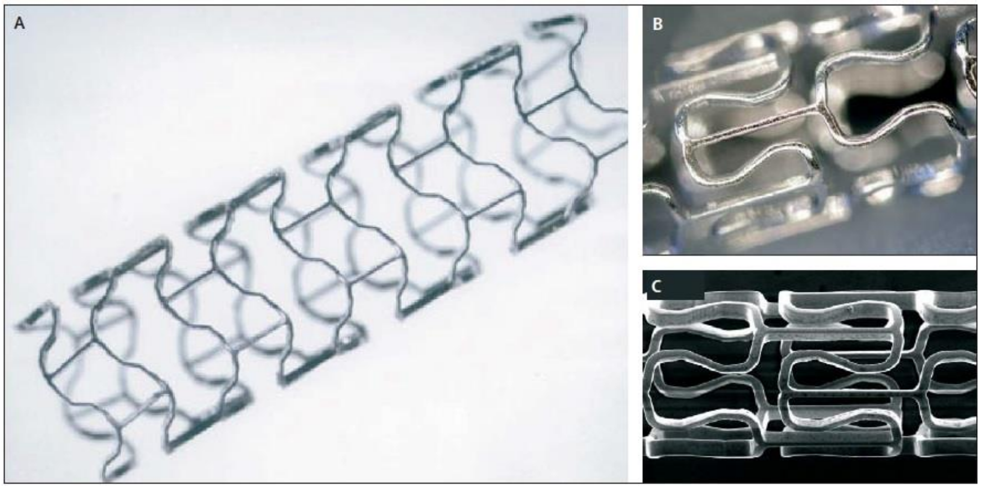

Figure 2.3: Bioabsorbable magnesium stent (BIOTRONIK, Berlin, Germany) (a) after expansion; (b) before expansion; (c) a high magnification image [38]

2.2.10.2. Screws, plates and pins

As a means of support for internal fixation of bones, several screws made of titanium or stainless steel are used. But they remain inside the body for the entire lifespan or can be removed after healing. So far, Mg-0.8Ca [39], MgYREZr [40], LAE442 [41] and ZEK 100 [42] have been used for clinical trials.

2.2.10.2.1. Magnezix

Proudly known as the implants of tomorrow, SYNTELLIX AG is a medical technology company based in Germany has created innovative bioabsorbable screws and pins called MAGNEZIX. It has the CE mark, also known as *Conformité Européene* in French which literally means European Conformity. These screws are not removed but they get resorbed inside the body. It is advantageous for both patients and doctors. These are uniquely designed with self-cutting tips which simplifies operative procedures and also has different thread pitches which aid in absolute fracture stability due to interfragmentary compression.

2.3. Corrosion

Corrosion is defined as a destructive attack on the surface of a material due to an electrochemical reaction with its environment. When positive ions are released from the anode, simultaneously the electrons flow towards the cathode and hence deterioration takes place.

2.3.1. Magnesium corrosion mechanisms

The physical and chemical features and processes involved when a material is exposed to an environment constitute the mechanism for corrosion. The following are some key points during corrosion of magnesium.

(i) The surface film formed on magnesium is partially protective.
(ii) For each atom of magnesium dissolved in water, one molecule of hydrogen is produced.
(iii) E_p, defined as pitting potential of magnesium is more negative than free-corrosion potential E_{corr} in NaCl solutions.
(iv) Localized corrosion could possibly lead to fall out of particles.

2.3.2. Corrosion of magnesium in simple electrolytes

The overall reaction for the corrosion of pure magnesium could be understood by the following equation:

$$Mg + 2\,H_2O \rightarrow Mg\,(OH)_2 + H_2$$

The partials could be written as follows:

$$Mg = Mg^{2+} + 2e^-$$

$$2\,H_2O + 2e^- = H_2 + 2\,OH^-$$

In chloride containing solutions, magnesium and its alloys undergo pitting corrosion. Above a threshold potential, called pitting potential this localized corrosion phenomenon occurs. In general, magnesium has a standard potential of -2.37 V NHE in acid solution [43]. But the working potential at steady state is approximately 1 V more positive. This is because, in acid solutions, $Mg(OH)_2$[44] and also MgO [45] are formed as a thin film. In basic solutions, a thick $Mg(OH)_2$[46] is formed over this thin film.

2.3.2.1. Negative difference effect (NDE)

Magnesium was found to be passive by King [47] when cathodically polarized in a certain potential range. But when anodically polarized, hydrogen evolution rate was found to increase and this phenomenon in literature is termed as "negative difference effect". This phenomenon has become controversial since its first introduction by Petty et al. in 1954 [48].

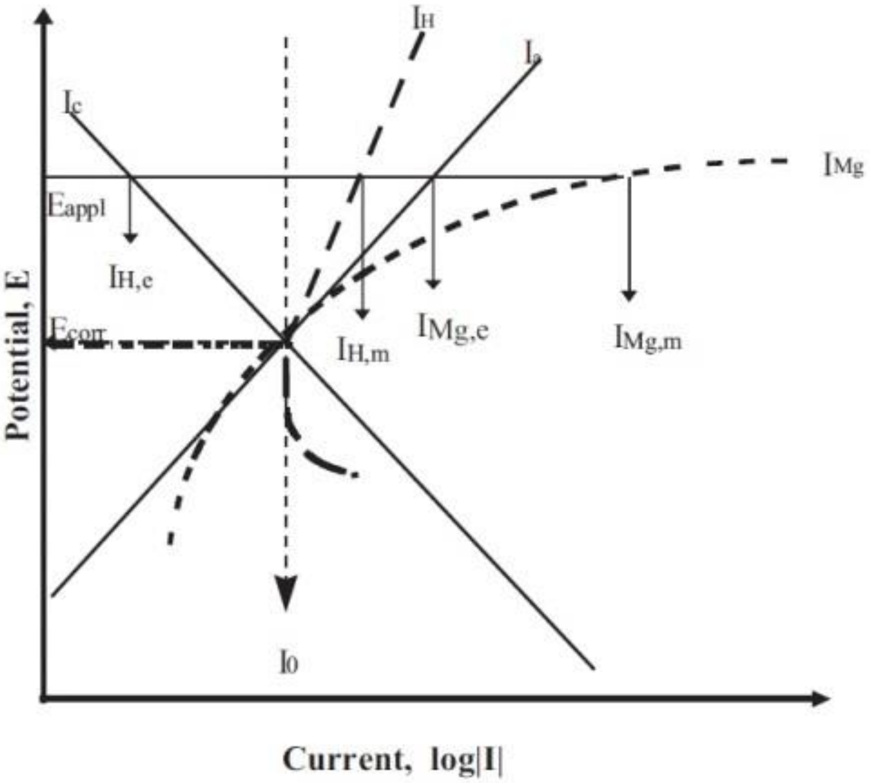

Figure 2.4: The negative difference effect [49]

The Figure 2.4 shows the phenomenon of NDE experimentally. I_a and I_c in the figures represent the anodic and cathodic partial reactions. At the corrosion potential E_{corr}, their rate of reactions are equal to I_s. With a greater potential value E_{appl}, the rate of cathodic reaction is expected to be $I_{H,e}$ along the curve I_c and the anodic reaction rate is expected to increase to $I_{Mg,e}$ along the curve I_a. With increasing potential, hydrogen evolution rate increased experimentally rather than decreasing [50].

2.3.3. Types of corrosion

In the following sections several corrosion types that can take place in magnesium and its alloys have been explained in detail.

2.3.3.1. General attack Corrosion

This type of deterioration is uniformly distributed corrosion over complete exposed area of a metal. In natural environment, the main cause for this type of corrosion is oxygen. The kinetics of several reactions determines the nature and severity of this corrosion process. Normally when several reactions take place simultaneously, the rate is governed by the slowest reaction. To prevent such attacks, it is essential to use paints or metallic coatings such as galvanizing. Also it is possible to use cathodic protection (Sacrificial Anode or Impressed Current - ICCP) and anodic protection.

2.3.3.2. Localized Corrosion

It is the selective removal of material by corrosion when it is in contact with a corrosive environment. This happens usually when there are heterogeneities in the material. The following are the three types of localized corrosion.

2.3.3.2.1. Pitting

This type of corrosion is most difficult to predict and design against when cavities or "holes" are produced in the material in disguise. This is the most dangerous form of corrosion. It happens due to the localized damage by chemical or mechanical means, due to nonmetallic inclusions or poor coatings with localized damage. These pits could appear as cup shaped or hemispherical.

2.3.3.2.2. Crevice

As the title suggests, it occurs in the gap or crevice between the two welded surfaces, which could be metal-metal or metal-nonmetal. Several factors like pH, temperature, halide ions, oxygen concentration, and alloy composition influence this type of corrosion. Some of the remedies to prevent this type of corrosion are to use alternatives like butt joints instead of riveted or bolted joints and so on.

2.3.3.2.3. Filiform

This type of corrosion reaction occurs in pure magnesium where the surface film is not very stable. Since the pitting potential is more negative than free-corrosion potential, localized corrosion takes place. At some point after the film breaks, the region that is in contact with the solution becomes anode and the larger area which is the film becomes cathode. In magnesium they appear as irregular pits in the beginning and spread around laterally. Only specific regions like the second phases gets corroded that become anodic while the remaining surface is unattacked. It is dangerous as it appears that the material is not damaged but on the contrary it has severely damaged deep inside the structure.

2.3.3.3. Galvanic Corrosion

When a metal is in contact with another metal which is nobler in a corrosive environment, the accelerated corrosion phenomenon is called Galvanic Corrosion. The potential difference between these two metals is the driving force for corrosion. The noble member undergoes "cathodic protection". To prevent such attack, it is essential to choose metals which are near to each other in the electrochemical series. Since the cathode/anode area ratio is directly proportional to the acceleration rate of corrosion, one has to avoid the presence of a large cathode and small anode.

2.3.3.4. Environmental Cracking

This is a form of corrosion cracking that happens with one or combination of the following phenomenon: Stress corrosion cracking, Corrosion fatigue and Hydrogen Embrittlement.

2.3.4. Corrosion of magnesium in biological electrolytes

2.3.4.1. Physiological solutions

There are several electrolytes available or can be prepared with ion concentration nearly equal to those of human blood plasma. They are called balanced salt solutions (BSS) made to a physiological pH and isotonic salt concentration. Since many of them are fairly complicated to prepare, it is always advisable to buy. The following are different solutions:

2.3.4.1.1. Hank’s Stock Solutions (HBSS)

This is a salt rich in bicarbonate ions, formulated by John Hanks, a microbiologist in 1940 [51].

2.3.4.1.2. Simulated Body Fluid (SBF)

This is first evaluated by Kokubo et al. to measure the changes on a surface of bioactive glass ceramic. A detailed preparation procedure is given in [52].

2.3.4.1.3. Phosphate Buffer Saline (PBS)

This is commonly used in biological research and it contains disodium hydrogen phosphate, sodium chloride, potassium chloride and potassium dihydrogen phosphate. These solutions can be prepared using tablets or pouches bought commercially.

2.3.4.2. Different testing methods

To determine the corrosion behavior and mechanisms, different tests could be adopted.

2.3.4.2.1. Unpolarized-type measurements

a) Weight loss measurements (WL)

This is the simplest test which requires only a sample, corrosion medium (SBF at a temperature of 37 ^{o}C) and an accurate micro-balance to determine mass loss over a period of time. The corrosion medium volume to surface area of the sample should be high enough to counter the minimal changes in pH of the medium during testing. An advantage of this method is that it is easily understood by the users and material producers. But this method bears several disadvantages. It is an average result and does not give the rate within a certain period (kinetics). The weight loss is determined by accurately removing only the surface and there is experimental constraint in doing it.

b) Hydrogen evolution measurement (HEM) [53]

The dissolution of an atom of magnesium in aqueous solution at its corrosion potential generates a molecule of hydrogen gas. Hence the measured hydrogen gas is equivalent to measuring the amount of magnesium dissolved. Hydrogen gas formed due to the corrosion products that have been formed and from the undermined fallout particles would still be equal to the amount of dissolved magnesium. This measurement is not affected by the corrosion products formed.

But a disadvantage is that multiple samples are needed and it gives little information regarding corrosion mechanism.

c) pH monitoring (pH)

This is a simple and low cost technique used to monitor the corrosion reaction. With the change in pH, one can identify the possible corrosion reactions taking place and regulate the degradation behavior of the material.

2.3.4.2.2. Polarized-type measurements

a) Potentiodynamic polarization studies (PDP)

This involves changing the potential of the working electrode in the positive direction and monitoring the current such that the sample corrodes. Tendency of a material for passivation and presence and effect of inhibitors and oxidizers could be easily recognized. Since the measurement can take place over several orders of magnitude of current, it is plotted on a logarithm scale.

2.4. Processing methods for magnesium

2.4.1. Solid phase processing

When the working temperature is below the solidus of the metal matrix phase, these synthesis techniques can be classified as solid-state syntheses. It possesses great advantages in creating a metastable phase in the microstructure and the composition levels could be easily controlled in developing a material.

The following are different techniques:

2.4.1.1. Powder Metallurgy Technique

This is very commonly used technique to synthesize a variety of high strength equilibrium and non-equilibrium alloys. Raw materials in their powder form could be blend and given a certain shape by consolidating them and then sintering at a temperature below the melting point of the base material. The blending in a reactive ball milling involves a continuous cold welding, fracturing and re-welding of powder particles. Such a process produces frictional heat at the interface which results in local melting and consolidation. An advantage over the liquid phase processing is the possibility of better strength properties due to minimal segregation effects and no mold-metal interface reaction products.

2.4.1.2. Additive manufacturing

A fabrication technique that involved creating metal and polymer parts layer by layer is called Additive manufacturing. Such a technique involves the assistance of computer-aided design (CAD) systems. One of the examples is Selective laser melting (SLM) that uses laser beam to selectively melt powders. Other synthesis techniques used are zone solidification technique and conventional PM followed by spark plasma sintering technique.

2.4.2. Liquid phase processing

2.4.2.1. Conventional casting

For synthesizing magnesium based alloys, casting is a conventional technique. Ferrous crucibles could be used for casting as molten magnesium does not have affinity to iron as molten aluminum does. But molten magnesium burns unless an inert atmosphere is used, unlike aluminum which forms an impervious oxide that limits further oxidation. A flux could also be used that acts as a cleaning agent. Fluxless processes involve using argon, CO_2, SF_6 or mixture of these gases. SF_6 and CO_2 attributes to global warming and it was attributed that SF_6 is 24000 times more potential for global warming than CO_2

2.4.2.2. Liquid infiltration

This method is used to synthesize composites where the reinforcing force is made as a porous mold and the metal matrix is melted and poured through its interstices. Two variants, i.e., pressure less and pressure-assisted infiltration exists.

2.4.2.3. *In-situ process*

This is also a process used to synthesize composites where the desired ceramic reinforcements are formed in-situ by controlled metallurgical reactions. Reaction temperature could be controlled to attain the required particulate size.

2.4.2.4. *Spray Forming*

Here, the molten alloy is atomized using an inert gas and deposited onto a substrate to build up bulk materials layer by layer. It is possible to produce non-uniform distribution of reinforcement particulates.

2.4.2.5. *Disintegrated melt deposition*

This technique was developed in the early 90s and patented by the National University of Singapore (NUS) [54].This process is of great technological potential as it is economical and comes with advantages of conventional casting process and spray forming. A more detailed description of the setup is given in the subsequent sections.

2.4.3. Hot extrusion

When a block of metal is forced under high pressure through an orifice of a die, this metal forming operation is termed Extrusion [55]. High compressive stresses are developed during the reaction of the extruded billet with the container. There are two types of extrusion processes, direct and indirect. In direct extrusion the metal is driven through the die by the ram. In indirect extrusion, with the ram and die stationary, the container and the billet is made to move. This process requires less power as there is no relative motion between the container and the billet. A third process to produce hollow shapes is impact extrusion, usually restricted to softer metals like aluminum. The following are the process control parameters:

(a) <u>Type of extrusion (back or direct)</u>
The pressure required for initial ram travel is high and when the metal flows through the die, this maximum pressure value is called breakthrough pressure. This pressure decreases with the length of the billet in the container. In order to stop the ram and leave a small discard in the container, the pressure builds up rapidly in the end.

(b) <u>Extrusion ratio</u>
This is defined as the ratio of the initial cross sectional area of the billet to the final after extrusion. For our experiments, a constant extrusion ratio of 20.25:1 is kept.

(c) <u>Working temperature</u>
To decrease flow stress or resistance to deformation with increasing temperature, magnesium is hot-extruded. The temperature is set below the melting point and also below the temperature at which hot shortness occurs. To avoid the problem of oxidation, they are

sprayed with graphite. Also the internal heating is taken into account due to the extensive deformation.

(d) Speed of deformation

High extrusion speeds result in temperature rise due to extensive deformation and it leads to hot-shortness. Low extrusion speeds result in greater cooling of billets, which increases the flow stress and hence the pressure required to extrude rises. Hence an optimum speed is kept.

2.5. Deformation behavior of magnesium

During deformation, grains seek preferred orientations, i.e., texture. Most of the energy is dissipated as heat during deformation and only some part is stored inside in the form of dislocations. Several factors like strain, strain rate, orientation, type of deformation, temperature and initial grain size are responsible for deformation microstructure.

2.5.1. Slip

The plastic deformation in magnesium is accompanied by two modes of deformation: slip and twinning. Twinning is due to the limited availability of slip systems to accommodate deformation. In HCP magnesium the following are the possible slip systems:

(a) basal slip in {0 0 0 1} planes along <1 1 $\bar{2}$ 0>
(b) prismatic slip in {1 0 $\bar{1}$ 0} planes along <1 1 $\bar{2}$ 0>
(c) pyramidal slip <a> in {1 0 $\bar{1}$ 1} planes along <$\bar{1}$ 2 $\bar{1}$ 0>
(d) pyramidal slip <c+a> type I in {0 0 0 1} planes along <1 1 $\bar{2}$ 0>
(e) pyramidal <c+a> type II slip in {2 $\bar{1}\bar{1}$ 2} planes along <1 1 $\bar{2}$ 3>

The closest packed plane is typically where the slip is active and hence for magnesium it is the basal plane.

2.5.2. Twinning

After basal slip, twinning is an important deformation mode that gets activated in magnesium. This is due to elevated temperatures, finer grain sizes and solute additions. The critically resolved shear stress (CRSS) for tension twin {10$\bar{1}$2} is only 33 MPa. This is also called as extension twin as it supplies extension along the c-axis. The Table 2.6 gives an idea of possible twinning systems in magnesium.

Table 2.6: Several twin systems available in pure magnesium

Twin Plane	Misorientation	Shear
$\{10\bar{1}2\}$	86°	0.131
$\{10\bar{1}1\}$	56 °	0.138
$\{10\bar{1}3\}$	64 °	0.138
$\{10\bar{1}1\}$-$\{10\bar{1}2\}$	38 °	0.208
$\{10\bar{1}3\}$-$\{10\bar{1}2\}$	22 °	0.192

2.5.3. Misorientation

A grain boundary is characterized by its boundary plane, misorientation axis and angle. An angle-axis pair defines the orientation between two coordinate systems. The difference in orientations of different grains is termed as misorientation and this angle-axis pair is used to denote grain boundary misorientation.

In EBSD data acquisition, a correlated misorientation takes into account the misorientation between neighboring points whereas an uncorrelated plot takes random points.

2.5.4. Schmid factor

When the shear stress on a slip plane is applied along a particular direction, slip takes place if this value exceeds some critical value. This value is called critical resolved shear stress and it is governed by Schmid Law. In a material where many slip systems can act, a term called schmid factor is calculated and in order to figure out the primary slip system, it is the one with the greatest schmid factor.

2.6. New Alloy Development based on Zn, Ca and Er

2.6.1. Introduction

Today, the advancement in the field of biodegradable magnesium cardiovascular stents have attained a great height and they have been tried on animals [38,56]. Different designs are applied for bone implants in the form of screws, plates or other fixture devices. For tissue engineering applications, open-porous scaffolds have been tried and tested [57–60]. It is very essential to understand the interface and the behavior of biological implants made of magnesium and its alloys in the biological environment. The influence of the alloying elements on the formation of protective interfaces should be the priority in designing a material [61].

Several alloying additions were already investigated for biomedical applications [62–66]. Among them, magnesium alloys containing calcium is the most popular choice due to its properties similar to bone [13]. But a few studies show the galvanic coupling effect due to the presence of

Mg_2Ca phase [39]. Alloying element zinc is second best to aluminum for non-biomedical alloys as it elevates strength, reduces grain size of magnesium alloys [67]. It also helps in refinement of second phases and makes the matrix more noble, which reduces galvanic coupling [68]. Rare-earth elements with minor additions are believed to exhibit anti-carcinogenic properties [69] and some of these elements like yttrium has been shown to reduce the pitting potential of magnesium alloys [70]. The element erbium has not been discussed in detail and minor additions of this element to magnesium could possibly help in lowering its corrosion rate. Also the combined effect of fine grain size and secondary phases due to the alloying additions needs to be understood due to the additions of calcium, zinc and erbium.

2.6.1.1. Calcium

In terms of physiological functions, Calcium (Ca) is an essential metal element for human beings. Also in terms of metallurgical properties, this is an excellent gran refiner and it can reduce the effect of oxidation during solidification conditions [71,72]. When added in limited amounts, it can increase the mechanical properties and corrosion resistance of Mg alloys [39].This also helps in grain boundary strengthening. In binary Mg-Ca system, the phase Mg_2Ca improves creep resistance due to all three strengthening mechanisms (solid-solution strengthening, precipitation strengthening and grain boundary pinning). The recommended daily allowance (RDA) of calcium by the doctors is 1000 mg for adults [3]. Addition of calcium is essential to inhibit oxidation during the solidification process as it forms a thin and dense CaO film on the surface of molten metal [44]. Mg-Ca is also a good age-hardening system [74].

2.6.1.2. Zinc

As an alloying element in Mg, zinc is second best to aluminum in terms of its effectiveness. As one among the most essential elements in the human body, zinc with a density of 7.14 g/cm^3 is present in several enzymes that regulate our metabolism [75]. It helps in DNA synthesis and also aids in different senses [68,76]. The RDA is 10-15 mg and about 100 mg could be tolerated [64,77]. In terms of metallurgical properties, addition of zinc enhances ductility and deformability [78]. It also increases hardness through solid solution strengthening and age hardening effect, as the solubility decreases with temperature. But when added in large amounts, it is possible to cause embrittlement when aluminum is present [20].

2.6.1.3. Rare earth

These elements are introduced in the form of master alloys (element in combination with magnesium) in magnesium alloys. This could be in the form of mischmetal. As rare earths are expensive, mischmetal is a naturally containing ore with elements like lanthanum, cerium, praseodymium, neodymium and other impurities is introduced. When several rare-earths have to be added, the master alloys containing one or two element in larger amount and the other elements in different amounts could be considered. These in terms of solubility with pure magnesium, the rare-earth elements could be classified into two groups: The first group consists of limited solubilities such as Neodymium (Nd), Lanthanum (La), Cerium (Ce), Praseodymium (Pr), Samarium (Sm), Europium (Eu) and the second group consists of elements with large solid solubilities such as Lutetium (Lu), Ytterbium (Yb), Thulium (Tm), Erbium (Er), Holmium (Ho), Dysprosium (Dy), Terbium (Tb), Gadolinium (Gd) and Yttrium (Y).They exhibit solid solution strengthening and also form intermetallic phases with magnesium which can lead to precipitation strengthening [79]. The effect of individual rare earth element on pure magnesium and its alloys have been discussed in the following section.

2.6.1.3.1. Neodymium

A Mg-Nd binary alloy was investigated by Birbilis et al. [80]. These alloys synthesized using high-pressure die cast (HPDC) technique showed improved corrosion behavior for Mg_3Nd intermetallic phase over pure Mg when tested using micro-electrochemical cell method [81]. Neodymium (Nd) containing wrought magnesium alloys of composition (Mg-4Y-3RE) were synthesized by Argade et al. using friction stir processing technique (FSP) [82]. The corrosion behavior was found to be improved by the shift of open circuit potential (OCP) towards positive potentials with grain refinement by FSP. The effect of Nd addition on AZ91 alloys were investigated by Zhang et al. [83]. The microstructure was tailored by significantly reducing the twins and dislocations, which decreased the anodic dissolution rate. Also the phase Al_3Nd formed inhibited the micro-galvanic corrosion.

2.6.1.3.2. Lanthanum

The effect of lanthanum on the corrosion behavior of magnesium was studied by Birbilis et al. [80]. The intermetallic phase formed in the eutectic was $Mg_{12}La$ and these phases exhibited significant corrosion resistance over pure magnesium. Mg-0.69La was investigated by Willbold et al. to study low rare earth elements on the biodegradation and biocompatibility of magnesium and they did not produce systematic or local cytotoxicological effects [84].

2.6.1.3.3. Cerium

Mg-0.4Ce extruded and heat treated alloys investigated by Tekumalla et al. revealed an improved corrosion resistance [85]. Song et al. studied the effect of Ce in decreasing the size of β-$Mg_{17}Al_{12}$ and forming fine needles of $Al_{11}Ce_3$ intermetallic compounds that increased the corrosion resistance of AZ91 alloy [86]. Mg-0.23Ce investigated by Willbold et al. [84] showed no gas cavities during in-vivo tests, these alloys were slowly degrading and showed good biocompatibility.

2.6.1.3.4. Yttrium

Sudholz et al. studied the binary additions of yttrium on magnesium and termed that it has a relatively unique impact on corrosion behavior in comparison to that of traditional REs [87]. Tests conducted in 0.1 M NaCl electrolyte solution revealed an increase in corrosion potential with increasing additions of yttrium (2-18 wt.%). The micro-cell method to study the electrochemical behavior of intermetallic particles revealed that $Mg_{24}Y_5$ phase which is about 200 nm large is responsible for enhanced corrosion resistance of Mg-Y alloys, which has an E_{corr} value 40-50 mV more noble than pure Mg. Y entering the α-Mg in solution also had an effect in retarding anodic kinetics. Gu et al. [88] studied binary Mg-1Y alloy and concluded that yttrium addition favors in the application of magnesium based stents as it did not induce significant toxicity to osteoblasts (MC3T3-E1). Peng et al. have used zone solidification method to synthesize high purity Mg-Y biomaterials in MagIC - Magnesium Innovation Centre, GKSS, Germany [89]. Their studies have shown that the corrosion and mechanical properties of the purified middle region of zone solidified materials were better compared to that of common casting method. Liu et al have a different opinion on the influence of yttrium on the corrosion of Mg-Y binary alloys [90]. The corrosion rate increased with increasing Y-containing intermetallic in 0.1 M NaCl while it decreased in 0.1M Na_2SO_4 solution due to the protective surface film formed. The corrosion in NaCl propagated by filiform type and the initiation is due to the presence of second phases. Earlier studies have revealed the addition of RE element as a quaternary addition, where the behavior of individual alloying element is not readily revealed [86,91].

2.6.1.3.5. Erbium

As an alloying element to magnesium, erbium is relatively new. It was used earlier as a misch-metal along with other rare-earths but its effects have not been discussed in detail. The Mg-Er phase diagram is shown in the Figure 2.5. Several intermetallic compounds like $Mg_{24}Er_5$, MgEr, Mg_2Er are formed at different wt.% Er. The mechanical properties for binary Mg-Er alloys are listed in Figure 2.5. The sample Mg-3.6Er is cast, homogenized at 500 ^{o}C for 8h and aged at 200 ^{o}C for 8h by Zhongjun et al [92]. An increment in UTS for Mg-2Er was observed by Wu et al., where the sample was die cast, homogenized at 520 ^{o}C for 48h, extruded at 400 ^{o}C and annealed for 400 ^{o}C for 1h [93]. Increased Er additions enhanced the ductility value but minimized the UTS value of Mg-Er alloys [93].

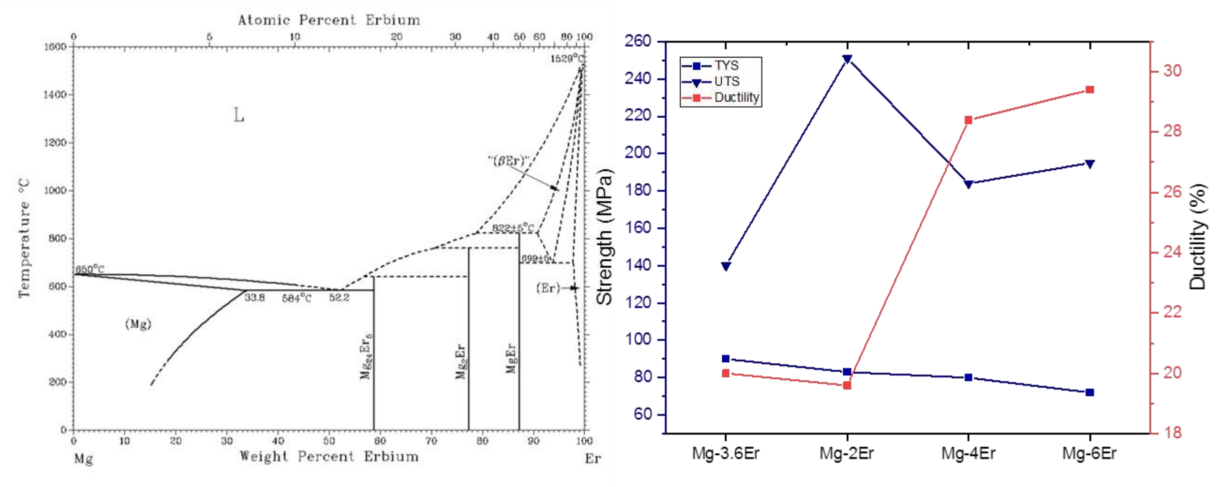

Figure 2.5: Mg-Er binary phase diagram [94] and previous studies on determining tensile properties of Mg-Er binary alloys

2.6.2. Mg-Ca binary alloys

The Mg-Ca phase diagram is shown in Figure 2.6. Under equilibrium condition, the solubility of Ca in Mg is 1.34 wt.%. A eutectic is present at 16.2 wt.% and at the temperature of 516 °C. Formation of an eutectic structure in the alloy is encouraged when the calcium content is above 0.7 wt.%. When the Ca content is less than 45 wt.%, the phases are α-Mg and Mg_2Ca. As the solubility decreases with temperature, these alloys exhibit precipitation effect. Above 5 wt.% Ca addition, the alloy is very brittle at room temperature [13].

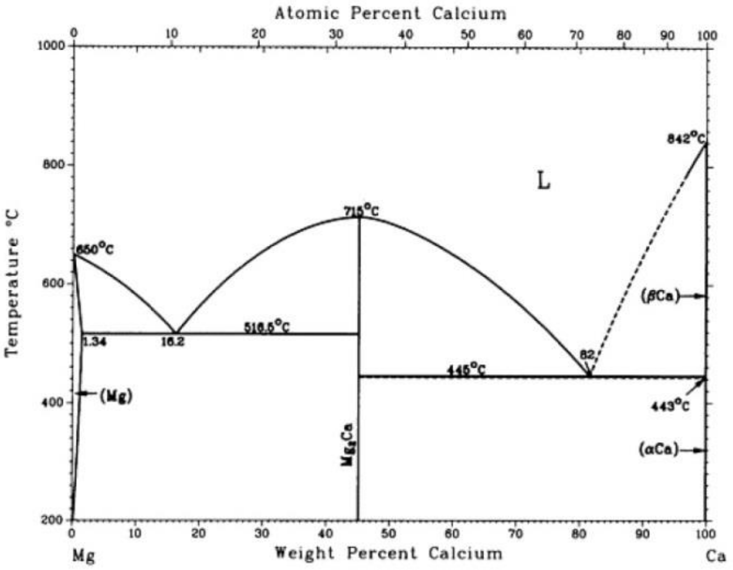

Figure 2.6: Mg-Ca binary phase diagram [94]

Mg-Ca alloys with calcium contents from 1 to 20 wt.% were fabricated by Z. Li et al. were found to be very brittle at room temperature [13]. In this study, the Mg-1Ca was concluded to exhibit suitable bio corrosion properties. Wan et al. have designed chemical composition of Mg-Ca alloys from 0.6 -2 wt.% [95]. The tests carried out on SBF solution demonstrated that Mg-0.6Ca has a good potential as a new biomedical material. Another study by Kirkland et al. on developing alloys with calcium contents from 0.4 to 28 wt.% was investigated [96].

2.6.2.1. Microstructure, Mechanical properties and corrosion behavior

The optical microstructures of Mg-Ca alloys are shown in the Figure 2.7. The secondary phase Mg_2Ca is distributed both inside the grain and along the grain boundaries. This Mg_2Ca can exhibit a faster corrosion rate if present in abundance [3].

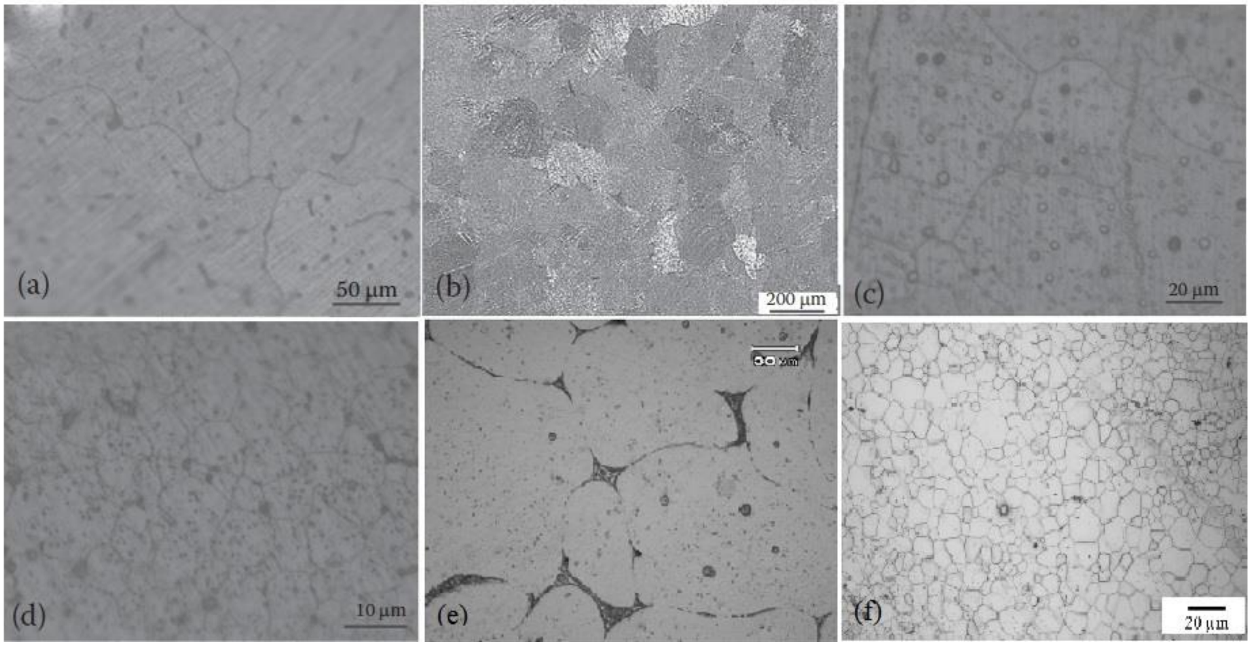

Figure 2.7: Typical optical microstructures of Mg-Ca alloys: (a) Mg-1Ca as-cast [13] (b) Mg-1Ca as-forged [97](c) Mg-1Ca as-rolled [13] (d) Mg-1Ca as-extruded [13] (e) Mg-1.6Ca as-cast [95] (f) Mg-0.54Ca as-extruded [98]

Drynda et al. [3] studied alloying of low calcium amounts (upto 4 wt.%) that led to increment in ultimate tensile strength up to 210-240 MPa. The grain size was not affected for various increments in calcium content. Murakoshi et al. [99] synthesized extruded Mg-xCa alloys (x=0.5, 1, 1.5 and 2 wt.%). With increasing calcium content, the mechanical properties were enhanced but their influence was not much. Harandi et al. [97] studied the effect of forging process on the mechanical properties and corrosion behavior of Mg-1Ca alloy. With increasing forging temperature from 250 °C till 450 °C, the hardness increased due to the presence of much finer and equiaxed grains. Li et al. [13] fabricated binary Mg-xCa (x=1, 2 and 3 wt.%) alloys. The mechanical properties were enhanced for as-rolled condition as compared to as-cast. They further enhanced for as-extruded alloys. This is as a result of thermomechanical processing leading to refinement of grain sizes. But for as-cast alloys, there is no increment in the mechanical properties with addition of calcium. Han et al. [100] prepared Mg-5wt.%Ca alloy and studied their compressive properties. The deformation due to extrusion refined primary Mg grains and also break the network structure of brittle Mg_2Ca, enhanced the mechanical properties. The mechanical properties of Mg-Ca binary alloys are summarized in Figure 2.8.

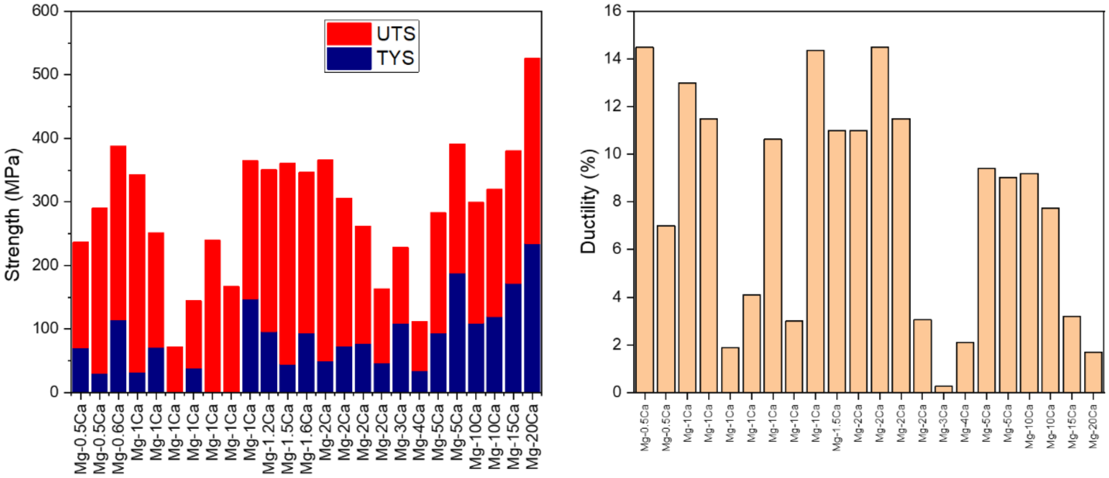

Figure 2.8: Summary of the mechanical properties of the binary Mg-Ca alloys

Drynda et al. studied five different extruded test specimens of magnesium-calcium alloys (Mg-xCa ,x= 0.4, 0.6, 0.8, 1.2 and 2.0 wt.%) for the cell culture experiments [3]. The specimens were also given fluoride coating. First, these bars were immersed in sodium hydroxide solution to establish a thick hydroxide layer and then immersed in hydrofluoric acid to convert this layer into a fluoride. Among all the alloys, 0.8 wt.% addition had the lowest degradation rate.

Kirkland et al. [101] tested the bio-corrosion behavior of a number of binary Mg alloys in a different test media called Minimum Essential Medium (MEM, Invitrogen). With Ca content greater than 1 wt.%, the corrosion rate increases rapidly. But it is surprising to note that the corrosion rates have been found similar to Mg-5Ca and Mg-16.2Ca.

Binary Mg-xCa alloys with various calcium contents from 0.5 to 10 wt.% were fabricated using casting process by Bakhsheshi Rad et al. [102]. With increasing Ca content, the corrosion rates were increased due to the excessive presence of an intermetallic Mg_2Ca phase, mostly present in the grain boundaries. Thus, in this work it was concluded that Mg-0.5Ca alloy is optimum as biodegradable implant.

Harandi et al. [97] studied the effect of forging process on the corrosion behavior of Mg-1Ca alloy and they found that with increasing forging temperature, greater is the precipitation of Mg_2Ca phase that can accelerate the corrosion rate of the alloy.

Zeng et al. studied in-vitro corrosion of as-extruded Mg-Ca alloys to study the influence of Ca concentration [98]. Their results reveal that Ca possibly plays a dual role. It accelerates corrosion due to the formation of Mg_2Ca phase and also decreases the corrosion rate due to the refinement of grain size. Among Mg-0.54Ca, Mg-0.79Ca and Mg-1.35Ca, the alloy Mg-0.79Ca represented the promising candidate for degradable biomaterial due to the highest hardness, ultimate tensile strength and corrosion resistance.

Jung et al. has elucidated an in-vivo corrosion mechanism of Mg-10Ca in a rat femoral condyle through a TEM study assisted by FIB technique [103]. The fabricated alloy consisted of a 3D lamellar network of Mg and Mg_2Ca. During corrosion, Mg_2Ca was attacked due to the Ca and O interdiffusion and this changed the structure into nanocrystalline. The surface and interior of the implant formed needle-type calcium phosphates which are similar to hydroxyl apatite that provided a bioactive environment for bone mineralization.

Using melt-spinning technique, Gu et al. fabricated Mg-3Ca ribbons and these showed more uniform corrosion morphology and induced no toxicity of L-929 cells [104]. A typical corrosion surface morphology of Mg-Ca alloys [13] is shown in Figure 2.9. A summary of the corrosion rates of different binary Mg-Ca alloys are presented in Table 2.7.

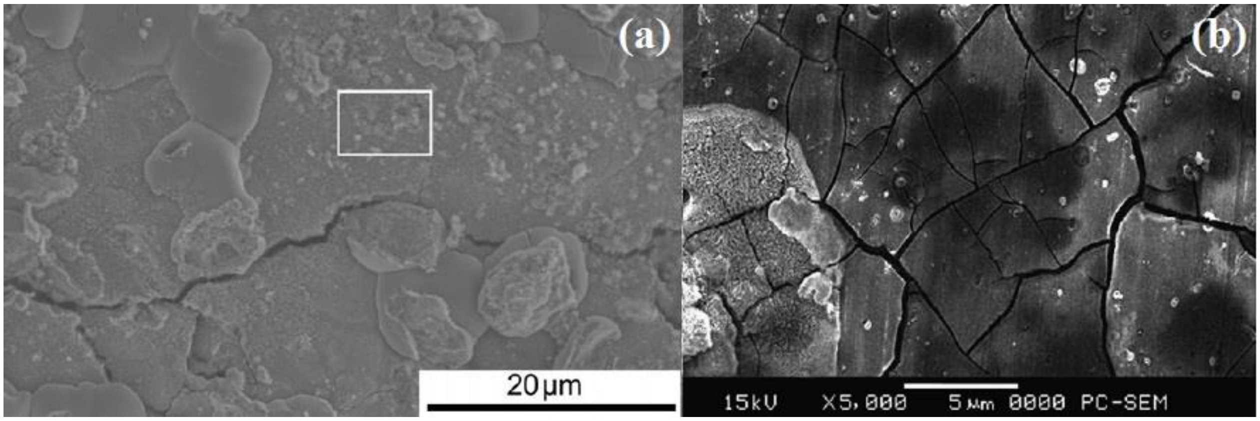

Figure 2.9: Typical corrosion morphology of as-cast Mg-1Ca immersed in SBF for 250h and as-cast Mg-2.5Ca immersed in SBF for 84h [13]

Table 2.7: Summary of the corrosion rates of the binary Mg-Ca alloys in different corrosive media

Sample	**Condition**	**SBF**	**Kokubo solution**	**MMEM**	**Hanks**	**I_{corr} ($\mu A/cm^2$)**	**References**
Mg-0.5Ca	As-cast	0.2 mm/day		0.1 mg/day			[105]
Mg-0.54Ca	As-extruded					174	[98]
Mg-0.7Ca	As-cast		1479 mpy			0.00197	[106]

Mg-0.79Ca	As-extruded					99.8	[98]
Mg-1Ca	As-cast	0.5 mg/day		0.87 mg/day			[105]
Mg-1Ca	As-cast		1876 mpy			0.00224	[106]
Mg-1Ca	As-cast	1.43 mm/y				0.00197	[97]
Mg-1Ca	Forged	1.9 mm/y				0.00371	[97]
Mg-1Ca	As-cast				3.16±0.5 mm/y		[107]
Mg-1Ca	As-cast	12.56 mm/y					[13]
Mg-1Ca	As-extruded	1.74 mm/y					[13]
Mg-1Ca	As-rolled	1.63 mm/y					[13]
Mg-1.35Ca	As-extruded					231	[98]
Mg-2Ca	As-cast	2.03 mg/day		20.3 mg/day			[105]
Mg-2Ca	As-cast		6.89 mm/y			301.9	[108]
Mg-2Ca	As-cast		2017 mpy			0.00312	[106]
Mg-3Ca	As-cast		2881 mpy			0.00395	[106]
Mg-3Ca	As-cast	21 ±1.4 mm/y				929.3±60.1	[104]
RS15 Mg-3Ca	As-rolled	1.68 ±0.2 mm/y				74.2±9.9	[104]
RS30 Mg-3Ca	As-rolled	1.25±0.3 mm/y				55.6±14.3	[104]
RS45 Mg-3Ca	As-rolled	0.39±0.1 mm/y				17.1±4.9	[104]
Mg-4Ca	As-cast		3604 mpy			0.0047	[106]
Mg-4Ca	As-cast		9.04 mm/y			395.7	[108]

2.6.3. Mg-Zn alloys

The Mg-Zn phase diagram is shown in the Figure 2.10.

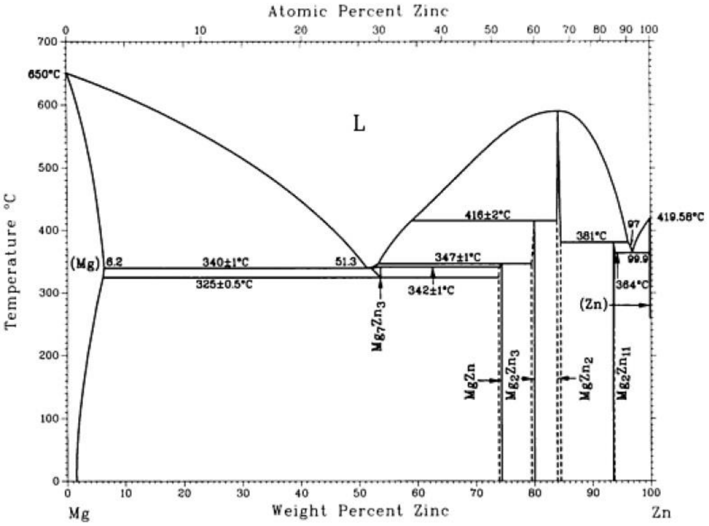

Figure 2.10: Mg-Zn binary phase diagram [94]

As seen in the phase diagram, the maximum solid solubility of Zn in Mg is 6.2 wt.%. For numerous applications, alloys within this solubility limit of Zn have been investigated whose microstructure consists of α-Mg primarily [68,76,77,109–111]. With an increasing Zn content, these alloys have a high glass-forming capability [109,112,113]. Zn based alloys have limited magnesium concentration [64].

2.6.3.1. Microstructure, Mechanical properties and corrosion behavior

Zhang et al. studied Mg-6Zn by fabricating using solid solution treatment and hot-working [68]. He found that zinc elevates the corrosion potential of magnesium in simulated body fluid (SBF). And also these materials did not induce in vitro cytotoxicity and were harmless to L-929 cells.

Yu et al. studied the bio-corrosion performance of Mg-3Zn in SBF [114]. They implemented heat-treatment using solutionizing and aging to alter the microstructure and the volume of precipitates. The solutionized samples exhibited low corrosion rate with the dissolution of (α-Mg + MgZn) eutectic phases. Due to increased precipitates, the corrosion behavior of aged samples was worst due to micro-cathodic effects.

Song et al. studied Mg_xZn_y second phases and their effect on the corrosion behavior in Mg-5Zn alloy by conducting T4 and T6 treatments [115]. Similar results were obtained, the solutionized samples exhibited better corrosion resistance in NaCl solution but the aged samples exhibited worst corrosion resistance due to the presence of large volume of precipitates and it was attributed to the micro-cathodic effect of second phases.

Peng et al. used backward extrusion to improve the properties of Mg-xZn (x=0.5, 1, 1.5 and 2wt.%) alloys [76]. He found an increment in the strength and elongation due to this process. The microstructure was homogeneous, with fine second precipitates.

Tensile and tensile-creep properties of blend and hot-pressed Mg-xZn (x=2.9, 3.3, 4 and 4.4 wt.%) were studied by Boehlert et al. [116]. Mg-2.5Zn was synthesized by Parande et al. [117] using blend-press-sinter powder metallurgy technique. For sintering, they used a hybrid microwave setup and then these compacts were extruded. The alloy exhibited not only excellent mechanical properties but good damping characteristics too.

The optical microstructures of pure Mg and Mg-Zn alloys are shown in Figure 2.11. The mechanical properties of binary Mg-Zn alloys are represented in Figure 2.12.

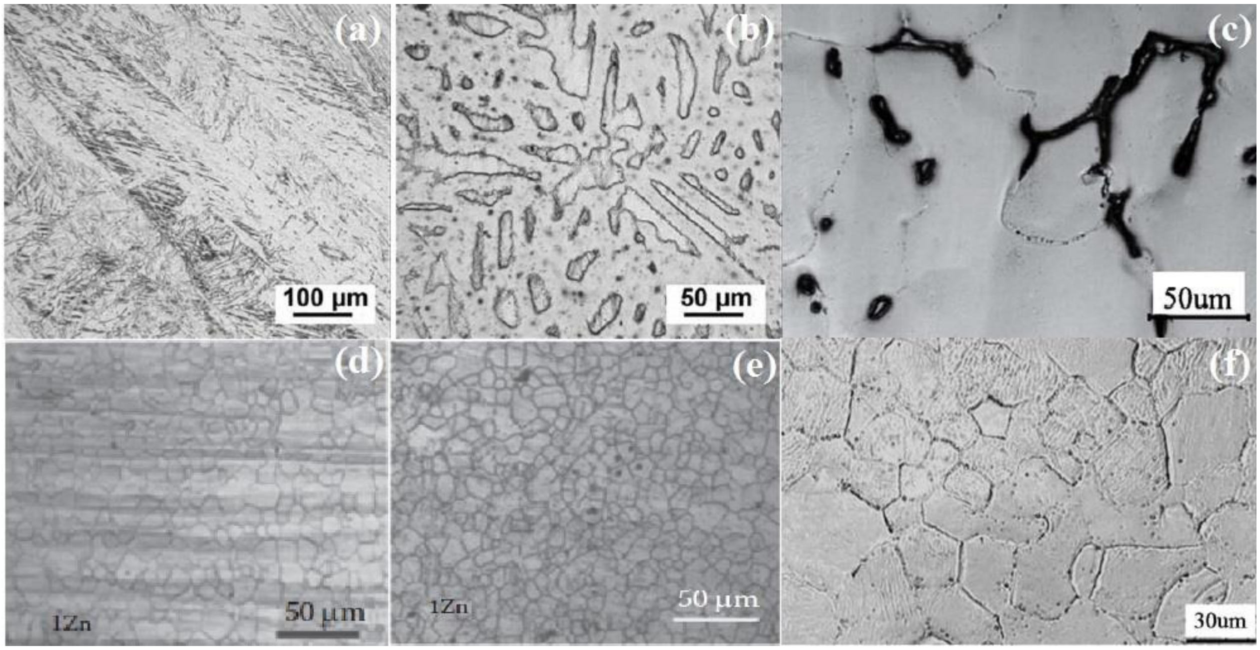

Figure 2.11: Typical optical microstructures of (a) Pure Mg(as-cast) [110] (b) Mg-1Zn (as-cast) [110] (c) Mg-6Zn (as-cast) [68] (d) Mg-1Zn (as-extruded, parallel to extrusion direction) [76] (e) Mg-1Zn (as-extruded, perpendicular to extrusion direction) [76] (f) Mg-6Zn (as-extruded) [68]

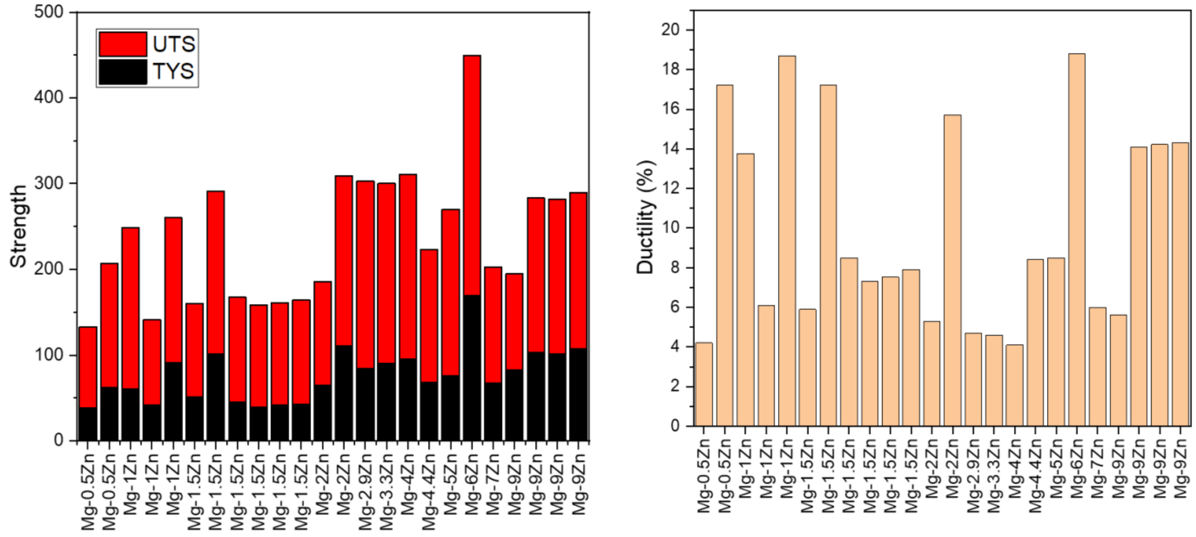

Figure 2.12: Summary of the mechanical properties of the binary Mg-Zn alloys

Zhang et al. patented a Mg-6wt.% Zn alloy and tested in vitro and in vivo degradation behavior in SBF [68]. The mechanical properties deteriorated rapidly in the initial stage of corrosion but later on it was slow. In-vivo cytotoxicity tests conducted on rabbits resulted in this material proven to be Grade 0-1, which means it is safe as an implant. This means that zinc released during degradation is safe and the excess Mg was excreted by kidneys but the mechanism of hydrogen adsorption was still to be studied.

Lu et al. conducted immersion test of as-cast Mg-3Zn in SBF and studied the 3D tomography of the corroded sample using µ-CT [118]. They visualized the corrosion phenomenon around the secondary phases.

Kubasek et al. [77] studied the structural characteristics and corrosion behavior of biodegradable binary Mg-1Zn and Mg-3Zn alloys. They found that zinc improves the corrosion resistance.

Cai et al. [109] tested the corrosion behavior of as-cast Mg-xZn alloys (x=1, 5 and 7 wt.%) in SBF solution. They found that the corrosion resistance of the alloys increased with increasing Zn content of upto 5 wt.% and beyond that resulted in MgZn intermetallic which acted as a cathode that led to micro-galvanic corrosion acceleration.

Peng et al. [76] studied as-cast and backward extruded Mg-xZn (x=0.5, 1, 1.5 and 2 wt.%) alloys and measured the corrosion rates in SBF. He concluded that the corrosion rates decreased after backward extrusion process and with the increase of Zn content more than 0.5 wt.%, the corrosion properties are decreased.

Lotfabadi et al. studied the effects of solution heat treatment on the corrosion of Mg-Zn alloys [119] and found that it is beneficial to enhance the corrosion resistance. The reduction of microgalvanic effect of secondary phases is responsible for this.

Liu et al. also studied the effects of heat treatment on corrosion behaviors of Mg-3Zn alloy in 0.1 mol/L NaCl solution [120]. The T4 treatment was found to be beneficial, while T6 treatment decreased the corrosion resistance.

A typical corrosion surface morphology of Mg-6Zn in comparison to pure Mg is shown in Figure 2.13. The summary of corrosion rates of Mg-Zn alloys are presented in Figure 2.14.

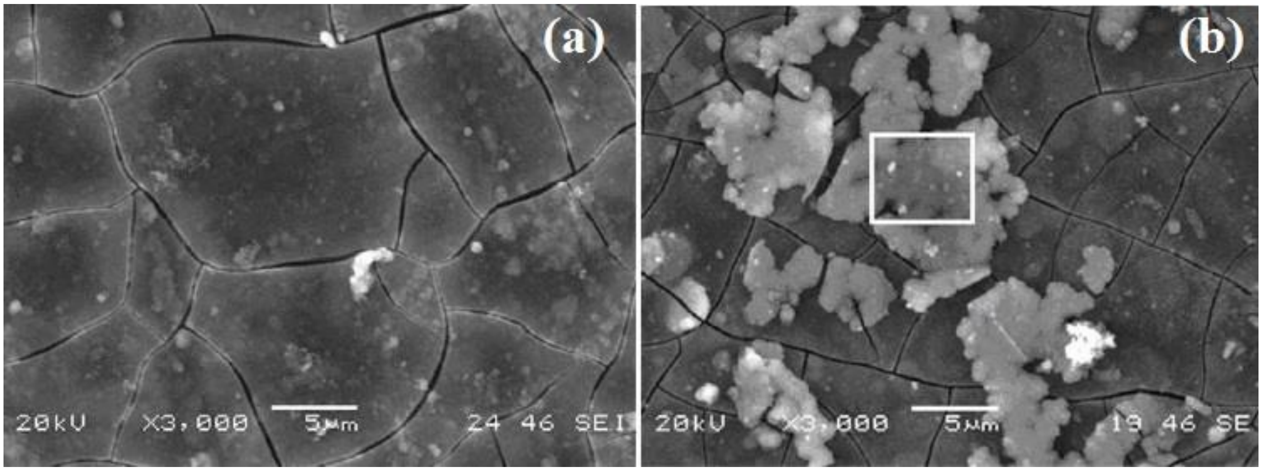

Figure 2.13: Typical corrosion morphology of pure Mg (a) and Mg-6Zn (b) after immersion in SBF for 30 days [68]

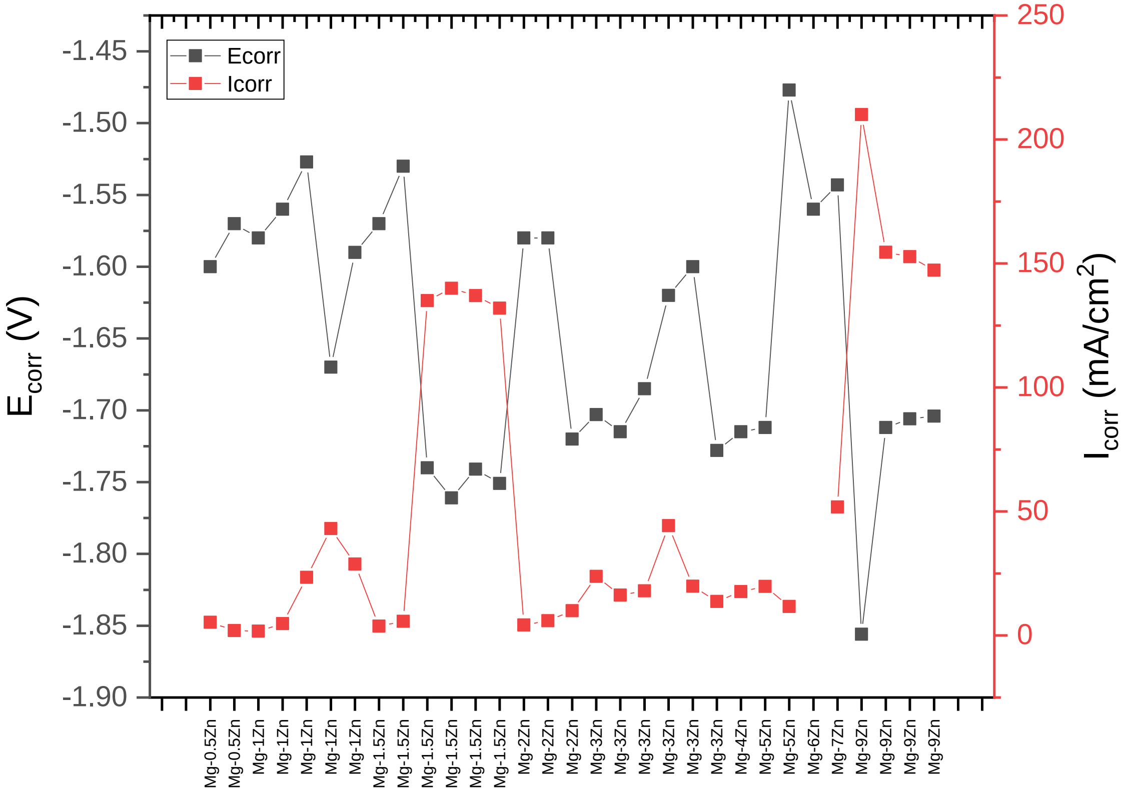

Figure 2.14: Summary of the corrosion rates of the binary Mg-Zn alloys in different corrosive media

2.6.4. Mg-Zn-X alloys

2.6.4.1. Influence of Ca on Mg-Zn

MgZnCa glasses were studied by Zberg et al. and due to the extended solubility of Zn (35 at.%) in the amorphous structure, these materials showed marginal hydrogen evolution during in vitro and in vivo degradation [121].

A similar approach was carried out by Datta et al. by synthesizing Mg-35 at.% Zn-5 at.% Ca amorphous alloys after 5h of mechanical alloying using SPEX shaker mill [122].

Xu et al. synthesized Mg-xZn-1Ca with x= 10, 20 and 30 wt.% using melting and solidification method [123]. The corrosion rate measurements tested in phosphate buffer saline solution was found to be better than 99.9% pure Mg but inferior to that of AZ31B.

Yin et al. varied the Ca content by synthesizing Mg-5Zn-xCa (x=1, 2 and 3 wt.%) and studied the biocompatibility of these alloys[124]. The mechanical properties enhanced with increase in Ca content but it reduced the corrosion resistance. But all the alloys did not induce toxicity to L-929 cells during the cytocompatibility evaluation.

Lu et al. studied the bio-corrosion behavior of Mg-3Zn-0.3Ca in SBF[125]. Heat treatment to alter the grain size and secondary volume fraction were done to study their effects on the bio-corrosion behavior and they have seen its improvement.

With the focus shifted from concentrating on the amount of zinc, calcium also was varied in similar fashion by Zander et al. [126] and studied the formation and distribution of microstructural phases and in-vitro degradation behavior in Dubecco's Phosphate Buffered Solution (PBS) and Hanks' balanced salt solution without glucose (HBSS) at 37^{o}C. The phase $Mg_6Ca_2Zn_3$ acted as a temporary local corrosion barrier and also as cathodic site for the matrix phase.

Zhang et al. varied the amounts of zinc in Mg-xZn-1Ca (x=1, 2 and 3 wt.%) and studied the mechanical properties, degradation behavior in Hanks' solution at 37^{o}C and cytotoxicity in L-929 cells. By tailoring the Zn content, tensile strength can be increased from 105 MPa to 182 MPa and the ductility from 4.2% to 9.1%. The degradation rates declined due to the formation of a protective layer of magnesium hydroxide and Mg/Ca phosphates. L-929 cells were not induced by toxicity and these alloys are considered suitable for biomedical applications[107].

Bakhsheshi-Rad et al. have compared the microstructure and bio-corrosion behavior of Mg-xZn and ternary Mg-Ca-xZn (x=1.25, 2.5 and 4) using scanning electron microscopy, electrochemical and immersion tests. The binary Mg-Zn alloy consisted of $Mg_{12}Zn_{13}$ phase along with α-Mg and the ternary Mg-Ca-Zn alloys comprised of α-Mg along with Mg_2Ca, and $Ca_3Mg_xZn_{15-x}$ ($4.6 \leq x \leq 12$). For binary alloys, the polarization test in Kokubo SBF showed that corrosion rate of Mg-4Zn is the least[127].

Sun et al. calculated the mechanical properties of extruded Mg-4Zn-0.2Ca before and after immersion in SBF solutions [128]. It was found that after 30 days immersion, the yield strength dropped from 240 MPa to 160 MPa, ultimate tensile strength from 297 MPa to 220 MPa and the elastic modulus from 45 GPa to 40 GPa. Ductility was drastically reduced from 21.3% to 8.5% but these values were still enough to introduce them as a biomaterial. The addition of Zn and Ca was beneficial in enhancing the corrosion potential and reduce the degradation rate.

2.6.4.2. Influence of Y on Mg-Zn

Zhang et al. [129] studied the corrosion behavior of Mg-Zn-Y alloys with long period stacking ordered structures. In this work, they concluded that the X-phase ($Mg_{12}YZn$) is responsible for the acceleration of galvanic corrosion in α-Mg phase. But with moderate volume fraction and continuous distribution, the samples exhibited low corrosion rate, as observed for $Mg_{97}Zn_1Y_2$ alloy.

Perez et al [130] studied corrosion behavior of Mg-Zn-Y by introducing mischmetal in phosphate buffer saline solution. With increased mischmetal addition, due to more number of volume fraction of particles the number of galvanic microcells increased and it led to increase in corrosion rate. Therefore they concluded that with high Zn content and low RE content, optimization of corrosion resistance was possible with the formation of a protective $Mg(OH)_2$ and phosphate layers.

Wang et al. tried the nano-quasicrystals approach to synthesize Mg-Zn-Y alloys using melting and pouring in a wedge-shaped water-cooled copper mold [131]. Among the alloys synthesized, $Mg_{71}Zn_{26}Y_2Cu_1$ nano-QC alloy possessed high corrosion resistance in simulated seawater and it was attributed to the formation of nano-QCs and Mg-Y intermetallics.

Hanzi et al. used microalloying technique to synthesize Mg-Zn-Y based alloys using direct chill casting (DCC) technique followed by hot-extrusion [132]. By this technique, it was possible to promote the formation of grain-boundary-pinning second phases and to prevent them from coarsening. Both ZW21 ($Mg_{97}Zn_2Y_1$) and WZ21 ($Mg_{97}Y_2Zn_1$) showed promising results by degrading slowly and homogeneously in SBF.

Zhao et al. [133] studied corrosion behavior of $Mg_{100-3x}(Zn_1Y_2)_x$ in Dulbecco's modified eagle medium (DMEM) with 10% fetal bovine serum (FBS) as a simulated body fluid. They found that with increasing volume fraction of LPSO phase, the degradation rate was found to increase. Also, microalloying with zirconium and a secondary treatment like warm extrusion mitigated the degradation rate due to grain refinement.

Addition of aluminum to Mg-Zn-Y was tried and tested by Wang et al. [134] and the corrosion behavior in 3.5 wt.% NaCl hindered the cathodic hydrogen evolution and the surface film remained uniform and compact thereby improving the corrosion resistance.

2.6.4.3. Influence of Er on Mg-Zn

Addition of zinc (x=1, 2, 4, 6, 8, 10, 12 wt.%) to Mg-xZn-2Er were studied by Wang et al [135]. For additions of zinc upto 2 wt.%, the microstructure consisted of W-phase and α-Mg matrix. With further additions, the phases Mg_4Zn_7 and I evolve and W-phase disappeared. Among all the alloys, addition of 6 wt.% Zn was found to be beneficial to enhance the mechanical properties.

The effect of Zn/Er weight ratio on phase formation and mechanical properties of as-cast Mg-Zn-Er was studied by Li et al [136]. They have seen that when this ratio is less than 0.8, W-phase with a face-centered cubic structure is obtained. Above 6 and until 10, formation of I-phase with an icosahedral quasicrystalline structure is feasible. When the ratio is in the range of 1 and 4, these two phases co-exist.

To investigate the effect of heat-treatment on the microstructure evolution and the mechanical properties of Mg-Zn-Er system, Zhao et al. synthesized Mg-Zn-0.63Er containing icosahedral quasicrystalline phase (I-phase) [137]. Rod like $MgZn_2$ particles formed during synthesis was responsible for enhanced tensile strength.

Zhao-hui et al. adopted ultrasonic treatment on the molten Mg-Zn-Er alloy to study their effects on their mechanical properties both at room and high temperatures respectively [138]. With the ultrasonic vibration power of 600 W and time of 100s, the cavitation and acoustic streaming helped in refinement of microstructure and enhanced mechanical properties.

Leng et al. [139] studied the degradation behavior of Mg-8Y-1Er-2Zn alloy containing LPSO phase in SBF. Their research proved that these materials could retain their mechanical properties after immersing in SBF for 240h. (Y.S=216 MPa from 275 MPa, U.T.S = 286 MPa from 359 MPa and ductility of 6.8% from 19%)

Addition of Ca to Mg-6Zn-0.5Er to study the microstructural control and hardening response was done by Zheng et al.[140]. Addition of Ca leads to refinement of precipitates and was responsible for improving the peak-aged hardness greatly to 87 HV.

Liu et al. [141] studied Mg-6Zn-xEr (x=0.3,0.5, 1, 1.5, 2) in their as-cast, as-extruded and extruded-T5 states and found that 0.5wt.% addition had a great effect on enhancing age hardening response. They attributed it to the refinement of microstructures and the precipitation of β′ phase.

Wang et al. [142] studied the effect of W-phase on the mechanical properties of as-extruded Mg-xZn-zEr (x=2, 4 and 6 wt.%) alloys and also the effect of extrusion temperature. With increasing Zn and Er contents, the W phase fraction increased and it led to an increase in the mechanical properties. For Mg-6Zn-6Er alloy hot-extruded at 400^oC exhibited better comprehensive mechanical properties.

Wang et al. [143] also studied the alloys with Mg-xZn-yEr (x/y=6) composition and found that during hot extrusion, the I-phase that was formed during casting destroyed, leading to fine precipitation and distribution of nano-scale quasicrystalline particles.

Liu et al. [144] studied the influence of both I-phase and W-phase on Mg-9Zn-xEr (x=3, 4.5 and 6 wt.%) alloys and found that with increasing content of erbium, the volume fraction of secondary phases increased (W-phase). This enhanced the strength, compensating the ductility values.

An uniform degradation behavior was achieved with the formation of stacking faults by Zhang et al. [145] in Mg-8Er-1Zn prepared by a combined process of direct-chill semi-continuous casting, heat-treatment and hot-extrusion.

The following Figure 2.15 provides a summary of tensile properties of Mg-xZn-yEr alloys.

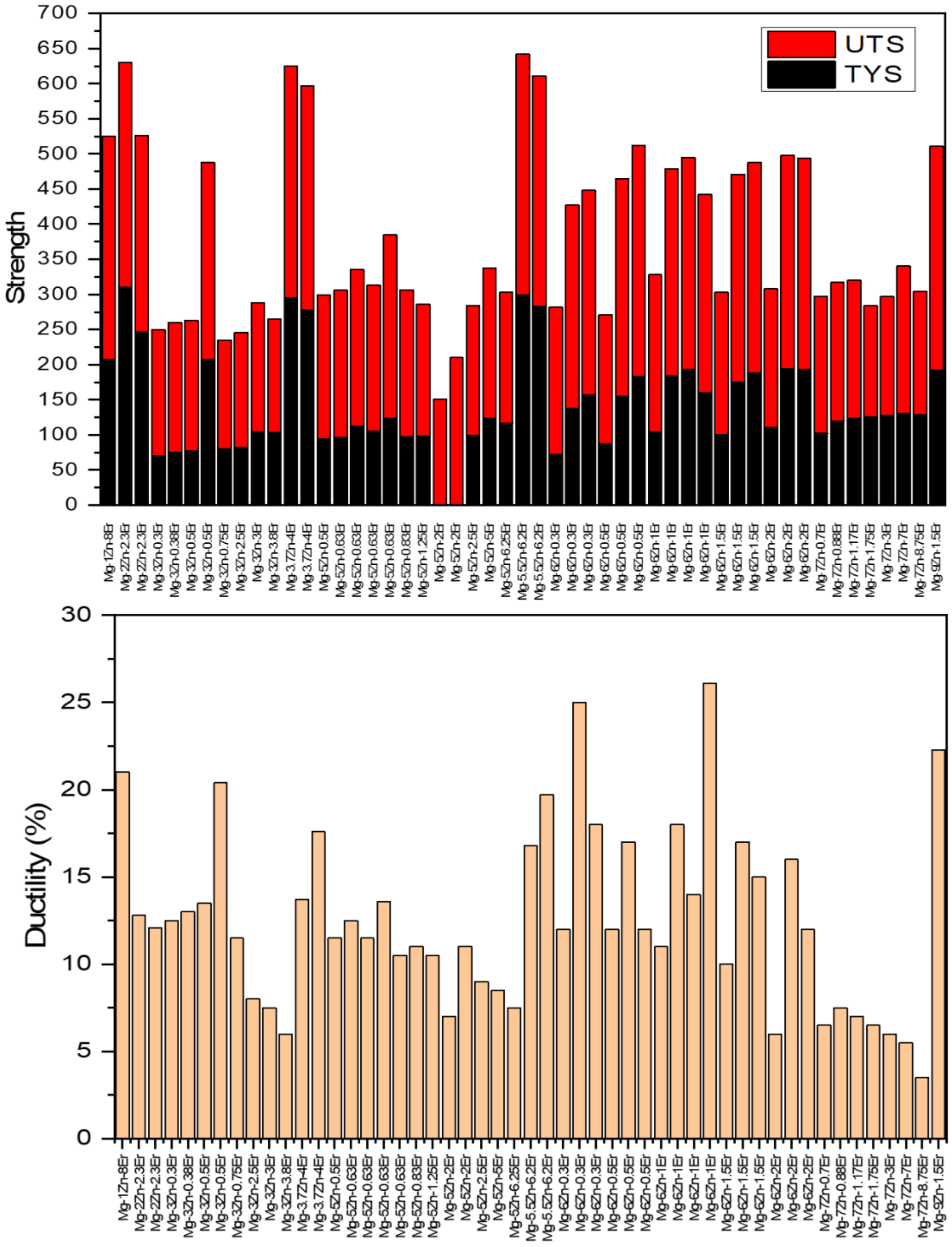

Figure 2.15: Mechanical properties of Mg-Zn-Er alloys

With regard to corrosion and bio-corrosion of Mg-Zn-Er, there are only few studies available. Anticorrosion phase LPSO was developed on a Mg-8Y-1Er-2Zn biomaterial by Leng et al. that imposed good corrosion resistance [139]. These phases are of 18R type consisted of long stripes in the extruded alloys which are uniformly distributed. Zhang et al. [145] created a special defect structure with stacking faults on a Mg-8Zn-1Er alloy. These stacking faults which have high free energy get corroded first, leaving the bare metal uncorroded. It should be noted that for both these alloys, high amount of rare earth material was used.

2.6.5. Mg-based quaternary alloys

To further enhance the mechanical properties and corrosion behavior of Mg-Zn based bio-materials, a fourth element could be introduced during alloying.

Hao et al. investigated a quaternary Mg-8Er-5Sn-0.5Zr considering a Zn/Er ratio of 1.6 [146]. The extruded and annealed alloy exhibited superior mechanical properties (Yield stress = 310 MPa and elongation 14%) and the microstructure comprised of α-Mg, block W phase and high-density fine lamellar-shaped LPSO phase.

Xu et al. [147] synthesized a novel Mg-4Er-4Gd-1Zn alloy reinforced with stacking faults by combined process of direct-chill semi-continuous casting, heat treatment and hot-extrusion. Due to these profuse nano-spaced basal plane stacking faults, the mechanical properties at room temperature were phenomenal and their study provides a new perspective for developing magnesium alloys.

Nominal additions (0.5, 1, 2 and 4 wt.%) Er on ZK60 alloys were fabricated using semi continuous casting by Zhang et al. to study the dynamic recrystallization behavior by hot compression tests using Gleeble 1500D thermo-mechanical simulator [148].

Chen et al. [149] also synthesized ZK60 alloys with erbium additions using semi-continuous casting followed by hot extrusion with an extrusion ratio of 25 at 400 ^{o}C. The solutionized bars were aged at 200 ^{o}C for 10h. The static precipitation after aging let to decrease in defects and hence the plasticity was compensated. Several studies have been conducted in Mg-Zn quaternary alloy systems with elemental additions of Dy, Zr, Nd, Er, Y, Ca, Gd, Mn [130,150–165]

2.7. Surface Treatments

Even if a material is biodegradable, the corrosion phenomenon could be too rapid and inhomogeneous. This is because magnesium alloys have a tendency for localized corrosion [166]. Therefore to further improve the corrosion behavior, it is essential to carry out surface treatments in the form of coatings and provide a layer made of either ceramic, polymer or a composite [167]. So far in the literature, there is advancement in the development on coatings for aircraft components. Also in the field of electronic devices, the coatings are used for aesthetic purposes. But in the recent decade there is an increase in the scientific work published in the area of coatings for biological applications.

Coatings could be broadly classified into two types:

(a) Conversion coatings
(b) Deposited coatings

2.7.1. Conversion coatings

These are grown in-situ and it is due to a certain chemical reaction between the material and environment [168]. The surfaces are converted chemically into an oxide layer. This inward and outward growth of oxide layer changes the component geometry. In the automotive industry, varnishing is a well-known example of an organic coating [168]. Pure magnesium surfaces have high alkalinity and hence a surface treatment prior to the application of an organic coating is essential [169]. Other than the integrity of the coating deposited and providing appropriate corrosion protection, these coatings for biomedical applications exhibit bioactivity, and other biological functions. Also they should enable biodegradation.

Several techniques have been adopted for conversion coatings and they are listed below:

(a) Chemical conversion (immersion)

(b) Plasma electrolytic oxidation

(c) Anodization

(d) Ion implantation

The oxide film that forms in the atmosphere for aluminum and titanium alloys are dense and protective. But for magnesium alloys, this magnesium oxide film that is formed on the surface in a normal environment and the hydroxide later in atmospheric humidity shows limited protective effect [170].

The surface layer is very thin and it consists of an inner layer of thickness 2.5 nm MgO and the outer layer $Mg(OH)_2$ with a thickness of 2.2 nm, as studied by Santamatia et al using X-ray photoelectron spectroscopy (XPS) and photocurrent spectroscopy (PCS) [171–173]. Other than introducing $Mg(OH)_2$, different mixture of oxides and hydroxides from electrolytic baths can be made chemically. But one effective corrosion protective coating, i.e., chromate coatings were not environmentally friendly and they are banned in EU in 2007. Also they are carcinogenic and hence could not be used for biomedical applications. But chromate-free coatings like phosphating (magnesium phosphate [174–176], zinc phosphate [177,178], manganese phosphate [167,179–182], zirconium oxide [183]) have been developed whose layer thickness is in the order of several micrometers [181,184]. Also formation of a hydroxyapatite (HA) layer on the surface of magnesium alloys are of a great interest today. This layer is similar to that of the mineral phase of bone. Amorphous carbonated calcium-magnesium phosphate layers were formed by Rettig and

Virtanen after immersion in SBF for 5 days [185,186]. Different SBF solutions form different types of coating, this calcium phosphate formation is a type of precipitation process [187].

As a form of pre-treatment to eradicate surface contamination, a standard practice is acid pickling [188]. It has been found that a fluoride containing coating on Mg alloys can enhance corrosion resistance [189–192].

2.7.1.1. Fluoride coatings

These are one among the few coatings that can increase new mineral deposition in bones. For the normal diet, fluorides are essential and it aids in the skeletal growth.

Jian-zhong et al. studied fluoride coatings on ingot-cast AZ91D using HF treatment. This coating could protect from corrosion only in fluoride solutions [193]. Conceicao et al. studied the effect of HF treatment on corrosion behavior and surface composition of AZ31 alloy [194]. Several compounds such as hydroxides, oxides and fluorides formed at the surface whose thickness depends on the immersion time and acid concentration. It was suggested to use lower concentration and longer immersion time for thick hydroxide layer.

Yan et al. studied the formation mechanism of these fluoride coatings of AZ31B and its effect on the mechanical and corrosion properties were tested using a three-point bending corrosion test [195]. Hydroxyapatite formation on fluoride coated AZ31B after immersion in SBF shows good bioactivity [196]. These tests revealed that this material is ideal for biodegradable applications.

Using powder metallurgy route, Pereda et al. synthesized compacts and hot-extruded of pure magnesium [197]. They were treated with potassium fluoride solutions for different time periods to provide fluoride coatings which provided higher corrosion resistance.

Jian Zhang et al. studied fluoride treatment on a patented Mg-Nd-Zn-Zr alloy (JDBM) to improve its degradation kinetics [198]. Cytocompatibility tests showed many live cells retained in the coated than the bare alloy.

In vivo experiments by introducing MgF_2 coated layer on Mg-0.8Ca on marrow cavities of both tibiae of 10 New Zealand White rabbits were carried out by Thomann et al. [199]. Analysis was done after 3 and 6 months of implantation were carried out and it was found that the coated implants exhibited greater strength than the bare samples after 6 months.

Andreas et al. developed MgF_2 coating on Mg-xCa (x=0.4, 0.6, 0.8, 1.2 and 2 wt.%) alloys to enhance the degradation kinetics [3]. The degradation kinetics enhanced for Ca content greater than 0.8 wt.% and it improved for coated samples.

2.7.2.Deposited coatings

This could be classified into three sections:

(a) Metallic coatings
(b) Inorganic coatings
(c) Organic coatings

2.7.2.1. Metallic coatings

As magnesium is highly reactive, it is a challenge to deposit metals on magnesium's surface that has a low electrode potential. If the coating is locally damaged then it is susceptible to galvanic corrosion, and hence leads to immediate degradation of the material. Also for the biocompatibility part, many metals cannot fit into these criteria and hence non-degradable coatings are not to be used. Recent studies of coating pure magnesium on a magnesium alloy substrate were done [186].

2.7.2.2. Inorganic coatings

Diamonds like carbon (DLC) coatings on magnesium alloys were studied but since these coatings are not biodegradable, their interest is limited.

2.7.2.3. Organic coatings

Functionalized organic coatings like gelatin, PEG/PLGA copolymer, polyphosphazene for applications like drug delivery is made by dipping magnesium alloys in an organic based solution.

2.8. Conclusion

Mg-Ca alloys have good biocompatibility and biodegradability. But these alloys could undergo fast corrosion due to the presence of intermetallic phases. Mg-Zn alloys also need to be further improved by investigating the mechanisms controlling the influence of Zn contents. Thus with regard to Mg-Ca alloys, several other biocompatible elements like Zr, Mn and Zn would be appropriate alloying additions to further develop them. Addition of Er to Mg alloys was not extensively studied to enhance the corrosion resistance, but the mechanical property increment were significant and their study provides a new perspective for developing magnesium alloys [130–139]. Also, since it is high soluble rare-earth element (similar to Y, Gd and Dy), they increase the viability of the cell lines. Influence of W-phase and i-phase on the corrosion behavior of Mg-Zn-RE alloys has not been studied in detail. In the literature, it could be observed that multielementary compositions give more choices to design a material. Also, fluoride coatings could further enhance the corrosion resistance and induce biocompatibility. The area of bio corrosion studies is cross-disciplinary in nature. It involves several branches of science including material science, engineering, biochemistry, chemistry, medicine. When experiments and data collection/interpretation are conducted by experts of only one or some of these fields, there is an unfortunate consequence that most important details could be foreseen. Therefore, some experimental standards have to be defined to minimize errors and increase data repeatability. For magnesium based materials, it is necessary to devise tests according to earlier successful studies conducted, as some of the ASTM standards for corrosion tests are not applicable [200].

CHAPTER 3

EXPERIMENTAL PROCEDURE

3. Experimental Procedure

3.1. Overview

To study the individual effects of low weight percent zinc and rare earth element erbium on the microstructural, corrosion and mechanical properties of pure magnesium, Mg based alloys were primarily synthesized in house by disintegrated melt deposition technique (DMD, liquid-phase) followed by hot-extrusion. The raw materials required for the synthesis were procured from various suppliers. The as-received raw materials were weighed and prepared as per the casting requirements. DMD technique was employed to synthesize Mg and its alloys. The deposited ingots obtained from the DMD process were machined into billets using a lathe and subsequently hot extruded into rods. The extruded rods were then further machined for mechanical characterization. The details of the processing techniques and parameters utilized in the current study are explained in detail in the subsequent sections.

3.2. Materials

Magnesium turnings of 99.9% purity (ACROS organics, USA), pellets of zinc, calcium and Mg-30 wt.% Er master alloy of 99% purity (Sunrelier Metal Co. Limited, Shanghai, China) were used as matrix and alloying additions respectively. Five compositions were decided prior to casting by changing the stoichiometry of alloying additions.

3.3. Primary Processing

The synthesis of magnesium-rare earth alloys was successfully accomplished using the DMD technique. The following section provides details of the processing methodology used.

3.3.1. Equipment and materials preparation for casting

3.3.1.1. Preparation of graphite crucible

A graphite crucible of size A12 with a diameter of 125 mm was drilled at the centre using a vertical drilling machine. Initially, a 10 mm drill bit was used as a pilot drill and then the crucible was drilled using a 25 mm drill bit. A graphite nozzle was hammered into the drilled hole at the base of the crucible. A plug was placed which is supported by stainless steel foil to ensure that the melt was contained within the crucible until it was ready to be deposited into the mold. A long wire was attached to the screw on the plug to aid in the pulling out of the plug for the melt to flow down into the mold beneath. A pictorial representation of the crucible setup is shown in Figure 3.1.

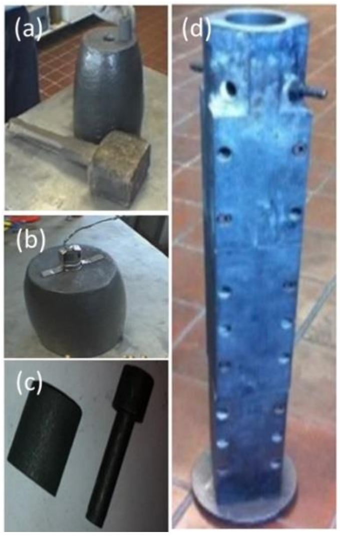

Figure 3.1: Components of DMD (a) Hammering the nozzle (b) Nozzle (c) Plug arrangement (d) Stainless steel mold

3.3.1.2. Preparation of mold

During the preparation of the mold, utmost care has to be taken to avoid dust and impurities. In order to provide a better interface between the mold and metal, spraying of graphite was done on the mold. It was rested for a while and later the mold assembly was carried out by tightening the screws.

3.3.2. Superheating of raw materials in graphite crucible

3.3.2.1. Lowering the base of the setup

Assembled mold was placed at the base and inside the bottom most container of the DMD setup. The position of the stainless steel mold was carefully aligned so that the opening at the top of the mold was in line with the hole at the bottom of the furnace. Two argon inlets were connected to the entry of the mold so as to disintegrate the melt that was to be flowed through as shown in the Figure 3.2. A refractory material is placed on the top to avoid damage of argon inlets during pouring.

3.3.2.2. Setting up the furnace

A schematic of the setup is shown in Figure 3.2.

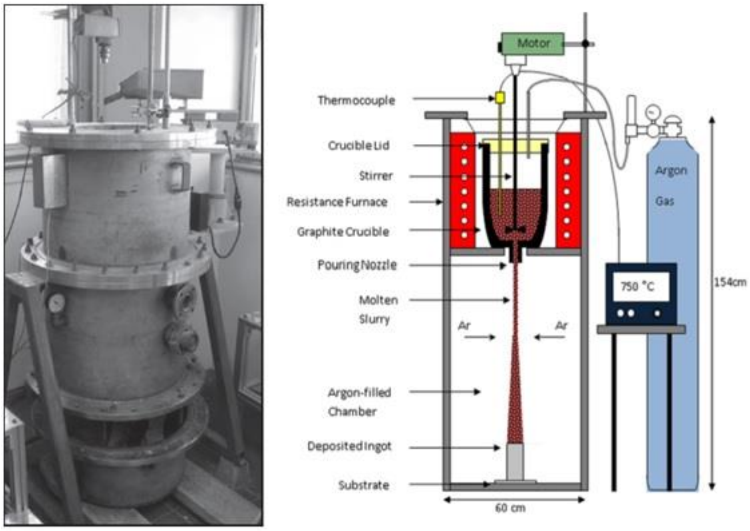

Figure 3.2: Photograph of actual DMD setup developed at the National University of Singapore and its schematic diagram (dimensions are appropriate and not drawn to scale)

The setup consisted of three chambers. After the insertion of crucible, stirrer and thermocouple was installed in place as shown in the Figure 3.3.

Figure 3.3: Magnified view of the gas inlet-stirrer-thermocouple setup

Stirrer was then connected to the motor. The raw materials were placed inside the crucible and covered. Argon gas inlet was inserted to create an inert environment during casting. The thermocouple was adjusted and the top of the furnace is covered with insulated materials to provide an enclosed environment and to minimize extensive heat loss.

3.3.3. Stirring

The temperature controller unit CAL-9000 was switched on along with the inert gas supply to the crucible. A certain gas flow rate of 5 L/min was set. After some time when the superheat temperature was reached, the motor was switched on to stir the molten metal at a uniform speed of approximately 450 rpm. Stirring was carried on for 5-10 minutes using a mild steel twin blade stirrer of 45° pitch. The stirring was done to facilitate the incorporation of the reinforcement particles in the Mg matrix with a uniform distribution. Later inert gas supply to mold was switched on.

3.3.4. Pouring of molten metal into mold

After the superheat temperature was reached and stirring was complete, the plug was pulled out from the base of the crucible to allow the melt to freely flow through the 10 mm centrally drilled hole of the nozzle into the mold. The resultant melt stream was disintegrated using two linear argon gas jets at a distance of 0.20 m from the melt pouring point. The gas flow rate was maintained at 25 L/min. The disintegrated melt slurry was subsequently deposited onto a circular metallic substrate located around 0.49 m from the gas disintegration point.. After casting, the base of the setup was lowered. Argon inlet into the mold was switched off and rubber hoses supplying argon gas was disconnected from the mold. The mold is then removed and dismantled to get the ingot. A typical dismantled mold and ingot obtained after casting is shown in Figure 3.4.

Figure 3.4: (a) Dismantled mold (b) Ingot of Mg-2Zn-0.6Ca-1Er

3.4. Secondary Processing

The 40 mm diameter ingots were machined by a lathe machine to a diameter of 36 mm and cut into billets with a length of approximately 45 mm. Further lathe machining was performed to ensure both ends are perpendicular to the surface. The ends were filed so as to prevent sharp edges and were then sprayed with colloidal graphite for lubrication purpose.

3.4.1. Extrusion

The billets were first soaked at 400 °C for 60 minutes in a constant temperature furnace before extrusion. Extrusion was then performed at 350 °C on a 150 ton hydraulic press using an extrusion ratio of 20.25:1, producing rods of 8 mm diameter. A typical extrusion set-up is shown in Figure 3.5.

Figure 3.5: Extrusion setup

3.4.2. Post-Extrusion

Extruded rods were machined by OKUMA CNC lathe machine to produce tensile specimens. Sections of approximately 8 to 10 mm in height were also cut by a slow speed diamond blade to be used for various characterization studies.

3.5. Density and Porosity measurements

Density measurements were performed to quantify the percentage of porosity in the synthesized materials. The extruded rods were cut into smaller samples using the Precision Diamond Cutting Machine and were subsequently polished to remove any surface contamination. The experimental mass densities of Mg-based materials developed were determined using Archimedes' principle. This involved weighing the polished samples in air and then in distilled water using an AD ER-182A electronic balance with an accuracy of 0.0001 g. A schematic diagram for density measurements is shown in Figure 3.6.

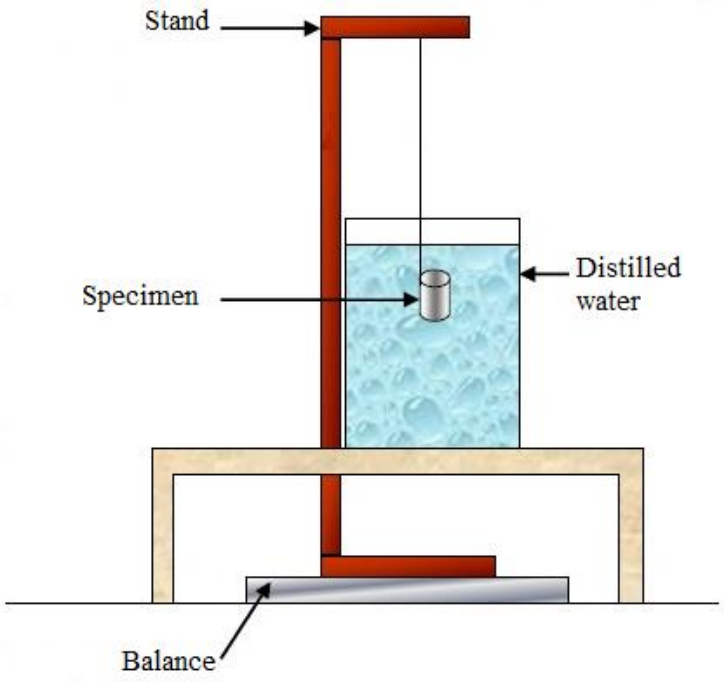

Figure 3.6: Schematic diagram for density measurement

3.6. X-Ray Diffraction Studies

X-ray diffraction (XRD) analysis was carried out on the polished samples (along the cross section of extruded rods, unless specified otherwise) of the developed Mg-materials using an automated Shimadzu LABX XRD-6000 diffractometer. The samples for x-ray diffraction (XRD) analysis were exposed to Cu Kα radiation (λ= 1.5406 Å) at a scanning speed of 2^{o}/min. The Bragg angles and the values of interplanar spacing, d, obtained were matched with standard values for Mg, Zn, Ca, Er and other related phases.

3.7. Microstructural Characterization

3.7.1. Sample Preparation

3.7.1.1. For optical micrographs

The specimens were mechanically polished using SiC papers up to 4000 grit on a Struers Labopol-5. These samples are then polished using 6 µm diamond paste[1], followed by 3 µm finish[2] and with 1µm finish[3]. The polishing discs were manufactured by Struers Ltd. The 'MD Nap'

---

[1] MD Dac cloth
[2] MD Mol cloth
[3] MD Nap cloth

polishing cloth was again used for the final polishing, using 0.25 µm. Ethanol or water-free lubricant was used throughout the whole polishing process to prevent the oxidation of the samples. The samples were ultrasonically rinsed in ethanol and dried in cold air after each polishing step.

3.7.1.2. For EBSD

The sample preparation method for EBSD is the same as above, except in the end an ion-polishing is given on the surface. A Model 1060 SEM Mill by Fischione Instruments is used. Here, the top surface should be given at least a 1 µm diamond finish before giving a surface finish. The area of interest is placed in the center with respect to the sample holder (stub). Selecting certain milling angles and beam voltage will allow us to carefully prepare a sample with better surface finish.

3.7.1.3. For TEM

Initial thickness is brought down to 100 µm, and then a 3 mm hole is punched out and then taken to ion polishing. A Precision Ion Polishing System (PIPS) from GATAN is used to produce TEM samples. Ion polishing is done using two miniature penning guns oriented at a certain milling angle. Low angle of 3° is used to minimize beam damage and heating in the sample. Low rotation speed is adapted and a beam voltage of 3.5 keV is used.

3.7.2. Etching method

The samples were cut longitudinally, polished and etched using suitable etching solutions to reveal the grain boundaries. The solution used for etching is acetic picral, which is comprised of 5mL acetic acid, 10 mL water, 6g picric acid and 100 mL ethanol (95%). Gentle agitation of the specimen is given during immersion time period of 15s so that it results in an uniform etch.

3.7.3. Optical Microscopy

The grain size and morphology was determined by image analysis of the respective optical micrographs obtained using the LEICA - DM 2500M Metallographic Optical Microscope. The grain boundaries were then traced out from the micrographs. The grain size analysis was then accomplished by the SCION image analyzer software and a Microsoft Excel program was written to calculate the grain size and aspect ratio of the grains. For every sample, a minimum of 1000 grains were analyzed.

3.7.4. Scanning electron microscopy

A JEOL JSM-7800F LV scanning electron microscope with sub-nanometric spatial resolution and nanoscale analytical capabilities in EDS was used. This microscope has a very good spatial resolution of 0.8 nm at 15 kV. It is comprised of secondary and backscattered electron detectors in the chamber, in-lens and low-vacuum mode.

3.7.4.1. Energy Dispersive Spectroscopy (EDS)

To perform elemental analysis in the microstructures, an EDS detector is introduced during the microstructural observation. Line-scan, point analysis and map analysis could be carried out.

3.7.4.2. Electron Back-scattered Diffraction (EBSD)

To perform quantitative microstructural analysis and to identify the orientation (texture) of the alloys in the Scanning Electron Microscope, EBSD is used. Using this technique, one can not only understand the spatial information, but visualize the grain size, local texture, local strain and accurately identify minor phases. This technique can also be used in conjunction with EDS. The scanning microscope is coupled with Oxford Instruments EDS/EBSD coupled system (80 mm^2 SDD spectrometer and HKl Nordlys Max2 EBSD camera)

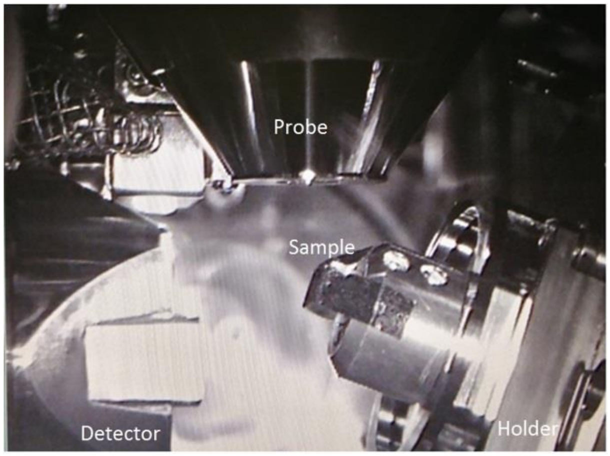

Figure 3.7: EBSD setup as seen using SEM camera

3.7.4.2.1. Components of a EBSD system

A schematic of the EBSD setup as seen using SEM camera is represented in Figure 3.7. The following are the components of a EBSD system:

(a) Sample tilted to 70º relative to the normal incidence of the electron beam, in order to increase the contrast of the diffraction pattern and maximize the number of electrons scattering from the sample. One can also use a pre-tilted holder for this purpose.

(b) Phosphor screen where electrons scattered from the sample are fluoresced.

(c) Camera with optics to capture the diffraction pattern

(d) Fore scatter diodes (FSD) on the screen to generate images of the sample before collecting EBSD data.

(e) Software for acquisition and a computer.

3.7.4.2.2. Optimizing parameters

For acquisition of a pattern, it is important to understand several parameters that need to be optimized.

(a) Accelerating voltage: With increasing voltage, the wavelength reduces and so does the width of the Kikuchi bands in the diffraction pattern. With more energy deposited on the phosphor screen, a brighter pattern will be generated with minimum integration time. But for charging and thin samples that does not require the beam to penetrate, lower accelerating voltage is adopted.

(b) Probe current: The effects are same as that of accelerating voltage. But when it is too high, it is possible to lose spatial resolution, as it increases the electron beam size.

(c) Working distance and magnification: Tilt compensation and dynamic compensation has to be made as the image gets foreshortened due to tilt at low magnifications.

Due to inelastic scattering of the electrons at the sample surface, a diffraction pattern is produced. These diffracting beams interfere constructively when Bragg's equation is satisfied, producing Kikuchi band. These bands from every atomic plane collectively form a pattern called Kikuchi pattern. A computer automated program matches these patterns with the theoretical patterns and determines the crystal structure. In our study, the following parameters were used as seen in Table 3.1.

Table 3.1: Optimization parameters used for EBSD acquisition

Parameter	Value, unit
Accelerating voltage	20 kV
Probe current	13
Working distance	15 mm
Spot size	3

3.7.5. Transmission electron microscopy

Belonging to the Joint Center of Electron Microscopy and the laboratories of the Chevreul Research Federation, TEM FEI Tecnai G-20 is a very versatile transmission electron microscope. It consists of a LaB_6 filament operating at an accelerating voltage of 200 kV. It can also work in STEM mode and consists of GATAN energy filter for filtered imaging and Energy Loss Microanalysis (EELS). For local chemical analysis, a BRUKER EDS system is equipped. CCD camera is available for digital acquisition.

3.8. Mechanical Characterization

3.8.1. Damping characteristics

Impulse excitation technique was used as seen in Figure 3.8 to measure the resonant frequency and internal friction of samples. For predefined shapes like rectangular bars, cylindrical rods and disc shaped samples it is also used to calculate the elastic properties. Measurements are done by tapping the sample with a small hammer and capturing the induced vibration signal with a microphone. The captured vibration signal is sent to the RFDA software where it is analyzed and the resonant frequency, internal friction and elastic properties are determined according to ASTM E 1876. The equation used to calculate Young's modulus is:

$$E = T\,\frac{m.f_f^2}{w}\left(\frac{l}{t}\right)^3$$

where, E = Young's modulus, f_f = Flexural frequency, m = mass, l = Length, w = Width, t = Thickness, T = Correction co-efficient

Figure 3.8: Impulse excitation technique

3.8.2. Microhardness measurements

The microhardness measurements were carried out on the as-polished samples using Matsuzawa MXT 50 automatic digital Microhardness tester. Vickers indenter under a test load of 25 gf and a dwell time of 15 s was used to perform the micro hardness tests in accordance with the ASTM: E384-11e1. Vickers indenter is a square-based pyramidal shaped diamond indenter with face angle 136° and the hardness value was calculated by dividing the force applied to the indenter by the surface area of the permanent impression made by the indenter. The average of the measured two diagonals of the indentation is then plugged to the following equation:

HV = [(constant) * (test force) / indent diagonal] squared

The constant used in this equation is a function of the indenter geometry and the units used for quantifying diagonal dimensions and force. An assumption of zero elastic recovery after loading was made once the indenter was removed. To reduce vibrations and to ensure the flatness of the sample during indentation, special precautions were taken during the measurements. Prior to measurements, the microhardness tester is calibrated by the standard block. The tests were conducted on three samples for each composition for 10-15 repeatable readings.

3.8.3. Tensile properties

A fully automated servo-hydraulic mechanical testing machine, Model-MTS 810 was used to determine the tensile properties of the developed Mg-based materials. The tests were conducted in accordance with ASTM: E8/8M-13a as seen in the Figure 3.9. The crosshead speed was set at 0.254 mm/min. Specimens with 5 mm diameter and 25 mm gauge length was used. Instron 2630 - 100 series clip-on type extensometer was used to measure the failure strain. For each composition, a minimum of 5 tests were conducted to obtain repeatable values. The tensile testing equipment is represented in Figure 3.10.

Dimensions and Tolerances:

G - Guage length: 25.0 ±0.1 mm

D - Diameter: 5.0 ± 0.1 mm

R - Radius of fillet: 5.0

A - Length of reduced section: 30

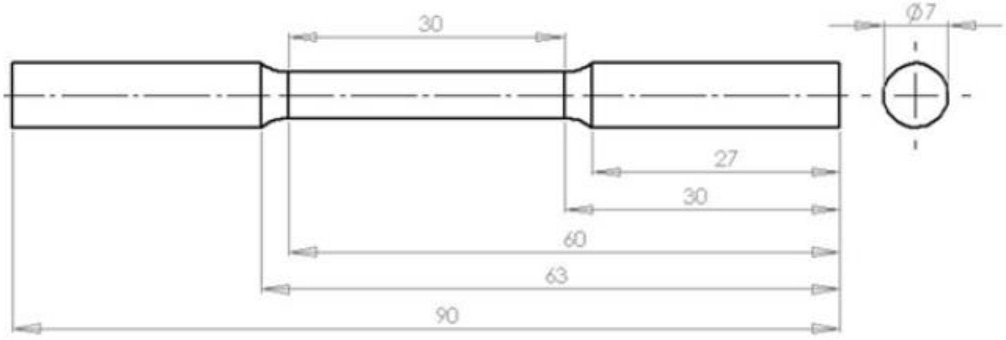

Figure 3.9: Schematic diagram of Tensile Sample Specifications

Figure 3.10: Tensile testing equipment

3.8.4. Compressive properties

The compressive properties of the developed Mg-based materials were determined in accordance with ASTM: E9-09 using MTS 810 testing machine with a crosshead speed set at 0.04 mm/min. Compressive test specimens of 8 mm diameter with length to diameter ratio, l/d =1, were used. For each composition, a minimum of 5 tests were conducted to obtain repeatable values.

3.8.5. Fractography

The fracture surface analyses of all the Mg-materials, tested under tension were studied using JEOL JSM-5800 LV SEM. The samples after tensile test were broken and the fracture surfaces are carefully stored in order to avoid oxidation and contamination. The region close to the fracture surface is cut and they are analyzed in SEM.

3.9. Electrochemical behavior

3.9.1. Phosphate buffer saline (PBS) solution preparation

A tablet of PBS was dissolved in 200 mL of deionized water at pH of 7.4 and at 25^{o}C. The composition of a tablet of PBS is listed in the following Table 3.2.

Table 3.2: Composition of one tablet of PBS dissolved in 200 mL of deionized water at pH 7.4 and at 25°C

Material	Composition, M
Phosphate buffer	0.01
Potassium chloride	0.0027
Sodium chloride	0.137

3.9.2. Immersion test

The sections of length 5mm from the extruded rods were cut and polished using a 2000 grit silicon-carbide paper and cleaned with ethanol and dried. These were immersed on PBS contained beakers that were placed in a water bath maintained at a temperature of 37 °C. The samples before and after immersion were weighed. The ratio of PBS solution to the surface area of the sample was kept at 0.25 mL/cm^2 in all the experiments. After every time interval (1, 3, 5 and 7 days), the samples were removed from the beaker, cleaned to remove corrosion products with chromic acid (ASTM G1-90), washed in ethanol, air dried and weighed immediately after cleaning. The reason for choosing chromic acid for cleaning the corrosion products is because it has a negligible corrosion attack on magnesium alloys but it ensures the proper removal of corrosion products, which increases with heating [201].

3.9.3. Hydrogen evolution test

The sections of length 5mm from the extruded rods were cut and polished using a 2000 grit silicon-carbide paper and cleaned with ethanol and dried. These were immersed in PBS contained beakers placed in a water bath maintained at a temperature of 37 °C. The samples before and after immersion are weighed. Each sample was covered with an inverted flask and a graduated cylinder was used to collect hydrogen bubbles. Using this method, the volume of hydrogen released was measured. The setup is shown in the Figure 3.11.

Figure 3.11: H_2 evolution setup

3.9.4. Potentiodynamic Polarization test

Electrochemical measurements were carried out using a VOLTAMETER electrochemical workstation. A standard three-electrode setup was used to perform electrochemical measurement: i.e., a test sample, a platinum wire and a saturated calomel electrode act as working electrode, counter electrode and reference electrode, respectively. Variations in the open circuit potential (OCP) were recorded with immersion times up to 60 minutes. Then the potentiodynamic tests were commenced. Tests were performed three times to confirm the reproducibility of the results. Samples (10 mm * 8 mm * 2 mm) were obtained and connected to a wire that provides an electrical connection. The exposed end of the wire was first fixed on the back side of the sample by using silver paint (Agar). The sample was mounted in cold resin (Metprep) to isolate the corrosion medium, leaving an exposed area of 0.5 cm^2 as working electrode. The scan rate of the polarization curves measurement was 0.1 V/s. The polarization started from -2.5 V to 2.5 V. 0.5 wt.% NaCl solution was use as electrolyte. Before the test, the specimens were ground successively with SiC abrasive papers from 180 grit to 4000 grit, then polished to 1 µm, ultrasonically rinsed in the ethanol and finally dried in cool air. Before starting the test, every specimen was immersed for 10 min to keep the data at a stable level. The corrosion rate is calculated using corrosion current (i_{corr}) determined using Tafel plot. The equation used to determine corrosion rate (CR) in mm/year is as follows:

$$CR = 3.27 * (i_{corr}) * (\frac{e}{d})$$

where i_{corr} is corrosion current (in µA/cm^2), e is Equivalent weight (Atomic Weight/valency), d is Density (g/cm^3)

Atomic weight of Mg is 24 g and valency is 2. Therefore, Equivalent Weight e=12. Density of magnesium is 1.7 g/cm^3.

Figure 3.12: Potentiodynamic polarization setup

3.10. Coating procedure

3.10.1. Fluoride treatment

The samples were first polished upto 2000 grit roughness, followed by rinsing in 95% ethanol and ultrasonicating in 95% ethanol solution for 5 minutes to remove dirt and clean the surface. Followed by cleaning procedure, the coating treatment involves immersion of samples in a 40% hydrofluoric acid (HF) solution for 12h and 24h at room temperature, followed by rinsing in distilled water and drying in air. The experiment was conducted in a fumehood and care was been taken to ensure uniform coating throughout the surface area of the samples.

3.10.2. Characterization

3.10.2.1. Surface wettability and energy

Static contact angle test was performed using the sessile drop method with an optical contact angle system (OCA20, Germany). Reference liquid deionized water was used to determine the dispersive surface energy component (γ_S^d) and polar surface energy component (γ_S^p) using the Owens and Wendt approach. This drop formed on the end of the pipette tip is lowered onto the surface and after the drop is detached, this pipette is detached. Then a graduated eye piece is used to measure this contact angle. This is done after the drop has come to rest (after approx. 2 sec), a tangent is drawn to the intersection. The following equation was used:

$$\gamma_L\ (1 + cos\theta) = 2[\sqrt{(\gamma_L^d)(\gamma_S^d)} + \sqrt{(\gamma_L^p)(\gamma_S^p)}]$$

Where$\gamma_L$represented reference liquid surface energy and (γ_L^d), (γ_L^p) for its dispersive and polar component respectively. The values used for deionized water are: γ_L= 72.1 mN/m, γ_L^d =19.9 mN/m,

γ_L^p = 52.2 mN/m. For each liquid five drops (4 µL each) to each disk sample and three independent samples were tested.

3.10.2.2. Raman spectroscopy

The corroded and coated samples were analyzed using a Labram confocal Raman microspectrometer (Horiba, Jobin-Yvon) equipped with a 100* (N.A 0.9) Olympus objective. The substrates were mounted on the automated XY stages of the microscope without further sample preparation. A video camera provided an optical view of the samples. Raman scattering was excited along the optical axis of the microscope objective with a 473 nm wavelength laser beam (diode laser Cobolt 06-MLD – Cobolt Company). The laser power delivered on the sample was less than 5 mW to avoid any laser beam damage of the particle. Both automated point mode and mapping mode were used for generating 2D and 3D Raman data sets, respectively.

3.10.2.3. X-ray photoelectron spectroscopy (XPS)

X-ray photoelectron spectroscopy (XPS) characterization was carried out using the Kratos AXIS UltraDLD spectrometer using a monochromatic Al Kα X-ray source (10 mA, 12 kV). C 1s, O 1s, Fe 2p and La 3d high resolution spectra were obtained using 20eV pass energy while keeping a pressure in the analysis chamber below 5×10^{-9} during analysis. All spectra have been calibrated by giving the adventitious C 1s spectral component (C–C, C–H) a binding energy (BE) of 284.8 eV. A Shirley background 15 was subtracted from the spectra for quantification. The analysed area was about 300 µm × 700 µm.

This technique is used on the surface of the corroded samples to identify the elemental composition and chemical state of the atoms present. After corrosion, the samples are removed from PBS solution and they are dried. Careful attention is given such that the samples for XPS analysis do not undergo contaminated by the environment. It is also used to quantify the atomic percentage of some elements, such as C, Zn, Ca, P, Er, Mg and O, on the outermost surface layer during depth profile from the first 3-10 nm top layers of the sample.

3.11. Biocompatibility tests

3.11.1. Cytotoxicity tests

The cytotoxicity of the F-coated Mg samples was evaluated by the extraction method (ISO 10993-5), using a pre-osteoblastic cell line MC3T3-E1 (ATCC® CRL-2594 ™). The F-coated Mg samples were sterilized at 170 °C for 1 hour. Extracts of the Mg samples were prepared at a time interval: 72 h, by adding 6 cm^2 of sample in 1 mL of MEM-α culture medium with 10% of SBF and incubated at 37 °C and stirring at 80 rpm. Then, the complete culture medium was also incubated as a control. MC3T3-E1 cells were seeded at 4×10^3 cells / well in a 96-well tissue culture polystyrene plate (TCPS) and incubated at 37 °C, 5% CO_2 for 24 h. After the incubation, then the cell culture medium was replaced by the extraction medium (100 µL) on the cell layer.

The plate was incubated for 24 h at 37 °C and 5% CO_2. Finally, cell viability was assessed by using a fluorometric assay with AlamarBlue® reagent. It is an indicator that changes color and becomes fluorescent during the chemical reduction of the culture medium related to the metabolic activity of the cells. This test is therefore based on the measurement of the oxidation-reduction rate of this dye. This response, which can only take place with living cells, is proportional to cellular activity. Briefly, after incubation with the extraction medium or the culture medium (control), the medium of each well was replaced with 200 μL of AlamarBlue® 10% solution and the plate was incubated at 37 °C. and 5% CO_2 for 2 h. The fluorescence reading was measured using a fluorometer (Twinkle LB970TM, Berthold). The cell viability rate was calculated relative to the control.

Results and discussion

CHAPTER 4

MICROSTRUCTURE AND MECHANICAL PROPERTIES

4. Microstructure and mechanical properties

4.1. Introduction

During the development of model alloys, tailoring the microstructures has been given a substantial importance. This chapter outlines the investigations and observations carried out in the alloy development by carefully designing the compositions and alloying additions. The elements considered for alloying additions are zinc, calcium and erbium. Several compositions have been designed and developed and they have been tested for various properties. The microstructures and mechanical properties have been discussed in detail in the following sections of this chapter.

This section presents microstructure, tensile, compressive, damping and hardness behavior of Mg-Zn-RE system. The main aim of this part of the study is to understand the microstructural evolution and to evaluate the mechanical properties of pure magnesium through the addition of minimal alloying additions like zinc, calcium and erbium.

4.2. Results

The DMD technique was successful in synthesizing Mg and its alloys and all the experiments conducted were successful with highest output. This technique used two argon gas jets to disintegrate the liquid metal stream that allowed rapid cooling of the molten metal which results in fine-grained microstructure. Also, the homogeneous distribution of alloying elements was ensured after the melt was stirred before pouring down. To achieve high output of the product, care was taken to properly align the mold and the nozzle of the crucible. During melt processing, inert atmosphere condition was used to prevent the reaction between the air and the melt. If proper solidification conditions were not met, there is a high probability of the presence of macropores and agglomeration of alloying elements. Also since magnesium is unable to form stable carbides, there was no detectable reaction between the liquid melt and the graphite crucible.

4.2.1. Macrostructure

Synthesis of pure Mg, Mg-2Zn, Mg-2Zn-2Er, Mg-2Zn-0.6Ca-1Er, Mg-2Zn-0.6Ca and Mg-3Zn-0.5Er were successfully carried out by the DMD process followed by hot extrusion.

Figure 4.1: Macrographs of a cast ingot, a machined billet and an extruded rod

Figure 4.1 represents the three stages of synthesized material. The ingot labelled Mg alloy casting is the solidified alloy obtained after DMD process. The ends of the ingot consist of cracked structure. This is due to the non-uniform pouring of atomized melt that takes place during the beginning and end of the process and it is discarded from the ingot. The remaining ingot is cut in order to prepare billets of dimensions d=36mm and l=45mm using lathe. A shiny Mg billet could be seen in the figure. The visual observation of the surfaces of the as deposited pure Mg and alloy cast ingots indicates no macrostructural defects [202] like macropores as seen in Figure 4.1. Before extrusion, the billets are sprayed with graphite. Also following extrusion, these defects were not present. The shiny appearance on the extruded rods is lost due to the graphite spray prior to extrusion.

4.2.2. Density measurements

The results of the density measurements conducted on pure Mg and Mg alloys are tabulated in Table 4.1.

Table 4.1: Density measurements for pure Mg and its alloys in both as-DMDed and as-extruded conditions

Material	**Density (g/cc)**	
	As-DMDed	**As-extruded**
Pure Mg	1.679	1.711
Mg-2Zn	1.684	1.723
Mg-2Zn-2Er	1.697	1.726
Mg-2Zn-0.6Ca-1Er	1.694	1.722
Mg-2Zn-0.6Ca	1.687	1.718
Mg-3Zn-0.5Er	1.702	1.735

From the values of experimental and theoretical densities, it can be seen that near-dense materials ($\rho_{\text{pure Mg}}$ = 1.7 g/cc) have been developed. As-DMDed materials exhibit density values lower than that of as-extruded materials. This could be due to the porosity that is present in as-DMDed materials. As-DMDed pure Mg exhibits density value of 1.679 g/cc. Addition of 2Zn slightly enhanced the density value and the increment is observed for other alloys as well. As-extruded pure Mg exhibits density value of 1.711 g/cc and there is a slight increment from as-DMDed material. Additions of alloying elements have not significantly enhanced the density of pure Mg. This could be due to the minor addition (<4 wt.% alloying additions). The porosities and other defects have been eliminated after hot-extrusion and the extruded rods are completely dense.

4.2.3. X-ray Diffraction studies

Figure 4.2 shows the x-ray diffraction pattern of the extruded pure Mg and its alloys containing Zn, Ca and Er in longitudinal direction. These diffractograms could be used to identify the change in crystallographic orientation (texture) due to the alloying additions used here like zinc, calcium and erbium. They are also used to identify the phases present in the alloys. For x-ray diffractograms of as-extruded pure Mg, the primary peaks are detected at $2\theta=32^o$, 34^o and 36^o when Cu-Kα radiation source is used. The peaks at these angles correspond to $(10\bar{1}0)$ prismatic, (0002) basal and $(10\bar{1}1)$ pyramidal planes of the HCP Mg-crystal. The XRD pattern in pure Mg indicates a typical extrusion texture (c/a = 1.634) with most of the basal planes aligned (nearly) parallel to the extrusion direction. For Mg-2Zn alloy, $MgZn_2$ phase is indexed at $2\theta=40.2^o$, and the basal texture is not as pronounced as pure Mg. The peak at 34^o has a reduced intensity as compared to pure Mg. For Mg-2Zn-2Er alloy, the basal plane at 34^o has the highest intensity. W-phase ($Mg_3Er_2Zn_3$) is indexed for this alloy at $2\theta=23.4^o$ and 37.2^o. For Mg-2Zn-0.6Ca-1Er and Mg-2Zn-0.6Ca alloy, $MgZn_2$ phase could be seen. These alloys exhibit similar intensity patterns for the primary peaks of magnesium. I-phase is detected for Mg-3Zn-0.5Er at $2\theta=38.5^o$.

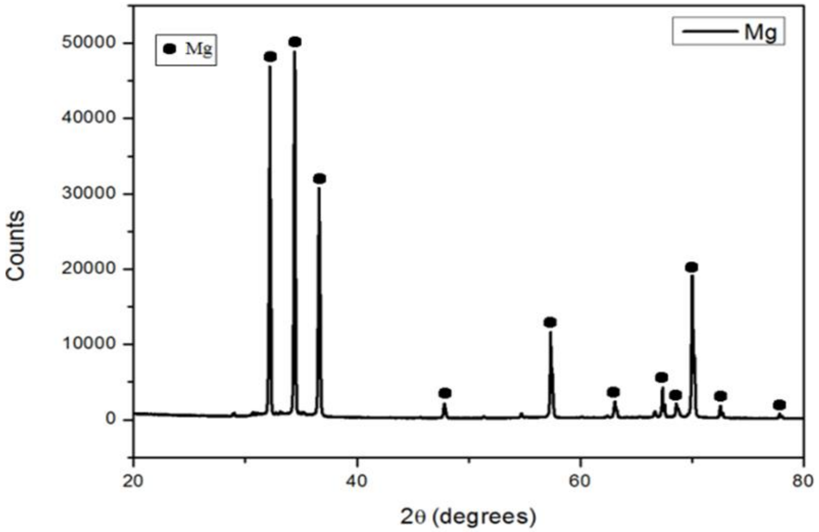
● Mg
Mg
Counts
50000
40000
30000
20000
10000
0
20
40
60
80
2θ (degrees)

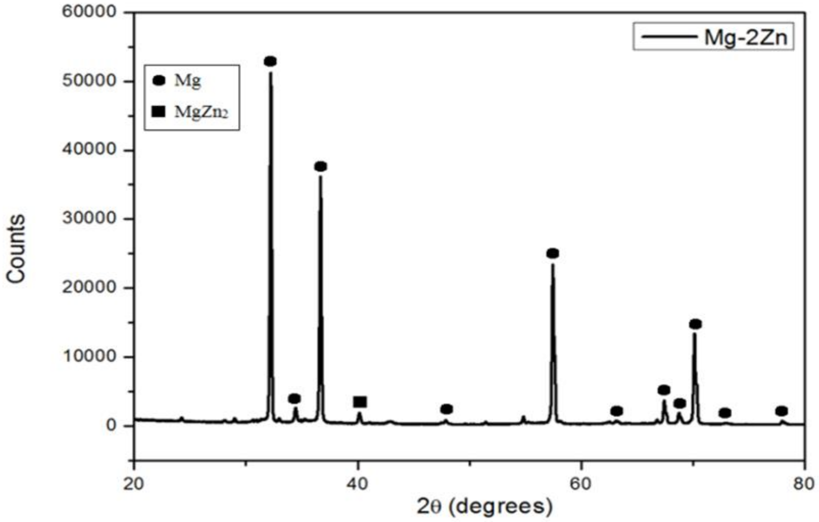
Mg-2Zn
● Mg
■ MgZn2
Counts
60000
50000
40000
30000
20000
10000
0
20
40
60
80
2θ (degrees)

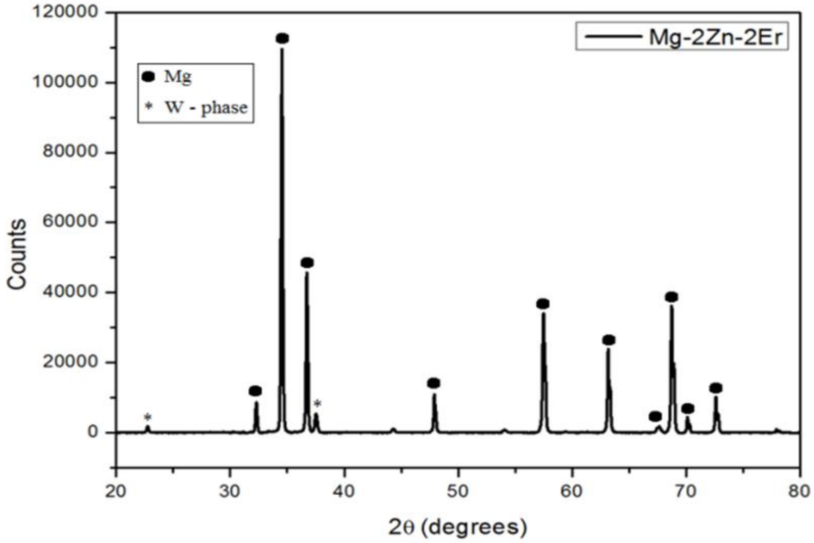
Mg-2Zn-2Er
● Mg
* W - phase
Counts
120000
100000
80000
60000
40000
20000
0
20
30
40
50
60
70
80
2θ (degrees)

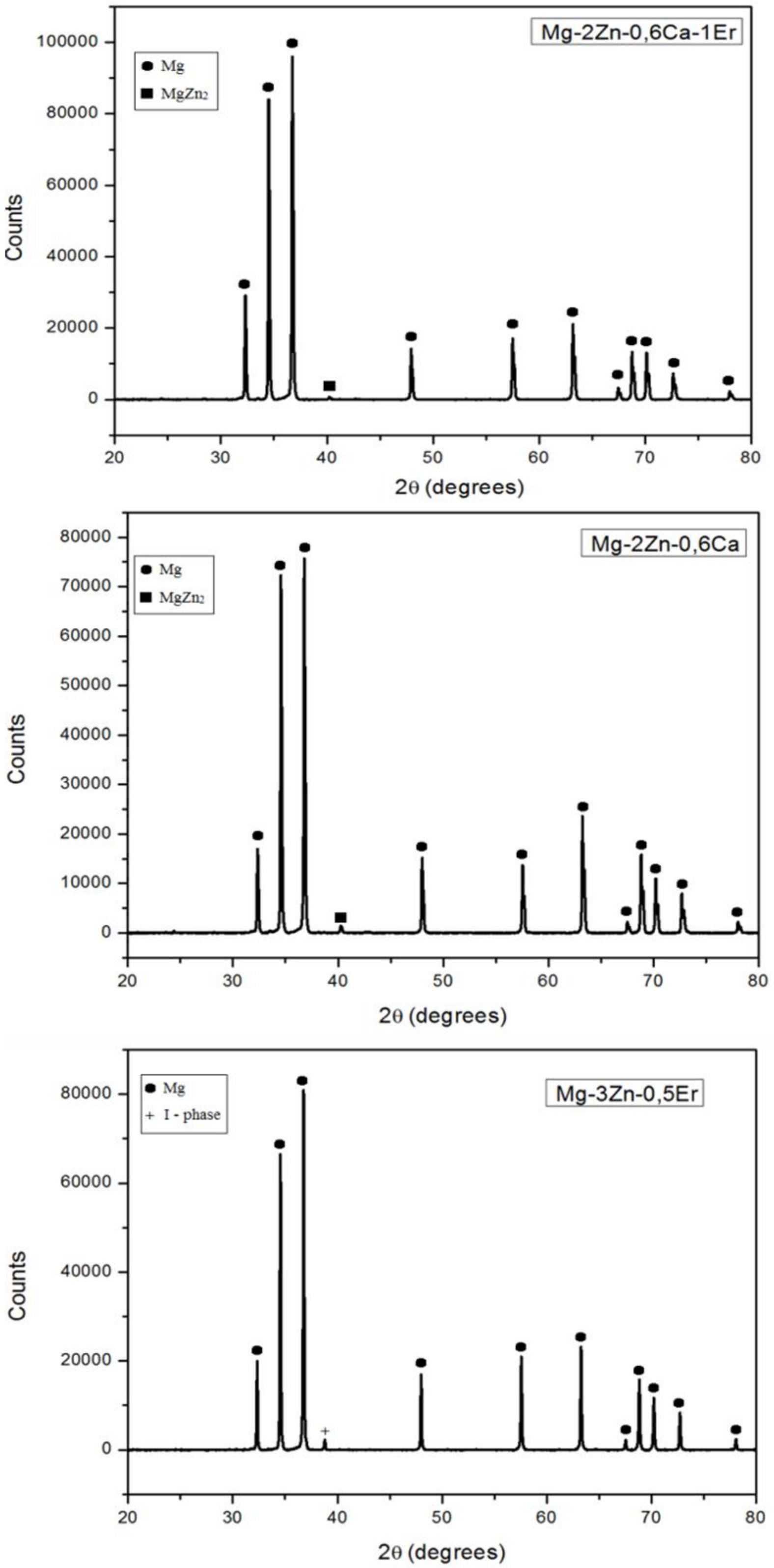

Figure 4.2: XRD plot of transverse sections of pure Mg and its alloys

For the alloys, the intensity of basal peak at 34° is found to be different to each other. This shows that the addition of Zn, Ca and Er resulted in a change in the crystallographic orientation, i.e., the basal planes are not completely parallel but aligned at an angle to the extrusion direction. It could possibly indicate the weakening of strong basal texture of Mg due to Zn, Ca and Er addition, which could be seen for samples in transverse direction where the alloys have minimal to no basal (0002) peak. The relative intensities of these peaks in both transverse and longitudinal directions have been listed in Table 4.2.

Table 4.2: X-Ray Diffractogram results of as-extruded Mg-Zn-Ca-Er alloys

Material	**I/I_{max}**					
	$(10\bar{1}0)$ Prism		**(0002) Basal**		**$(10\bar{1}1)$ Pyramidal**	
	T	**L**	**T**	**L**	**T**	**L**
Pure Mg	0.9602	0.1546	1	1	0.6295	0.6959
Mg-2Zn	1	0.1611	0.053	1	0.706	0.8778
Mg-2Zn-2Er	0.079	1	1	0.066	0.417	0.2899
Mg-2Zn-0.6Ca-1Er	0.3035	0.2094	0.875	1	1	0.8775
Mg-2Zn-0.6Ca	0.224	0.2162	0.955	1	1	0.78
Mg-3Zn-0.5Er	0.246	0.2139	0.821	1	1	0.7988

*T represents XRD taken along transverse section of Mg-Zn-Ca-Er samples.

I is the XRD intensity from prismatic, basal and pyramidal plane of pure Mg.

I_{max} is the maximum XRD intensity from either prismatic, basal and pyramidal plane.

4.2.4. Optical microstructure

4.2.4.1. As-DMDed

The optical microstructures of as-DMDed Mg alloys are represented in Figure 4.3. The as-DMDed alloys include the matrix with higher grain sizes and the formation of intermetallic secondary phases could be identified as black irregular shaped particles of different sizes. The grains were of the order of 300-600 μm and after etching, they can be clearly visible under naked eye.

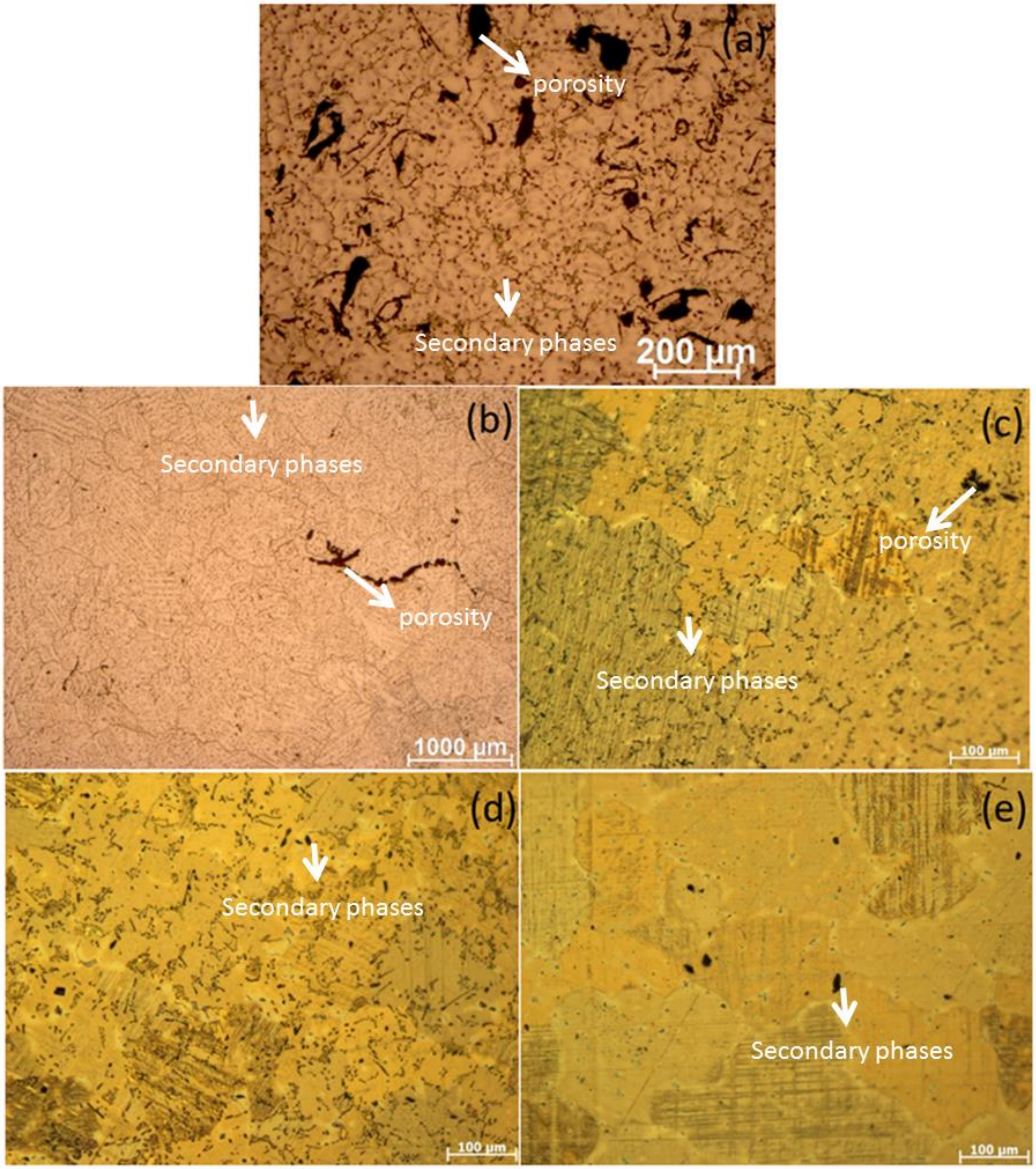

Figure 4.3: Optical microstructures of as-DMDed (a) Mg-2Zn (b) Mg-2Zn-2Er (c) Mg-2Zn-0.6Ca-1Er (d) Mg-2Zn-0.6Ca and (e) Mg-3Zn-0.5Er

4.2.4.2. As-extruded

After extrusion, the alloys exhibited fine grained microstructures. The optical microstructures of as-extruded Mg and its alloys revealing the microstructural characteristics such as grain morphology and secondary phases are represented in this section, along with their corresponding histograms calculated using the software ImageJ[4]. From the figures, it could be seen for all the alloys, a fine-grained microstructure were obtained after hot extrusion. This is due to grain refinement process due to the presence of alloying elements. The mechanism responsible for this is the dynamic recrystallization (DRX). For the alloys, the coarse secondary phases which are broken during the deformation process are aligned in the extrusion direction. The grain size is the highest for pure Mg whereas for Mg-2Zn-2Er, it is the least.

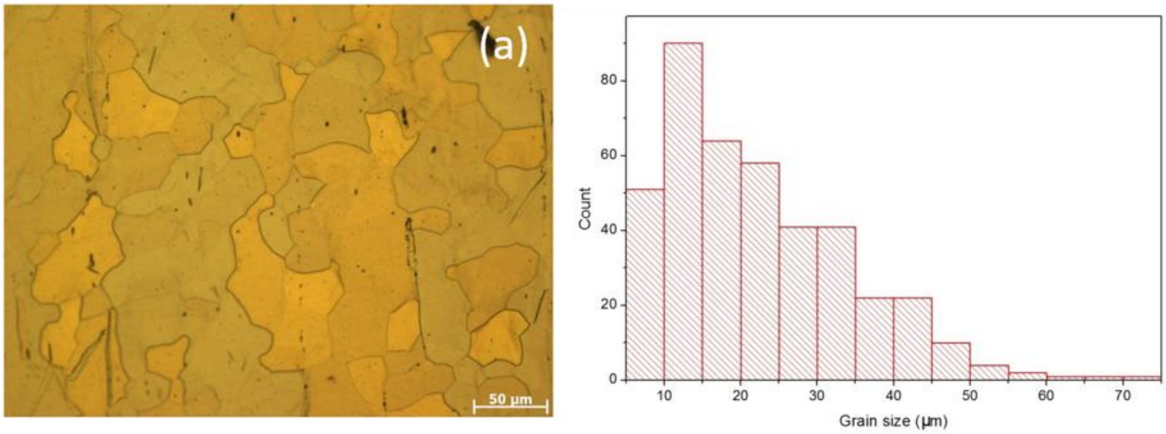

Figure 4.4: Optical microstructure and grain size histogram for as-extruded pure Mg

Pure Mg is a single phase (α-Mg) with a large grain size (22.42 µm) as seen in Figure 4.4. The grains are equi-axed. The grain size distribution indicates that the increased number fraction of grains is in the range of 10-15 µm. Few grains <10 µm were also observed. There were no twins observed. The microstructure is colored yellow due to acetic picral etchant. The average grain size is measured to be 22.42 µm.

---

[4] Schneider, C. A.; Rasband, W. S. & Eliceiri, K. W. (2012), "NIH Image to ImageJ: 25 years of image analysis", Nature methods 9(7): 671-675, PMID 22930834.

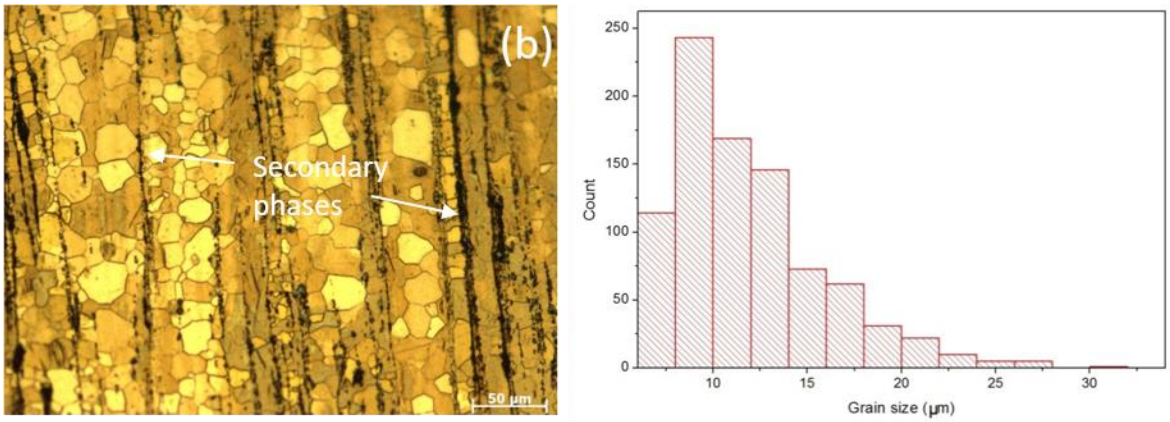

Figure 4.5: Optical microstructure and grain size histogram for as-extruded Mg-2Zn

For Mg-2Zn alloy as seen in Figure 4.5, several extrusion lines could be seen. The grains are equiaxed and it has a reduced grain size as compared to pure magnesium. The secondary phases which are marked in the figure are aligned along the extrusion direction. In the histogram, increased number fraction of grains is in the range of 6-10 µm. The average grain size of this alloy is measured to be 15.99 µm.

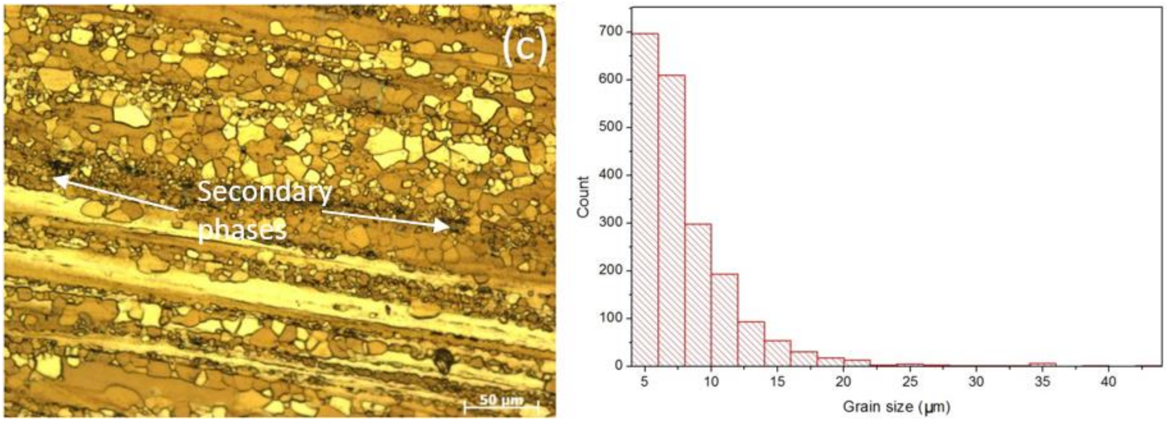

Figure 4.6: Optical microstructure and grain size histogram for as-extruded Mg-2Zn-2Er

The alloy Mg-2Zn-2Er shows a bimodal grain structure as seen in Figure 4.6. It consists of fine grains as seen in the histogram (several grains in the range 5-10 µm) and unDRXed region. This shows that the addition of 2Er to Mg-2Zn further reduces the grain size and the overall microstructure of magnesium alloys. Very fine secondary phases are found adjacent to the fine grains. The average grain size of this alloy is measured to be 6.6 µm.

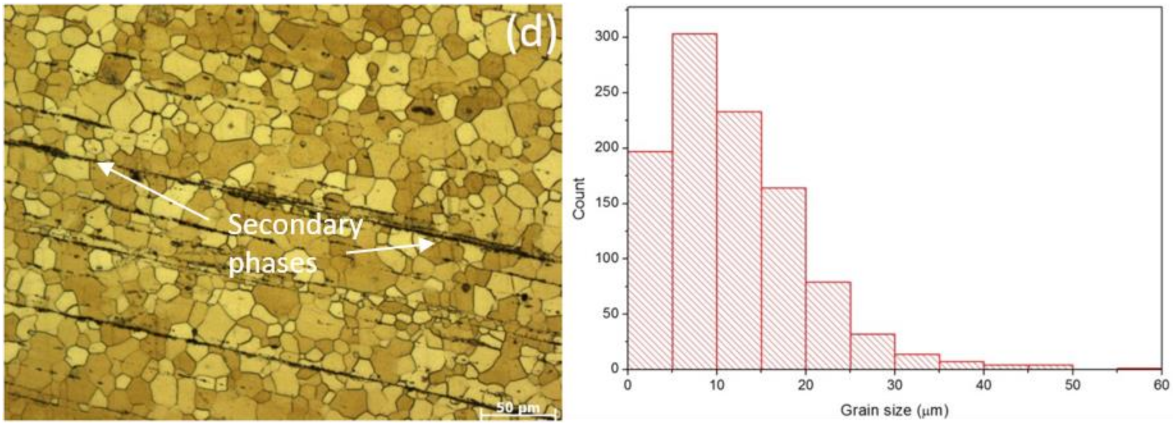

Figure 4.7: Optical microstructure and grain size histogram for as-extruded Mg-2Zn-0.6Ca-1Er

The optical microstructure and grain size distribution for the alloy Mg-2Zn-0.6Ca-1Er is represented in Figure 4.7. The grain size distribution resembles to that of pure Mg and Mg-2Zn but the average grain size measured is finer (11.57 µm). The grains are more equiaxed for this alloy. The secondary phases are indexed in the figure.

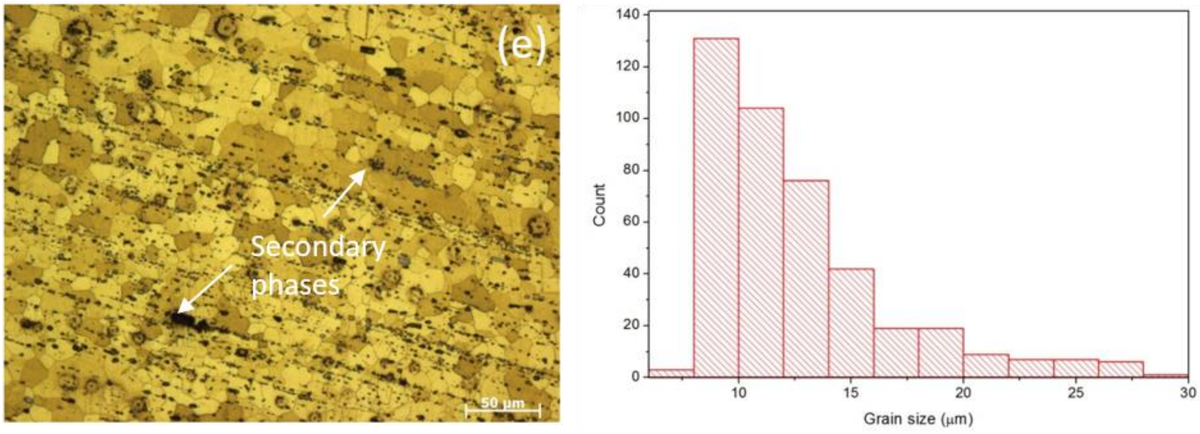

Figure 4.8: Optical microstructure and grain size histogram for Mg-2Zn-0.6Ca

The grain size distribution and optical microstructure for Mg-2Zn-0.6Ca as-extruded alloy is represented in Figure 4.8, where a lot of secondary phases were seen along the extrusion direction. The grains in the size range 1-5 µm were very less and a lot of grains were in the range 5-10 µm. The average grain size was measured to be 11.87 µm, which is very close to that of Mg-2Zn-0.6Ca-1Er.

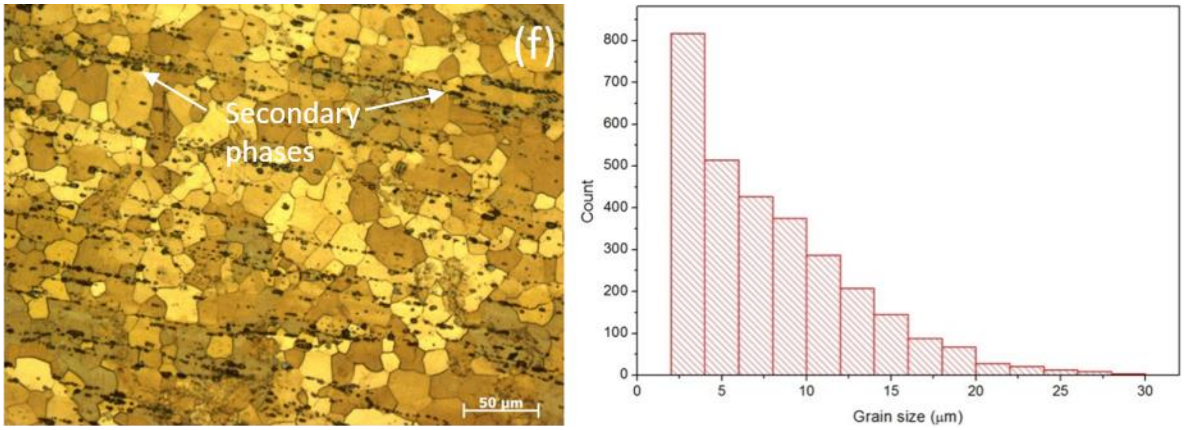

Figure 4.9: Optical microstructure and grain size histogram for Mg-3Zn-0.5Er

The optical microstructure and grain size distribution for Mg-3Zn-0.5Er as-extruded alloy is represented in Figure 4.9. Extrusion lines were not seen in this alloy, but a lot of secondary phases were present along the extrusion direction as labeled in the figure. There were no grains detected in the range 1-2 μm but a lot of grains were identified in the range 2-4 μm.

To identify the composition of these secondary phases, energy dispersive spectroscopy (EDS) analysis along with back-scattered electron imaging was carried out and they are explained in the subsequent sections.

4.2.5. Scanning electron microscopy

4.2.5.1. SEM-EDS

4.2.5.1.1. As-DMDed alloys

Figure 4.10 - Figure 4.13 shows the SEM microstructures and EDS analysis of the as-DMDed alloys containing the phase constituents α-Mg grains with intermetallic phases located at the grain boundaries and within the matrix too. The secondary phases that are uniformly distributed throughout the microstructure exhibit varied composition, mostly rich in magnesium. They are present in the form of a network like structure, which are bright and white in the SEM images. The Backscattered electron (BSE) images are recorded due to the elastic scattering interaction between the specimen atoms and the high-energy electrons originating in the electron beam, that are reflected or back-scattered out of the specimen interaction volume. This mode of imaging is chosen to detect contrast between areas with different chemical composition. The reason why the phases appear white in color is that the heavy elements like erbium which has high atomic number backscatter electrons more strongly than the light elements with low atomic number. Their volume fraction remains the same, as there is not much variation in the composition of the constituents in the alloys. They exhibit complex morphologies and different kinds were identified, including roughly circular, rod-shaped and irregular.

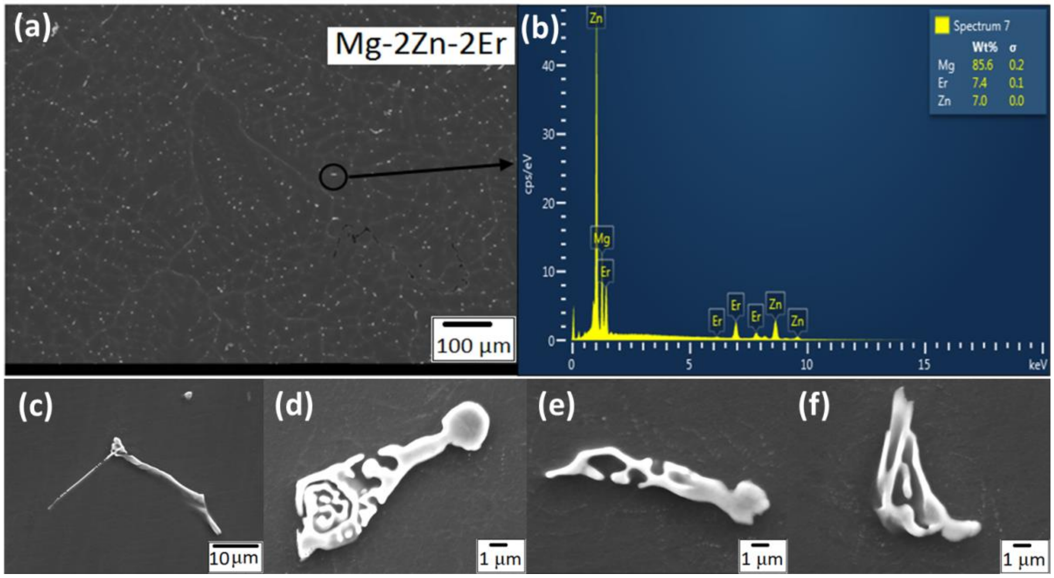

Figure 4.10: SEM-BSE images and EDS spot analysis of as-DMDed Mg-2Zn-2Er (a) Low magnification BSE image (b) EDS analysis of the secondary phase, (c)-(f) Secondary phases of different shapes

The SEM-EDS analysis for as-DMDed Mg-2Zn-2Er is shown in Figure 4.10. Figure 4.10a shows the low magnification image of this alloy, where the secondary phases exhibit a network like structure. Figure 4.10b shows the EDS spectrum of a secondary phase and it corresponds to Mg-7 wt.% Zn-7.4 wt.% Er. The secondary phases exhibit several morphologies as seen in Figure 4.10 (c)-(f).The size of these phases were between 5-10 µm.

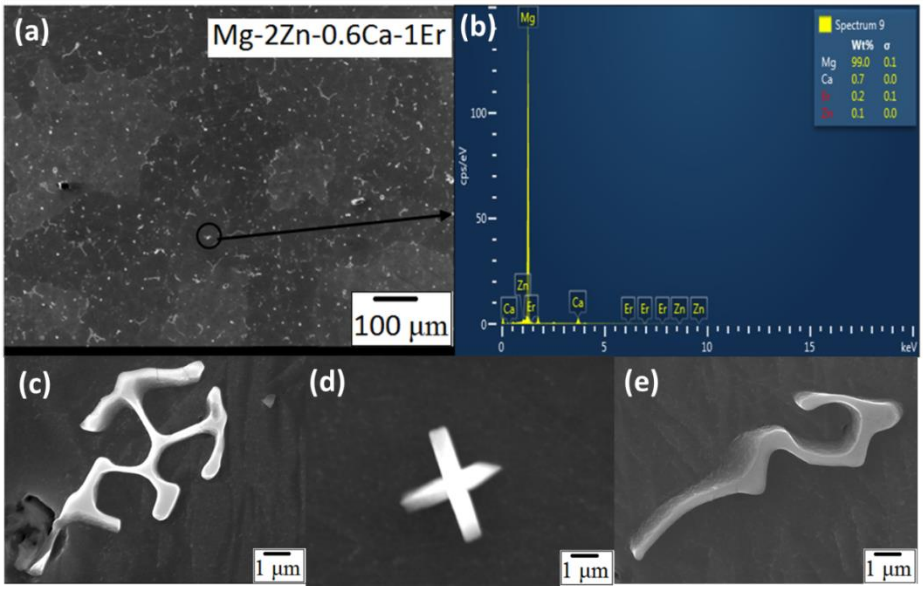

Figure 4.11: SEM-BSE images and EDS spot analysis of as-DMDed Mg-2Zn-0.6Ca-1Er (a) Low magnification BSE image (b) EDS analysis of the secondary phase, (c)-(e) Secondary phases of different shapes

The SEM-EDS analysis for as-DMDed Mg-2Zn-0.6Ca-1Er is shown in Figure 4.11. Figure 4.11a represents the low magnification image of this alloy. The EDS analysis shown in Figure 4.11b for the rounded particle indicates that it is mostly pure Mg. Several morphologies were exhibited by the phases and they are indexed in Figure 4.11 (c)-(e).

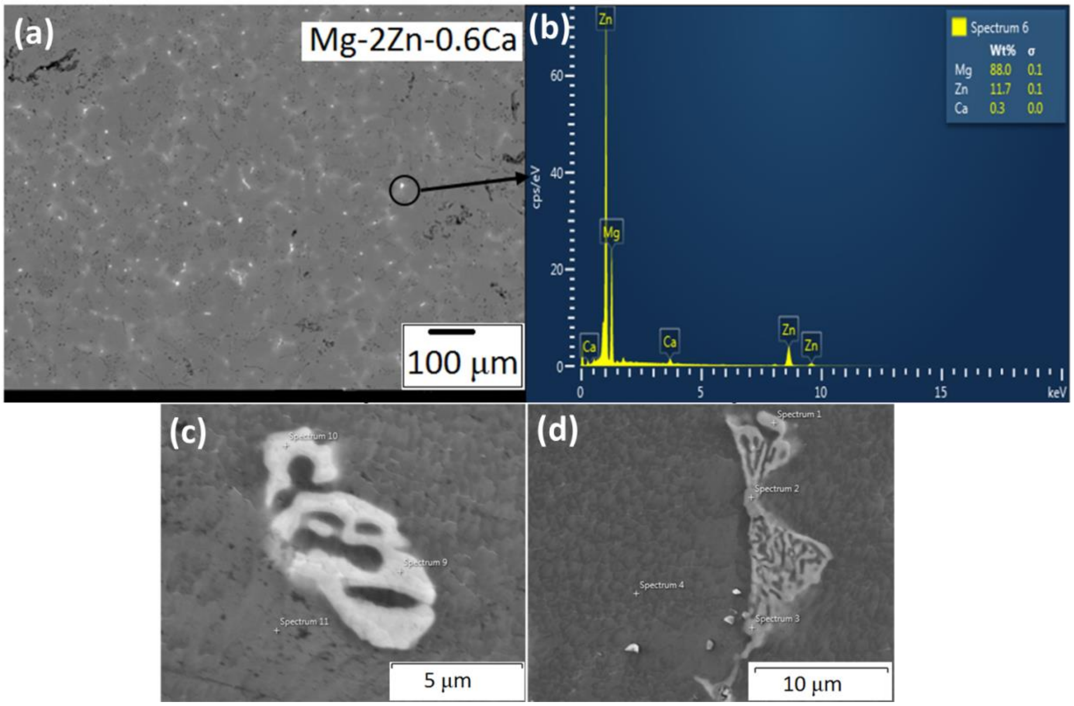

Figure 4.12: SEM-BSE images and EDS spot analysis of as-DMDed Mg-2Zn-0.6Ca (a) Low magnification BSE image (b) EDS analysis of the secondary phase, (c)-(d) Secondary phases of different shapes

The SEM-EDS analysis for as-DMDed Mg-2Zn-0.6Ca is shown in Figure 4.12. The secondary phases were not as much as that of Mg-2Zn-0.6Ca-1Er. They are dispersed in the microstructure. The EDS analysis shown in Figure 4.12b on the phase in Figure 4.12a corresponds to Mg-11.7 wt.% Zn-0.3 wt.% Ca. Large secondary phases were present and some of them are represented in Figure 4.12 (c) and (d).

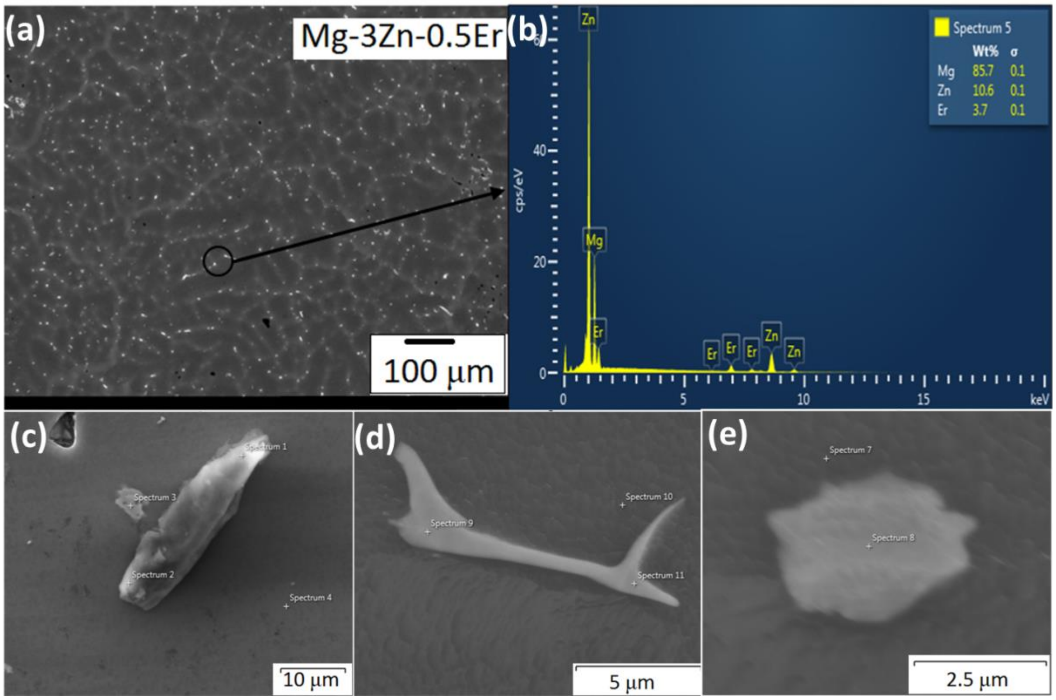

Figure 4.13: SEM-BSE images and EDS spot analysis of as-DMDed Mg-3Zn-0.5Er (a) Low magnification BSE image (b) EDS analysis of the secondary phase, (c)-(e) Secondary phases of different shapes

The SEM-EDS analysis for as-DMDed Mg-3Zn-0.5Er is shown in Figure 4.13. The secondary phases exhibit network like structure, similar to that of Mg-2Zn-2Er. The EDS analysis shown in Figure 4.13b on the phase in Figure 4.13a corresponds to Mg-10.6 wt.% Zn-3.7 wt.% Er. Large secondary phases were present of different morphologies and sizes and some of them are represented in Figure 4.13 (c)-(e).

The SEM-EDS analysis was also conducted for alloys after extrusion and they are represented in the next section.

4.2.5.1.2. As-extruded alloys

The SEM images and EDS analysis of the as-extruded alloys along the extrusion direction (ED) are shown in Figure 4.14-Figure 4.18. For all the microstructures, the secondary phases are clearly visible due to BSE contrast. The grain structure is also seen for all the microstructures.

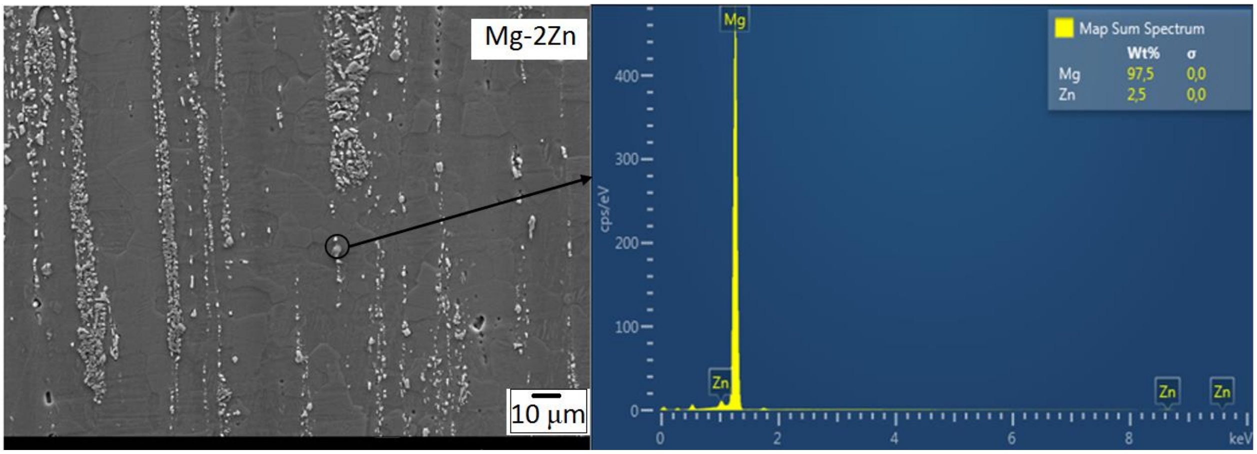

Figure 4.14: SEM-BSE image and ESD analysis of as-extruded Mg-2Zn

For Mg-2Zn as shown in Figure 4.14, the secondary phases are aligned along the extrusion direction. Several secondary phases could be seen throughout the sample observation area. EDS analysis on the marked phase shows the composition to be Mg-2.5 wt.% Zn.

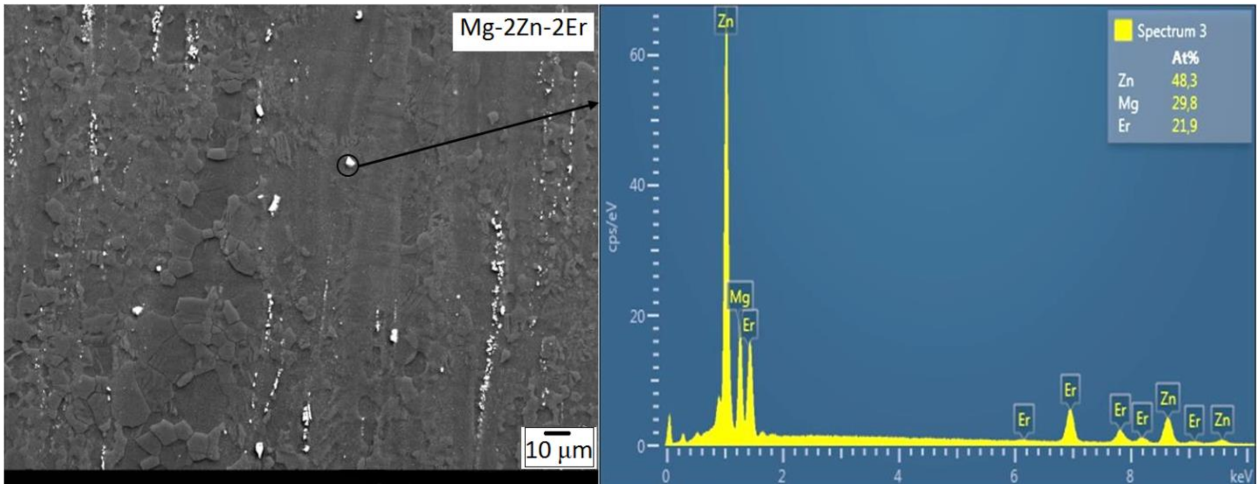

Figure 4.15: SEM-BSE image and ESD analysis of as-extruded Mg-2Zn-2Er

For Mg-2Zn-2Er as shown in Figure 4.15, the EDS analysis shows Er concentrations within the matrix to vary between 1-2 wt.%. These values are within the solid solution limit of Er in the Mg crystal structure. The broken secondary phases correspond to Mg29.8Zn48.3Er21.9, which is close to $Mg_3Zn_3Er_2$, or W-phase in the EDS analysis. These W-phase particles were of different sizes and several nano-scale particles could also be seen.

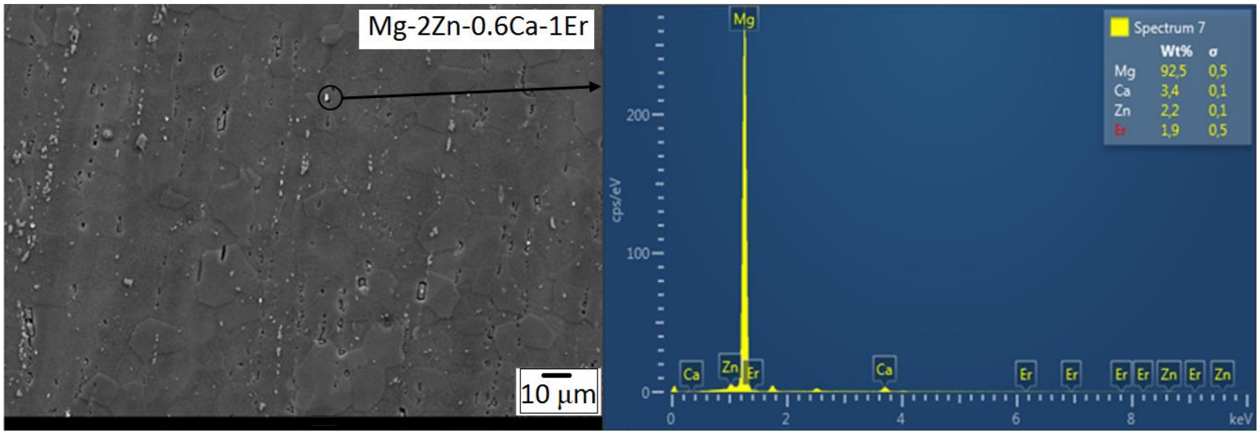

Figure 4.16: SEM-BSE image and EDS analysis of as-extruded Mg-2Zn-0.6Ca-1Er

The SEM-EDS analysis for as-extruded Mg-2Zn-0.6Ca-1Er is represented in Figure 4.16. Several morphologies were identified, including rod, globular and polygonal. The EDS analysis on the indexed phase shows the composition as Mg-2.2 wt.% Zn-3.4 wt.% Ca-1.9 wt.% Er.

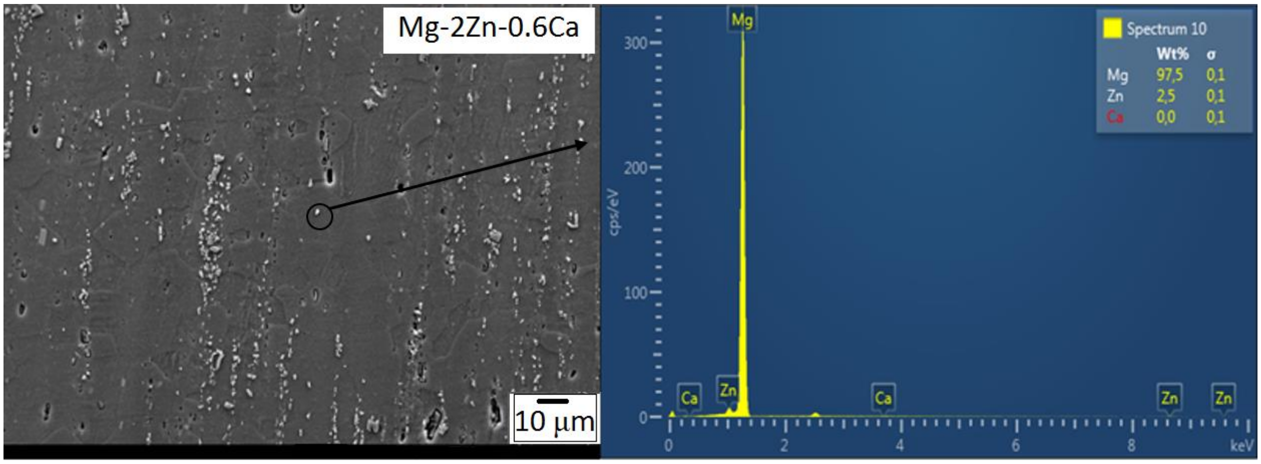

Figure 4.17: SEM-BSE image and EDS analysis of as-extruded Mg-2Zn-0.6Ca

For Mg-2Zn-0.6Ca as shown in Figure 4.17, several secondary phases could be identified, but they were not as much as Mg-2Zn. The EDS analysis on the indexed phase shows the composition mainly Mg-Zn type (Mg-2.5 wt.% Zn). This shows that most of Ca has gone into the matrix.

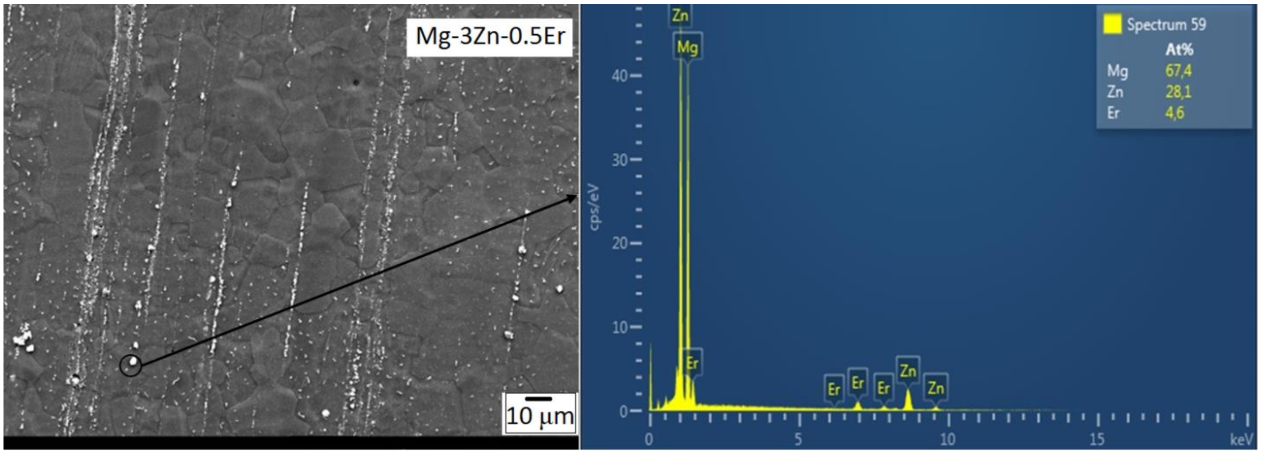

Figure 4.18: SEM-BSE image and EDS analysis of as-extruded Mg-3Zn-0.5Er

For Mg-3Zn-0.5Er, the secondary phases are aligned along the extrusion direction as seen in Figure 4.18. The EDS results as seen for Figure 4.18 indicate that the composition of the particle are Mg-28.1 at.% Zn -4.6 at.% Er. It indicates that the Zn/Er (at.%) ratio values of the particles are close to that of Zn/Er (at.%) for the I-phase ($Mg_3Zn_6Er_1$).

During the SEM-EDS investigation of as-DMDed and as-extruded alloys, the important phases have been identified and also the confirmation of the distribution of elements, mainly Er within the Mg crystal lattice. For detailed characterization of these secondary phases, TEM investigation has been carried out and they are listed in Section 4.2.11.

4.2.5.2. EBSD micrographs

The results of EBSD measurements conducted on pure Mg and its alloys are obtained and they are shown in Figure 4.19. In the maps, the (0002) basal plane is indicated by red color, and the blue color represents the plane lying 90° away from the (0002) plane. The secondary phases that have not been indexed in EBSD for the alloys have been shown as black particles. A streak like pattern along the extrusion direction could be clearly seen for Mg-2Zn and Mg-3Zn-0.5Er. It could be seen that the addition of Zn, Ca and Er in small quantities has reduced the grain size of pure Mg by one order of magnitude. For Mg-2Zn-2Er, a varied grain sized microstructure (fine DRXed and coarse unDRXed) with several textural components could be observed as seen in Figure 4.19c. Very coarse and partially recrystallized grains have a dominant prismatic textural component (indicated in the figure as coarse unDRXed) and hence the overall microstructure exhibits this texture. For all other alloys, a uniform grain structure could be seen with reasonably equiaxed grains present everywhere. Mg-2Zn-0.6Ca exhibits basal texture with almost all the basal planes oriented perpendicular to the extrusion axis. To study the intensity of textures, pole figure measurements have been recorded and they are shown in the subsequent section.

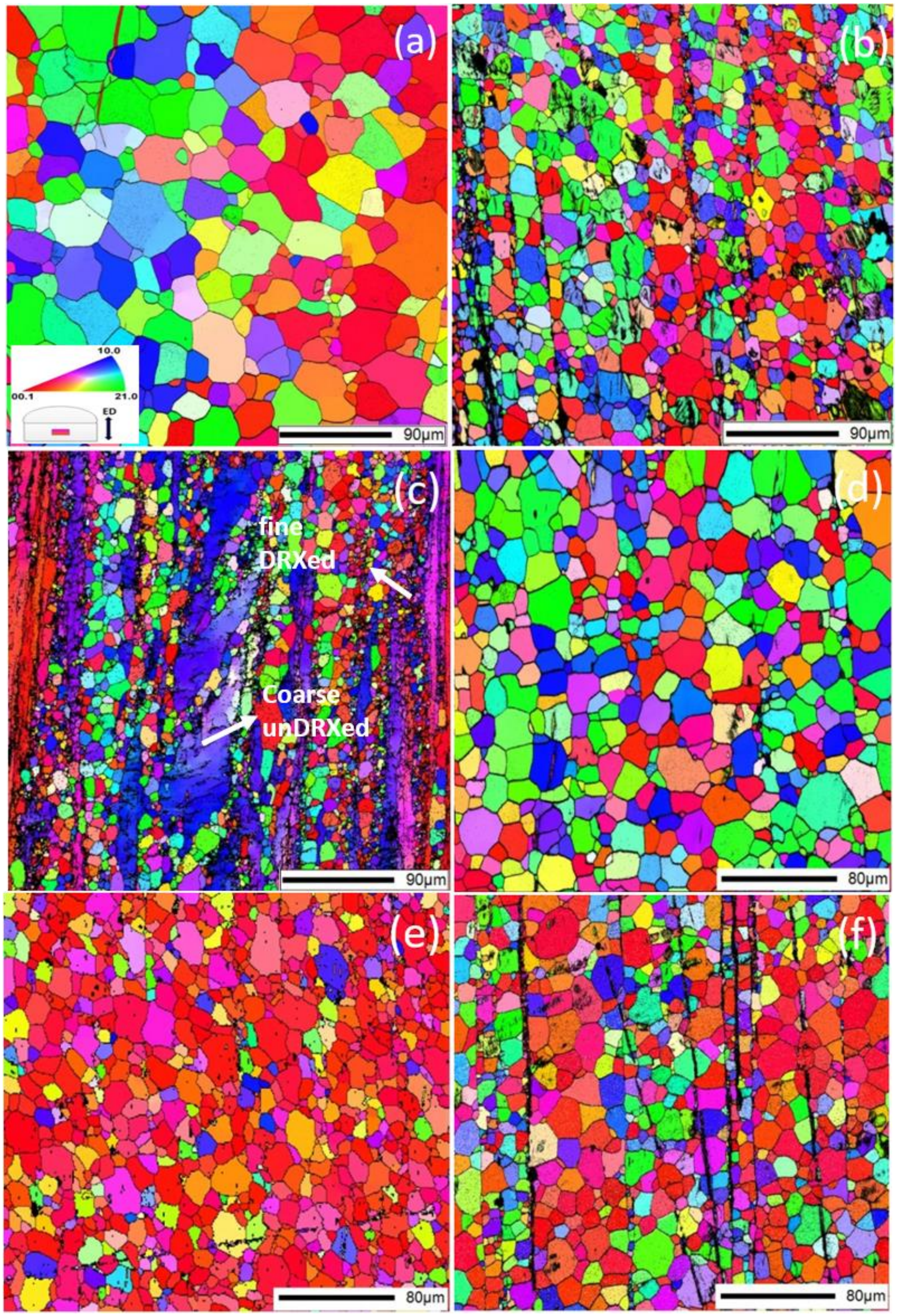

Figure 4.19: Inverse pole figures of (a) Pure Mg (b) Mg-2Zn (c) Mg-2Zn-2Er (d) Mg-2Zn-0.6Ca-1Er (e) Mg-2Zn-0.6Ca and (f) Mg-3Zn-0.5Er

4.2.5.3. EBSD-Pole figures

The results of EBSD measurements conducted on pure Mg and its alloys are obtained in the form of pole figure maps as shown in Figure 4.20. The texture intensities are represented in the form of multiples of a uniform density (m.u.d). In the unalloyed pure Mg sample, nearly all the grains have got their basal planes oriented perpendicular to the extrusion axis. The maximum level is 11.15. An ideal basal texture is rarely observed for pure Mg with peak intensities rotated about the transverse direction by ~ 10^{o}. But this is not the case for the alloys. For Mg-2Zn, the sample had their basal plane oriented at an angle of 20-30^{o} to the extrusion axis and these poles have clearly rotated away from ND towards TD. Also, more random components of texture are formed. For Mg-2Zn-2Er, the basal texture disappears and a prismatic texture component arises along ED. The texture components are dispersed for Mg-2Zn-0.6Ca-1Er and Mg-3Zn-0.5Er. Thus we could see that after hot-extrusion, the texture of pure magnesium and that of the alloys are quite different as an influence of different alloying additions.

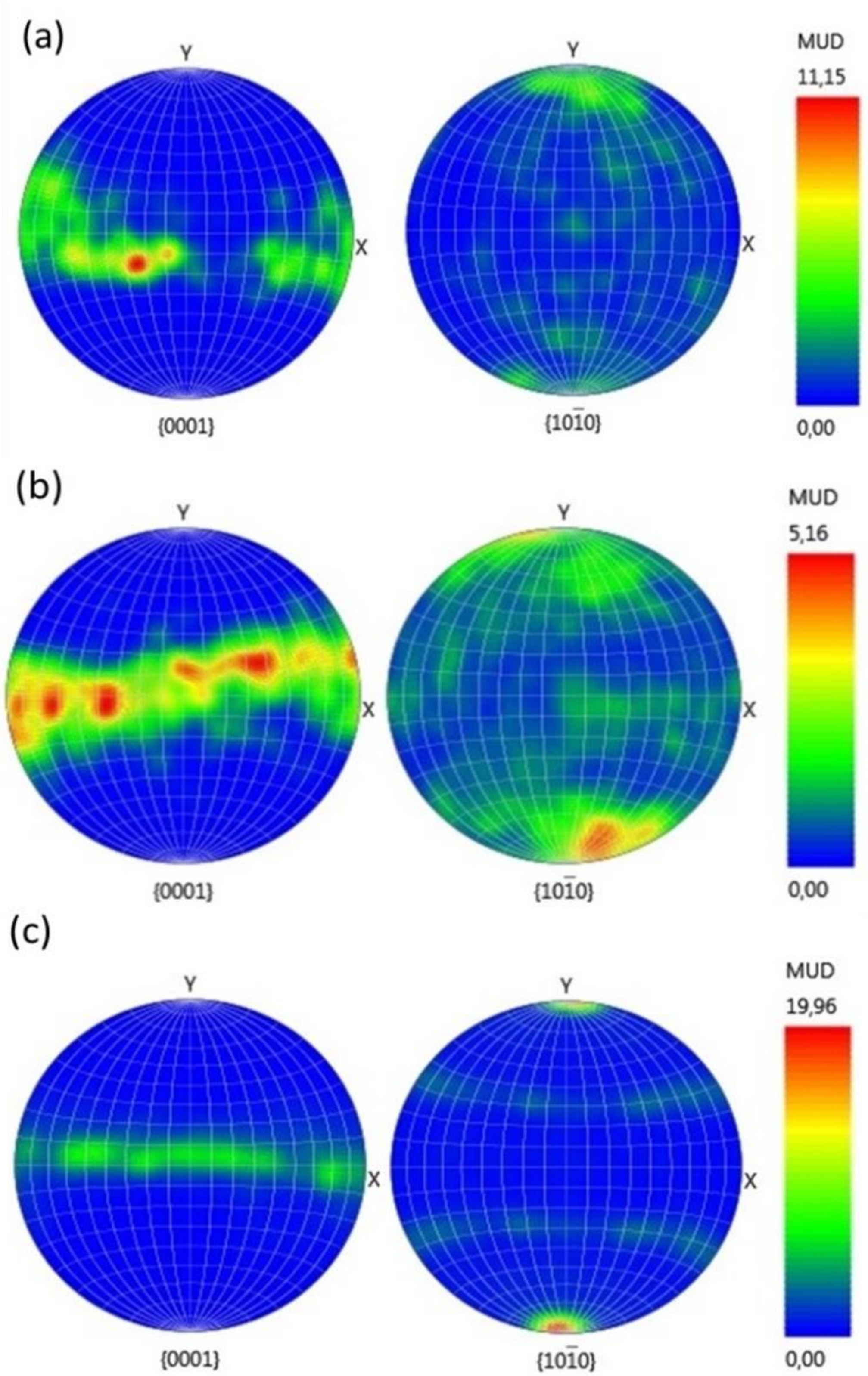
(a)
Y
X
{0001}
Y
X
{10$\bar{1}$0}
MUD
11,15
0,00
(b)
Y
X
{0001}
Y
X
{10$\bar{1}$0}
MUD
5,16
0,00
(c)
Y
X
{0001}
Y
X
{10$\bar{1}$0}
MUD
19,96
0,00

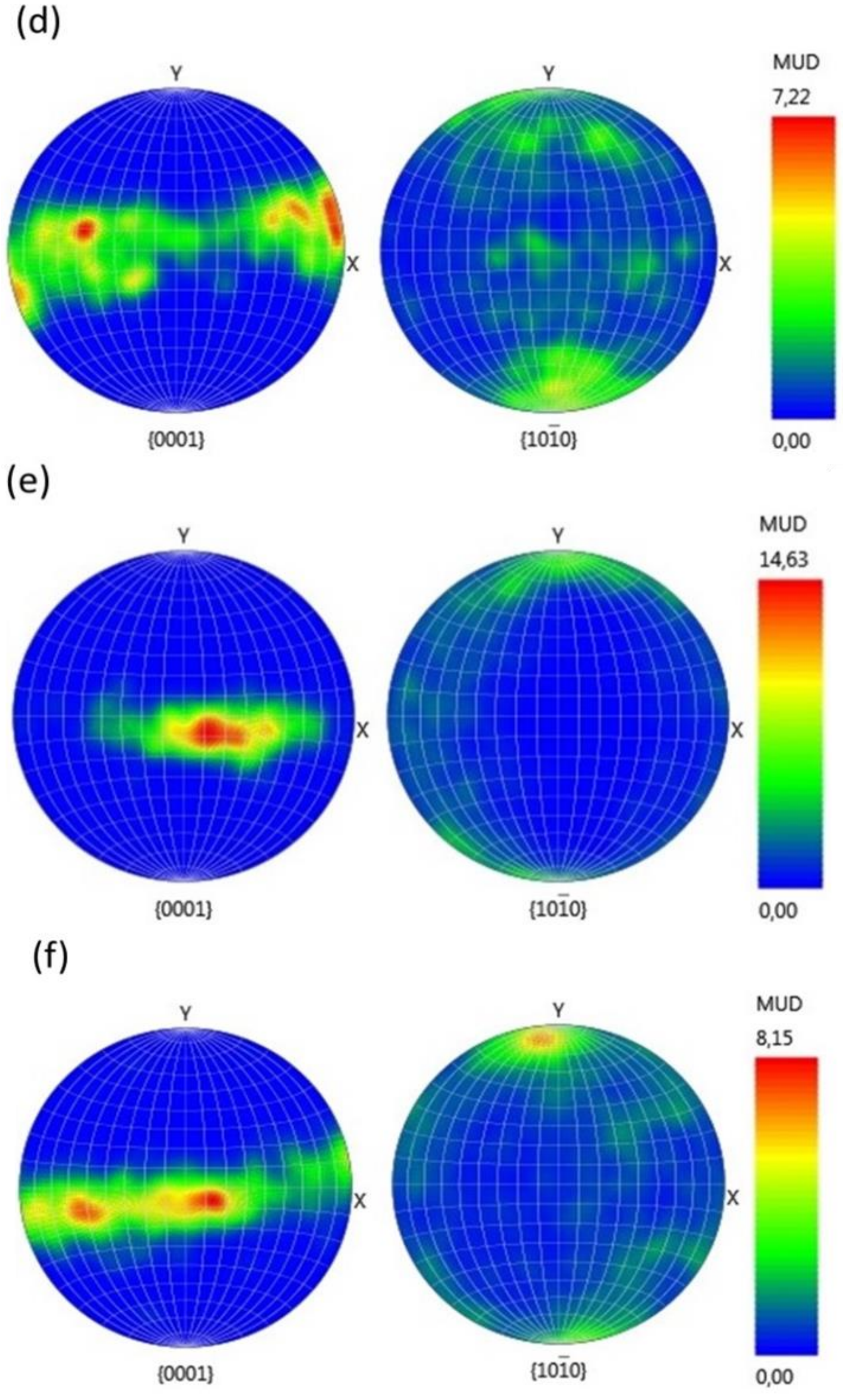

Figure 4.20: Pole figures of (a) Pure Mg (b) Mg-2Zn (c) Mg-2Zn-2Er (d) Mg-2Zn-0.6Ca-1Er (e) Mg-2Zn-0.6Ca and (f) Mg-3Zn-0.5Er

4.2.5.4. EBSD-Schmid factor

To accommodate the imposed strain, a material needs to have a variety of deformation modes. Schmid factor gives some idea about the activation of these different deformation modes with different CRSS. The average schmid factors for basal and multiple slip of as-extruded Mg-Zn-RE alloys can be acquired, as shown in Table 4.3. These schmid factors were calculated under the hypothesis of tensile load parallel to extrusion direction. For Mg, the schmid factor value is relatively less for basal slip, which is m_{basal}=0.1942. Mg-2Zn-0.6Ca exhibits m_{basal} = 0.1948 and this value reduces for other alloys. This is because pure Mg has the texture with {0002} pole perpendicular to extrusion direction and Mg-2Zn-0.6Ca also has strong basal texture. With Er additions it is observed that the average Schmid factor on basal plane decreases. For Mg-3Zn-0.5Er, m_{basal}=0.1646 and for Mg-2Zn-2Er the value for m_{basal} is least which is 0.1316. The schmid factor values for prismatic $(1\bar{1}0)$ [110] and <c+a> planes $(1\bar{1}1)$ [110] does not change much for the alloys. These values are in the range 0.418-0.448 for prismatic $(1\bar{1}0)$ [110] slip and in the range of 0.434-0.456 for $(1\bar{1}1)$ [110] slip.

Table 4.3: Average schmid factors for pure Mg and its alloys calculated using EBSD

Material	**Schmid Factor (m)**				
	(001) [110]	**$(1\bar{1}0)$ [110]**	**$(1\bar{1}1)$ [110]**	**$(1\bar{1}0)$ [001]**	**(110) [001]**
Pure Mg	0.1942	0.442	0.4563	0.1958	0.1942
Mg-2Zn	0.1879	0.4427	0.4487	0.1864	0.1879
Mg-2Zn-2Er	0.1316	0.4443	0.4385	0.1359	0.1316
Mg-2Zn-0.6Ca-1Er	0.1825	0.446	0.4512	0.1825	0.1852
Mg-2Zn-0.6Ca	0.1948	0.4182	0.4347	0.1949	0.1948
Mg-3Zn-0.5Er	0.1646	0.4481	0.4489	0.1658	0.1646

4.2.5.5. EBSD-Misorientation Angle Distribution (MAD)

The results of EBSD measurements conducted on pure Mg and its alloys are obtained in the form of misorientation angle distributions as shown in Figure 4.21. To study the micro-texture, the grain boundary fraction as a function of misorientation angle for adjacent grain was measured. The MAD for pure Mg and Mg-2Zn is similar with an increased amount of high angle grain boundaries. Mg-2Zn-2Er exhibits large fraction of low angle grain boundaries (57.8%) and Mg-3Zn-0.5Er shows greater high angle grain boundaries (81.6%). The peak at 30° that is indexed for all the alloys is characterized by recrystallization texture [203]. Also it suggests the strength of basal texture [204], which is high for Mg-2Zn and Mg-2Zn-0.6Ca. Barring Mg-2Zn-2Er, all other alloys are mainly composed of large angle grain boundaries, with greater than 80% number fraction.

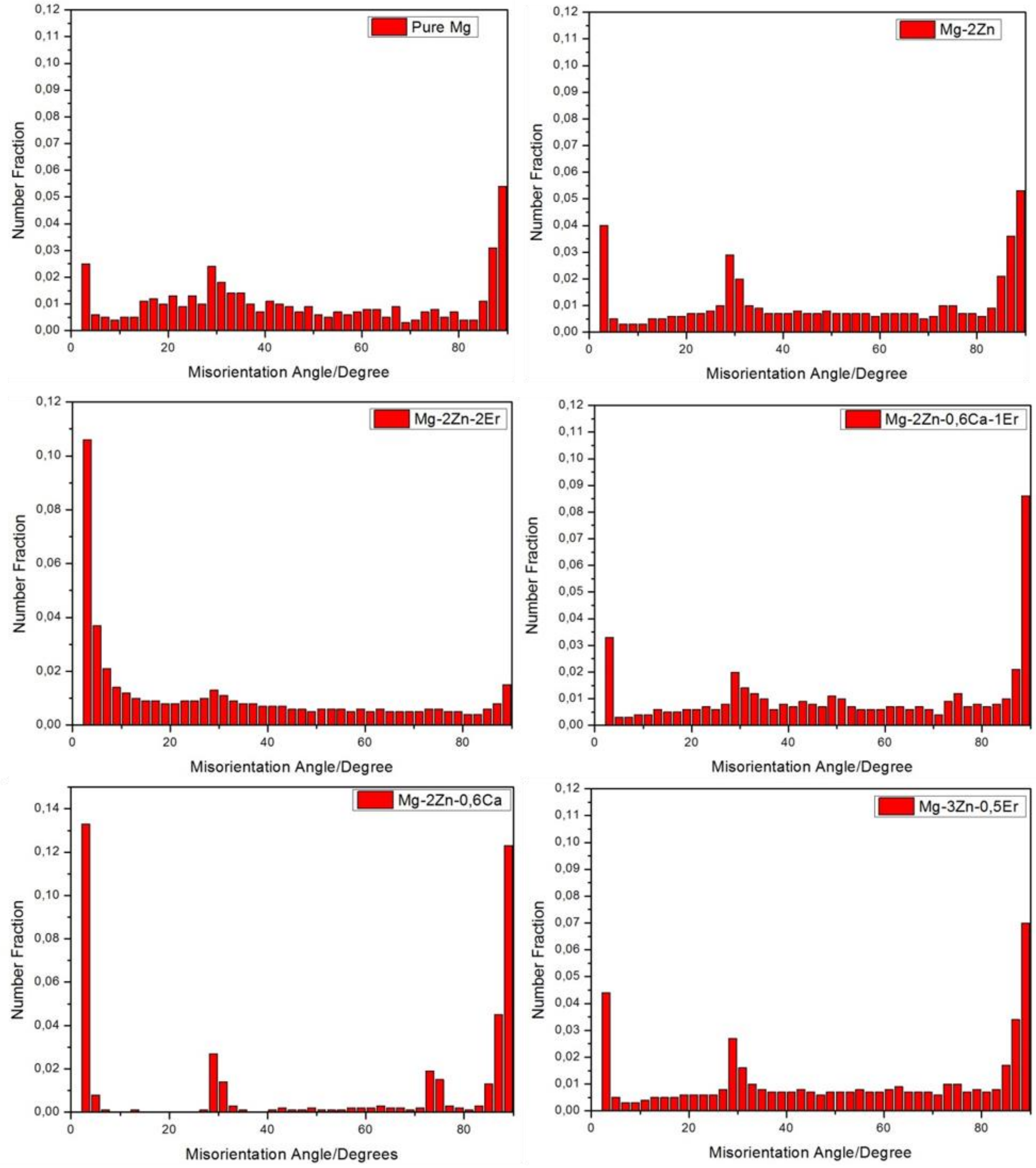

Figure 4.21: Misorientation Angle Distributions for as-extruded (a) Pure Mg (b) Mg-2Zn (c) Mg-2Zn-2Er (d) Mg-2Zn-0.6Ca-1Er (e) Mg-2Zn-0.6Ca and (f) Mg-3Zn-0.5Er

4.2.6. Impulse excitation measurement

The elastic modulus and damping characteristics of Mg-Zn-Ca-Er alloys are shown in Figure 4.22 and Table 4.4. For all the materials, the vibration ceased after 0.5s. The vibration signal is plotted as a function of amplitude versus time, where the amplitude is fitted as a sum of exponentially damped sinusoidal functions. The graphs clearly indicate that the damping characteristics were not significantly changed with the addition of alloying elements, as the behavior of these plots are similar. Table 4.4 represents damping loss rate (L), damping capacity and the elastic modulus (E) values for the alloys.

Pure Mg has the highest damping loss rate of 7.2. With the addition of alloying elements, the damping loss rate decreased. The value is 6.9 for Mg-2Zn and the value of L reduced to 6.4 for Mg-2Zn-2Er. L value for Mg-2Zn-0.6Ca and Mg-2Zn-0.6Ca-1Er are similar and it is 6.8. Damping loss rate gives an indication of the material to stop or absorb vibration. These values for the alloys are in the range of 6.4-7.2. Damping capacity is also a similar indicator that measures the relative ability of a material to absorb vibration. An increased vibrational energy without dissipation into heat can result in increased amplitude. This could be seen for Mg-2Zn-2Er which has low damping loss rate value of 6.4 but the amplitude of vibration is high as compared to other alloys. The values of elastic modulus for pure Mg and the alloys are in the range of 43-45 GPa. The highest value is exhibited by pure Mg, which is 45.26 and for Mg-2Zn-2Er it is the lowest, which is 43.3. It is significant to note that the elastic modulus did not change significantly with the addition of Zn, Ca and Er, which is very important for the biomedical applications of magnesium.

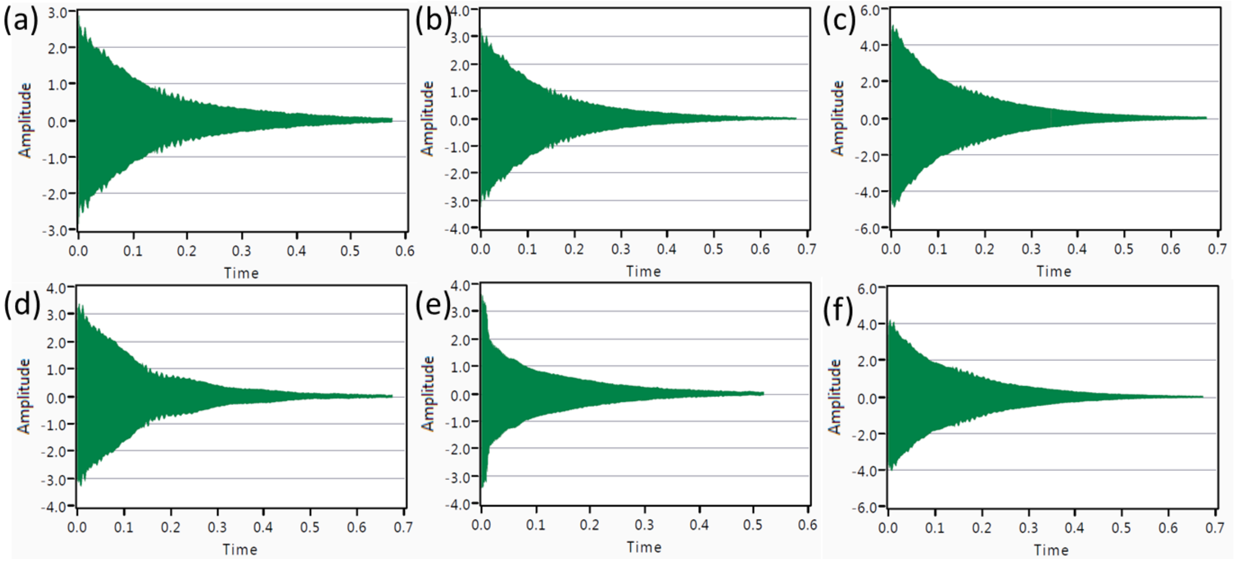

Figure 4.22: Vibration signal of as-extruded (a) pure Mg, (b) Mg-2Zn, (c) Mg-2Zn-2Er, (d) Mg-2Zn-0.6Ca-1Er, (e) Mg-2Zn-0.6Ca and (f) Mg-3Zn-0.5Er alloys

Table 4.4: Impulse excitation measurement results

Material	Damping Loss Rate (L)	Damping Capacity	Elastic Modulus (E) (GPa)
Pure Mg	7.2	0.000275	45.26
Mg-2Zn	6.9	0.000269	44.9
Mg-2Zn-2Er	6.4	0.000247	43.3
Mg-2Zn-0.6Ca-1Er	6.8	0.000261	44.45
Mg-2Zn-0.6Ca	6.8	0.000260	44.4
Mg-3Zn-0.5Er	6.6	0.000253	43.8

4.2.7. Microhardness

The microhardness measurements of pure magnesium and its alloys are shown in Table 4.5. When compared to pure magnesium, the addition of alloying elements has significantly improved the hardness value. Among as-DMDed alloys, Mg-2Zn exhibited the lowest hardness value of 37.28. Addition of 2Er enhanced the hardness value to 54.11. Addition of 0.6Ca to Mg-2Zn enhanced the hardness value to 47.82 but with the addition of 1Er to this ternary alloy, the hardness value dropped to 44.45. Increased Zn addition (3 wt.%) with minimal Er (0.5 wt.%) addition increased the hardness value to 45.59.

Compared to as-DMDed alloys, the as-extruded alloys exhibit better hardness values. Pure Mg exhibits the least hardness of 33.84. A 17% increase in hardness value is seen for Mg-2Zn after extrusion. Addition of 2Er to Mg-2Zn increased the hardness value significantly from 43.54 to 61.54 (↑41.34%). Addition of 0.6Ca to Mg-2Zn led to an increase by 26.3%. Addition of 1Er to Mg-2Zn-0.6Ca did not significantly enhance the hardness value. The maximum hardness value exhibited among the as-extruded alloys is Mg-3Zn-0.5Er, 68.27 with an increment of 101.7% as compared to the hardness value of pure Mg.

Table 4.5: Microhardness and grain size measurements for as-DMDed and as-extruded Mg and its alloys

Material	Hardness	
	As-DMDed	As-extruded
Pure Mg	-	33.84±0.46
Mg-2Zn	37.28±0.57	43.54±0.37
Mg-2Zn-2Er	54.11±0.38	61.54±0.68
Mg-2Zn-0.6Ca-1Er	44.45±0.34	55.4±0.84
Mg-2Zn-0.6Ca	47.82±0.53	54.97±0.74
Mg-3Zn-0.5Er	45.59±0.54	68.27±0.95

4.2.8. Tensile and Compressive properties

The room temperature tensile properties of the synthesized pure Mg and Mg-Zn-Ca-Er alloys are shown in Table 4.6 and Figure 4.23. From the stress-strain curve plotted in Figure 4.23, the 0.2% tensile yield strength (0.2% TYS) and tensile fracture strain values of magnesium are increased significantly with the addition of alloying elements with a reasonable improvement in the ultimate tensile strength (UTS). Pure Mg exhibits TYS and UTS value of 96 and 150 MPa respectively. Addition of 2Zn increased the values to 145 and 180 MPa respectively. Among all the alloys, Mg-2Zn-2Er exhibited the highest TYS value of 192 MPa and the UTS value also increased to 234 MPa. In the figure it could be seen that this alloy exhibits minimum strain hardening. Addition of 0.6Ca to Mg-2Zn reduced the TYS value to 129 MPa but the UTS value enhanced to 214 MPa. Addition of 1Er to Mg-2Zn-0.6Ca did not significantly modify these values. For Mg-3Zn-0.5Er, there is a slight increase in the TYS value (150 MPa) as compared to Mg-2Zn (145MPa), but this alloy exhibits the highest UTS value of 250 MPa. The ductility values increased with the alloying additions. Pure Mg exhibited the ductility value of 8.3 and with addition of 2Zn, it increased to 10.2. Addition of 0.6Ca and 2Er to Mg-2Zn enhanced it to 16.2 and 14.4 respectively. Addition of 1Er to Mg-2Zn-0.6Ca increased the ductility value to 17.2 and the highest value is exhibited by Mg-3Zn-0.5Er, which is 19.8.

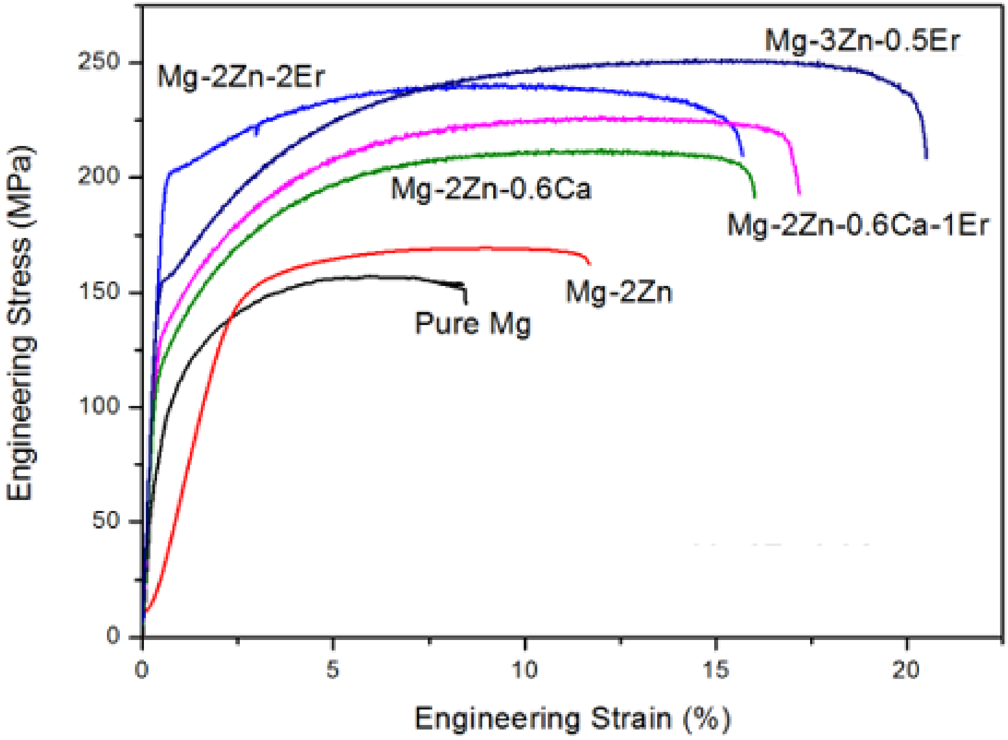

Figure 4.23: Tensile curves for (a) Pure Mg (b) Mg-2Zn (c) Mg-2Zn-2Er (d) Mg-2Zn-0.6Ca-1Er (e) Mg-2Zn-0.6Ca and (f) Mg-3Zn-0.5Er

Table 4.6: Tensile properties of pure Mg and its alloys

Composition	**0.2 TYS (MPa)**	**UTS (MPa)**	**Hardening capacity (H_c)**	**Tensile Fracture Strain (%)**
Pure Mg	96±3	150±3	0.5625	8.3±0.2
Mg-2Zn	145±3	180±5	0.241	10.2±0.3
Mg-2Zn-2Er	192±3	234±3	0.2187	14.4±0.1
Mg-2Zn-0.6Ca-1Er	128±4	225±2	0.6718	17.2±0.3
Mg-2Zn-0.6Ca	129±3	214±2	0.6977	16.2±0.4
Mg-3Zn-0.5Er	150±2	250±2	0.6667	19.8±0.3

The room temperature compression test results and the representative stress-strain curves of pure magnesium and the Mg-Zn-Ca-Er alloys are shown in Table 4.7 and Figure 4.24 respectively. It is observed that the addition of alloying elements has increased both the yield (CYS) and ultimate compressive strengths (UCS) with a marginal decrease in the compressive failure strain for Mg-2Zn-2Er. Pure Mg exhibits CYS and UCS value of 65 and 348 MPa respectively. Addition of 2Zn increased the values to 130 and 427 MPa respectively. Among all the alloys, Mg-2Zn-2Er exhibited the highest CYS value of 134 MPa and the UCS value also increased to 501 MPa. Addition of 0.6Ca to Mg-2Zn reduced the CYS value to 106 MPa but the UCS value was slightly enhanced to 436 MPa. Addition of 1Er to Mg-2Zn-0.6Ca did not significantly modify these values. For Mg-3Zn-0.5Er, there is a sudden decrease in the CYS value (44 MPa) as compared to Mg-2Zn (130 MPa) and also it exhibits reduced CYS value of 392 MPa.

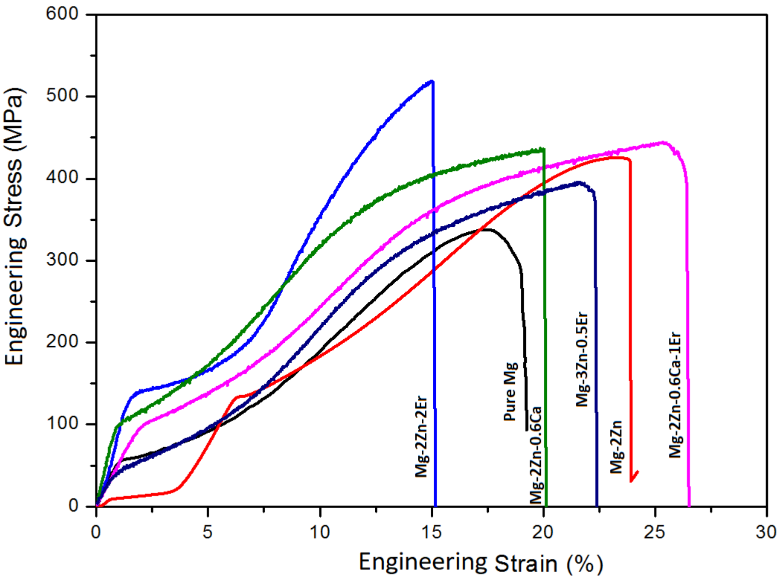

Figure 4.24: Compressive curves for (a) pure Mg (b) Mg-2Zn (c) Mg-2Zn-2Er (d) Mg-2Zn-0.6Ca-1Er (e) Mg-2Zn-0.6Ca and (f) Mg-3Zn-0.5Er

Table 4.7: Compressive properties of pure Mg and its alloys

Composition	0.2 CYS (MPa)	UCS (MPa)	Compressive Fracture Strain (%)
Pure Mg	65±1	348±3	20.1±0.3
Mg-2Zn	130±3	427±5	23.8±0.2
Mg-2Zn-2Er	134±3	501±6	16.1±0.1
Mg-2Zn-0.6Ca-1Er	111±2	442±2	25.3±0.2
Mg-2Zn-0.6Ca	106±2	436±3	20.9±0.3
Mg-3Zn-0.5Er	44±3	392±4	24.9±0.2

4.2.9. Tensile Fractography

The results of fractography analysis after tensile loading conducted on the fractured surfaces of magnesium alloys are shown in Figure 4.25. In case of pure magnesium, the fracture occurs primarily by cleavage mode [205]. But for the alloys, a mixed mode with dimpled and cleavage fractures were seen. For Mg-3Zn-0.5Er, a large number of dimples could be seen, which suggests that before tensile fracture this alloy suffers relatively large plastic deformation.

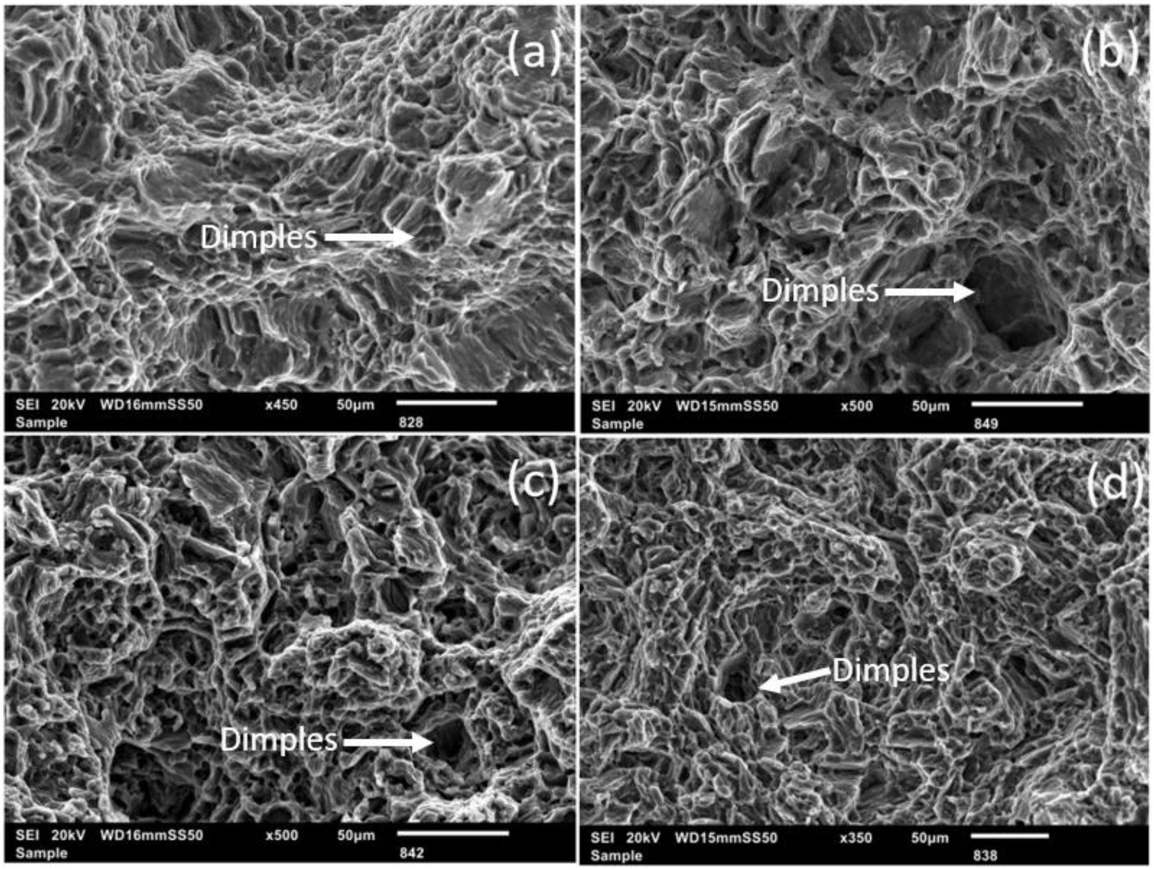

Figure 4.25: Fractography of (a) Mg-2Zn-2Er (b) Mg-2Zn-0.6Ca-1Er (c) Mg-2Zn-0.6Ca and (d) Mg-3Zn-0.5Er

4.2.10. Microstructure of tensile specimens

To understand further the mechanisms of tensile deformation, the area close to the deformed region of the samples after tensile fracture have been analyzed by using optical microscopy and EBSD techniques. The results are presented in the subsequent sections.

4.2.10.1. Optical Microscopy

The optical microstructures of as-extruded tensile fractured specimens are shown in Figure 4.26. Both pure Mg and the alloys show evidence of mechanical twinning in the tensile region. The twins are labeled in the figures. There are no voids seen. The secondary phases that are aligned in the extrusion direction could be seen for Mg-2Zn, Mg-2Zn-0.6Ca-1Er, Mg-2Zn-0.6Ca and Mg-3Zn-0.5Er. A large number of twins could be seen for Mg-3Zn-0.5Er, followed by Mg-2Zn-0.6Ca and Mg-2Zn-0.6Ca-1Er, and the ductility values for these samples as seen in the Table 4.6 supports this evidence. As seen in Table 4.6, Mg-3Zn-0.5Er exhibits the highest ductility value of 19.8%, followed by Mg-2Zn-0.6Ca-1Er which is 17.2% and 16.2% for My-2Zn-0.6Ca. Very few twins are observed in Mg-2Zn-2Er and they are seen in coarse unDRXed region. Further EBSD characterization of these regions have been carried out to identify the nature of twins.

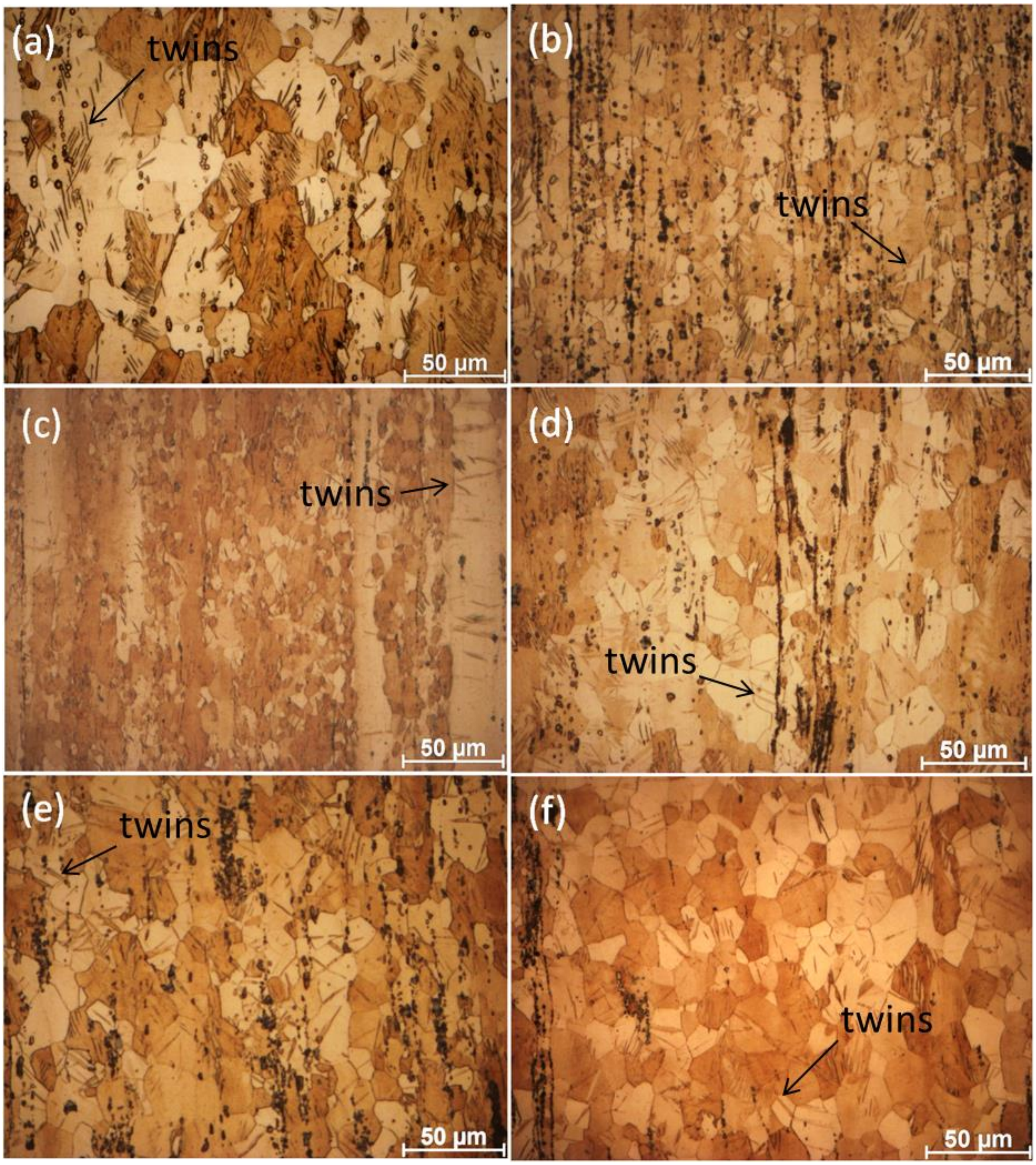

Figure 4.26: Optical microstructures of as-extruded fractured (a) Pure Mg (b) Mg-2Zn (c) Mg-2Zn-2Er (d) Mg-2Zn-0.6Ca-1Er (e) Mg-2Zn-0.6Ca and (f) Mg-3Zn-0.5Er

4.2.10.2. EBSD of tensile specimens

EBSD micrographs of as-extruded Mg-Zn-Ca-Er alloys after tensile fracture are plotted in Figure 4.27-Figure 4.31. In these figures, it could be seen that a large number of extension (tension) twins $\{10\bar{1}2\}$ are activated during uniaxial tensile deformation. Also a few contraction (compression)$\{10\bar{1}1\}$ type twins could be seen. The double twins were completely absent. This indicates that tension twinning is the main form of twinning during uniaxial tensile straining of as-extruded Mg-Zn-Er alloys.

For Mg-2Zn as-extruded tensile fractured sample as seen in Figure 4.27, a lot of tension twins and a few compression twins have been seen. The extension twins are represented blue in color and the compression twins are represented red in color. The misorientation profile drawn across two twins indicated in Figure 4.27 (circled in black is compression twin and circled in white is tensile twin) is shown in Figure 4.28. The misorientation angle for the twin circled in white is 86^{o} which indicates that it is a tensile twin and the misorientation angle for the twin circled in black is 56^{o} which indicates that it is a compression twin.

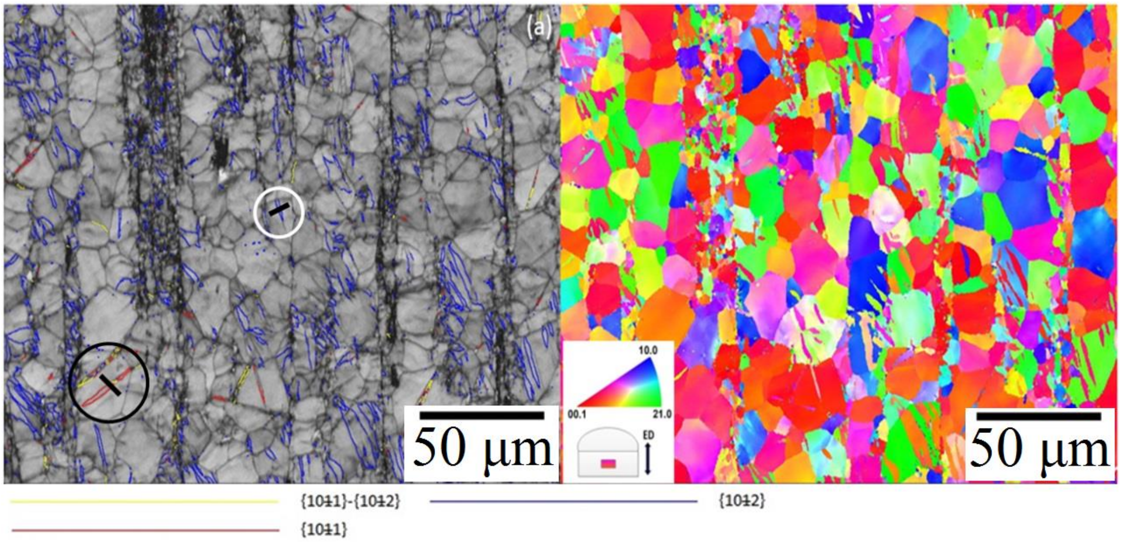

Figure 4.27: Band contrast maps and the corresponding EBSD maps of as-extruded Mg-2Zn after tensile fracture

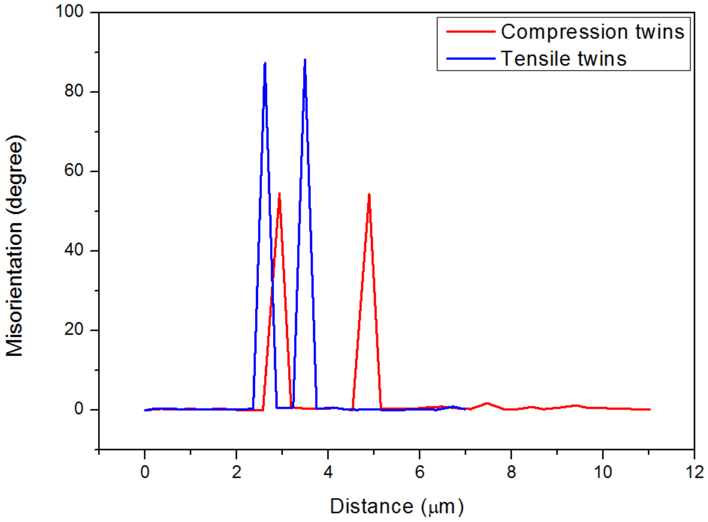

Figure 4.28: Misorientation profile for the twins of as-extruded Mg-2Zn after fracture

For Mg-2Zn-2Er as-extruded tensile fractured sample, as seen in Figure 4.29, only a few twins could be seen. The double twins are completely absent. This behavior could have probably caused by grain refinement.

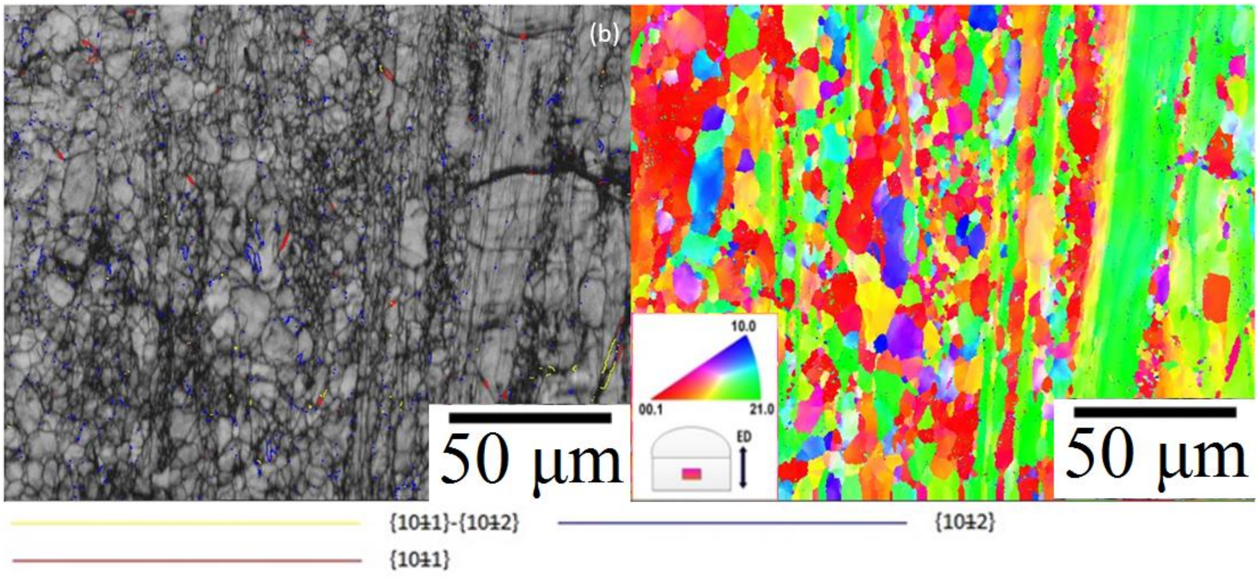

Figure 4.29: Band contrast maps and the corresponding EBSD maps of as-extruded Mg-2Zn-2Er after fracture

For Mg-2Zn-0.6Ca as-extruded tensile fractured sample, a lot of contraction twins were identified, as seen in Figure 4.30. They are marked as red in the band contrast maps. Tension twins were not identified and there is a small presence of double twins marked in yellow.

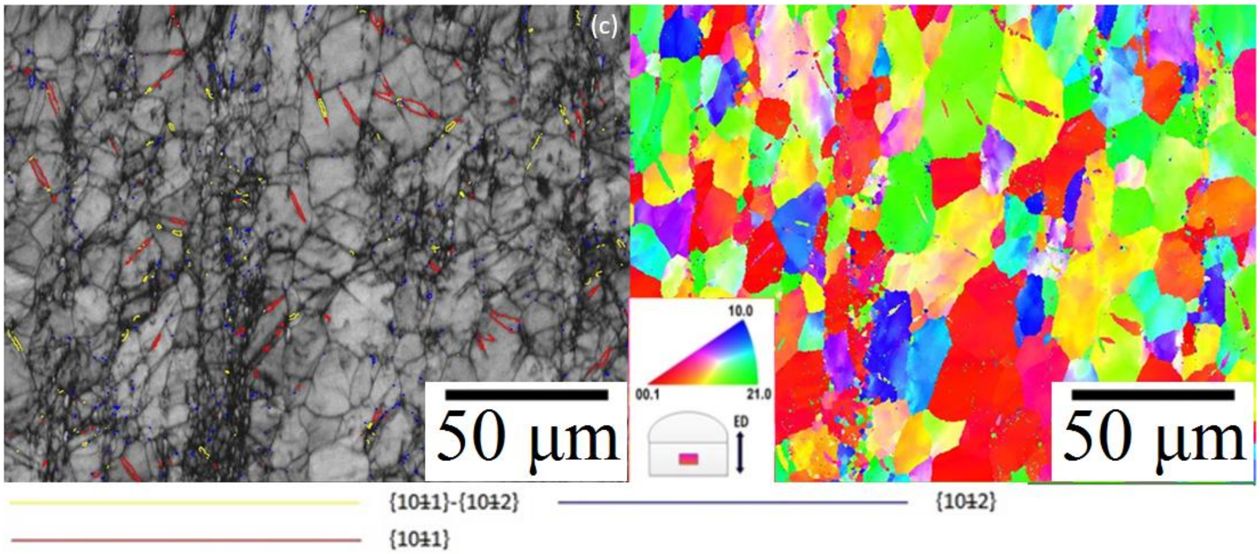

Figure 4.30: Band contrast maps and the corresponding EBSD maps of as-extruded Mg-2Zn-0.6Ca after fracture

For Mg-3Zn-0.Er as-extruded tensile fractured sample as seen in Figure 4.31, a lot of twins could be seen in the band contrast maps but they have not been indexed clearly. Since they are indexed blue in color and misorientation profiles show the misorientation angles to be 86^{o}, they are indexed as tensile twins.

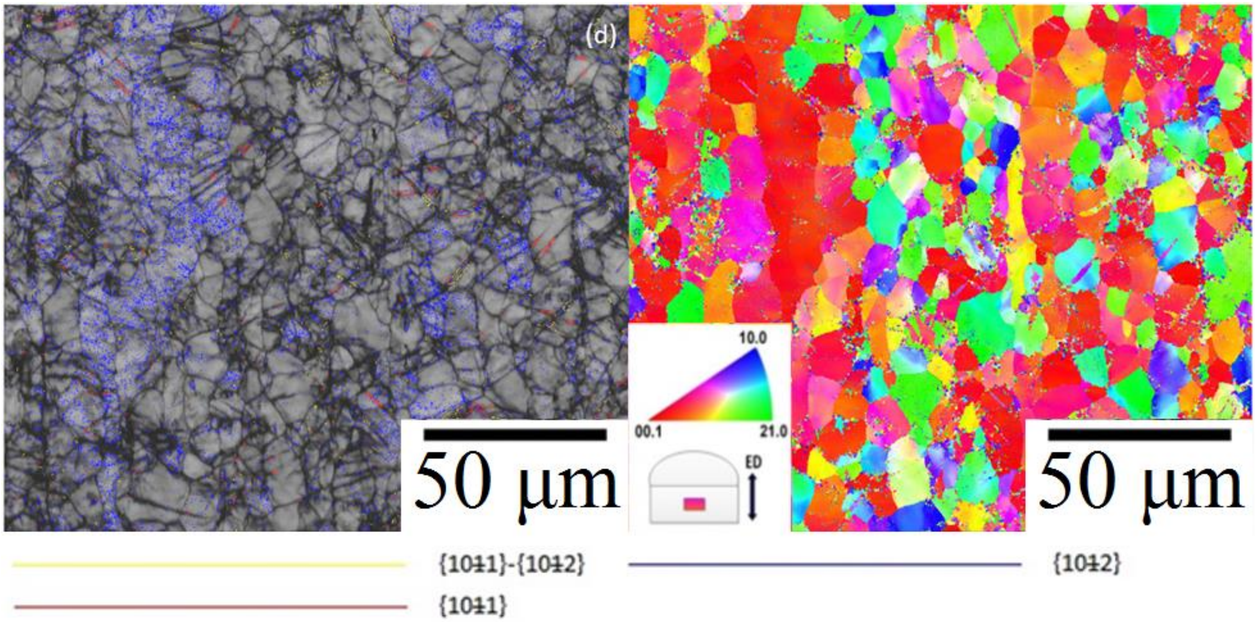

Figure 4.31: Band contrast maps and the corresponding EBSD maps of as-extruded Mg-3Zn-0.5Er after fracture

4.2.11. Transmission electron microscopy

TEM analysis for selected samples has been carried out to determine the compositions and structures of the secondary phase which present different morphologies in the as-DMDed and as-extruded samples. The samples that exhibit highest mechanical properties, i.e., Mg-2Zn-2Er and Mg-3Zn-0.5Er were chosen for TEM analysis.

4.2.11.1. Mg-2Zn-2Er

For Mg-2Zn-2Er as DMDed TEM micrograph as seen in Figure 4.32, a lot of nano-scale precipitates could be observed. A large chunk could be seen in Figure 4.32a is of 2 µm in size. This is found to be the undissolved Mg-30Er master alloy used during DMD synthesis of Mg-2Zn-2Er, there are very few. Different shaped (rod, polygonal) precipitates were observed with a size range of 100-500 nm. These precipitates are oriented in different directions. In Figure 4.32b, several precipitates were identified. A large number of $Mg_3Zn_3Er_2$ (W-phase) could be seen present as polygonal and rod-shaped particles. Few $MgZn_2$ particles in globular morphology could be seen in the microstructure. The large particle seen in Figure 4.32c which is marked 'A' is W-phase as recorded in selected area electron diffraction (SAED) pattern. For as-DMDed sample, the nanosized W-phase particles were the precipitates formed during the secondary processing. It could be recalled that the soaking of these alloys before extrusion was carried out at 400 ^{o}C for 1 hour. Although 400 ^{o}C is high for the precipitation to occur in these alloys, further reduction in temperature while processing might have influenced the precipitation process.

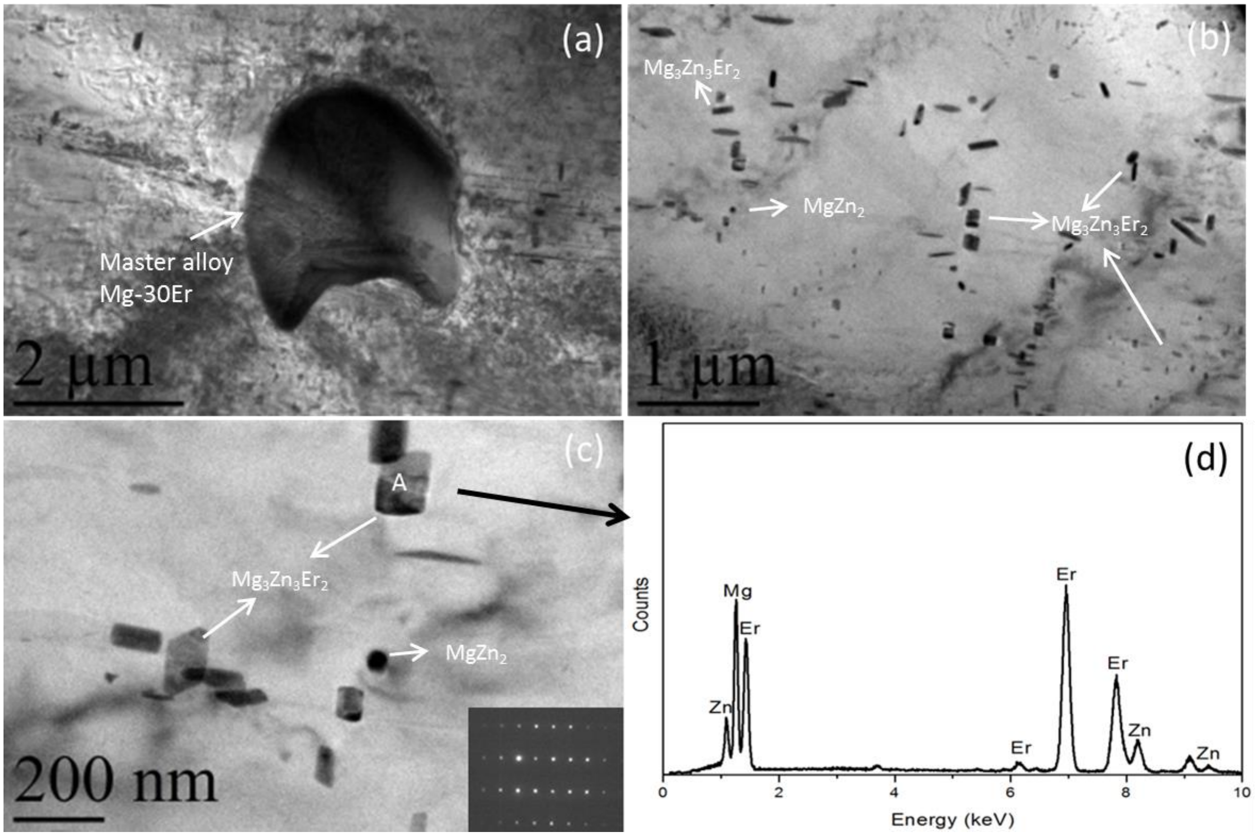

Figure 4.32: TEM micrographs, diffraction pattern and EDS analysis of as-DMDed Mg-2Zn-2Er

The TEM analysis for as-extruded Mg-2Zn-2Er is shown in Figure 4.33. They represent bright field images, diffraction pattern and EDS analysis. In Figure 4.33b, grain boundaries were seen and the fine nanoparticles were seen inside the grains. A lot of nano-scaled particles in the α-Mg matrix showing different morphologies could be seen with dimensions of 50-100 nm. There were no coarse phases seen in this alloy. The coarse phases seen in Figure 4.32 for as-DMDed alloy were broken down into fine precipitates and also during extrusion it led to the formation of new precipitates. The SAED pattern in Figure 4.33c and EDS analysis on particle 'A' marked in Figure 4.33c establishes that the composition corresponds to that of W-phase ($Mg_3Zn_3Er_2$) which is cubic and it belongs to the space group Fm-3m. The EDS plot shown by the compositional analysis in Figure 4.33d confirms the presence of Mg, Zn and Er in the particle marked 'A'. The size distribution of these secondary phases are plotted as a histogram in Figure 4.34. It could be seen that the average particle size of these phases is 56 nm, after extrusion. The difference between these two samples is the size of the precipitates after extrusion treatment. Similar results have been reported by Li et al. for Mg-Zn-Sr alloys [206].

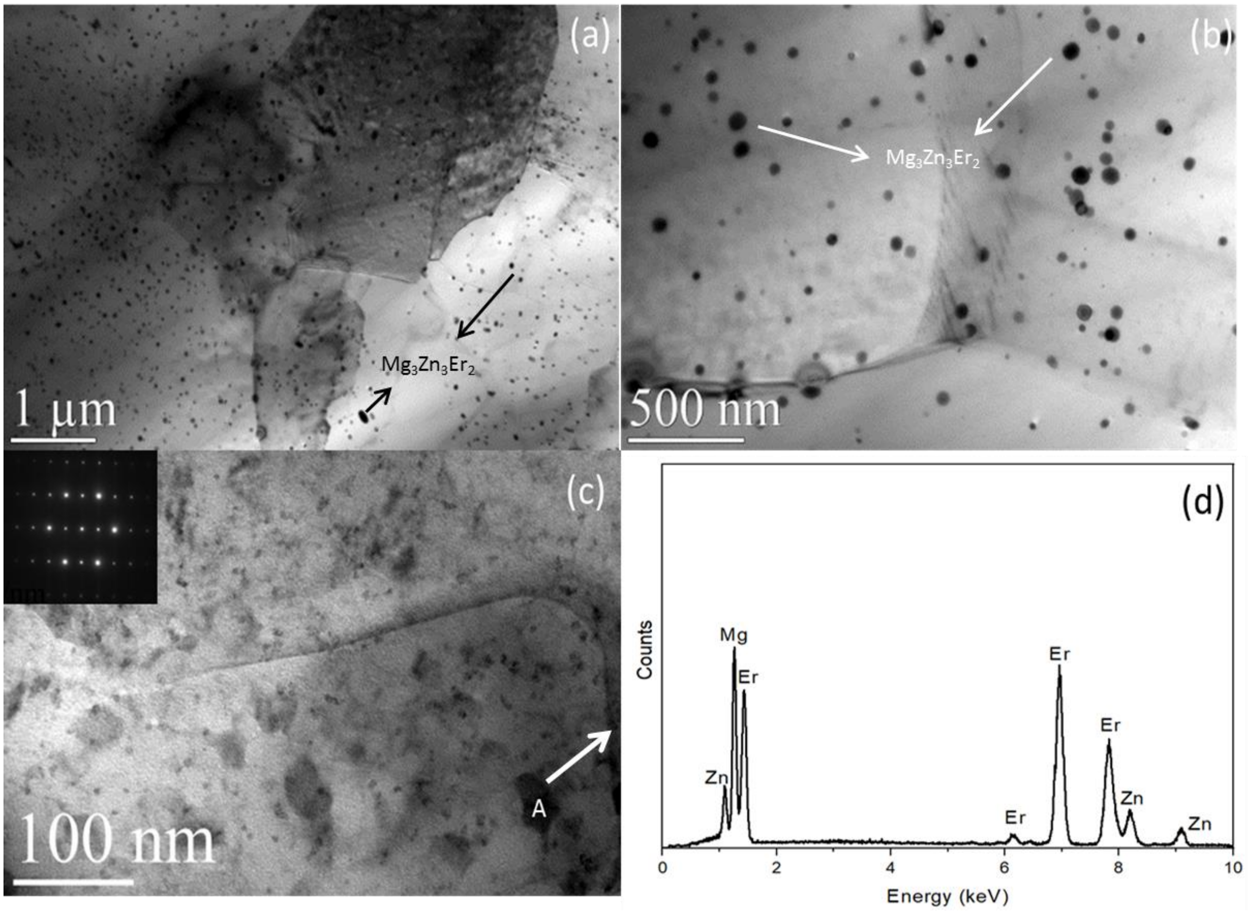

Figure 4.33: TEM micrographs, diffraction pattern and EDS analysis of as-extruded Mg-2Zn-2Er

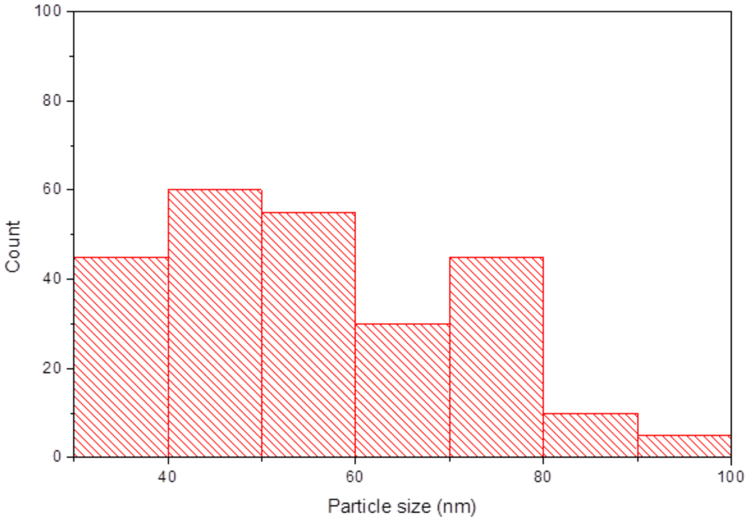

Figure 4.34: Size distribution of W-phases present in as-extruded Mg-2Zn-2Er alloy

For a better understanding of these phases and to identify the lattice spacing, high resolution TEM (HRTEM) analysis have been carried out. HRTEM images are constructed from the wave function coming out of the sample. Using GATAN digital micrograph software, the lattice spacing measurements have been determined for these phases. Fast fourier transform (FFT) gives the corresponding diffraction pattern of the region of interest in HRTEM analysis.

Figure 4.35 represents HRTEM analysis carried out for as-extruded Mg-2Zn-2Er. The inset figure in Figure 4.35 represents secondary phases which are globular and rod-shaped. HRTEM image of the larger globular particle is taken and it is presented in Figure 4.35. The lattice fringes of the HRTEM image could be clearly seen in the figure. A line is drawn perpendicular to these fringes and an integration width of 100 is considered to draw a box. A histogram can be plotted over this integration area, where the distance between every peak corresponds to d-spacing. For this phase, the value of d-spacing measured is 0.685 nm. This value is close to the d-spacing of W-phase with fcc structure in Mg-Zn-Y system identified by Padezhnova et al (0.6848 nm) [207].

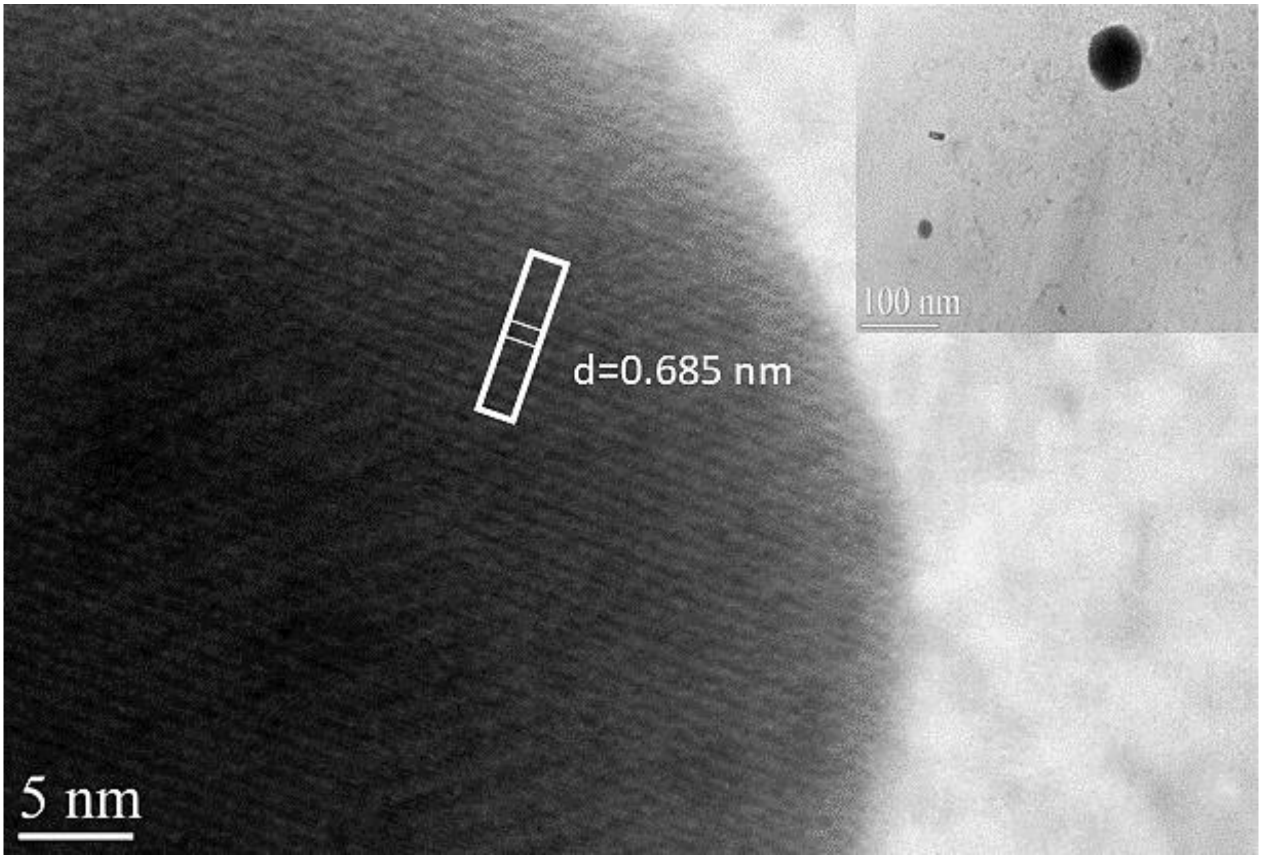

Figure 4.35: HRTEM analysis of the secondary nanometric phase in as-extruded Mg-2Zn-2Er. The inset is the low magnification image of the nanometric W-phase.

4.2.11.2. Mg-3Zn-0.5Er

TEM observations for as-extruded Mg-3Zn-0.5Er are represented in Figure 4.36. Here, different sized, shapes of the precipitates could be observed. The secondary phases were not seen as much as that in Mg-2Zn-2Er. Figure 4.36a shows a coarse polygonal shaped particle at the triple point. This coarse phase is the undissolved Mg-30Er master alloy. A few coarse particles but several fine nano precipitates were recorded which exhibit different shapes could be seen in Figure 4.36b. EDS analysis as shown in Figure 4.36c represents the composition of globular-shaped phases in Figure 4.36b and it corresponds to i-phase (Mg_3Zn_6Er). The size distribution of these secondary phases is plotted as a histogram in Figure 4.37. It could be seen that the average particle size of these phases is ~ 49 nm, after extrusion.

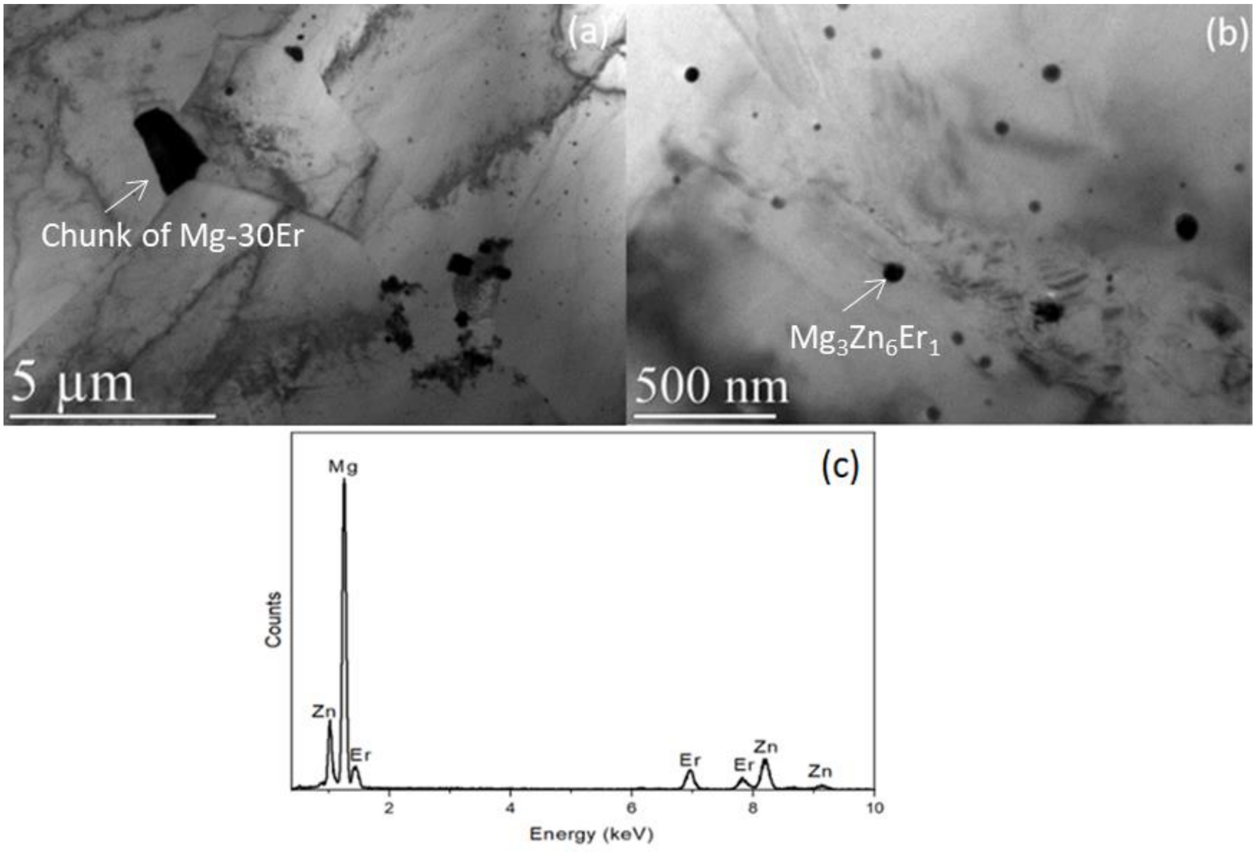

Figure 4.36: TEM micrographs and EDS analysis of as-extruded Mg-3Zn-0.5Er

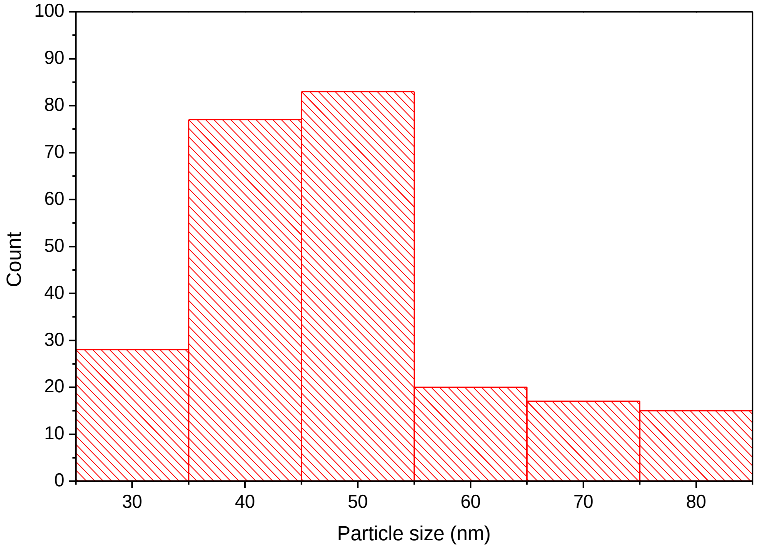

Figure 4.37: Size distribution of i-phases present in as-extruded Mg-3Zn-0.5Er alloy

The HRTEM analysis of i-phase has been carried out and it is presented in Figure 4.38. Figure 4.38a represents HRTEM image of the secondary phase which is globular in morphology. The FFT of this image is shown in Figure 4.38b. The peaks that are indexed correspond to a quasicrystal. These are novel class of intermetallic compounds which exhibit forbidden (5-fold) rotational symmetry. It shows a pentagonal dodecahedral morphology, i.e., the five-fold planes form low energy surfaces [208]. These unusual structures are said to exhibit extraordinary properties. For the histogram analysis of interplanar spacing represented in Figure 4.38a, the calculated value d=0.52 nm. This is close to the value observed for Mg-Zn-Y alloys by Singh et al., where the calculated value is d=0.52 nm [209]. It is also observed by Niikura et al. for a class of Mg-Zn-RE alloys [208].

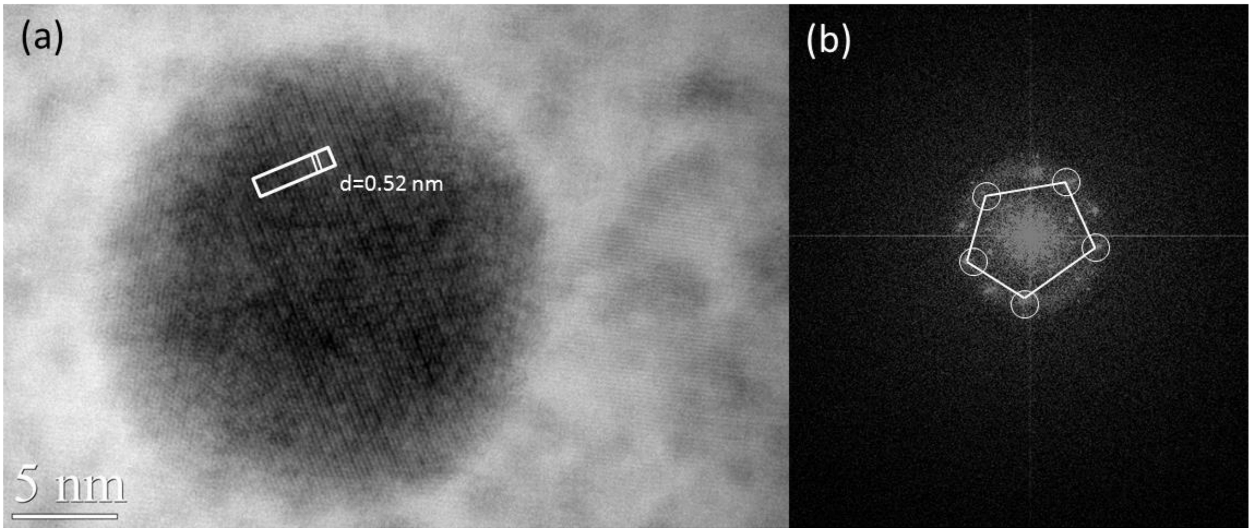

Figure 4.38: HRTEM analysis of the secondary nanometric phase in as-extruded Mg-3Zn-0.5Er, fast fourier transform (FFT) of the corresponding phase and its corresponding histogram indicating d-spacing

4.3. Discussion

4.3.1. Phases in Mg-Zn-Er system

4.3.1.1. Phase formation

Based on Mg-Zn phase diagram as seen in Figure 2.10, for Mg-2 wt.% Zn, the solidification temperature for the molten alloy is 620 ^{o}C. According to the Mg-Er phase diagram as seen in Figure 2.5, the Er content of α-Mg solid solution is about 15 wt.% at 200 ^{o}C. But neither phase diagram nor thermodynamic data is available for Mg-Zn-Er system. However, based on the Mg-Zn-Y ternary alloy phase diagram, the solid solution of Zn, Y decreased due to the elemental interaction. Hence the concentration of these elements in the liquid phase will be greater. Also, the addition of highly melting point element Er (T_m = 1529 ^{o}C) in the alloys can act as nucleation sites. The Mg-Zn-Er type ternary phases are formed due to these redundant Zn and Er elements that will easily precipitate at the grain boundaries. This has been observed in our work, as shown in Figure 4.15.

The crystallographic information used for identifying different phases is listed in Table 4.8. Some of these phases are present in the synthesized Mg-Zn-Ca-Er alloys. XRD studies presented in Figure 4.2 reveals the presence of $MgZn_2$ in Mg-2Zn, Mg-2Zn-0.6Ca and Mg-2Zn-0.6Ca-1Er. Two different type of ternary phases exist in Mg-Zn-Er alloys, i.e., $Mg_3Zn_3Er_2$ (W-phase) was present in the Mg-2Zn-2Er diffractogram and Mg_3Zn_6Er (i-phase) was present in Mg-3Zn-0.5Er diffractogram. The ternary phases are further validated using SEM-EDS and TEM-EDS analysis. These ternary phases are present in several morphologies (rod, globular, polygonal). The binary phases $MgZn_2$ and Mg_2Ca are h.c.p structured phases, same as that of Mg. W-phase detected for

Mg-2Zn-2Er in Figure 4.35 has cubic structure. I-phase detected for Mg-3Zn-0.Er in Figure 4.38 has icosahedral quasicrystalline structure.

Table 4.8: Crystallographic information of possible phases present in Mg-Zn-Ca-Er system[5]

Phase	**Structural Formula**	**Structure**	**Space group**	**Lattice Parameter**
Mg	Mg	Hexagonal	P63/mmc	a=3.2085 Å, c=5.2106 Å
$MgZn_2$	$MgZn_2$	Hexagonal	P63/mmc	a=5.223 Å, c=8.566 Å
Mg_2Ca	Mg_2Ca	Hexagonal	P63/mmc	a=6.225 Å, c=10.18 Å
W-phase	$Mg_3Er_2Zn_3$	Cubic	$Fm\bar{3}m$	a=6.912 Å
18R-LPSO	$Mg_{80.6}Zn_{8.3}Er_{11.1}$	Monoclinic	C/2c	a=11.67 Å, b=13.79 Å, c=31.32 Å, β=93.53°
14H-LPSO	$Mg_{83.3}Zn_{7.2}Er_{9.5}$	Rhombohedral	P63/mcm	a=11.1 Å, c=36.2 Å
i-phase	Mg_3Zn_6Er	Icosahedral quasicrystal	Point symmetry m-3-5 [209]	

4.3.2.2. Structure, composition and properties of i-phase

Several researchers have studied the structure and composition of i-phase and its influence on the tensile properties, impact toughness, wear and fatigue behavior in different alloy systems. Among all these alloys, extensive work has been carried out in Mg-Zn-Y system. Tsai et al. studied the Zn-Mg-Y phase diagram and calculated the equilibrium range of composition for the i-phase at 700 K, 773 K and 873 K [210]. Several new phases like Mg_3Zn_6Y, $Mg_{38}Zn_{60}Y_2$, $Mg_{24}Zn_{65}Y_{10}$, $Mg_{15}Zn_{70}Y_{15}$, $Mg_2Zn_3Y_3$ and $Mg_{12}ZnY$ have been documented. Lee et al. studied the formation range of i-phase in Mg-Zn-Y system for Zn/Y ratio of 2.7-9.5 at.% [211]. It was studied that these phases have higher stability and they can aid to grain boundary pinning and dislocation pinning. For Mg-Zn-Gd system, Luo et al. reported this ratio to be 1.5-40 at.% [212]. Mg-Zn-Er system was studied by Li et al. and they reported Zn/Er weight ratio between 6-10 results in formation of exclusive i-phase [213].

For hot-rolled Mg alloys, basal plane textures are commonly seen due to the activation of {10-12} twinning that leads to the reorientation of c-axis perpendicular to the rolling plane [214].

---

[5] https://www.fiz-karlsruhe.de/

It was reported earlier that i-phase can randomize texture in Mg-Zn-Y alloys [209]. This could be seen for the pole figure plotted for Mg-3Zn-0.5Er in Figure 4.20 that consists of weak basal texture and the dispersed texture components.

*4.3.2.3. Structure, composition and properties of W-*phase

The crystal structure of W-phase is fcc as highlighted in SAED patterns plotted for Mg-2Zn-2Er shown in Figure 4.33. Several researchers have studied the co-existence of W-phase with i-phase [212]. Due to its brittle nature, it is categorized as the phase containing low mechanical properties, but some investigations have proven an enhancement in mechanical properties after extrusion due to a uniform distribution of W-phases [215]. The crystal structure for W-phase, adapted from Mg-Zn-Y system from Luo et al. is presented in Figure 4.39 [212]. In this figure plotted for $Mg_3Zn_3Er_2$, it could be seen that 4 Er (Y1) atoms occupy the 4A positions; 4 Mg (Mg1) atoms occupy the 4 B positions. 8C (Mg2) positions are occupied by 8 (Mg+Zn) atoms with ratio of 1:3.

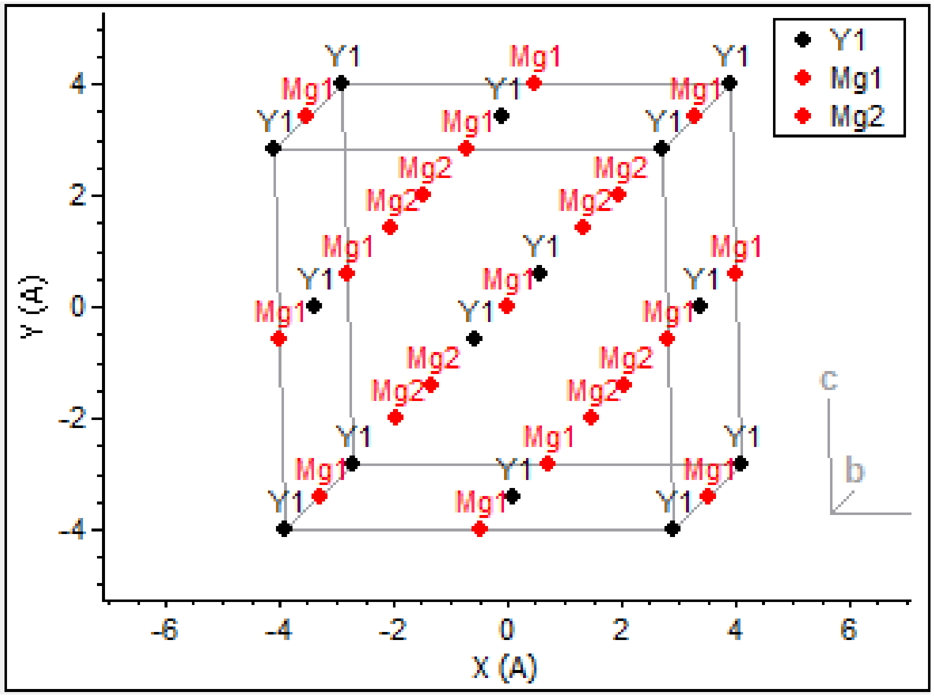

Figure 4.39: The crystal structure of the W-phase in the Mg-Zn-Er(Y) system[6]

4.3.2. Grain refinement

The grain size of as-DMDed alloy can be varied by changing the composition of the alloy under the given cooling conditions. Also, the grain sizes could be controlled by undercooling

---

[6] Plotted using K_{diff} software: http://kdiff3.sourceforge.net/

parameter, solidification interval, etc [216]. One such parameter, Growth restriction factor (GRF) is a term used to define an element's refining capability [217]. It is defined as:

$$Q = mC_o\ (k-1)$$

Where, C_o is the bulk composition of a binary alloy

m is the liquidus slope at C_o

k is the equilibrium partition coefficient.

The standard GRF values for different elements in magnesium are given in Table 4.9 [218].

Table 4.9: Slope of the liquidus line (m), Equilibrium Distribution Coefficient (k) and Growth Restriction Parameter m(k-1) for various alloying elements in magnesium

Element	**m**	**k**	**GRF = m(k-1)**	**System**
Zr	6.9	6.55	38.29	Peritectic
Ca	-12.67	0.06	11.94	Eutectic
Si	-9.25	0	9.25	Eutectic
Ni	-6.13	0	6.13	Eutectic
Zn	-6.04	0.12	5.31	Eutectic
Cu	-5.37	0.02	5.28	Eutectic
Ge	-4.41	0	4.41	Eutectic
Al	-6.87	0.37	4.32	Eutectic
Sc	4.02	1.99	3.96	Peritectic
Sr	-3.53	0.006	3.51	Eutectic
Ce	-2.86	0.04	2.74	Eutectic
Yb	-3.07	0.17	2.53	Eutectic
Y	-3.4	0.5	1.7	Eutectic
Sn	-2.41	0.39	1.47	Eutectic
Pb	-2.75	0.62	1.03	Eutectic

As seen in Table 4.9, GRF values for Ca and Zn are 11.94 and 5.31 respectively. Therefore, the grain sizes of Mg-2Zn and Mg-2Zn-0.6Ca were finer than pure Mg. Also, addition of 2Er further reduced the grain size of Mg-2Zn from 15.99 to 6.6 µm as seen in Figure 4.6. After fine grained as-DMDed products are obtained, further enhancement of mechanical properties can be carried out using hot-extrusion due to decrease in the grain size. The movement of dislocations will be prevented due to an increased fraction of boundaries. Trace addition of Er to reduce the grain sizes of Mg-9Zn-0.6Zr alloy was done by Zhang et al. [219]. Er addition on Mg-Al alloys were studied by Seetharaman et al [205]. The reduction in grain size was attributed to the capability of Al-Er related phases for grain nucleation and grain growth restriction. These elements are capable of segregating at the front of grain growth. Restriction of grain growth takes place due to an intensive constitutional undercooling in a diffusion layer ahead of the advancing solid/liquid interface [220]. It was studied that rare earth elements can change the solution degree of zinc and reduce the time of nucleation by decreasing the solidus curve [221]. The MgZnEr phases, especially i-phase can restrict grain growth during the recrystallization process. Also, Er solute atoms exert drag force on the grain boundary motion.

4.3.3. Extrusion

The increase in the mechanical properties after thermomechanical processing like hot-extrusion is due to the complete ramification of the coarse grained as-DMDed microstructure of the starting ingot. Alloys after extrusion exhibited finer grain sizes as shown in the optical microstructures presented in Section 4.2.4. Extrusion textures for magnesium alloys are developed by the combination of processes like deformation, recrystallization and grain growth, nucleation and growth of DRXed grains and shear band deformation that can lead to weakening of ideal basal texture [222]. Also the dispersion, dissolution and formation of certain new phases may take place during this process. Due to such a deformation, it leads to the generation of lattice defects and with increased defects the internal energy of the material increases. The microstructure evolves by reorganizing these defects to decrease this excess energy of the deformed system.

In the case of Mg-2Zn-2Er, W-phase with different morphologies in both as-DMDed and as-extruded alloys were seen in Figure 4.32 and Figure 4.33. They were present both at the matrix and interdendritic boundaries. An effective way of breaking these coarse secondary phases is hot-extrusion, which resulted in fine broken phases distributed along the extrusion direction as seen in the alloys in Section 4.2.4.2. These fine phases could result in enhancement of mechanical properties by minimizing the cavitation at the interface of the matrix and secondary phase.

The first stage in the evolution of microstructure during deformation is recovery, where a low energy dislocation structure is formed within the existing grains that have low angle boundaries. This leads to a decrease in the dislocation density. The second stage is recrystallization and it takes place when a sufficient temperature and deformation rate is achieved. This process leads to creation of new grains by accommodating the increased misorientation of the cells of the substructure. High-angle boundaries and substructures develop around particles. As seen for Figure 4.19, the black regions in inverse pole figures correspond to intermetallic particles which have not got indexed in EBSD. In these figures, it could be observed the nucleation of new grains at the vicinity of these coarse particles. Particle stimulated nucleation can occur that leads to the growth of dislocation free new grains. Static or dynamic type of recrystallization (DRX) takes place depending on whether a separate heat-treatment has been introduced or if the nucleation and grain growth takes place during deformation.

The DRX has taken place in all the alloys, but partial DRX has taken place in Mg-2Zn-2Er after hot-extrusion. The plot of recrystallized grains for as-extruded Mg-2Zn-2Er could be seen in Figure 4.40. Here, different types of grains were indexed using Channel5 software. Different colors indicate different state of the grains. The recrystallized grains were shown in blue, deformed grains in red followed by substructured grains in yellow. The grain reconstruction done in Tango[7] takes each grain and measures the internal average misorientation angle within the grain. The minimum angle used to define a subgrain (θ_c) is 1^o. Any grain exceeding this angle is classified as deformed. Substructure is defined for those grains consisting of subgrains whose internal misorientation is under 1^o, but the misorientation from subgrain to subgrain is above 1^o. Remaining grains are denoted as recrystallized. Most of the substructured and deformed grains have a dominant prismatic textural component and hence the overall microstructure exhibits this texture. From the recrystallization fraction plot, it could be seen that the recrystallized grains made up only about 29% of the total grain area.

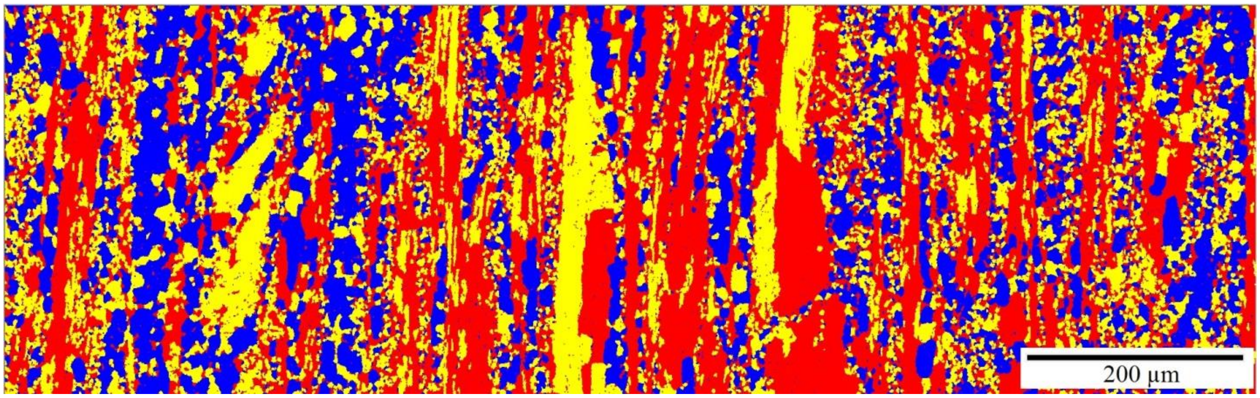

Figure 4.40: Different types of grains indexed using Channel5 software for as-extruded Mg-2Zn-2Er. (Recrystallized = Blue (28.86%), Substructure = Yellow (29.75%), and deformed = Red (41.39%))

DRX nucleation rate is related to the extrusion temperature. Since all the alloys were extruded at the same temperature, the increased amount of Er could have caused partial DRX. Very small nano-sized precipitates present in this alloy could lead to precipitation strengthening effect to a certain extent. Normally, basal texture is predominantly seen in as-extruded Mg-Zn-RE alloys [223], and it could be seen for all the samples barring Mg-2Zn-2Er. The presence of these W-phase particles and the incomplete DRX could be a reason for this. These particles leading to DRX via PSN could also be seen for several different Mg based alloys.

Segregation of RE element at the grain boundaries might retard recrystallization and weaken basal texture [224]. Also PSN effect led to randomize texture, a typical example is that of the extruded WE54 Mg alloy [225]. Decreased texture intensities for Mg-2Zn-0.6Ca-1Er and Mg-3Zn-0.5Er have led to an increase in the elongation values of 17.2 and 19.8% respectively.

---

[7] https://nano.oxinst.com/products/ebsd/post-processing-software

4.3.4. Tensile properties

In the case of metals, slip takes place due to the movement of dislocations. Several factors like Hall-Petch strengthening, Dislocation strengthening, Precipitation strengthening, solid-solution strengthening and frictional contribution attribute to the strengthening of magnesium alloys. Several factors like grain size, grain orientation are to be considered to understand varied strain hardening behavior of magnesium alloys. Among all the alloys, Mg-2Zn-2Er with W-phase exhibited highest yield strength as seen in Figure 4.23. The individual strengthening factors are listed as follows:

4.3.4.1. *Grain boundary strengthening*

The contribution of Hall-Petch strengthening is given by Hall-Petch equation and that can be represented as follows:

$$\Delta\sigma_{GS} = KD^{-0.5}$$

Where K is the Hall-Petch co-efficient and for Mg it is 280 MPa µm$^{0.5}$, D is the grain size (in µm) for the alloys. Pure Mg has $\Delta\sigma_{GS}$ value of ~ 59.7 MPa and for the alloy with low grain size Mg-2Zn-2Er it is ~ 108.9 MPa. This clearly shows the effect of grain size on the strength of alloys, as there is vast difference in the grain sizes of pure Mg and the alloys. Minor Er additions to magnesium alloys have led to grain refinement strengthening as studied by Dongxia et al. on Al-Mg-Mn alloys [226].

4.3.4.2. *Solid solution strengthening*

Due to the enhanced solubility of the alloying elements like calcium, zinc [227] and erbium in magnesium is high, these alloying elements lead to solution hardening by remaining as dispersed solutes and impede the movement of dislocations. The elements are introduced within their solubility limit and the interruption in the regularity of Mg crystal lattice required activation in the form of temperature or stress for the movement of dislocations. The interruption in the regularity happens when these solute atoms dissolve in the interstitial or substitutional sites. The increase in yield stress due to solid solution strengthening contribution ($\Delta\tau_{SS}$) is related to the concentration of solute in weight percent (C_o) as follows [228]:

$$\Delta\tau_{SS} = AC_o^{\frac{2}{3}}$$

The contribution to strengthening of individual elements could be calculated provided the values of increase in strength as a function of weight percent is present.

4.3.4.3. Precipitation strengthening

The melting point of W-phase is 520 °C and the melting point of i-phase is 445 °C [229]. Therefore when these alloys are extruded at 350 °C, the secondary phases did not solid solute in Mg matrix. These high melting point precipitates pinned the grain boundaries. Several nano precipitates have been formed as seen in TEM images in Figure 4.33 and Figure 4.36 after hot-extrusion. These secondary phases with high hardness can accumulate stress near the particle-matrix interface due to de-cohesion. Hence the deformation of matrix can be blocked by these fine particles during tensile and compressive test. Orowan strengthening due to resistance of these broken hard phases could be given as:

$$\Delta\sigma_{Orowan} = \frac{0.13Gb}{\lambda}\ ln(\frac{d_p}{2b})$$

Where, d_p is the average particle size and λ is the interparticle spacing.

The d_p value calculated for as-extruded Mg-2Zn-2Er is 56 nm, as plotted in histogram in Figure 4.34. The same phenomenon has been reported by Wang et al. on Mg-Zn-Er alloys [143]. The secondary phases that are distributed uniformly can provide sufficient dispersion strengthening to the alloys by pinning the dislocations. The d_p value calculated for Mg-3Zn-0.5Er is 49 nm, as plotted in histogram in Figure 4.37. The i-phase which is a quasicrystal is stable against coarsening during hot-extrusion. This is because it has low interfacial energy with the α-Mg matrix [230]. Hence they exhibit good plasticity after thermomechanical process, which could be seen in the tensile test curves shown in Figure 4.23.

4.3.4.4. Dislocation strengthening

The Grain boundary map for as-extruded Mg-2Zn-2Er is plotted in Figure 4.41. Inside the unDRXed grains, low angle sub-structures are formed which could be clearly seen (indicated green in color in GB maps). The black areas that the patterns could not be indexed, represent W-phase. This means that the dislocation density is high in the unDRXed grains compared to the DRXed grains.

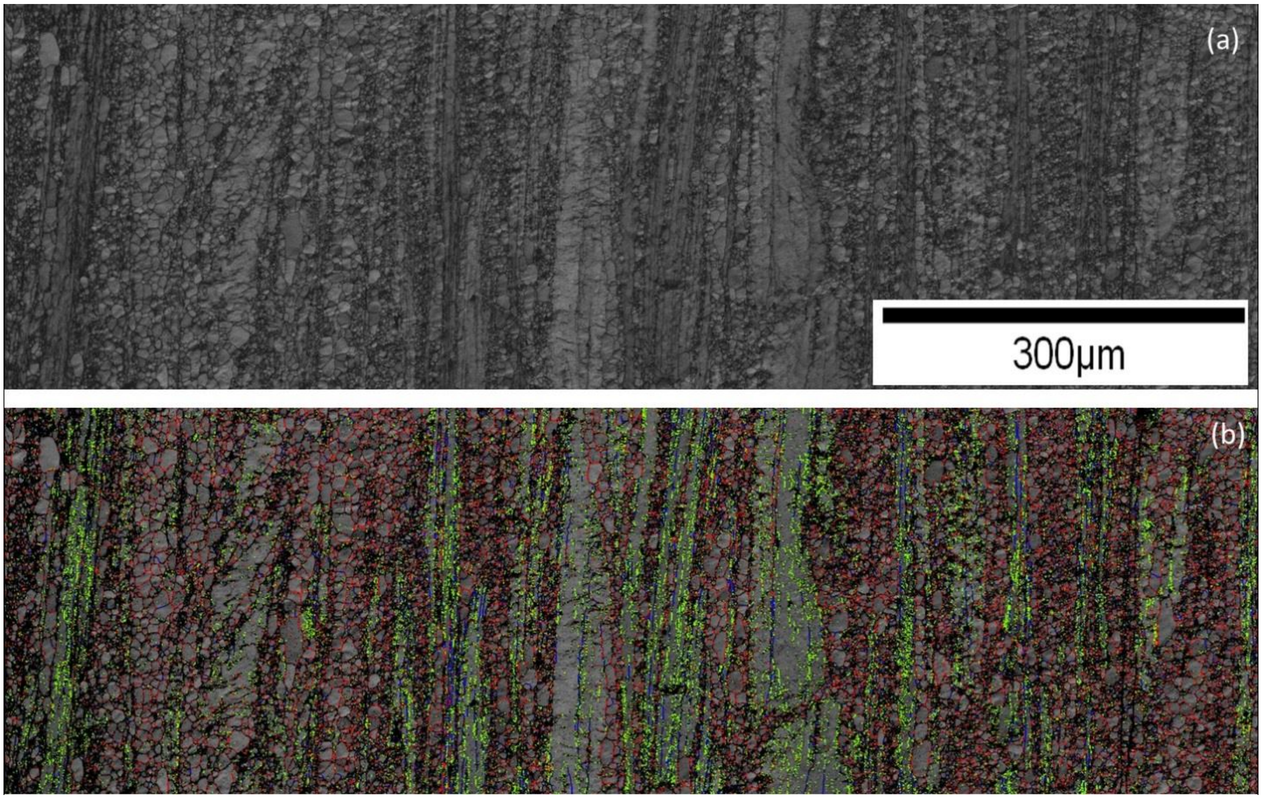

Figure 4.41: Band contrast (a) – Grain boundary (GB) map (b) for as-extruded Mg-2Zn-2Er. In the GB maps, low angle boundaries (2-5°) are in green, intermediate angle boundaries (5-15°) are in blue and high angle boundaries (>15°) are in red.

The equation used to calculate the dislocation strengthening component is:

$$\Delta\sigma_{disl} = f_{unDRX} M_{unDRX} \alpha G b \sqrt{\rho_{unDRX}}$$

Where, α is 0.2 for Mg [231], G is the shear modulus (16.6 GPa for Mg [232]), b is the Burger's vector ($3.21 * 10^{-10}$ m for Mg [232]), M_{unDRX} is the taylor factor for the unDRXed region, f_{unDRX} is the fraction of unDRXed grains (0.71) and ρ_{unDRX} is the dislocation density in the unDRXed region. The density of dislocations in the DRXed region is much lower and its contribution is neglected while calculating dislocation strengthening component.

For deformed Mg alloys, the value of ρ_{unDRX} is 10^{14} m^{-2}. Also the Taylor component calculated is $M_{unDRX} = 3.2$. Therefore, $\Delta\sigma_{disl}$ value 24.2 MPa for as-extruded Mg-2Zn-2Er, which is very small value as compared to $\Delta\sigma_{GB}$.

Grain orientation effect

For as-extruded Mg-Zn-Ca-Er alloys, as seen in the EBSD analysis, most of the grains have the ideal orientation for basal slip parallel to basal planes. Change in orientation will have an effect on the values of resolved shear stress on basal, prismatic and pyramidal planes. The equations for calculating the critical resolved shear stress in these slip planes could be given as:

$$\tau_x = m_x * \sigma$$

Where m is the Schmid factor. Using grain orientation distribution data calculated using EBSD, the average schmid factors m_{basal}, m_{prism}, $m_{pyramidal}$ can be calculated for as-extruded pure Mg and its alloys and they are shown in

Table 4.10: Parameters for dislocation slip systems of as-extruded pure Mg and its alloys

Material	**Basal <a>**		**Prism <a>**		**<c+a> Second order**		$\frac{\tau_{prism}}{\tau_{basal}}$	$\frac{\tau_{<c+a>}}{\tau_{basal}}$
	$M_{s.b}$	τ_{basal}	$M_{s.p}$	τ_{prism}	$M_{<c+a>}$	$\tau_{<c+a>}$		
Pure Mg	0.1942	18.643	0.4472	42.93	0.4563	43.81	2.303	2.350
Mg-2Zn	0.1879	27.246	0.4427	64.19	0.4487	65.06	2.356	2.388
Mg-2Zn-2Er	0.1316	25.267	0.4443	85.31	0.4385	84.19	3.376	3.332
Mg-2Zn-0.6Ca-1Er	0.1825	23.36	0.446	56.91	0.4512	57.75	2.444	2.472
Mg-2Zn-0.6Ca	0.1948	25.129	0.4182	53.95	0.4347	56.07	2.147	2.232
Mg-3Zn-0.5Er	0.1646	24.69	0.4481	67.22	0.4489	67.34	2.722	2.727

Using the above table, it could be seen that the CRSS values for three different slip planes are different for each material and they are different for all the alloys. More the value of $\tau_{non-basal}/\tau_{basal}$ there is difficulty of operation of non-basal slip [233]. The increase of $\tau_{prism}/\tau_{basal}$ and $\tau_{<c+a>}/\tau_{basal}$ for Mg-2Zn-2Er indicates the weakening of non-basal slip. This leads to decreased strain hardening ability in as-extruded Mg-2Zn-2Er alloy as seen in Figure 4.23.

4.3.5. Impulse excitation measurements

As seen in Section 4.2.6, pure Mg and its alloys exhibit elastic modulus values in the range of 43-45 MPa. For metallic implants, there are two important properties to investigate targeting orthopedic applications: elastic modulus and damping capacity. Stress-shielding effects are caused due to high elastic modulus (such as exhibited by steel and titanium) as compared to the natural bone and it decreases the stimulation of new bone growth leading to implant failure. Due to the high damping capacity of implants made of magnesium, it absorbs the vibratations caused due to the movement of joints. This suppresses the stresses developed at the interface of the implant materials. Hence the Mg-Zn-Ca-Er alloys developed exhibit elastic modulus close to that of bone and they can minimize stress-shielding effect.

4.3.6. Hardness

As seen in Section 4.2.7, the as-extruded alloys exhibit higher hardness values and Mg-3Zn-0.5Er exhibits the maximum hardness value of 68.27. The following are the reasons attributed to an increase in the hardness value of the alloys as compared to pure Mg:

(a) Constraint to localized deformation during indentation due to the presence of uniformly distributed and harder precipitates formed during DMD and hot-extrusion.

(b) Reduced grain size

Although W-phase containing Mg-2Zn-2Er exhibits finer grain size, the hardness value is lower than that of Mg-3Zn-0.5Er. A maximum of up to 82% increase in the hardness value of pure Mg was observed for Zn/Er = 1 and 101% increase in the hardness value w.r.t pure Mg was observed for Zn/Er = 6.

4.4. Conclusion

The important function of biodegradable magnesium implant is the uniform dissolution as the new bone/tissue grows and provides adequate mechanical support. Pure Mg as-DMDed has poor Vickers hardness and consists of porosities. Pure Mg as-extruded has low yield strength (~ 96 MPa), low tensile strength (~ 150 MPa) and this could lead to the deterioration of structural integrity before healing could take place. Hence, alloying methodology was adapted to improve the mechanical properties. Alloying with Zn, Ca and Er led to the precipitation of intermetallic phases $MgZn_2$, $Mg_3Zn_3Er_2$, Mg_3Zn_6Er phases at the grain boundaries and some inside the grains.

The primary conclusions of the first part of the study are listed as follows:

- Disintegrated melt deposition technique followed by hot-extrusion is a very safe, efficient and cost-effective which provides the highest yield and dense products.
- To achieve the first goal of tailoring the bulk microstructure of the alloys, hot-extrusion has been used and to enhance the mechanical properties, material selection method has been used by choosing biocompatible elements like zinc, calcium and erbium to synthesize several compositions.
- Successful synthesis of dense pure Mg and the alloys Mg-2Zn, Mg-2Zn-2Er, Mg-2Zn-0.6Ca-1Er, Mg-2Zn-0.6Ca and Mg-3Zn-0.5Er with highest yield have been achieved.
- Minimal addition of alloying elements led to an enhancement of the mechanical properties due to reduction in grain size, distribution of secondary phases that improves the strength based on the Orowan strengthening theory and the presence of solid solution strengthening.
- Room temperature tensile and compressive properties were enhanced and the presence of alloying additions has enhanced the ductility by a significant extent.

- The elastic modulus did not change significantly with the addition of Zn, Ca and Er, which is very important for the biomedical applications of magnesium.

CHAPTER 5

CORROSION AND ELECTROCHEMICAL STUDIES

5. Corrosion and electrochemical studies

5.1. Introduction

Magnesium is a very active element, i.e., it has a natural tendency to form oxides in any environment. $Mg(OH)_2$ has a greater negative chemical potential than that of Mg^{2+} or MgO, which suggests that Mg in oxidized state is more stable than in its metallic state [169]. Mg can corrode in pure water. Several reactions occur to Mg in an aqueous solution, some of which are listed below [234].

$$Mg = Mg^{2+} + 2e^- \qquad E^o = -2.363\ V$$

$$Mg + 2OH^- = Mg(OH)_2 + 2e^- \qquad E^o = -2.689\ V$$

$$Mg = Mg^+ + e^- \qquad E^o = -2.659\ V$$

$$Mg^+ = Mg^{2+} + e^- \qquad E^o = -2.067\ V$$

The surface film on Mg varies in its composition that depends on the environment and formation conditions. $Mg(OH)_2$ is the main constituent of the surface film when Mg is exposed to aqueous media. In dry conditions, MgO is the main composition of the surface film. Mg surface film is not as protective as the film formed on the surface of Al. This is because the Pilling-Bedworth ratio of MgO/Mg is smaller than 1, whereas the ratio of $Al_2O_3/(2Al)$ is greater than 1. Thus, MgO film does not provide surface protection as compared to Al_2O_3 [169].

When Mg consists of alloying elements, they also become the constituents of the surface film. They have a significant influence on the corrosion behavior of the phases, as the matrix phase is always preferentially corroded. The secondary phases can either act as a barrier to prevent further corrosion or it can act as a galvanic couple. Recently, biodegradable Mg alloys have become the topic of interest and a huge progress has been made in this field. Several coatings have been developed to control the biodegradation. The corrosion mechanisms for the newly developed alloys have to be properly understood.

5.2. Results

This chapter illustrates different corrosion tests (hydrogen evolution, potentiodynamic polarization tests) conducted in two different mediums (NaCl and PBS) on both as-DMDed and as-extruded alloys. Subsequent SEM images of the corroded samples have been recorded and based on the polarization curves, the corrosion mechanisms have been discussed in this section. Every experiment has been repeated twice to assure repeatability.

5.2.1. H_2 evolution test for as-extruded alloys

The main cathodic reaction during corrosion of magnesium alloys is the reduction of hydrogen ions and hence measuring the volume of hydrogen gas provided the corrosion rate of Mg alloys [235]. This method is reliable to determine the average corrosion rates of Mg alloys. But such curves are difficult to reproduce, as magnesium is highly reactive in aqueous solution and there will be relative errors. Several trials have been performed and the error bars have not been included for a clearer picture.

5.2.1.1. NaCl medium

The results of H_2 evolution test in 0.5 wt.% NaCl solution for as-extruded alloys at room temperature are plotted in Figure 5.1. For pure Mg, after 20 hours, the degradation took place rapidly and the experiment had to be terminated after 50 hours as the immersed tube was devoid of the solution. A large number of gas bubbles were formed and it could be seen evidently arising from the sample. But for the alloys, the test was conducted upto 92 hours and the degradation rates were less than that for pure Mg. The alloys other than Mg-2Zn exhibited similar behavior. Among the alloys, Mg-2Zn showed an increase in corrosion rates whereas Mg-2Zn-2Er showed the least.

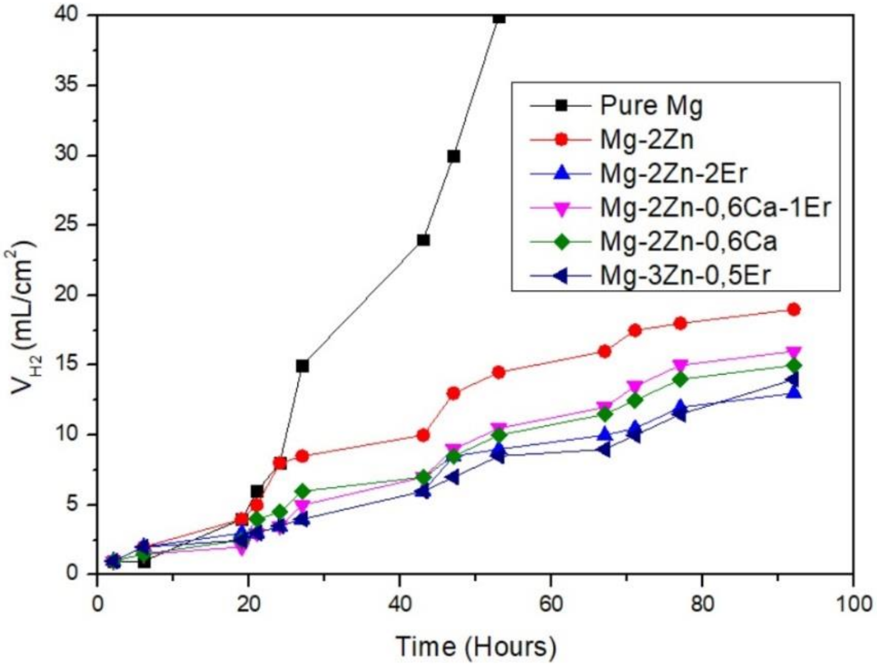

Figure 5.1: H_2 evolution test results for as-extruded Mg and its alloys in 0.5 wt.% NaCl solution at room temperature

5.2.1.2. *PBS medium*

The results of H_2 evolution test in PBS solution for as-extruded alloys at 37°C are plotted in Figure 5.2. The volume of hydrogen increased with increasing time for all the alloys; however, the rates were different from alloy to alloy as can be seen in Figure 5.2. Immersion until the first 10 hours shows similar degradation rates for all the materials. Pure Mg degrades faster after 20 hours of immersion and after 80 hours, the degradation was so much that entire measuring tube was occupied by hydrogen after consuming the solution within. The degradation behavior is similar for the alloys, where Mg-2Zn-2Er and Mg-2Zn-0.6Ca showed minimum degradation rates.

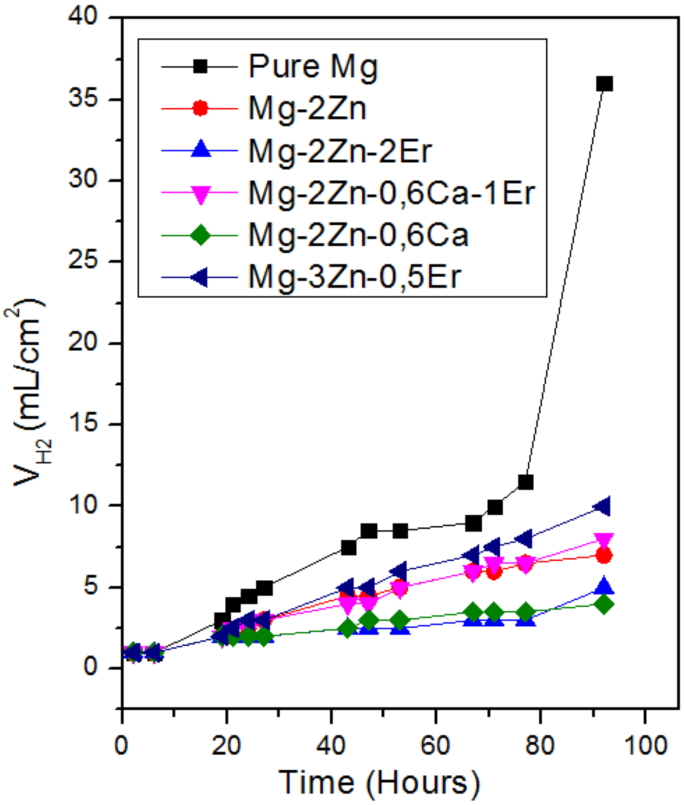

Figure 5.2: H_2 evolution test results for as-extruded Mg and its alloys in PBS solution at 37°C

In both the mediums, an undesired initial "hydrogen burst[8]" was not seen for both pure Mg and its alloys. The behavior appeared to be relatively homogeneous for the alloys, barring pure Mg which failed to cope up after certain time interval (28 hours in NaCl and 80 hours in PBS solution). That is when fresh sites are exposed to the corrosive medium after the oxide layer has been penetrated or removed. The surfaces after this test were rough and for pure Mg, corrosion takes place at the edges.

---

[8] Unexpected and undesired large volumes of hydrogen evolution

5.2.2. Potentiodynamic Polarization test

As compared to H_2 evolution test that measures average corrosion rates over certain duration of time, potentiodynamic polarization tests or PDP curves represent the corrosion behavior at a particular point of time. The tests are conducted for both NaCl and PBS medium and they are presented in the subsequent sections.

5.2.2.1. NaCl medium

The curves for PDP test of as-extruded Mg and its alloys in NaCl solution at room temperature are plotted in Figure 5.3. After the test, the alloy surfaces turned into black after exposing to the medium. The cathodic polarization curves look similar for all the materials. The anodic part changes for different materials, and there is a knee point beyond which the partially protective surface film fractures and the corrosion takes place quickly. Since there is some amount of measurable anodic current density below the knee point, the film that is mainly constituted of $Mg(OH)_2$ is not considered as real passive. Table 5.1 shows the electrochemical polarization parameters and the calculated corrosion rate obtained from the polarization plot.

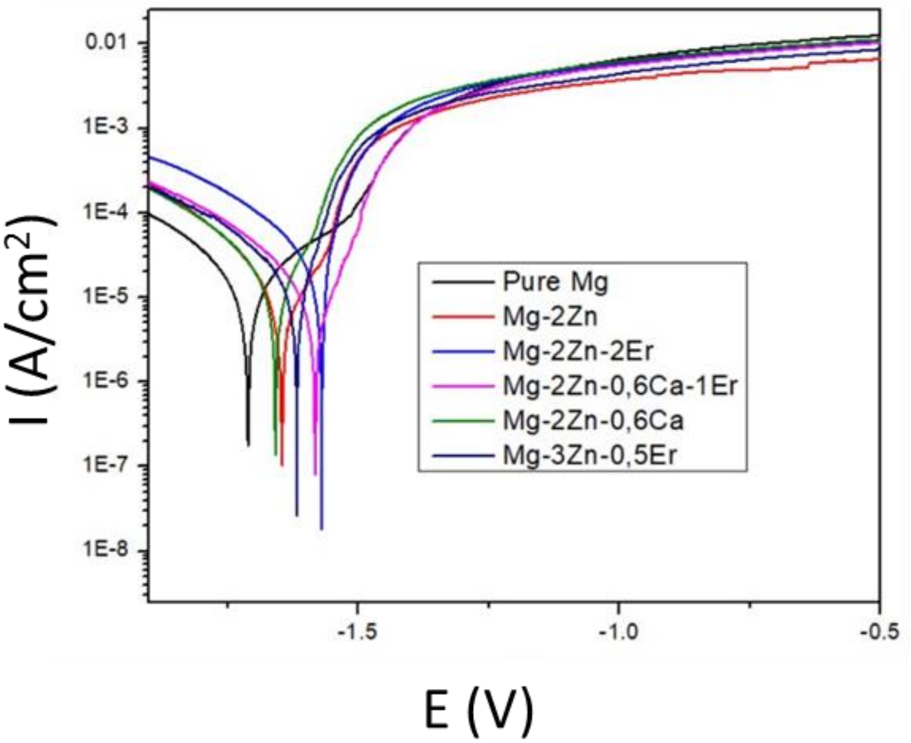

Figure 5.3: PDP results for as-extruded Mg and its alloys in NaCl solution at room temperature

Table 5.1: Electrochemical polarization parameters values obtained from Figure 5.3

Material	E (V)	I (A/cm^2)	Rp (Ω/cm^2) (x10^4)	Corrosion rate (µm/y)
Pure Mg	-1.711	5.63 x 10^{-7}	0.829	12.98
Mg-2Zn	-1.645	1.041 x 10^{-7}	1.58	2.41
Mg-2Zn-2Er	-1.57	1.82 x 10^{-8}	8.626	0.42
Mg-2Zn-0.6Ca-1Er	-1.582	8.15 x 10^{-8}	1.94	1.88
Mg-2Zn-0.6Ca	-1.658	1.394 x 10^{-7}	1.189	3.22
Mg-3Zn-0.5Er	-1.617	2.64 x 10^{-8}	6.125	0.61

As seen in the figure, Mg-2Zn alloy is less susceptible to corrosion (E_{corr} = -1.645 V vs. standard calomel electrode (SCE)) as compared to pure Mg (E_{corr} = -1.711 V vs. SCE). Shifting of corrosion potential to a more positive value implies that addition of Zn improves the nobility of magnesium alloys. Mg-2Zn-2Er exhibits much lower corrosion current density and higher corrosion potential (E_{corr} = -1.57 V vs. SCE) as compared to pure Mg. Also, the breakdown potential (E_{pt}) for Mg-2Zn alloy is greater than pure Mg ($E_{pt2} > E_{pt1}$), hence pure Mg can undergo localized corrosion faster than Mg-2Zn. Slightly higher amount of zinc results in lower corrosion resistance as seen for Mg-3Zn-0.5Er (E_{corr} = -1.617 V vs. SCE) in comparison with Mg-2Zn-2Er. For Mg-2Zn-0.6Ca-1Er, the corrosion potential also was more positive (E_{corr} = -1.582 V vs. SCE) as compared to pure Mg. Thus, these polarization curves demonstrate that Zn, Ca and Er are beneficial to enhance the corrosion resistance of Mg-based alloys.

The corrosion rates calculated using the equation in Section 3.9.4 are tabulated in Table 5.1. In the table, it could be seen that for pure Mg the corrosion rate is very high as compared to the alloys. The corrosion rate calculated for pure Mg is 12.98 µm/y. This value is 2.41 µm/y for Mg-2Zn. With the addition of 2Er to Mg-2Zn, the corrosion rate is reduced to 0.42 µm/y. Mg-2Zn-0.6Ca exhibits corrosion rate of 3.22 µm/y and with the addition of 1Er to the ternary alloy the value reduces to 1.88 µm/y. Among Mg-Zn-Er ternary alloys, Mg-3Zn-0.5Er also exhibits lower corrosion rate of 0.61 µm/y.

The surface morphologies were observed in SEM after removing the corrosion products using chromic acid, as seen in Figure 5.4. Pure magnesium suffered intensive corrosion during immersion; black corrosion products wearing off its surface. Many deep pits were found and one such pit could be seen in Figure 5.4a. It should be noted that the presence of these pits are detrimental to the final corrosion rate and will lead to the total destruction of the material. For Mg-2Zn, corrosion took place along the interconnected boundaries as seen in Figure 5.4c, leaving most of the surface uncorroded. In the case of Mg-2Zn-2Er, it is same as that of Mg-Zn with corrosion taking place at the interconnected boundaries, but less frequently seen as shown in Figure 5.4e. In both of these alloys, no pits were observed.

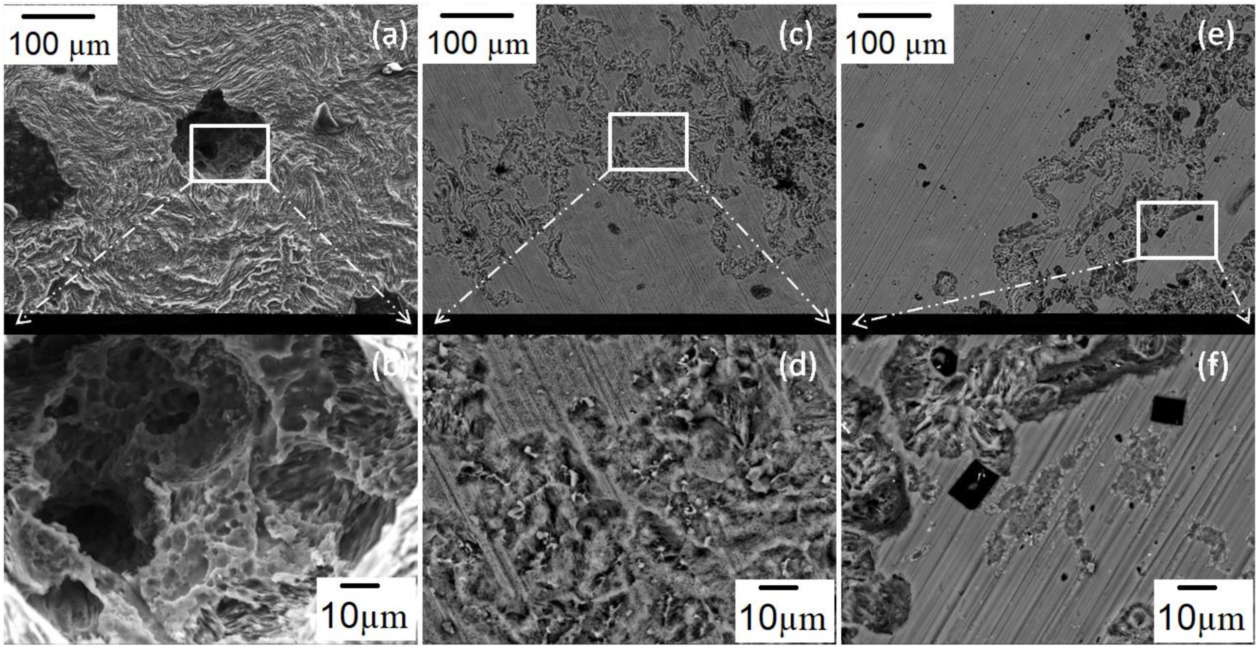

Figure 5.4: Secondary electron and back-scattered images of (a) pure Mg, (c) Mg-2Zn and (e) Mg-2Zn-2Er as-extruded alloys immersed in 0.5 wt.% NaCl for 3h. (b), (d) and (f) are the corresponding magnified images of the rectangular sections shown above for each material

5.2.2.2. PBS medium

The curves for PDP test of as-extruded Mg and its alloys in PBS solution at 37^{o}C are plotted in Figure 5.5. The electrochemical polarization parameters for this figure and the calculated corrosion rate is tabulated in Table 5.2. The results are similar to that of tests conducted in 0.5 wt.% NaCl solution, except that the potential values are more electropositive. The corrosion potential of the alloys are nobler than that of pure magnesium. Pure Mg exhibited a corrosion potential of -1.634 V vs. SCE. Addition of 2Zn led to a more positive value of -1.619 V vs. SCE. With the addition of rare earth to Mg-2Zn, the corrosion potential was more positive for Mg-2Zn-2Er (E_{corr} = -1.51 V vs. SCE). Mg-2Zn-0.6Ca exhibits slightly reduced corrosion current i_{corr} (1.7 x 10^{-8} A/cm^{2}) as compared to other materials. These electrochemical results prove that the alloys have better corrosion resistance than that of pure magnesium. Mg-2Zn-2Er alloy exhibits excellent corrosion resistance while pure Mg suffered severe dissolution. These values are in good agreement with the hydrogen evolution test results.

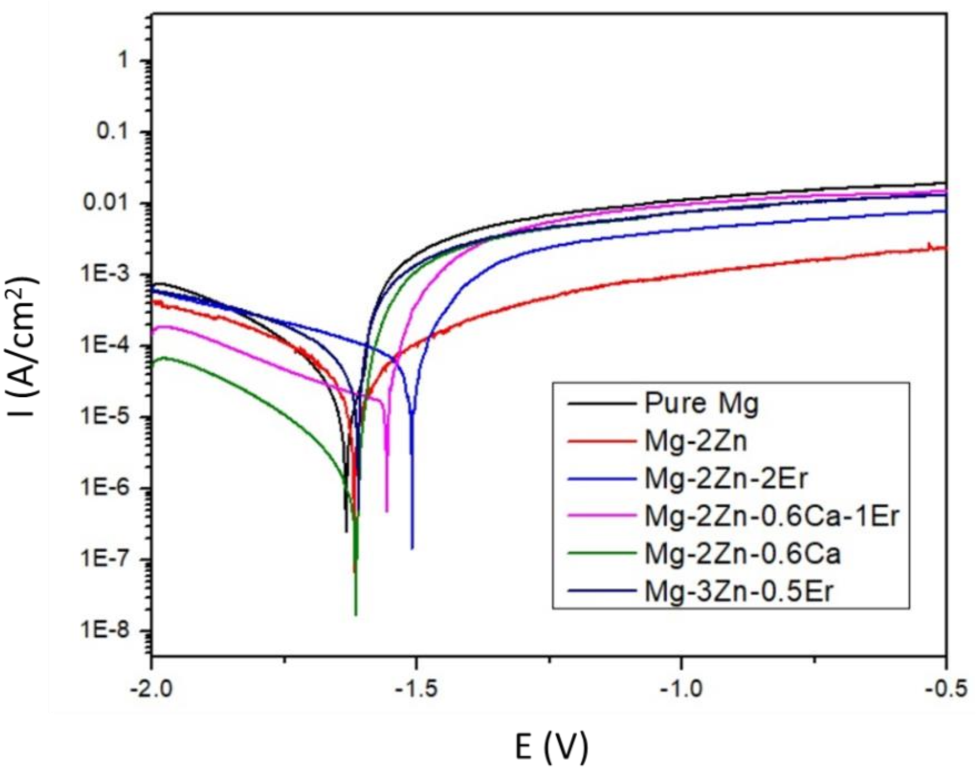

Figure 5.5: PDP results for as-extruded Mg and its alloys in PBS solution at 37°C

Table 5.2: Electrochemical polarization parameters values obtained from Figure 5.5

Material	E (V)	I (A/cm^2)	Rp (Ω/cm^2) (x 10^4)	Corrosion rate (µm/y)
Pure Mg	-1.634	5.572 x 10^{-7}	0.6353	12.86
Mg-2Zn	-1.619	2.7 x 10^{-7}	2.312	6.23
Mg-2Zn-2Er	-1.51	7.47 x 10^{-8}	1.027	1.72
Mg-2Zn-0.6Ca-1Er	-1.558	1.91 x 10^{-7}	0.3173	4.41
Mg-2Zn-0.6Ca	-1.616	1.7 x 10^{-8}	9.505	0.39
Mg-3Zn-0.5Er	-1.612	2.14 x 10^{-7}	0.314	4.94

The corrosion rates calculated using the equation in Section 3.9.4 for samples tested in PBS medium at 37 °C are tabulated in Table 5.2. In the table, it could be seen that, similar to samples tested in NaCl medium the corrosion rate value is high for pure Mg. The corrosion rate calculated for pure Mg is 12.86 µm/y. This value is 6.23 µm/y for Mg-2Zn. With the addition of 2Er to Mg-2Zn, the corrosion rate is reduced to 1.72 µm/y. Mg-2Zn-0.6Ca exhibits corrosion rate of 0.39 µm/y and with the addition of 1Er to the ternary alloy the value is 4.41 µm/y. Among Mg-Zn-Er ternary alloys, Mg-3Zn-0.5Er exhibits slightly higher corrosion rate of 4.94 µm/y.

5.2.3. Immersion test

5.2.3.1. NaCl medium

5.2.3.1.1. As-DMDed alloys

Immersion test for as-DMDed alloys were carried out for 1 day and 3 days in 0.5 wt.% NaCl solution and the results are plotted in Figure 5.6. After subsequent day and cleaning with chromic acid, it was found that the weight loss values exceeded above 30% for all the samples after Day 3.Mg-2Zn suffered weight loss of 28% after Day 1 and 37% after Day 3 of immersion. Similar results were observed for all the samples. Since the values are too high, further corrosion tests including electrochemical measurements have not been performed.

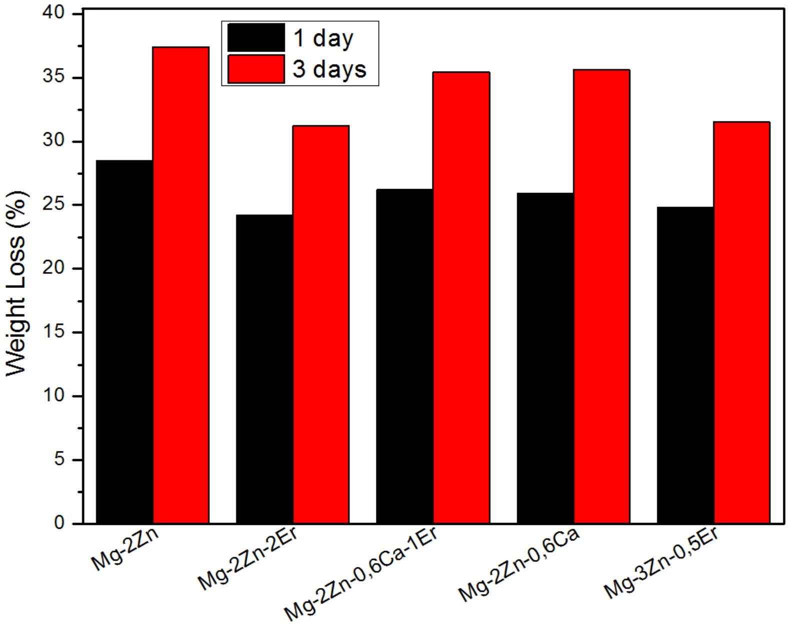

Figure 5.6: Immersion tests results for as-DMDed Mg alloys in NaCl medium

5.2.3.1.2. As-extruded alloys

The results of immersion test in 0.5 wt.% NaCl solution for as-extruded alloys at room temperature are plotted in Figure 5.7. The inset figure shows a clearer picture of the weight loss measurements for the alloys. All the alloys suffered weight loss as a result of severe corrosion. Pure Mg underwent rapid degradation after first day of immersion (38% weight loss) and thereafter the degradation process is moderate. But for the alloys, the degradation process is moderate from 1st day of immersion and there is no rapid degradation as compared to pure Mg. Among the alloys, Mg-2Zn-2Er exhibited higher degradation rates (4.2 wt.% after 7th day) and Mg-2Zn-0.6Ca exhibited the least (2 wt.% after 7th day). After the end of the experiment, corrosion products were detached from pure Mg and the alloys and it remained as sediments in the beakers. A lot of sediment was found on the pure Mg container, which is evident from the weight loss measurements in the figure below.

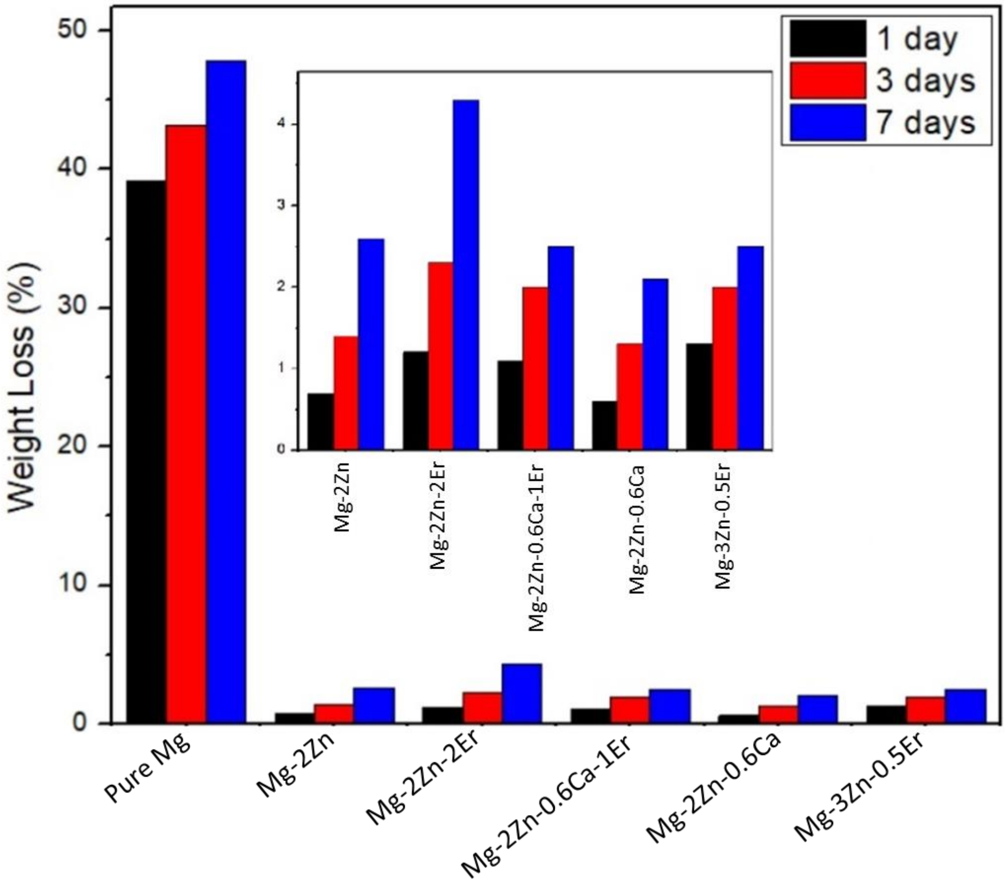

Figure 5.7: Immersion test results for as-extruded Mg and its alloys in 0.5 wt.% NaCl for 1, 3 and 7 days

The subsequent stereomicrographs of the samples after corrosion after 1, 3 and 7 days are shown in Figure 5.8-Figure 5.13. The edges of pure Mg sample lost its structural integrity after first day, which could be seen in Figure 5.8. The material loss took place mostly at the edges and after 7th day of immersion, severe corrosion is observed. A 47% weight loss was recorded after 7 days of pure Mg immersion in NaCl solution.

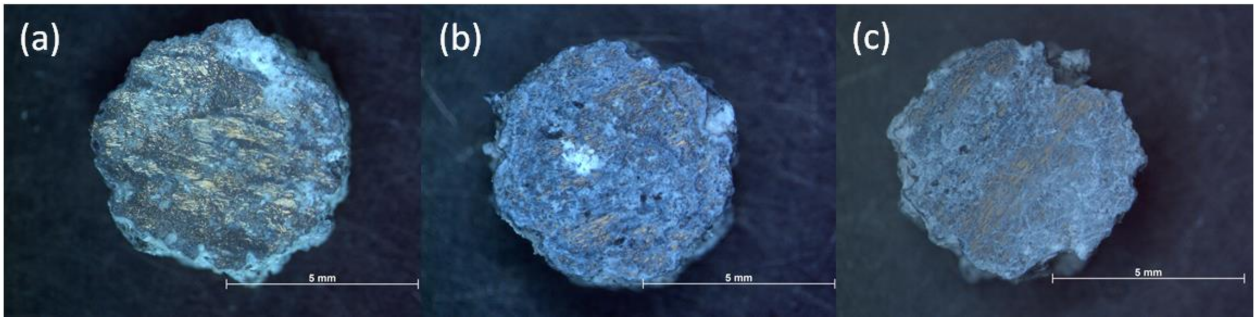

Figure 5.8: Immersed pure Mg samples in NaCl at 25 ^{o}C after (a) 1 day (b) 3 days and (c) 7 days

For Mg-2Zn, as seen in Figure 5.9, few regions of the sample is covered with the corrosion products after the first day (0.7% weight loss) and it gradually increases for 3rd day (1.4% weight loss). For 7th day, there is some material loss observed at the edges and also it starts at the surface of the sample (2.6% weight loss).

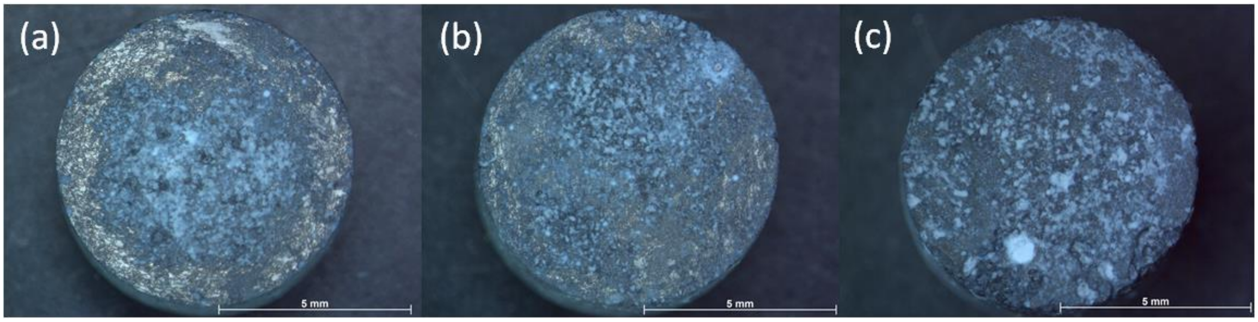

Figure 5.9: Immersed Mg-2Zn samples in NaCl at 25 ^{o}C after (a) 1 day (b) 3 days and (c) 7 days

The corrosion macrostructures for Mg-2Zn-2Er could be seen in Figure 5.10. After 1st day of immersion the corrosion has not taken place throughout the sample as compared to Mg-2Zn. But a significant weight loss has been determined for all the samples, and slightly more than that for Mg-2Zn. On Day 1, 1.2 wt.% loss was recorded, followed by 2.4 wt.% after Day 3. The material loss is detected at the edges of the sample after 7 days of immersion which attributed to more than 4.2% weight loss.

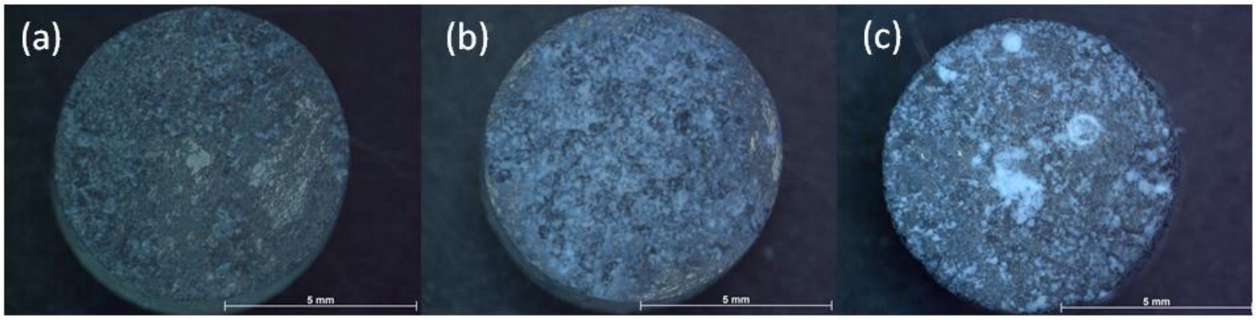

Figure 5.10: Immersed Mg-2Zn-2Er samples in NaCl at 25 ^{o}C after (a) 1 day (b) 3 days and (c) 7 days

The samples Mg-2Zn-0.6Ca-1Er as seen in Figure 5.11 also appears to be same as that of Mg-2Zn-2Er. But in the macrostructure of the surface, a few uncorroded regions appear even after 7th day of immersion. After Day 1, the corrosion occured at the centre of the specimen leaving few regions of the sample uncorroded.

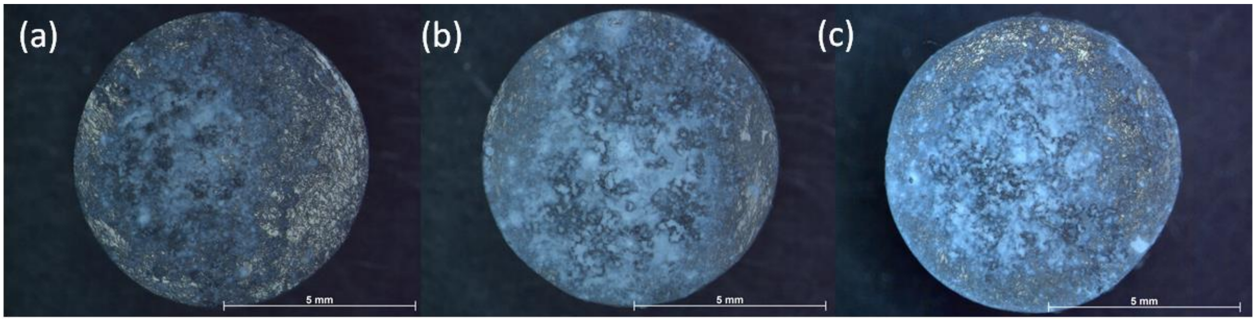

Figure 5.11: Immersed Mg-2Zn-0.6Ca-1Er samples in NaCl at 25 ^{o}C after (a) 1 day (b) 3 days and (c) 7 days

As seen in Figure 5.12, Mg-2Zn-0.6Ca exhibited the least weight loss among all the alloys. In Mg-2Zn-0.6Ca, the corrosion phenomenon is minimal for first 3 days of immersion. After 7th day, only the center of the sample has got corroded and there are still regions that are uncorroded.

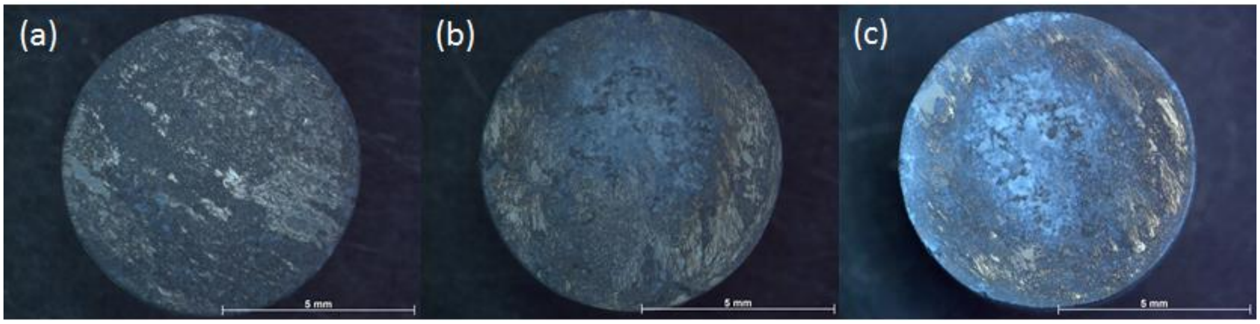

Figure 5.12: Immersed Mg-2Zn-0.6Ca samples in NaCl at 25 ^{o}C after (a) 1 day (b) 3 days and (c) 7 days

The corroded surface of Mg-3n-0.5Er as seen in Figure 5.13 shows less corrosion occurring after Day 1. After 7th day of immersion, the sample appears to be too corroded. Few small pits on the corroded surface could be evidently seen.

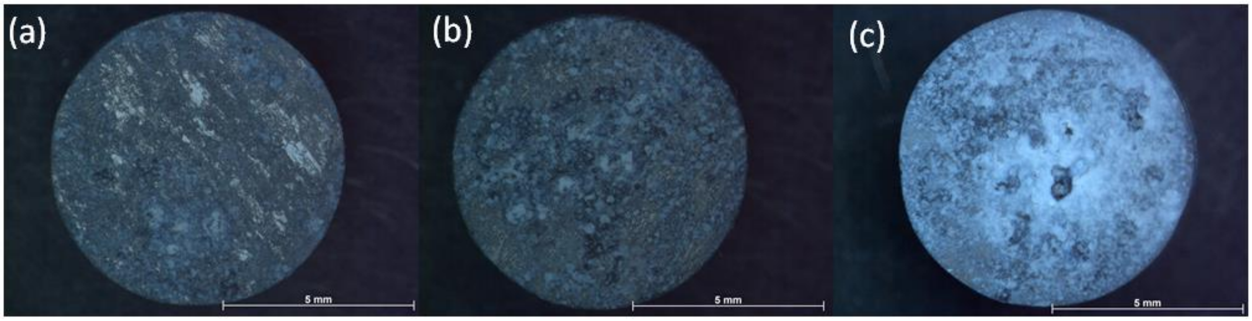

Figure 5.13: Immersed Mg-3Zn-0.5Er samples in NaCl at 25 °C after (a) 1 day (b) 3 days and (c) 7 days

5.2.3.2. PBS medium at 37°C

5.2.3.2.1. As-DMDed alloys

The inferior mechanical properties of as-DMDed alloys (Hardness) and the microstructure that consisted of several porosities, segregation of elements have not permitted the testing of these alloys in PBS medium at 37°C targeting biomedical applications, as it could result in undesired fast degradation as seen for the alloys tested in 0.5 wt.% NaCl medium. Hence as-extruded alloys will be tested and discussed.

5.2.3.2.2. As-extruded alloys

The results of immersion test in PBS solution for as-extruded alloys at 37°C are plotted in Figure 5.14. The results are similar to that of immersion test in NaCl medium except that the degradation levels were not too high. As compared to the alloys, pure Mg undergoes rapid degradation after first day of immersion and it continues for other tests too. For the alloys, there is very minimal degradation rates recorded. Mg-2Zn exhibits weight loss of 0.3% after Day 1, followed by 0.7 wt.% after 3rd day of immersion and 1.2 wt.% after 7 days. The weight loss appeared slightly higher for Mg-2Zn-2Er. Among the alloys and in this test, Mg-2Zn-0.6Ca shows higher degradation rates and Mg-2Zn-0.6Ca-1Er shows the least.

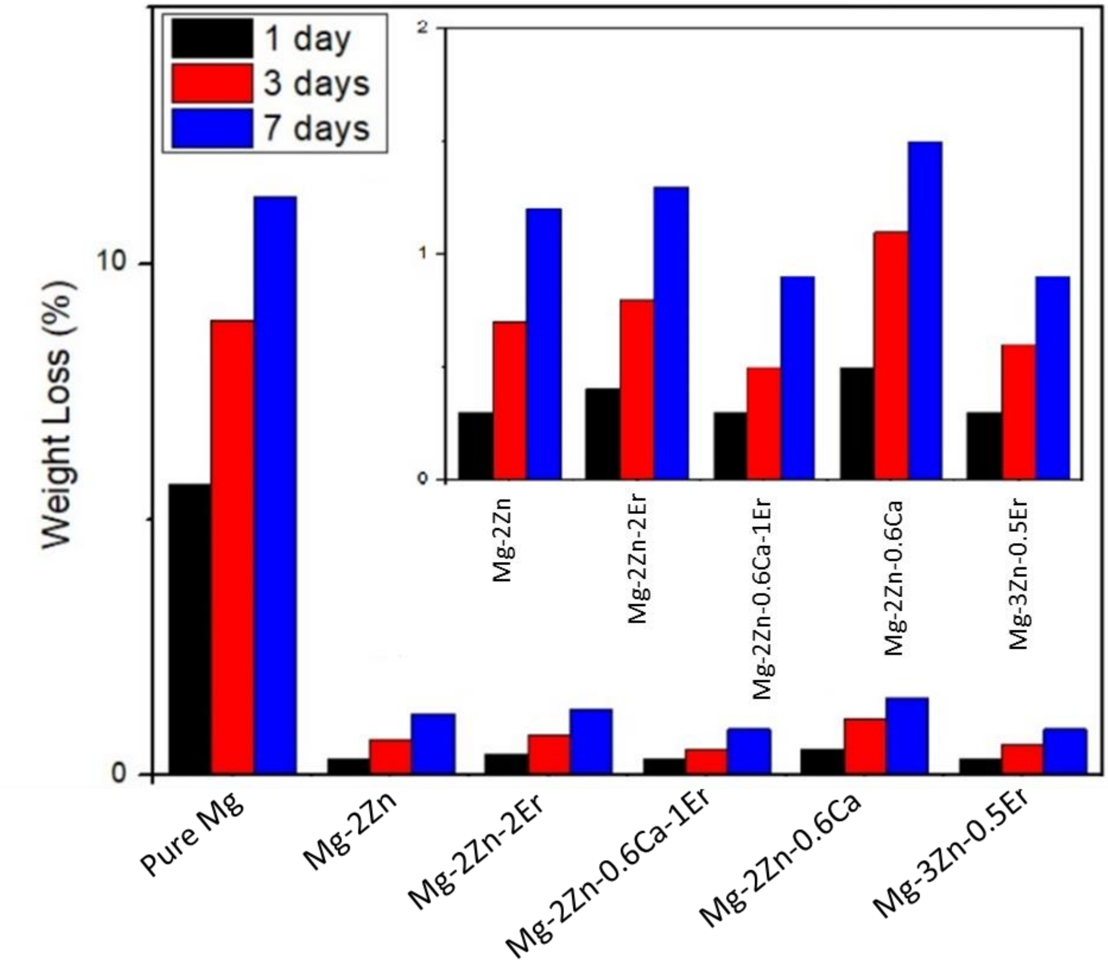

Figure 5.14: Immersion test results for as-extruded Mg and its alloys in PBS solution at 37^{o}C for 1, 3 and 7 days

The macrostructures of the corrosion products formed on the surface of pure Mg and its alloys after immersing in PBS solution for 1 day at 37^{o}C is represented in Figure 5.15. As can be seen in Figure 5.15, pure Mg and its alloys are covered with a very thick layer of corrosion products. All the materials lost its lusture after immersing in PBS. If carefully observed, these layers have a needle shaped morphology and they are easily worn off from the material. For pure Mg, black corrosion products could be seen in the edges only after 1st day of immersion. But for the alloys, this deposition was less and there appears a few uncorroded regions as well.

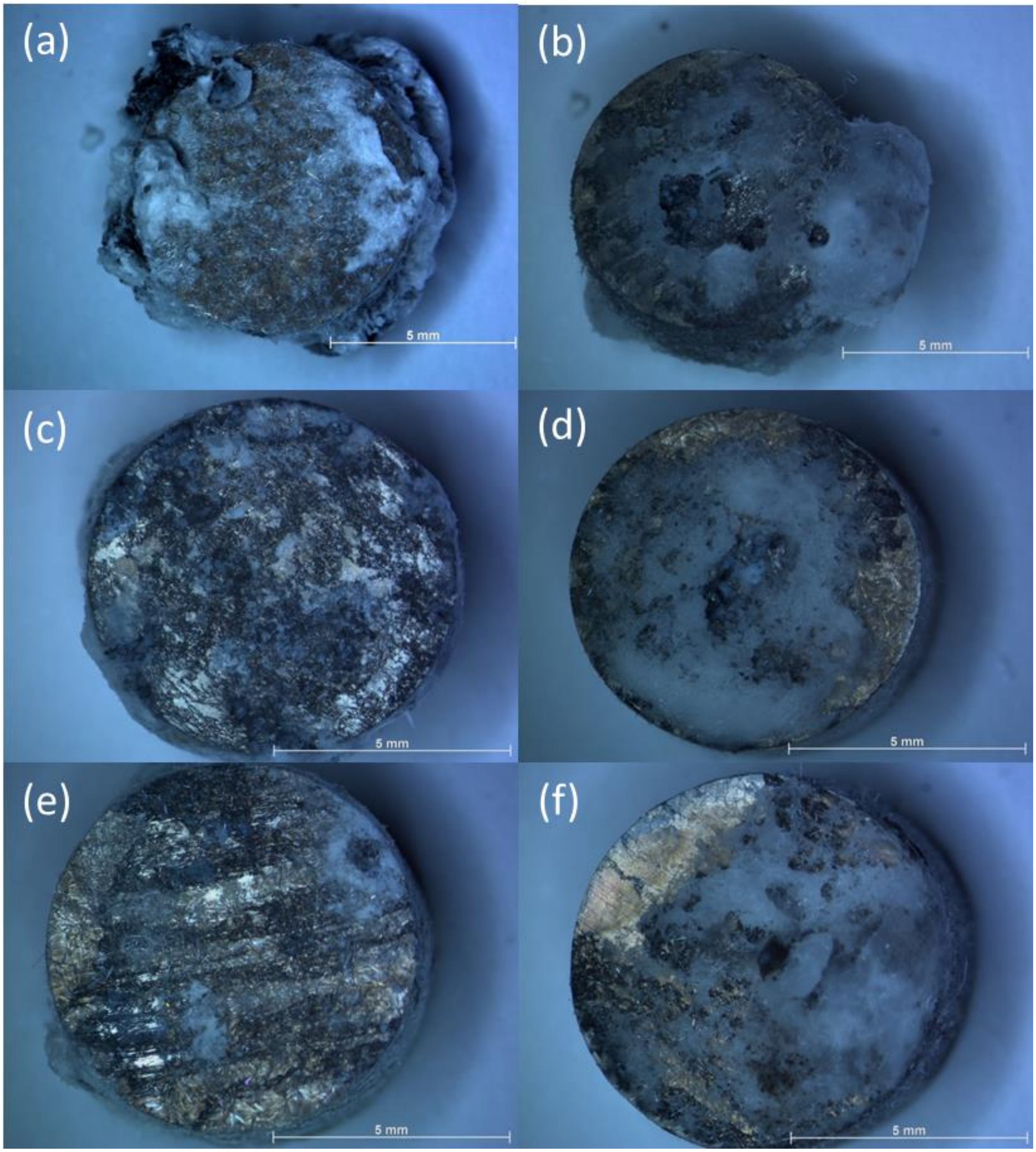

Figure 5.15: (a) Pure Mg (b) Mg-2Zn (c) Mg-2Zn-2Er (d) Mg-2Zn-0.6Ca-1Er (e) Mg-2Zn-0.6Ca and (f) Mg-3Zn-0.5Er after 1 day of immersion in PBS solution at 37^{o}C

5.2.4. X-ray photoelectron spectroscopy

As Mg-2Zn-2Er alloy composition exhibited enhanced corrosion resistance in PDP tests, further surface analysis was carried out to study the corrosion mechanism. To study the corrosion film composition of Mg-2Zn-2Er after performing the test in PBS solution, XPS analysis has been carried out. The signals of Mg, O, Zn and Er that were observed in the corrosion film are represented as XPS spectrum in the form of counts per second vs. binding energy in Figure 5.16. In addition to these peaks, P and Na signals were identified from PBS solution and C peak was identified. The deconvolution of these peaks was made and they are represented in Figure 5.17. The peak for O 1s was identified at position 531.7 eV. For Zn, a definite peak was not detected but some signals were identified, corresponding to binding energy value of 1020 eV. The peaks for Mg were identified at 2 different positions, 2s at 88eV and 2p at 50eV. A very short but significant peak for Er was identified at 170 eV for 4d 5/2. The contents of PBS, Na (1s) and P (2p) were also identified at the surface film that is formed during corrosion, and they are detected at 1072 eV and 134 eV respectively.

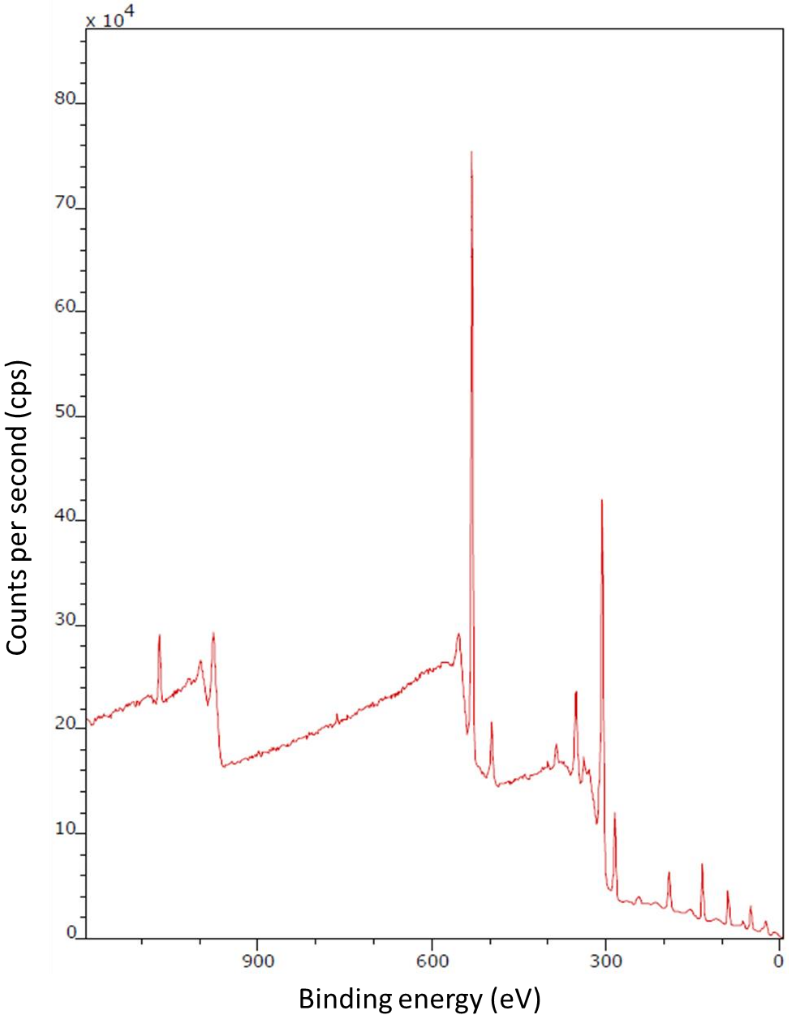

Figure 5.16: XPS spectrum of the corrosion layer formed after Mg-2Zn-2Er is immersed in PBS solution

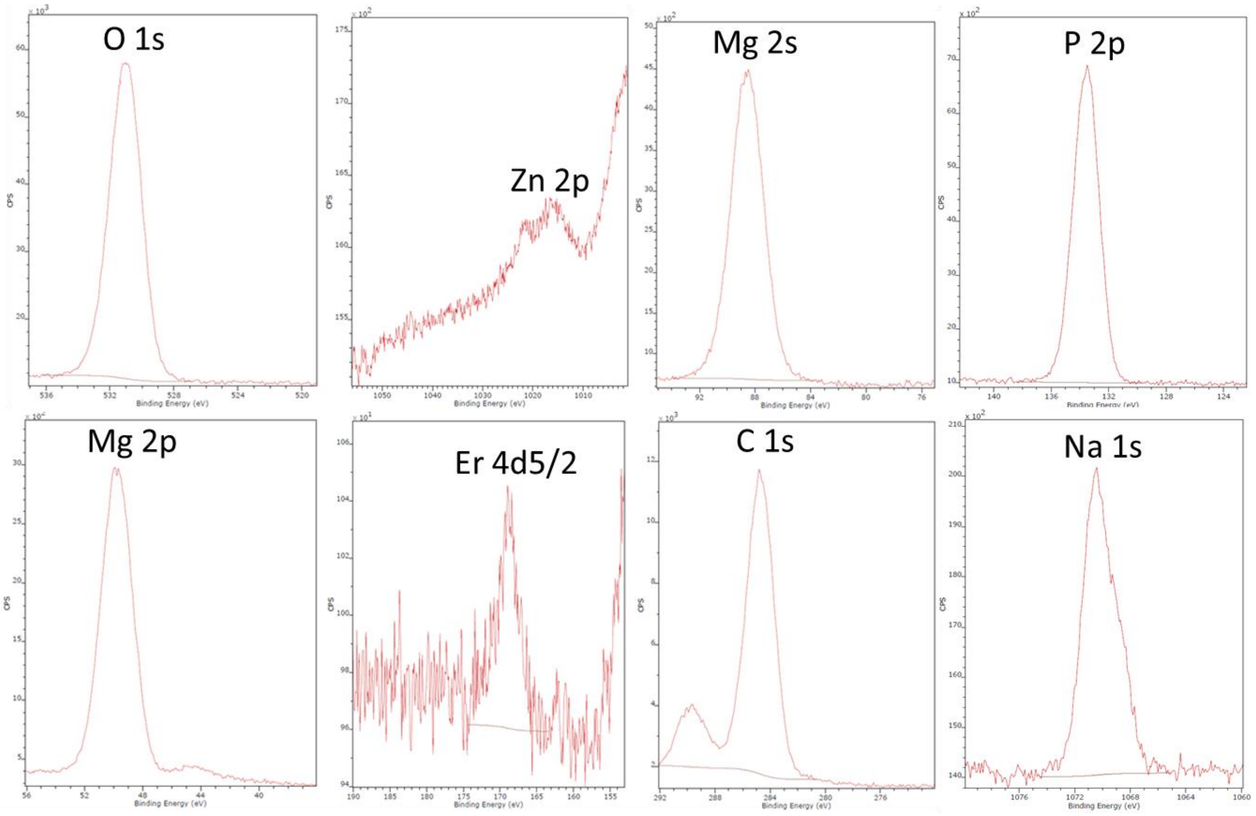

Figure 5.17: Deconvolution of the XPS spectra drawn in Figure 5.16.

5.3. Discussion

5.3.1. Reactions

The presence of oxide film on the surface is porous and they exhibit only limited protection. In a physiological environment, a set of electrochemical reactions could be constituted for the dissolution of magnesium and the deposit layer formed, and they are given as:

$$Mg \rightarrow Mg^{2+} + 2e^{-} \text{ (Anodic reaction)}$$

$$2H_2O + 2e^{-} \rightarrow H_2 + 2OH^{-} \text{ (Cathodic reaction)}$$

$$Mg^{2+} + 2OH^{-} \rightarrow Mg(OH)_2$$

$$Mg(OH)_2 + Cl^{-} \rightarrow MgCl_2 + 2OH^{-}$$

The reaction involves evolution of H_2 gas and this $Mg(OH)_2$ provides initial protection, but not unlike Al_2O_3 that forms a passive and protective film over the surface of Al and its alloys. PBS solution constitutes Cl^{-} ion and this reacts with semi-passive layer $Mg(OH)_2$ to form $MgCl_2$. This layer again dissociates into ions and leads to an increase in OH^{-} concentration at the surface. The degradation of loose $Mg(OH)_2$ gives rise to more free, fresh and active surface vulnerable for dissolution and devoid of protection.

5.3.2. Microstructure

To study the corrosion behavior of Mg and its alloys, understanding and tailoring the microstructure plays a significant role. Several microstructural parameters like grain size, secondary phase distribution and texture influence the corrosion process. The secondary processes like hot-extrusion can lead to uniform distribution of alloying elements, reduction in grain size and broken/ uniform distribution of secondary phases. This phenomenon could possibly reduce the corrosion rate of Mg and its alloys. They are discussed in the subsequent sections.

5.3.2.1. Grain size

The effect of grain size on corrosion plays an important role. This could be done by introducing large fraction of grain boundaries. Although it is a promising approach to enhance the mechanical properties, its effect on the corrosion behavior has not been properly understood.

Grain size refinement of pure Mg without alloying additions has enhanced the corrosion resistance [236]. Grain size of α-phase also plays a major role. This is an important microstructural parameter other than the presence of secondary phases. If there is complete recrystallization taking place after hot-extrusion, the specimens with equiaxed grain structure can exhibit better corrosion resistance over as-cast samples [237]. This has been observed in Figure 5.6 where the as-DMDed samples exhibited complete degradation as compared to as-extruded alloys. Complete recrystallization is speculated to have caused increased coherency of the oxide/hydroxide layer in fine grained as-extruded Mg [238]. A reduced grain size exhibiting enhanced corrosion resistance has been reported earlier by several researchers [239–241]. Finer the grain size, lower is the intensity of microgalvanic coupling between the grain interiors and grain boundaries [82]. If the grain size is fine and the secondary phases are continuous then the corrosion products that are formed on the surface retards the corrosion of β-phase. But if the grain size is coarse then the secondary phases are agglomerated and they are distributed widespread and hence do not provide sufficient protection to α-phase. The grain size of as-extruded Mg-2Zn-2Er as seen in Figure 4.6 is 6.6 µm and it exhibits the best corrosion resistance both in NaCl and PBS solution.

The oxide layer may start developing cracks due to the compression stresses between the matrix, as studied by Kainer et al [242]. This is due to the structural discontinuity between the two crystal structures. But with increased grain boundary density might help in compensating for this mismatch between the layers and reduce the compressive stresses [243]. Pilling-Bedworth ratio (PBR) which is used to calculate the stability of the passiveness of oxide film is defined as the ratio of the volume of the elementary cell of a metal oxide to the volume of the elementary cell of the corresponding metal (from which the oxide if formed). If the value is less than 1 then the oxide layer is likely to be broken being too thin and provides no protection to the matrix. A typical example is magnesium, whose PBR is 0.81. This pseudo-passive layer for pure magnesium is crystalline in nature, unlike aluminum and stainless steels. Grain refinement studies on corrosion was also carried out by Birbilis et al. and they reported the stability of oxide layer due to a large volume fraction of grain boundaries per unit area with high misorientation angles [240]. The stability is due to the lower mismatch between the oxide layer and the metal surface.

5.3.2.2. Secondary phases

Intermetallics and secondary phases have a great influence in the corrosion behavior of magnesium. The corrosion rate depends on the amount, size and distribution of secondary phases [244]. Several intermetallics can be anodic or cathodic to magnesium, which depend on its electrochemical potentials. An example for the influence of secondary phase is the corrosion behavior of AZ91 in a concentrated NaCl solution. $Mg_{17}Al_{12}$ (β-phase) is cathodic (nobler) with respect to Mg matrix. It plays a dual role, i.e., it can act as a barrier to prevent corrosion or can act as a cathode to accelerate corrosion. This role of β-phase depends on its volume fraction and distribution in AZ91 alloy [11]. When there is low volume fraction of this phase and it is distributed randomly, the corrosion gets accelerated by micro-galvanic coupling. But for a high volume fraction, continuously distributed refined phase can inhibit the corrosion by influencing the intensity of micro-galvanic coupling. This leads to more uniform and shallow morphology as compared to the occurrence of a localized corrosion. β-phase is more stable in NaCl and is more inert as its corrosion current density is much lower than that of α-phase.

The shift in the corrosion potential to the positive direction as seen in potentiodynamic polarization tests in Figure 5.3 and Figure 5.5 was influenced significantly by the presence and distribution of secondary phases like MgZn, $Mg_3Zn_3Er_2$ which are more cathodic and are thermodynamically stable than Mg. Since these phases are cathodic to the matrix, it is likely that galvanic effect would persist. Corrosion in Mg-Al alloys with a coarse grain structure takes place due to the presence of discontinuously distributed β phase. Conversely, in a grain refined microstructure of Mg-2Zn and Mg-2Zn-2Er, the secondary phases are distributed finely and continuously that can inhibit the development of corrosion. The continuous distribution of W-phase in as-extruded Mg-2Zn-2Er could be seen in the TEM analysis represented in Figure 4.33. To simulate the corrosion phenomenon, a schematic diagram is represented in Figure 5.18 for Mg-2Zn-2Er. The second phase particles of type $Mg_3Zn_3Er_2$ (W-phase) which is cathodic to the matrix leads to micro-galvanic coupling due to the difference in their standard electrochemical potentials. But, these second phase particles which are small and continuously distributed both inside and along the grain boundaries stop corrosion from grain to grain as represented in the figure, termed as barrier effect. Therefore, the corrosion rate of Mg-2Zn-Er is lower.

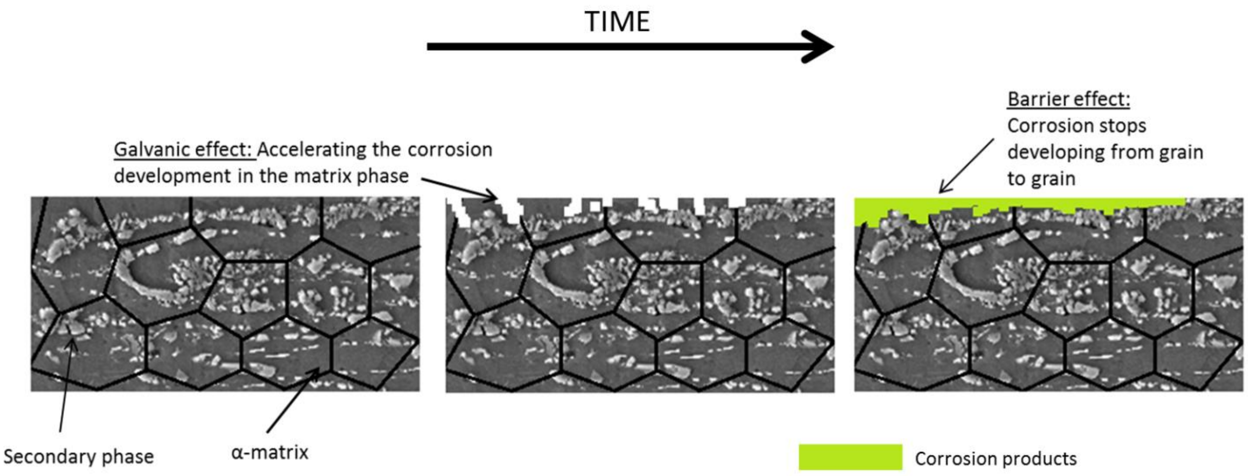

Figure 5.18: Schematic diagrams of morphology during corrosion process of Mg-2Zn-2Er

The effect of different morphologies of secondary phases on the corrosion behavior is not accounted during this phase of study. But, it is expected that in Mg-2Zn-2Er, the broken W-phases, most of them in nano-size that are distributed uniformly could be a reason for its enhanced corrosion resistance. Also, the standard potential of zinc (-0.762 V) is less negative than that of pure magnesium (-2.372 V) versus the Standard Hydrogen Electrode (SHE) at 25^{o}C. Thus, zinc has enhanced the corrosion potential of magnesium alloys.

The corrosion studies on i-phase strengthened Mg-Zn-Y alloys is very limited [245]. In an earlier study on the corrosion resistance of Mg-Zn-Y alloys, due to an increased corrosion potential of i-phase, the corrosion behavior of the alloy was enhanced [246]. This indicates that i-phase could help in the development of corrosion protection film. Corrosion process of a Mg-Zn-Y alloy with the composition $Mg_{68}Zn_{28}Y_4$ alloy with I-phase was studied by Shi-Fei et al. in 3.5 wt.% NaCl solution [247]. They demonstrated excellent corrosion resistance of i-phase which reduced the overall corrosion rate of the alloy [247]. It was seen that with the corrosion process, the amount of i-phases increased per unit area. Surfaces of quasicrystals are known to exhibit good tribological properties and high oxidation resistance [248]. This could explain the enhanced corrosion resistance of Mg-3Zn-0.5Er alloy with i-phase.

In an electrochemical study on Mg-Zn-Y alloys by Zhang et.al [229], the alloys were optimized with low Zn content to facilitate better corrosion resistance. They interpreted the role of i-phase and W-phase on the corrosion behavior of Mg-Zn-Y alloys and it was found that the corrosion resistance of the alloys with the i-phase or W-phase is superior to that of the alloy with both i-phase and W-phase. The three alloys consisted of Y-contents of 0.36, 0.82 and 1.54 wt.% respectively. The alloy with 0.36 wt.% Y consisted of only i-phase in Mg matrix that exhibited the best corrosion resistance, which is followed by the alloy with 1.54 wt.% Y consisted of only W-phase in Mg matrix. Increasing Y-content reduces i-phase in the Mg matrix and enhances W-phase content. As per the corrosion resistance values, it could mean that W-phase could possibly act as a relatively weak cathode phase in Mg-2Zn-2Er.

Microstructural characterization of Mg-Zn-Ca-Er alloys as represented in Section 4.2.5.1.2 suggest that the alloys are composed of primary Mg matrix and secondary phases of the type $MgZn_2$, $Mg_3Zn_3Er_2$, Mg_3Zn_6Er distributed along the grain boundaries. Among these alloys, the main difference is the composition of the individual constituents, grain size to a minimal extent and the volume fraction of secondary phases. With the enhancement of cathodic potential, there is an increase in the cathodic current density for all the samples for the tests in both PBS and NaCl solution. For NaCl medium, as seen in Figure 5.3, the corrosion current densities were similar in the cathodic region, indicating similar cathodic hydrogen evolution rates. But for test in PBS, as seen in Figure 5.5, pure Mg demonstrates a higher value and thus it indicates a faster cathodic hydrogen evolution rate.

Other than secondary phases and grain size effects, texture and dislocation density also play a role on corrosion behavior of magnesium alloys to a certain extent [249,250]. Guang-Ling Song suggests that grains of magnesium shows anisotropic corrosion behavior. Increased corrosion resistance in rolled AZ31 was estimated by Song et al. in the surfaces parallel to basal plane direction [250]. The extruded materials usually consist of basal texture and this has been cited to be more corrosion resistant than its cross-section surface which is composed of {10-10} and {11-20} crystallographic planes, as it is electrochemically stable [251]. This is because it has low surface energy compared to other planes. Therefore the increased corrosion resistance for Mg-3Zn-0.5Er could be explained using this phenomenon, apart from the enhanced corrosion resistance offered by i-phase.

5.3.3. XPS analysis

During the corrosion of samples in PBS, a substantial amount of Mg^{2+} ions are released into the solution. It was observed that apart from surface degradation of the alloys, the deposition of salts on the surface of the Mg-Zn-Ca-Er alloys is evidenced by the macrostructures as seen in Figure 5.15. The analysis of these products in corroded Mg-2Zn-2Er showed them to consist primarily of magnesium, zinc, oxygen, sodium, phosphorous and erbium. Some of them belong to the salts found in PBS solution that reacted with Mg-2Zn-2Er and others form precipitates which are deposited on the alloy surface. Formation of magnesium phosphate on the surface of Mg-2Zn-2Er could be explained due to the presence of phosphorous and magnesium. These results are is consistent with the biocompatibility reports of SBF corrosion on pure Mg by Keim et al. who found increased deposits of the same elements [252]. When magnesium materials are immersed within a corrosive solution like NaCl, the alloys are attacked by the chloride salts or oxygenated species within the media. During the PBS immersion of magnesium alloys, the chloride, phosphate, sodium and oxygenated species are attacking the surface.

From the XPS spectrum of the corroded Mg-2Zn-2Er plotted in Figure 5.16 and Figure 5.17, it is observed that the position of the O 1s peak observed at 531.7 eV correspond to OH^-. The element P also exists in the film that corresponds to binding energies of P 2p at 134 eV in the form of PO_4^{3-}. Hence in the corrosion film the products $Mg(OH)_2$, $Er(OH)_3$ are confirmed from the above results. Also by incorporating erbium, it is believed that it can replace Mg^{2+} cations and suppress the penetration of Cl^- anions into $Mg(OH)_2$ thereby enhancing the corrosion resistance of ternary and quaternary Mg alloys. Similar results were identified by Yang et al. for Mg-10Dy alloys, where the incorporation of stable Dy_2O_3 and $Dy(OH)_3$ into the corrosion layer reduced the corrosion rate of Mg-10Dy as compared to pure Mg [253]. Also it has been seen by Hanzi et al. for a Mg-Y-RE (WE43) alloy that Y dissolved in Mg matrix can increase the protective nature of the surface film [254]. Yao et al. observed the incorporation of neodymium (Nd) on the surface of $Mg_{82-x}Ni_{18}Nd_x$ (x=5, 15) which prohibited the penetration of the detrimental anions like Cl^- and CO_3^{2-}[255]. Ce incorporation in to AZ91 has resulted in the formation of CeO_2, which was studied by Song et al. that has a higher PBR and hence it is more compact [86]. The pseudo-passivation behavior of Mg-Y-Nd alloys was studied by Krishnamurthy et al. and this was attributed to the enrichment of Y and Nd on the corroded surface [256]. Hence the presence of Er^{3+} in the corrosion film of Mg-2Zn-2Er has enhanced the corrosion resistance.

5.3.4. Alloying additions

From Table 5.1 and Table 5.2, it could be seen that alloying additions reduced the corrosion rate of pure Mg. For a clear understanding of the effect of alloying additions on the degradation of pure Mg, a graph is plotted and it is represented in Figure 5.19. With the addition of Zn, Ca and Er, the corrosion rates have been reduced as compared to pure Mg. Mg-2Zn-2Er exhibits least corrosion rate (< 2 µm/y) for tests conducted in both media.

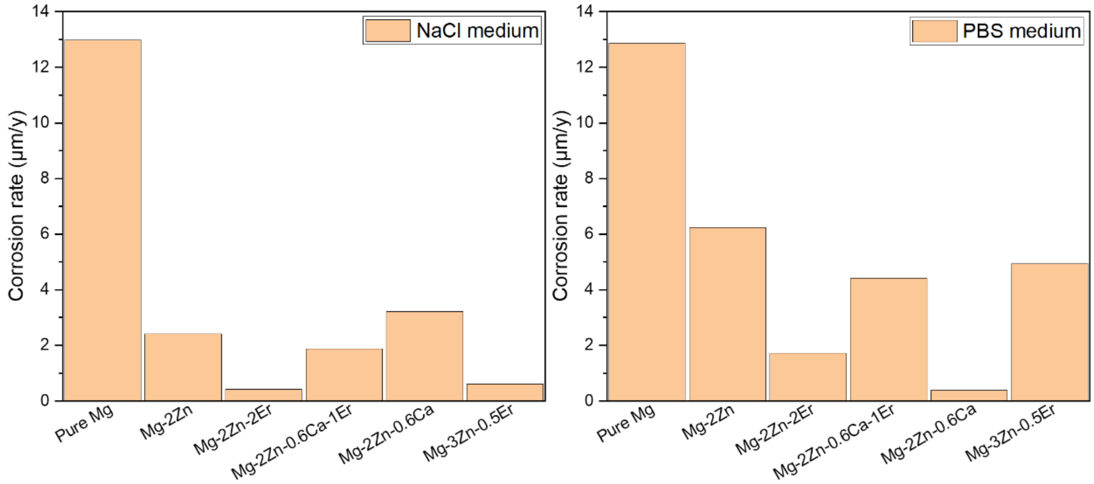

Figure 5.19: Corrosion rates of pure Mg and its alloys from Table 5.1 and Table 5.2

5.3.4.1. Zinc

It was studied earlier that when zinc is added beyond a certain limit, it has a positive effect on the corrosion film developed as it characterized by a relatively high hydrogen over-potential [257]. Also the charge transfer resistance of magnesium can be enhanced and hence lower the rate of corrosion [258]. Corrosion behavior of as-cast Mg-xZn (x=1, 5 and 7 wt.%) group alloys were studied by Cai et. al [109]. They observed that barring Mg-7Zn, all other alloys exhibited superior corrosion resistance to pure Mg which was used as a control group. Among these three alloys, Mg-5Zn exhibited the best corrosion resistance. Mg-7Zn resulted in galvanic coupling due to the segregation of dendritic phases at the grain boundaries. A degradable implant material Mg-6Zn was studied by Zhang et. al [68] calculated the zinc release rate to be 0.11 mg day^{-1}, which is much lower than the suggested intake of 15 mg day^{-1}. They also proposed that zinc release during the degradation of the implant is safe and poses no harm to human body.

The degradation rates calculated for our alloy Mg-2Zn is lower than that of pure Mg (Rp for Zn is greater as seen in Table 6.3 in PBS solution). The corrosion resistance has been improved by elevating the corrosion potential of magnesium (E_{corr} has increased by 0.025 V). Hence, zinc is a promising alloying element but its addition has to be controlled to attain higher corrosion resistance over pure Mg.

5.3.4.2. Calcium

The low density value of Ca like Mg endues this Mg-Ca system to be studied as bio implants due to the advantage of similar density to that of bone. Since Ca is a major component in human bone and essential in chemical signaling with cells, the release of Ca^{2+} and Mg^{2+} ions during biodegradation is expected to be beneficial to the bone healing [13]. Increased Ca leads to bone-like apatite growth after immersion in SBF for long time, which indicates better performance for its use as a biodegradable material [106].

The degradation rates for our alloy with 0.6Ca addition to Mg-2Zn have reduced. The corrosion resistance did not improve during PDP tests in NaCl solution but it was improved marginally (E_{corr} has increased by 0.003 V) during PDP tests in PBS solution. The redox potential of Ca is more negative (-2.76V_{SCE}) that that of pure Mg (-2.37V_{SCE}) and hence the Ca part becomes anodic. But since a very minimal addition is introduced (0.6 wt.%), it acts like a grain refiner and thus led to a reduction in the corrosion rate.

5.3.4.3. Rare earth

The impact of the RE alloying addition on the corrosion of the alloy can possibly be attributed to the following mechanisms:

When rare-earth elements like erbium are added as minor additions to magnesium alloys, it was observed that the number density and size range distribution of the native intermetallic phase (β-phase in the AZ class of alloys) may get altered. The addition might lead to the creation of a new intermetallic between erbium and the already existing intermetallics. Al-RE intermetallic could possibly improve the corrosion resistance according to recent studies. It was studied by Rosalbino et al. for Al-Mg alloys and he found that the presence of intermetallic compounds like Al_3Mg_2, Al_3Er and $Al_{66.7}Mg_{23.4}Er_{10}$ (τ) strongly modifies the electrochemical behavior of the alloys [259]. Hence the distribution and composition of secondary phases due to the addition of a ternary element Er to Mg-Zn alloys led to enhanced corrosion resistance of Mg-2Zn-2Er and Mg-3Zn-0.5Er.

Another way of enhancing corrosion resistance due to the presence of rare earth elements is referred to as the 'scavenger effect'. It is common for impurity elements like iron, nickel and cobalt to be present in magnesium alloys. These undesired elements could act as corrosion initiation sites. Minor addition of rare-earth elements interacts with these impurities and form compounds which does not have any role to play during corrosion. Therefore, any minor undetectable impurities have no effect on the degradation behavior of RE containing alloys. But in our alloys, there were no impurities like Fe, Co or Ni detected in both as-DMDed and as-extruded alloys. And therefore scavenger effect does not play a role in our alloys.

Surface oxide stability is important to slow down the corrosion kinetics and addition of Er could be beneficial in this regard. The effect of Er addition to Mg-2Zn has enhanced the corrosion resistance, as it could be seen for both NaCl medium and biological salt solutions. It is evident from Table 5.1 that the resistance to polarization (R_p) values are higher for Er incorporated alloys and poor for pure Mg. Incorporation of small amounts of Er (0.3 and 0.9) in an Mg-Al alloy was studied by Rosalbino et al. and these alloys exhibited better corrosion resistance in borate solutions [260]. For exhibiting better corrosion resistance in PBS solution as compared to NaCl medium, a viable explanation could be that the phosphates present in the solution could go into the reaction surface layer of Mg alloys and this behavior was previously been studied [185]. Er is chosen in this study because it has a hexagonal close packed structure, the same as Mg. This allows it to saturate the matrix and it could be that the small amount of Er addition led the element to be at the corrosion front to protect the surface. The Er present in the second phases are normally not reacted as they are cathodic, but they get into the solution after the anode surrounding to these phases gets undermined.

5.4. Conclusions

- Extrusion process is an effective way to enhance the corrosion behavior of magnesium alloys.
- Hot-extrusion resulted in finer grain sizes and tailored the second phases into finer features and distributed them uniformly which enhanced the corrosion resistance.

- Addition of alloying elements like zinc, calcium and erbium has significantly enhanced the corrosion resistance of magnesium alloys by forming secondary phases like i-phase (Mg_3Zn_6Er) and W-phase ($Mg_3Zn_3Er_2$) that are cathodic (nobler) to the matrix.
- The corrosion rate of Mg-2Zn-2Er has lowered by an order of magnitude over pure Mg and this is attributed to the presence of Er^{3+} in the corroded surface as per the XPS investigation and reduction in grain size.

CHAPTER 6

SURFACE MODIFICATIONS USING FLUORIDE CONVERSION COATING

6. Surface modifications using fluoride conversion coating

6.1. Introduction

As introduced in Chapter 5, magnesium based alloys have exhibited enhanced corrosion resistance. However, the requirements of implant materials are stringent. Alloying additions can only increase the bio-corrosion resistance to a certain extent and they cannot improve the bone response of magnesium. In this regard, a coating technique was hence required to be developed to provide a suitable host response to the material. Several coating techniques like Al [261], Ti [262] and phosphating (magnesium phosphate [174–176], zinc phosphate [177,178], manganese phosphate [167,179–182], zirconium oxide [183]) have been tried earlier but they did not improve the corrosion resistance significantly. Also, many of these coatings are not biocompatible. In this chapter, discussion on fluoride coatings on magnesium and its alloys to further protect the surface and reduce the initial corrosion rate of the alloys has been made. This study has demonstrated an encouraging level of improvement in the corrosion resistance of these alloys by exploring HF treatment.

6.2. Fluoride coatings

MgF_2 has the tetragonal structure, which is similar to rutile and it belongs to space group $P4_2/mnm$. In the unit cell of MgF_2, there are 2 molecules and the unit cell dimensions are a=4.621 Å and c=3.05 Å [263]. The aim is to develop compact and uniform fluoride coating on the surface. 40% HF solution was commercially available and it was an analytical reagent used for our studies. For an adult, the average intake of dietary fluoride is between 1.2 and 2.2 mg [3]. Since these coated MgF_2 layer have low solubility, toxic effects are not very severe as only limited thickness of the alloy surfaces get converted to MgF_2. During the coating process, there was no corrosion detected on the surface and at the interior.

6.2.1. Contact angle measurement

Contact angle measurements of the samples indicate the hydrophilic nature of the coated magnesium alloys and the coating quality. None of the droplets rolled off the surface and on an average five readings were recorded for every sample. Typical photographs of the water droplets on the surface of the samples are shown in Figure 6.1. The contact angle measurements are tabulated in Table 6.1.

The as-extruded pure Mg and its alloys showed an increased contact angle values for distilled water on their polished surfaces as compared to the coated ones. Among the uncoated materials, pure Mg exhibited the least contact angle of 78.2^{o} and Mg-2Zn-0.6Ca-1Er alloy exhibited the highest contact angle of 109.3^{o}. Mg-2Zn exhibited the contact angle of 109.1^{o}. Addition of

0.6Ca reduced this value to 97.8°. Both the ternary Mg-Zn-Er alloys showed similar contact angle of 106.2°. The increased contact angle values for the alloys as compared to pure Mg by 20-30° indicates that alloying additions have an effect on the contact angle measurements of magnesium.

After fluoride treatment, the contact angle was reduced for both pure Mg and its alloys, indicating an increase in the hydrophilicity. This behavior was seen for all the materials. A decrement of 25-27° was seen for pure Mg, Mg-2Zn and Mg-2Zn-2Er. For Mg-2Zn-0.6Ca-1Er, Mg-2Zn-0.6Ca and Mg-3Zn-0.5Er this decrement is about 50°. This could be due to the presence of Ca and excess amount of Zn for the fluoride coated alloys. Even after coating, the contact angle values exhibited by coated Mg-2Zn and Mg-2Zn-2Er were higher than that for uncoated pure Mg. Among the alloys, coated Mg-2Zn-0.6Ca exhibited the least contact angle of 46.2°, implying that it is most hydrophilic. The hydroxide layer, oxide and fluoride layer developed on chemically treated samples is the reason for increase in wettability.

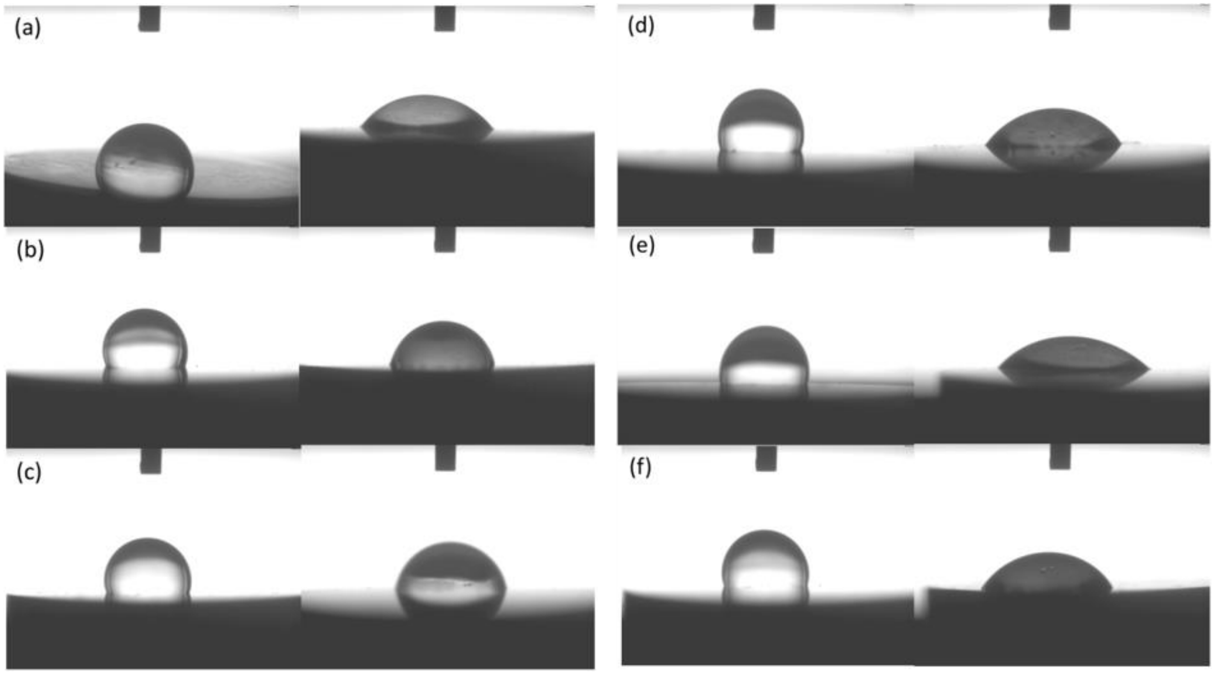

Figure 6.1: Contact angle photographs of (a) Pure Mg, (b) Mg-2Zn, (c) Mg-2Zn-2Er, (d) Mg-2Zn-0.6Ca-1Er, (e) Mg-2Zn-0.6Ca and (f) Mg-3Zn-0.5Er. Left figure is without coating and the right side is with coating.

Table 6.1: Contact angle measurements (in degrees)

Material	Before coating	After coating
Pure Mg	78.2	52.8
Mg-2Zn	109.1	82.7
Mg-2Zn-2Er	106.2	80.9
Mg-2Zn-0.6Ca-1Er	109.3	55.1
Mg-2Zn-0.6Ca	97.8	46.2
Mg-3Zn-0.5Er	106.2	59.3

6.2.2. Raman Spectroscopy

Figure 6.2 shows the Raman spectrum for as-extruded pure Mg and Mg-2Zn-2Er, HF conversion films and the corroded surfaces in PBS. Table 6.2 corresponds to the peak positions assigned for the Raman spectrum. A large number of peaks were indexed for the corroded samples. In the table, for the corroded samples it could be seen that an enhanced number of peaks within the line number 1000 cm^{-1}. For the corroded samples in PBS, the increased number of peaks corresponds to the vibrational spectra of phosphates. For the uncoated bare samples, the initial peak in the Raman shift corresponds to oxides and hydroxides. For pure Mg and Mg-2Zn-2Er alloy, only few peaks were detected.

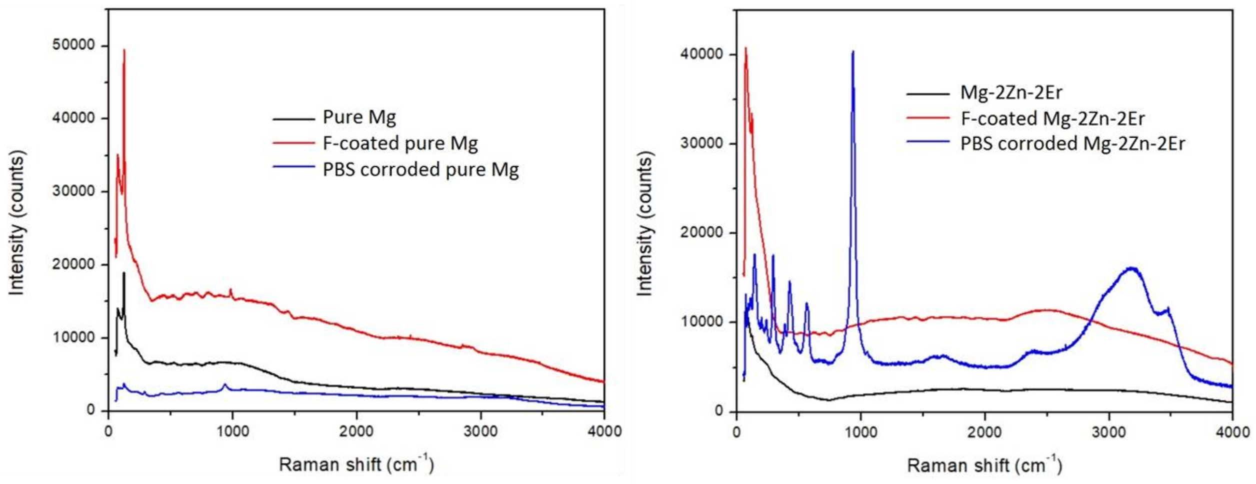

Figure 6.2: Raman spectroscopy results for pure Mg and Mg-2Zn-2Er as-extruded, fluoride coated and corroded samples in PBS

Table 6.2: Peak positions assigned for the Raman spectrum in Figure 6.2

Material	**Peak positions (cm^{-1})**						
Pure Mg	71.78	120.35	3660.56				
Mg (PBS)	71.95	121.58	286.8	424.53	562.26	699.98	818.43
	936.88	1088.38					
Mg (Coat F)	72.74	122.66	978.31	1446.36	2850.5	2914.2	
Mg-2Zn-2Er	73.64	121.05					
Mg-2Zn-2Er (PBS)	69.59	91.9	114.88	141.23	196.66	237.21	290.6
	384.55	425.1	564.33	934.4	1055.85	1659.61	2371.37
	3171.76	3445.95					
Mg-2Zn-2Er (Coat F)	72.33	119.49					

6.2.3. SEM-EDS

To observe the surface morphology of the fluoride treated samples, the SEM-BSE analysis was conducted and they are shown in Figure 6.3. The morphologies of the samples exhibit grains for all the alloys.

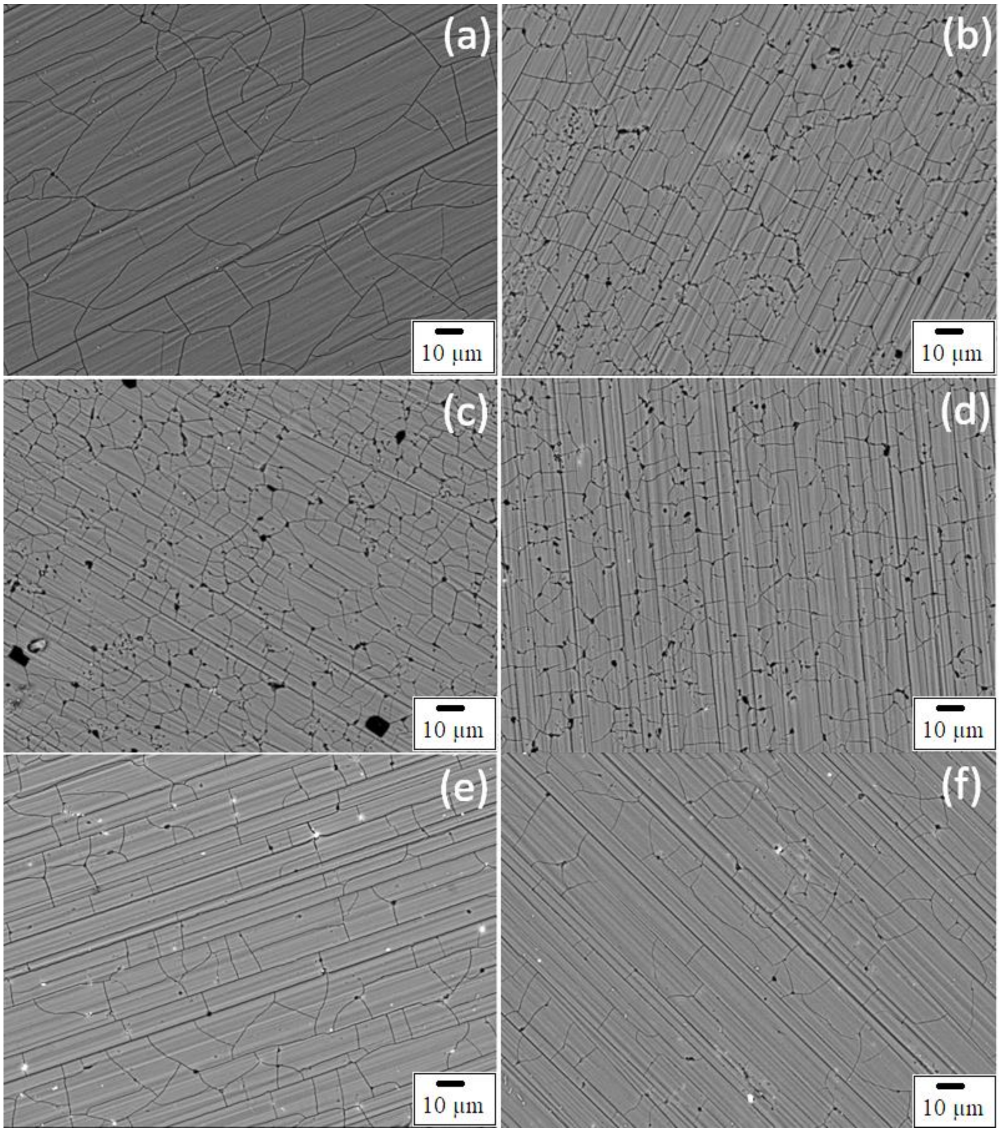

Figure 6.3: Fluoride coatings as seen in SEM-BSE for (a) Pure Mg (b) Mg-2Zn (c) Mg-2Zn-2Er (d) Mg-2Zn-0.6Ca-1Er (e) Mg-2Zn-0.6Ca and (f) Mg-3Zn-0.5Er

The grain sizes are larger for F-coated pure Mg. Along with the conversion film, some irregularly distributed black pores was formed on the surface of the samples. These pores were not observed for pure Mg coated surface. These irregular pores in the coating could be generated by the evolution of hydrogen during fluoride conversion treatment.

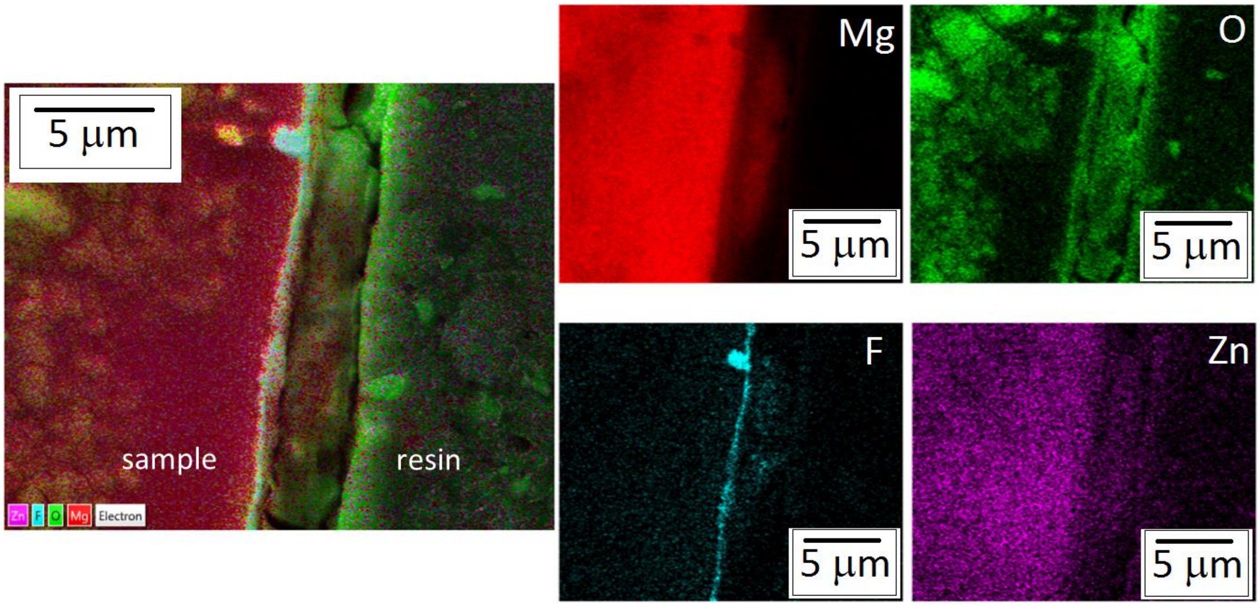

Figure 6.4: Cross section of fluoride coating on Mg-2Zn sample, and the EDS analysis

To study the elemental distribution on the coated surface, cross-section method was adopted. The SEM image of cross section of the fluoride treated Mg-2Zn as-extruded sample is shown in Figure 6.4. A 20 x 20 μm area was analyzed. This indicates that a uniform film is developed successfully on the surface of the Mg-2Zn sample. Pure Mg and pure Zn spectrum in the sample region shows that magnesium and zinc are uniformly distributed as Zn goes into the solid solution of magnesium. The coating layer is well adhered to the matrix chemically and it is expected to have a strong adhesive ability. Some oxygen concentration could be seen on the sample and it is not present much near the coated region. The figure on the left shows a superimposed EDS and BSE image of the coated cross-section.

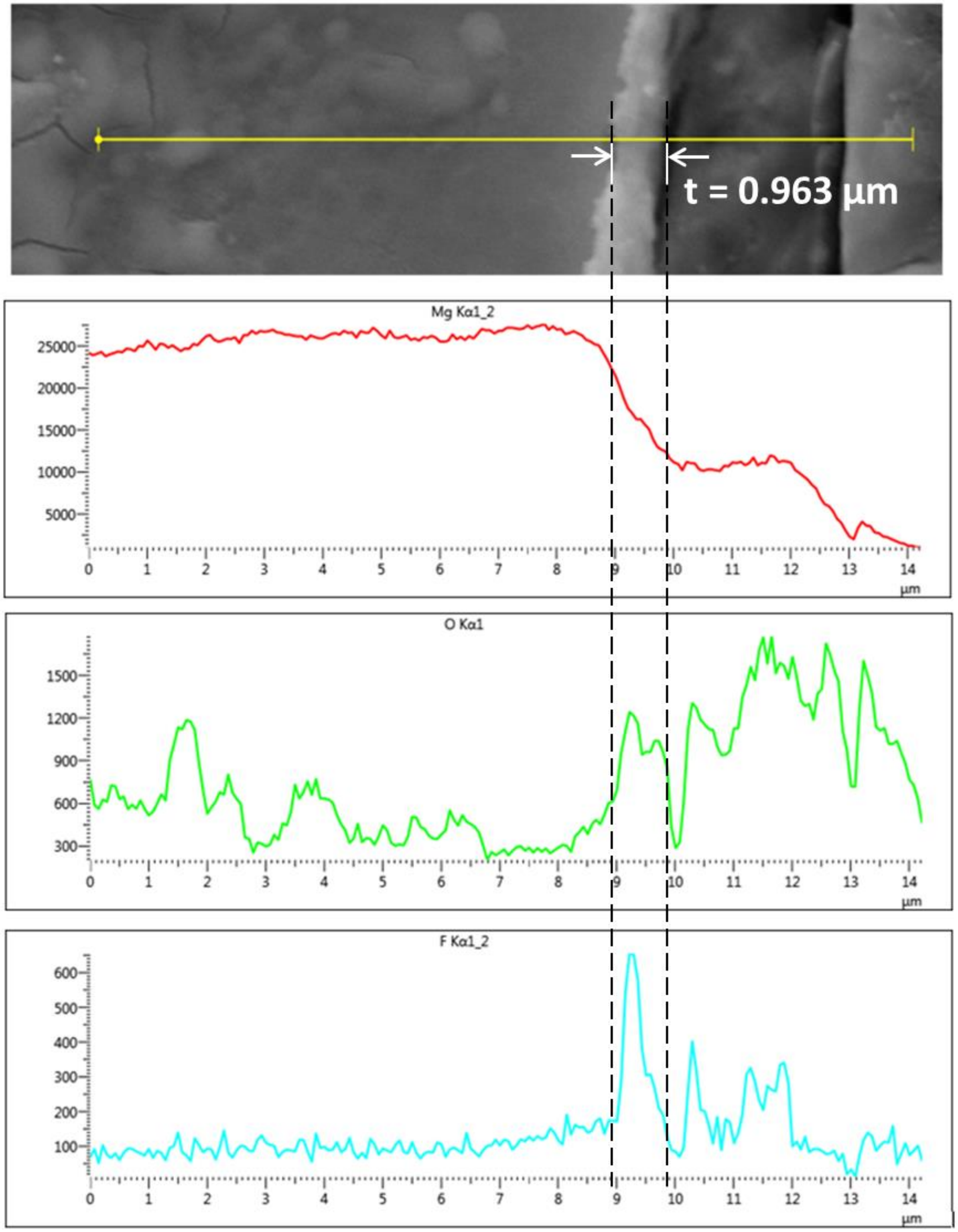

Figure 6.5: Line scan analysis demonstrating the thin fluoride coating on the cross section of Mg-2Zn extruded sample

Line scan analysis of the cross section of the fluoride coated Mg-2Zn sample has been made and it is represented in Figure 6.5. In the set of images, it could be seen that from left to right, the intensity of pure magnesium decreases. The white film that could be seen after 9 µm of the scan is the fluoride coating, where the peak for pure fluorine could be seen of ~ 1 µm thick. Ten line scans were taken and the average thickness value of MgF_2 layer was calculated to be 0.963 µm. There is some oxygen concentration in this region. The sample was scanned along the coating and it was seen that this coating was formed uniformly over the surface.

6.2.4. Corrosion in PBS

6.2.4.1. Potentiodynamic Polarization tests

An ideal corrosion-resistant coating prevents the direct electrolyte contact and electron transit and thus provides strong protection. Figure 6.6 shows the polarization curves of the fluoride treated samples. The electrochemical parameters obtained from these curves are shown in Table 6.3 along with the calculated corrosion rate.

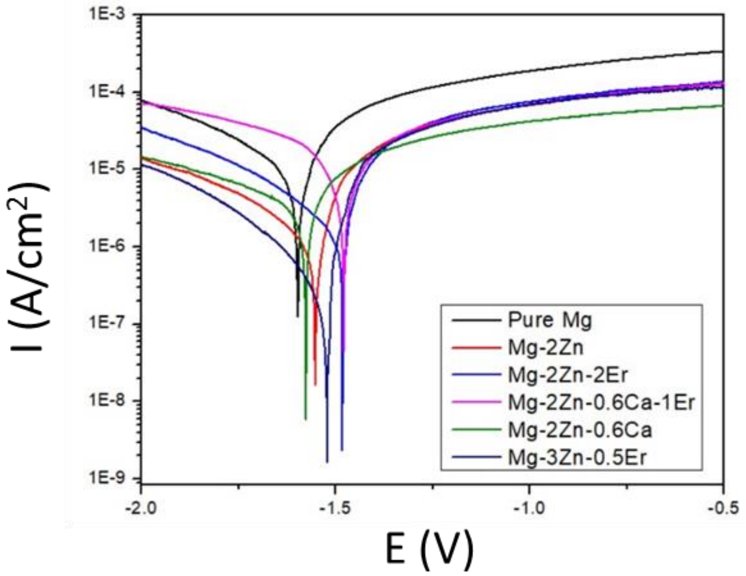

Figure 6.6: PDP results for fluoride coated as-extruded Mg and its alloys in PBS solution at 37°C

Table 6.3: Polarization parameters of the coated samples in PBS at 37°C

Fluoride coated Samples	**Polarization parameters**			**Corrosion rate (µm/y)**
	E_o (V)	**I_{corr} (A/cm^2)**	**R_p (Ω/cm^2) ($x\ 10^4$)**	
Pure Mg	-1.598	1.279×10^{-7}	1.249	2.95
Mg-2Zn	-1.553	1.652×10^{-8}	9.4	0.38
Mg-2Zn-2Er	-1.483	2.37×10^{-9}	62.57	0.05
Mg-2Zn-0.6Ca-1Er	-1.479	4.51×10^{-8}	3.279	1.04
Mg-2Zn-0.6Ca	-1.577	5.94×10^{-9}	29.79	0.13
Mg-3Zn-0.5Er	-1.522	1.676×10^{-9}	90.8	0.04

F-treated pure Mg exhibits corrosion potential of E_{corr} = -1.598 V vs. SCE. This is more positive than as-extruded pure Mg tested in PBS solution (E_{corr} = -1.634 V vs. SCE) as tabulated in Table 5.2. The coated pure Mg has both increased anodic corrosion current density and cathodic corrosion current density. Also at the breakeven potential, the corrosion current density observed is high. It could be seen as compared to the corrosion behavior of as-extruded samples in PBS solution in Figure 5.5 that the corrosion current density values observed in this test is two orders of magnitude lower. Addition of 2Zn has increased corrosion potential of F-coated Mg-2Zn to E_{corr} = -1.553 V vs. SCE. For Mg-2Zn-2Er, the E_{corr} value has increased further to E_{corr}= -1.483 V vs. SCE. Mg-2Zn-0.6Ca exhibited E_{corr} value of -1.577 V vs. SCE and addition of 1Er to this ternary alloy increased E_{corr} value by +0.098 V. Hence, it is safe to suppose that Er addition is beneficial. Hence by adopting a chemical conversion technique of incorporating a surface coating of MgF_2, a decrease in the degradation rate was accomplished.

The corrosion rates calculated using the equation in Section 3.9.4 for fluoride coated samples tested in PBS medium at 37 ^{o}C are tabulated in Table 6.3. In the table, it could be seen that, similar to bare samples tested in NaCl and PBS medium the corrosion rate value is high for coated pure Mg. The corrosion rate calculated for pure Mg is 2.95 µm/y. This value is 0.38 µm/y for Mg-2Zn. With the addition of 2Er to Mg-2Zn, the corrosion rate is reduced to 0.05 µm/y. Mg-2Zn-0.6Ca exhibits corrosion rate of 0.13 µm/y and with the addition of 1Er to the ternary alloy the value is 1.04 µm/y. Among Mg-Zn-Er ternary alloys, Mg-3Zn-0.5Er exhibits the lowest corrosion rate of 0.04 µm/y.

6.2.5. Comparison of corrosion measurements of coated and un-coated samples

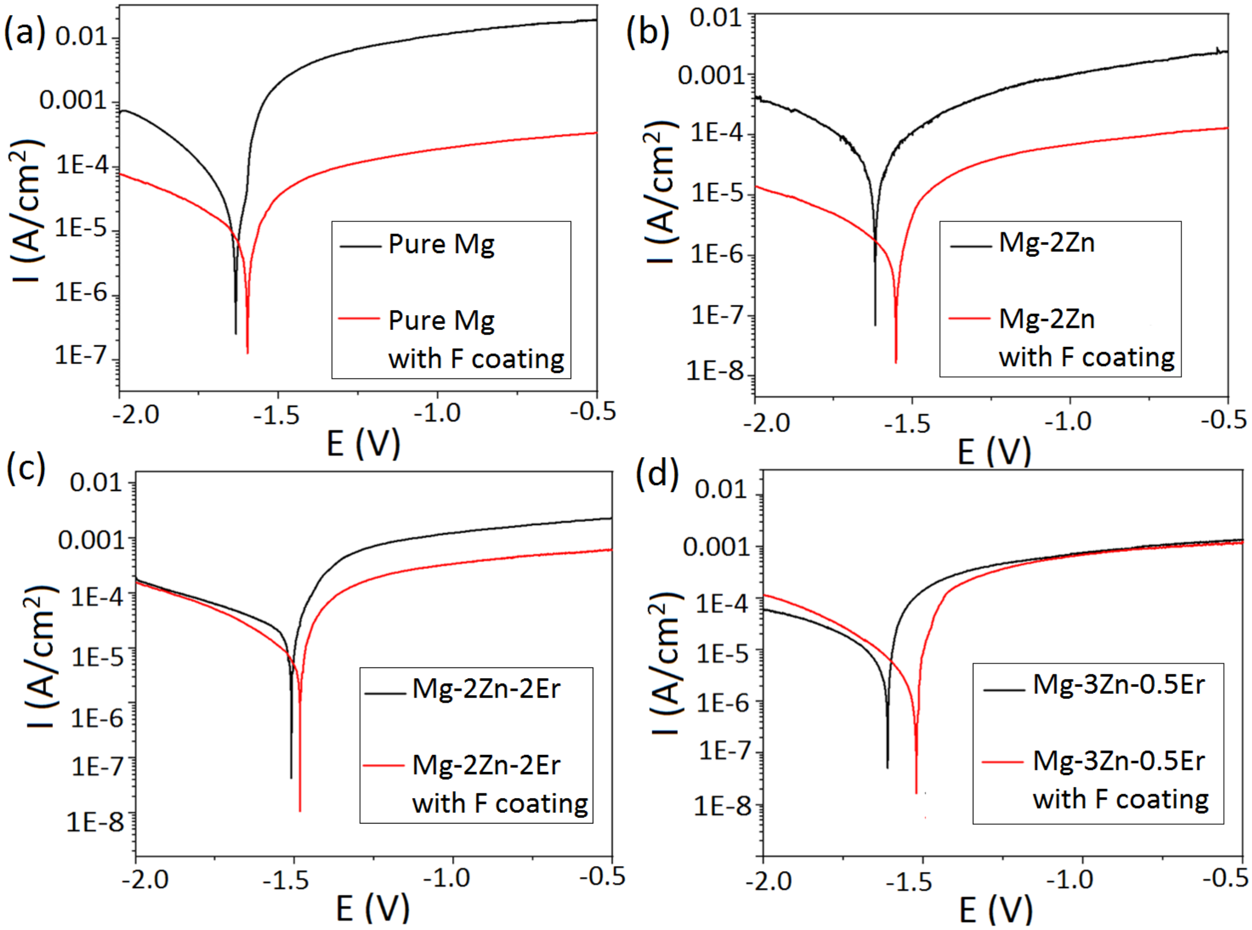

Figure 6.7: Potentiodynamic polarization curves of samples with and without coating in PBS at 37^{o}C: (a) Mg and F-coated Mg; (b) Mg-2Zn and F-coated Mg-2Zn; (c) Mg-2Zn-2Er and F-coated Mg-2Zn-2Er; (d) Mg-3Zn-0.5Er and F-coated Mg-3Zn-0.5Er

Potentiodynamic polarization measurements for bare samples and F-coated samples are plotted in the same graph for pure Mg, Mg-2Zn, Mg-2Zn-2Er and Mg-3Zn-0.5Er for comparison as shown in Figure 6.7. For the fluoride coated samples, there is a shift in the corrosion potential towards positive values (nobler). Also, the corrosion current has dropped to two orders of magnitude for coated samples. Pure Mg exhibits an increased corrosion potential of +0.036 V after coating. For Mg-2Zn, this increment is +0.066 V after coating. The corrosion current I_{corr} dropped by two orders of magnitude for Mg-2Zn-2Er and Mg-3Zn-0.Er after coating. The resistance for polarization (R_p) values has increased not only for the alloys but also for pure magnesium. Thus, it can be evidently said that fluoride coated samples provide sufficient corrosion protection to pure Mg and its alloys.

From Table 5.2 and Table 6.3, it could be seen that fluoride coating reduces the corrosion rate of pure Mg. For a clear understanding of the effect of coating on the degradation of pure Mg and its alloys, a graph is plotted and it is represented in Figure 6.8. There is a drastic improvement in the corrosion rate for coated pure Mg as compared to bare pure Mg. Also the coated Mg-2Zn-2Er and Mg-3Zn-0.5Er exhibits least corrosion rate (~ 0.04 µm/y) and these values suggests the enhancement of corrosion resistance due to fluoride coating treatment.

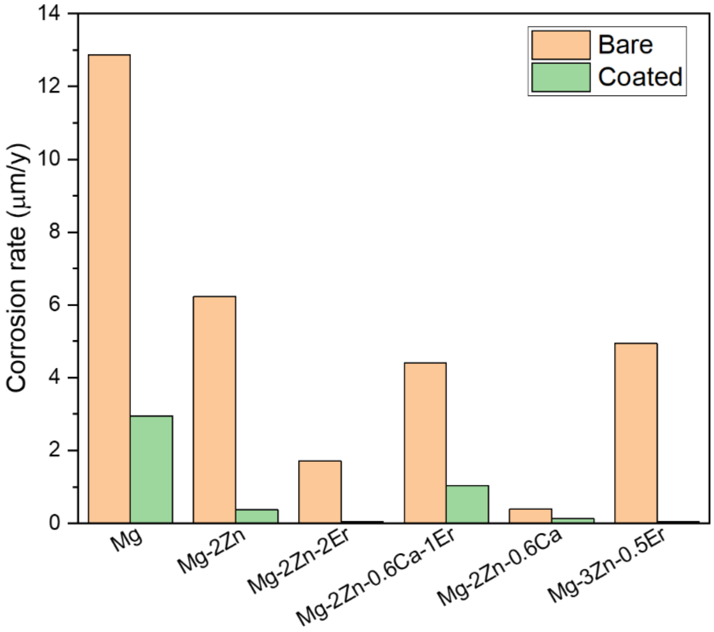

Figure 6.8: Comparison of corrosion rates for bare and coated samples tested in PBS medium at 37 ^{o}C

6.2.6. Biocompatibility assessment

6.2.6.1. Introduction

Magnesium makes an excellent metallic implant material due to its biodegradability, similar mechanical properties to that of human bone and excellent biocompatibility as compared to other materials [33]. Although the earlier interest of researchers was restricted towards light-weight structural applications, today it has become a promising candidate to serve as temporary implants. This is because it can provide suitable strength as compared to existing degradable polymer based implants. Most importantly they have low elastic modulus and hence it can reduce stress shielding effects and replace existing implants made of titanium and stainless steels [264]. Also the corrosion products are non-toxic as compared to other permanent implant materials which corrode slowly in human body, although these materials are not designed for safe degradation. To design a bio-implant, extensive care has been taken to balance strength, ductility, and degradability and hence an interdisciplinary study needs to be carried out. In this regard, alloying additions and coatings were carried out to reduce the degradation rates. It is well known that Mg-Al alloys have excellent corrosion resistance but they are not suitable for biomedical applications as Al increases the risk of neurotoxicity [265]. Hence in our studies, for the first time we have introduced zinc, calcium and erbium as a rare earth addition in minimum quantity. Zinc enhances the corrosion resistance by elevating the corrosion potential of magnesium alloy [68]. It is also an essential requirement for human body [266]. Calcium is a major component in bones and minor additions also enhance the corrosion resistance [3]. Minor additions of rare earth (RE) metals like erbium [267] to magnesium has proven to be non-toxic to a certain extent. But the current available Mg alloys tested for biomedical applications have high alloying content, which adds to the cost and also could induce toxicity after several years [267,268]. Recent studies have shown that fluoride agents can stimulate osteoblast proliferation and aid in new mineral deposition [269]. Several researchers have studied the fluoride coating on improving the corrosion resistance of magnesium alloys but there is an insignificant literature on its effect on the *in-vitro* cell culture studies [190].

To test the cytotoxicity of these alloys, EN ISO standard 10993 is used [270]. In the earlier chapters, the physical, microstructural, mechanical properties and electrochemical behavior of these materials have been reported. Addition of these elements enhanced both tensile and compressive properties of magnesium due to the reduction in grain size and particle strengthening. These materials have also been tested in phosphate buffer saline at 37 ^{o}C for its degradation resistance and there has been a significant improvement in these values for the coated materials as compared to pure Mg and its alloys. Therefore, these coated materials have been warranted further biocompatibility studies to serve as candidate materials for safe degradable implant materials.

6.2.6.2. Cell toxicity protocol

The fluoride coated samples were subjected to biocompatibility studies and the protocol of extraction test is given in Table 6.4.

Table 6.4: Protocol of the extraction method adapted for the coated materials

Time	**Method**
Day 1	• Sterilize the samples by heating it to 170^{o}C for 1h • Take 1 disc (alloy)/group and dip in 1 mL complete medium to reach ISO ratio 3 cm^2/mL for extraction for 3 days • Defreeze MC3T3 cells
Day 3	• Seeding 4000 cell/well in 96 well plate
Day 4	• Adding the extraction liquid directly without filtration to the cells, 100µl/well (n=6)
Day 5	• Changing medium into 10% blue alarma solution 200 µl/well and incubate 2 h at 37°C • Take 150 µl per well for analysis intensity of fluorescence

6.2.6.3. Cell toxicity tests

For the set, two groups of coated samples were given to identify whether the coating time influences the cytotoxicity tests. 12h and 24h fluoride coated samples were subjected to cell toxicity tests. During the test, the cell counts were measured for every sample using the intensity of fluorescence. The mean is calculated by averaging the cell counts and subtracting it with blank value. % to control positive is regarded as cell viability. The cell viability values are plotted in column graphs for two separate conditions and these values are explained in detail in the subsequent sections.

6.2.6.4. Cell toxicity results

Figure 6.9 shows the cytotoxicity results for 12h fluoride coated as-extruded pure Mg and Mg-Zn-Ca-Er alloys. The cell viability values exhibited by pure Mg and its alloys after 12h fluoride coating were greater than 70%, which is acceptable according to ISO 10993. Pure Mg after 12h F-coating exhibited cell viability value of 75%. Addition of 2 wt.% Zn enhanced the cell viability value to 82%. A slight increase in cell-viability was observed for Mg-2Zn-0.6Ca-1Er, which is 84%. Increased addition of Er led to an increased value of cell viability for Mg-2Zn-2Er, which is 89%. Mg-3Zn-0.5Er exhibited cell viability value of 93%. Among these alloys, coated Mg-2Zn-0.6Ca exhibited excellent cell viability value of 94%.

Figure 6.9 also shows the state of coated materials after subjecting to cell-toxicity tests. Apart from Sample 3 (12h F-coated pure Mg), the rest of the materials were not corroded significantly. The base of Sample 1 (12h F-coated Mg-2Zn) was not corroded significantly but the circumferential area started to degrade. For Sample 2 (12h F-coated Mg-2Zn-2Er) and Sample 4 (12h F-coated Mg-2Zn-0.6Ca-1Er), the base was subject to corrosion and the intensity is greater near the edges. Sample 5 (12h F-coated Mg-2Zn-0.6Ca) and Sample 6 (12h F-coated Mg-3Zn-0.5Er) did not show any signs of intense corrosion. These samples retained the shiny yellow coated appearance even after subjecting to cell-culture tests, indicating the beneficial effect of fluoride coating on these newly developed alloys.

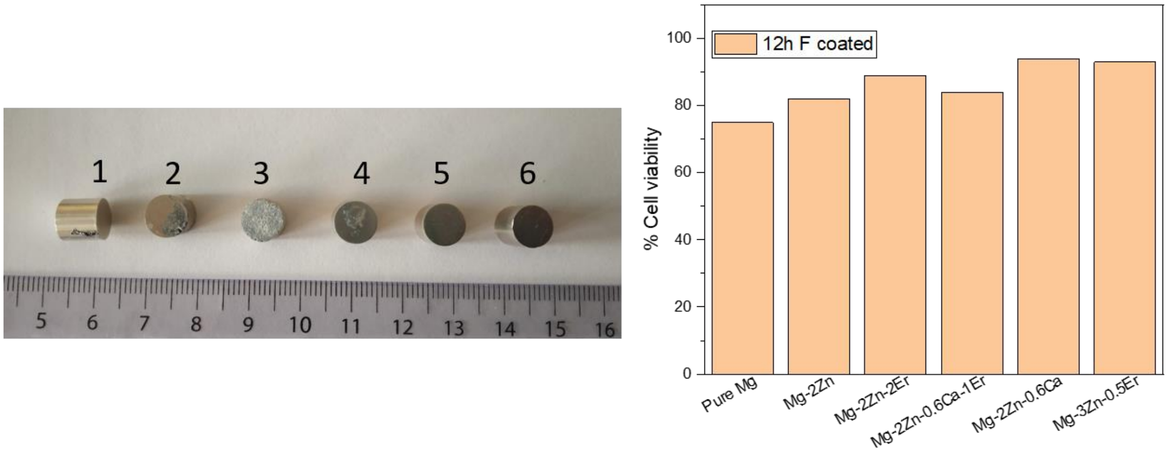

Figure 6.9: Cell toxicity results for as-extruded 12h fluoride coated Mg-Zn-Ca-Er alloys

The results of 24h fluoride coated as-extruded pure Mg and its alloys are represented in Figure 6.10.

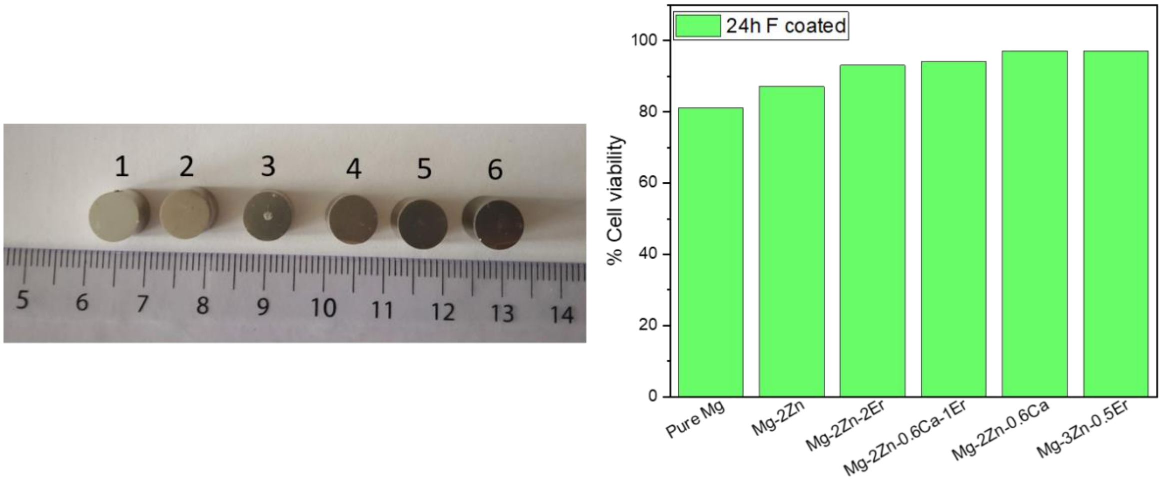

Figure 6.10: Cell toxicity results for as-extruded 24h fluoride coated Mg-Zn-Ca-Er alloys

Pure Mg exhibited cell viability value of 81% for 24h coating which is a slight improvement as compared to 12h coated sample. The Sample 3 in the pictorial representation (24h F-coated pure Mg) does not show any signs of intense corrosion, except at the centre. For Mg-2Zn, there is a slight improvement of 5% from 82% to 87%. The ternary alloy Mg-2Zn-2Er also registers similar level of improvement, from 89% to 93%. For other alloys, there is a significant improvement in the cell viability values with increased coating time. Among all the materials, coated Mg-2Zn-0.6Ca and Mg-3Zn-0.5Er shows the highest cell viability value of 97%. Barring Sample 3 (24h F-coated pure Mg) all the coated alloys exhibit shiny surface due to coating, even after cell-culture tests.

Overall the biocompatibility results indicate higher values of cell viability for the alloys as compared to pure Mg for both 12h and 24h coated samples, indicating the beneficial effect of Zn, Ca and Er in enhancing the biodegradability and biocompatibility of magnesium alloys. In both these tests, Mg-2Zn-2Er, Mg-2Zn-0.6Ca and Mg-3Zn-0.5Er alloys exhibited highest cell-viability values.

6.3. Discussion

6.3.1. Hydrophilicity of coatings

Surfaces which are hydrophilic in nature is necessary for bone repair materials which can be biocompatible in blood [271]. As reported by Subbaihdoss et al., wettability of the surface of a biomaterial has an influence in the cellular interactions [272]. The guidewires used in angioplasty are coated with polytetrafluoroethylene (PTFE) which is hydrophilic and this surface has low coefficient of friction and it is compatible with blood as long as the guidewire is inside the body. With time, the bare metal could develop biocompatibility issues due to changing oxide content on the surface upon storage and hence the hydrophilic coating is an added advantage. These surfaces are considered non-biofouling and enhance biocompatibility. This can also enhance bone cell adhesion, spreading and cell proliferation that can boost further growth of bone [273]. The surface energy of blood is 52 mN/m and that of distilled water is 72 mN/m at room temperature [274]. If a surface has to be defined hydrophilic, it should have a higher surface energy than that of the fluid.

With decrease in the contact angle, the hydrophilicity enhances and so does the adhesive interaction between the surface and the water drop. To calculate the hydrophilicity of any surface, water is normally used as a fluid. With fluoride coating, the surfaces became hydrophilic and this could be related to its chemical composition, microstructure and roughness. Previous studies on MgF_2/PCL coatings on ZK60 magnesium alloy has shown an increased surface roughness of the coated alloy [275]. AFM measurements on ZK60 Mg alloy was found to be 40.7 nm and that of fluoride coated sample, the value was increased to 66.3 nm. For cell adhesion and longevity, the surface roughness values of the coated implants should be in the range of 20-100 nm [276]. Hence the developed fluoride coated materials in this study with increased hydrophilicity could be successful candidates for biomedical applications.

6.3.2. Raman spectroscopy

6.3.2.1. Corroded samples

For Mg-2Zn-2Er, the Raman spectra of phosphate oxyanions show a symmetric stretching mode (v_1) at 934 cm^{-1}. The antisymmetric stretching mode (v_3) is indexed at 1055 cm^{-1}. The symmetric bending mode (v_2) is at 425 cm^{-1} and the v_4 mode is indexed at 564 cm^{-1}.

The low intensity Raman bands at higher wavenumber are attributed to the stretching vibration of OH$^-$ units. The Raman spectrum for Mg-2Zn-2Er corroded in PBS shows a series of low intensity bands at 2371, 3171 and 3445 cm^{-1}. These bands are corresponding to water stretching vibrations. This spectrum gives an indication of the phosphate layer that is developed on the alloys is subjected to corrosion. Through this, we can conclude that a phosphate layer is formed on the surface of the samples, which confirms XPS analysis carried out in Figure 5.17 where peaks for P and O were identified.

6.3.2.2. Coated samples

For F-coated pure Mg and Mg-2Zn-2Er samples, the peaks corresponding to peak positions 72 cm^{-1} and 122 cm^{-1} (Mg) and 119 cm^{-1} (Mg-3Zn-0.5Er) were intense than that of uncoated bare samples. The first line number 72 cm^{-1} is attributed to the B_g symmetry. These values are in coherence to the studies made by Krishnan et al. [277] on the first-order Raman spectrum of MgF_2. Hence it could be said that these peaks correspond to the signals from fluorine.

6.3.3. Fluoride coating mechanism

A common approach to achieve the required properties for corrosion resistance is surface modification. Immersion of Mg and its alloys in hydrofluoric acid results in several corrosive micro-batteries on the surface of the samples. Dissolution of magnesium in the micro-anode region can be represented as follows:

$$\mathrm{Mg} \rightarrow \mathrm{Mg}^{2+} + 2\mathrm{e}^{-}$$ **Equation 1**

The cathodic reaction acted in the micro-negativity polarity zone is as follows:

$$2\mathrm{H}^{+} + 2\mathrm{e}^{-} \rightarrow H_2 \uparrow$$ **Equation 2**

Meanwhile MgF_2 can thus be formed on the surface by the reaction of Mg^{2+} with F^- as follows:

$$\mathrm{Mg}^{2+} + 2\mathrm{F}^{-} \rightarrow \mathrm{MgF}_2 \downarrow$$ **Equation 3**

The rate of dissociation of magnesium into its ions and the rate of deposition of MgF_2 should occur with a dynamic balance. The MgF_2 deposited on the magnesium alloy surface is not soluble and hence there is a gradual growth of this barrier film formed on the surface. With increased MgF_2

formation as the reaction proceeds, the reaction interface of the dissolution of magnesium will be lowered. Thus, with an increment of the film thickness, the growth of the film was slowed down. After samples were immersed in the hydrofluoric acid for 24h, the barrier film on the surface was thick enough to terminate the reaction. The schematic illustration used to show the formation of the fluoride coatings on Mg alloys in represented in Figure 6.11. It shows a protective MgF_2 layer formed after a simple chemical conversion of the natural $MgO/Mg(OH)_2$ surface after immersing in HF.

An oxidation reaction that occurred in the formation of MgF_2 is shown as follows:

$$Mg + 2H_2O \rightarrow Mg(OH)_2 + H_2\uparrow$$

Since the solution is acidic, the formed $Mg(OH)_2$ is not stable in acidic solution. Hence, the reactions should occur as follows:

$$Mg(OH)_2 + 2HF \rightarrow MgF_2 + 2H_2O$$

The overall reaction occurred can be shown as follows:

$$Mg + H_2O + 2F^- \rightarrow MgO + MgF_2 + H_2\uparrow$$

After immersion, H_2 bubbles could be seen coming out of the surface and it could likely be the reason for the generation of pores in the coating film. With the coating taking place, these pores might be decreased as there is no pure magnesium available for dissociation. Or they could be filled by the due precipitation of MgF_2 phase, thus the bottom of the pores was closed and the sample substrate could not be exposed through the pores. The kinetics of these reactions that took place were extremely slow and hence the hydrogen evolution could not be observed by eyes during the treatment.

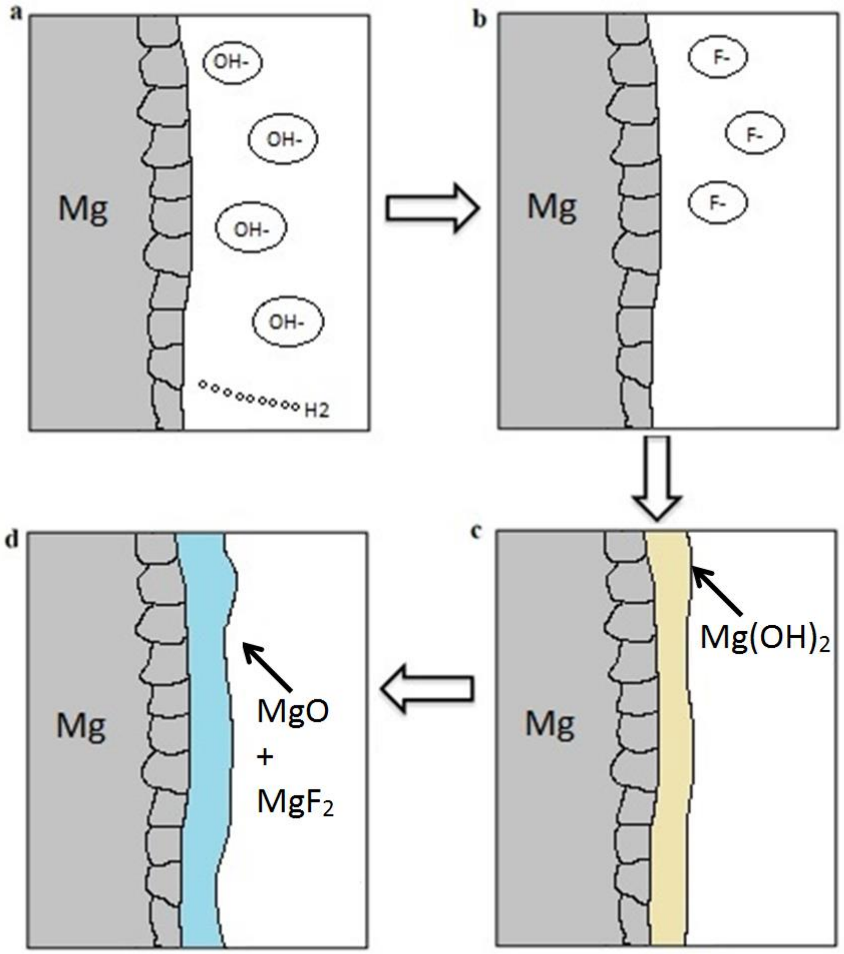

Figure 6.11: Schematic illustration of the formation of fluoride coatings on Mg alloys

6.3.4. Degradation

To control the degradation rate of magnesium and its alloys, the role played by this chemical conversion technique could be explained by considering the corrosion mechanism of magnesium in physiological solutions like PBS. When magnesium is immersed in PBS, magnesium hydroxide ($Mg(OH)_2$) is produced due to the reaction with water. But due to the chloride ions present in the solution, this self-protecting layer is unstable in their presence and it leads to the formation of magnesium chloride which rapidly degrades magnesium. To protect magnesium from degrading in physiological conditions, an optimum solution is to delay the formation of magnesium chloride. Hence, a controlled degradation behavior could be established by providing a fluoride coating barrier on magnesium substrate with optimum surface mineralization properties.

But F^- has a relatively high electronegativity, and it has a tendency to react with H^+ ions and can form $\mathrm{H}F_2^-$, $H_2F_3^-$ surface layers with strong binding energy. After immersing in PBS, the Cl^- replace F^- and the samples gradually lose its protective ability. The coated samples in PBS degrade and the compact fluoride coating detaches in certain regions. As this micrometer thick coated layer, that had provided initial corrosion resistance starts to corrode, corrosion propagates via a ‘through-hole’ and into the base material. A local penetration of the layer takes place that is revealed by accelerated hydrogen gas evolution. The preliminary studies have shown promising results and long run behavior of the fluoride coating in controlling the degradation rate of magnesium alloy needs to be investigated. To increase the hydrophilicity of the coatings, more soaking time can be chosen with optimum degradation properties.

Although, hydrophilic surfaces are generally preferable for better cell adhesion, the controlled degradation of grain refined magnesium has shown to enhance cell viability [278,279]. The coated alloys can be used as materials for stent where this coating will help in the first stage of degradation, i.e., during the “phase of function” where the stent provides mechanical support [3]. The coating can remain until the second stage starts during remodeling and physiological functions of the vessel.

6.3.5. Biocompatibility

The cells used for cell-toxicity measurements of magnesium alloys are MC3T3. It is an osteoblast precursor cell line which is derived from Mus musculus (mouse) calvaria, commonly known as house mouse. These cells were chosen such that they can replicate human bone cells when it is in contact with the implant by simulating a clinical situation to understand bone healing response. When magnesium alloys are in the vicinity of a body fluid, its inherent response is corrosion. The fluoride coated materials exhibited enhanced biocompatibility results as compared to as-extruded Mg and its alloys. Surface morphologies of the samples with after immersion in phosphate buffer saline illustrated that the magnesium phosphates were formed on the surface of samples. This magnesium phosphate layer is insoluble and it could inhibit the release of fresh Mg^{2+} ions from the surface. For bone implants, the prerequisite to bond to living bone is the formation of biologically active materials on the surface of the implant in the body. Both magnesium phosphate and MgF_2 are bioactive. Meanwhile, fluoride can enhance osteoblastic differentiation and interfacial bone formation [280]. Mg can also promote bone generation and osteoblast stimulation. It was demonstrated earlier that fluoride coatings also have good antibacterial properties. It could be concluded from this study that a lower corrosion rate exhibiting material could denote a lower cytotoxicity as fluoride coated materials exhibited lower corrosion rate and lower cytotoxicity as compared to as-extruded alloys. Biomaterials with anti-microbial properties are highly desirable because of reducing risk of infection. MgF_2 has enhanced antibacterial properties [281] and this is very beneficial to their application as a coating on medical implants.

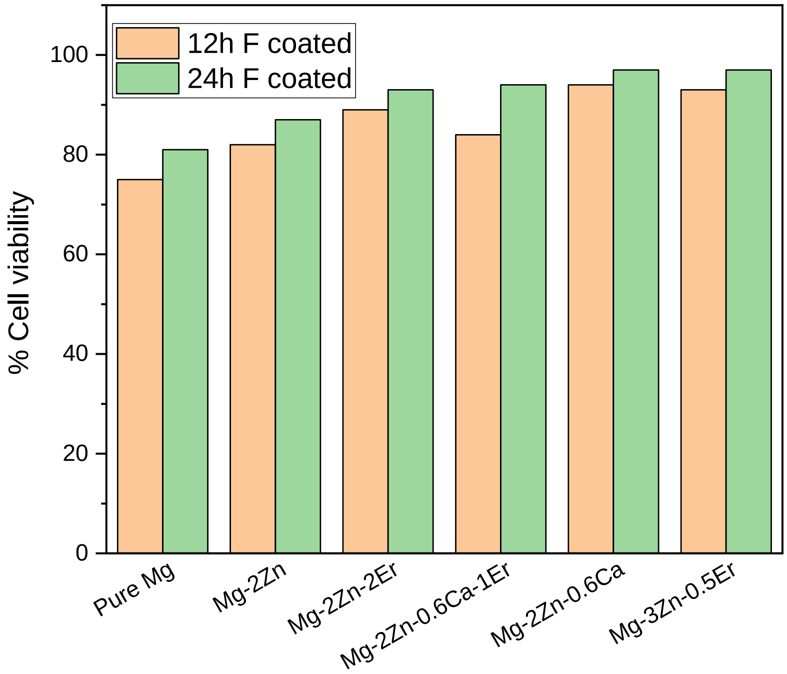

Figure 6.12: Property comparison profile of biocompatibility assessment of as-extruded, 12h F-coated and 24 F-coated magnesium alloys

The property comparison profile for biocompatibility studies on Mg-Zn-Ca-Er alloys are plotted in Figure 6.12. Alloying additions have certainly enhanced the cell viability values of these materials. And with enhanced coating time from 12h to 24h, there is a slight improvement in the degradation resistance of these newly developed alloys.

6.4. Conclusion

- Compact and uniform fluoride coatings were successfully developed using fluoride conversion treatment.
- HF treatment changed the surface of the alloy from hydrophobic to hydrophilic when contact angle measurements were conducted in deionized water.
- The corrosion behavior was calculated for coated samples and it was found that the samples exhibited enhanced corrosion resistance with fluoride coatings.
- Fluoride coatings have drastically reduced the cytotoxicity values and with increased coating time, the cell viability values increased for the alloys.
- The results serve as a useful tool to select an appropriate alloy and condition based on the cytotoxicity and biocompatibility of magnesium alloys.

CHAPTER 7

CONCLUSIONS

7. Conclusions

The main aim of this Ph.D project is to design and develop a new kind of biodegradable magnesium based alloys through the addition of zinc, calcium and rare earth element like erbium. This involved synthesis, microstructure, mechanical properties, degradation behavior, and surface modification followed by cell-culture studies. The following subsections summarize the conclusions obtained in this study.

In the first phase of the project, the material synthesis, microstructure and mechanical properties of Mg-Zn-Ca-Er alloys were studied in detail in comparison to pure Mg and the following conclusions were drawn.

The choice of alloying elements was made such that the alloys degrade slowly and present greater mechanical properties over pure Mg. Hence a design strategy was developed by adding minor additions of calcium and zinc which restrict grain growth, contributes to solid-solution and precipitation hardening and are non-toxic for human body. Addition of erbium was carried out as it led to the development of Mg-Zn-Er phases that enhance the corrosion resistance of these newly developed biodegradable alloys.

Conventional methods of synthesis like solidification could face several issues for magnesium production, namely:

1) Final product consisting of oxides
2) Retention of reinforcements and alloying additions (this is because most of the alloying additions have densities higher than that of pure Mg)

These issues collectively lead to impurities, non-homogeneous distribution of alloying elements. Disintegrated melt deposition technique followed by hot-extrusion is a safe, efficient and cost-effective methodology that provides highest yield and dense products. Enhanced strength values are attributed to the greater microstructural homogeneity provided by the DMD alloys. The DMD technique ensures the elimination of oxides into the deposited products, enhances the productivity by complete utilization of reinforcement addition and also attains higher solidification rates due to the disintegration of molten metal by argon gas.

The following are the advantages of DMD process:

1) It is a combination of casting and spray forming process.
2) The assembly design is such that it eliminates the need for separate melting and pouring units.
3) Least metal wastage and removes slag/oxides
4) Efficient incorporation of nanoparticles
5) Increased yield of the products with fine-grained microstructure with minimal porosity.

To achieve the first goal of tailoring the bulk microstructure of the alloys, hot-extrusion was adapted and the alloying additions and its compositions were carefully chosen to enhance the properties.

Equiaxed fine grained microstructures have been achieved in as-extruded pure magnesium and its alloys as compared to the coarse grained as-DMDed microstructures. Mg-2Zn-2Er exhibits a reduced grain size of 6.6 μm as compared to 22.42 μm for pure Mg. The secondary phases have been uniformly distributed and they are broken down in the as-extruded microstructures of the alloys. The microstructural characterization reveals the presence of $MgZn_2$, W-phase ($Mg_3Zn_3Er_2$) and i-phases (Mg_3Zn_6Er) in different alloys.

The ternary (Mg-2Zn-2Er, Mg-3Zn-0.5Er, Mg-2Zn-0.6Ca) and quaternary alloys (Mg-2Zn-0.6Ca-1Er) exhibited an increment in the tensile and compressive properties as compared to pure Mg and Mg-2Zn binary alloy. Among these alloys, Mg-2Zn-2Er exhibited highest TYS, CYS and UCS value of 192 MPa, 134 MPa and 501 MPa respectively. These values are attributed to a reduction in grain size, presence of solute atoms and secondary phases. Fractography studies reveal the dimples that are an indication of enhanced ductility behavior, along with the presence of twins in the area close to the fractured region as seen in EBSD analysis. The enhanced ductility is attributed to twin assisted plasticity. Microhardness studies revealed an enhancement of mechanical properties of as-extruded alloys compared to as-DMDed alloys. The damping behavior shows that the elastic modulus of the alloys has retained their values as that of pure magnesium, which is beneficial for its biomedical applications.

Corrosion rate can be slowed by careful control of the microstructural features through the introduction of alloying elements and processing conditions. As-DMDed alloys showed an excessive corrosive rate due to a coarse grain sized microstructure, inhomogeneities including porosities and segregation of elements. Whereas as-extruded alloys showed enhanced corrosion resistance due to the fine grain sized microstructure and an uniform distribution of secondary phases. Rare-earth element erbium has been introduced in small amounts below the solubility level of the element and it has significantly enhanced the corrosion resistance of Mg-alloys. This is due to the incorporation of erbium on the corroded surface. The element erbium took part in the oxide formation which was more efficient in protecting the material. The corrosion rates have been reduced significantly for Mg-2Zn-2Er (E_{corr} = -1.51 V vs. SCE) as compared to pure Mg (E_{corr} = -1.634 V vs. SCE) in PBS solution at 37 ^{o}C.

A compact fluoride coating has been introduced to magnesium alloys with a simple and cost-effective technique to minimize initial degradation rates and provide sufficient corrosion resistance in PBS solution at 37 ^{o}C. They resulted in a hydrophilic surface which is preferred for better cell adhesion and controlled degradation. These coatings are biocompatible and they can be further tailored to provide more protection to the surface. The corrosion potential for F-coated Mg-2Zn-2Er has increased slightly (E_{corr} = -1.483 V vs. SCE) when it is tested in PBS solution at 37 ^{o}C, indicating a beneficial effect to enhance corrosion resistance. The cell viability values increased with coating time and among 24h F-coated samples, Mg-2Zn-0.6Ca and Mg-3Zn-0.5Er exhibited the highest cell viability value of 97%. Hence fluoride coated magnesium alloys have demonstrated their abilities to perform as a biomedical material. The validation of cell-toxicity tests in different cell culture media has to be carried out before subjecting these alloys to further *in-vivo* tests.

8. Perspectives

In our study, it was observed that development of magnesium alloys with excellent mechanical, electrochemical, surface and biomedical properties is not an easy task, given that it involves several interdisciplinary domains. For synthesis of these alloys, the standard conditions of DMD technique and hot-extrusion were used. Different parameters like using lower temperature for hot-extrusion and a higher extrusion rate could be tried to modify the microstructure, formation and distribution of phases and hence the properties. Since this work involves formation of new phases, there is scope to study these new phases in detail using HRTEM. Although these materials were targeted for biomedical applications, they also could exhibit excellent high-temperature mechanical properties. Since Mg alloys suffer from creep at medium to high temperatures, the influence of Er on the structural integrity of magnesium alloys for automotive and aerospace sectors could be interesting to study. Tests including dynamic mechanical analysis to study the viscoelastic properties, three point bending tests after accommodating different movements of the implant material could be studied as well. Future work should concentrate on studying the corrosion behavior of W-phase and i-phase by using local electrochemical methods such as microelectrochemical investigations based on the microcapillary effect. This is to determine the corrosion potential of individual phase and its contribution to calculate the overall corrosion rate. Alkalanized fluoride coatings could be implemented on these alloys to study the conversion of hydroxide layer into fluoride layer and its effect on the corrosion behavior. Different cell mediums like endothelial cell culture studies could be carried out to discern the behavior of synthesized magnesium alloys using different standard protocols, to further validate these alloys for their biocompatibility and biodegradability.

Publications

Manuscripts in international peer-reviewed journals

D. Bhat Panemangalore, R. Shabadi, D. Tingaud, M. Touzin, G. Ji, Biocompatible silica-based magnesium composites, Journal of Alloys and Compounds 772 49-57 (2019) [doi: 10.1016/j.jallcom.2018.09.060]

D. Bhat Panemangalore, R. Shabadi, M. Gupta, G. Ji, Effect of fluoride coatings on the corrosion behavior of Mg-Zn-Er alloys, Surfaces and Interfaces 14 72-81 (2019) [doi: 10.1016/j.surfin.2018.11.007]

D. Bhat Panemangalore, R. Shabadi, M. Gupta, R. Ambat, G. Ji, A. Addad, L. Lesven, Microstructure and Corrosion Behavior of Extruded Mg-Zn-Er Alloys, Materials Science Forum 941 1766-1771 (2018) [doi: 10.4028/www.scientific.net/MSF.941.1766]

D. Bhat Panemangalore, R. Shabadi, M. Gupta, G. Ji, Conception of Bio-degradable Zinc, Calcium and Erbium based Magnesium alloy [Submitted to Journal of Alloys and Compounds]

D. Bhat Panemangalore, R. Shabadi, M. Gupta, G. Ji, In-vitro cytotoxicity assessment of new biodegradable magnesium alloys [manuscript under preparation]

Conference presentations

D. B. Panemangalore, R. Shabadi, G. Ji, M. Gupta, , Influence of chemical composition and conversion coatings on the corrosion properties of Mg-Sn-xY (x= 0.5, 1 and 2 wt%) alloys,, EUROCOR 2016, Montpellier, France, September 2016

D. B. Panemangalore, R. Shabadi, G. Ji, M. Gupta, Influence of zinc and erbium on the corrosion behavior of magnesium, ICONEST 2017, Bengaluru, India, August 2017

D. B. Panemangalore, R. Shabadi, G. Ji, M. Touzin, D. Tingaud, Biocompatible silica-based magnesium composites, Journées Annuelles de la SF2M, Lyon, France, October 2017

D. B. Panemangalore, R. Shabadi, M. Gupta, R. Ambat, G. Ji, A. Addad, L. Lesven, Microstructure and corrosion behavior of extruded Mg-Zn-Er alloys, THERMEC 2018, Paris, France, July 2018

Bibliography

[1] F. Witte, Reprint of: The history of biodegradable magnesium implants: A review, Acta Biomater. 23 (2015) S28–S40. doi:10.1016/j.actbio.2015.07.017.

[2] J.D. Robson, D.T. Henry, B. Davis, Particle effects on recrystallization in magnesium – manganese alloys : Particle-stimulated nucleation, Acta Mater. 57 (2009) 2739–2747. doi:10.1016/j.actamat.2009.02.032.

[3] A. Drynda, T. Hassel, R. Hoehn, A. Perz, F.-W. Bach, M. Peuster, Development and biocompatibility of a novel corrodible fluoride-coated magnesium-calcium alloy with improved degradation kinetics and adequate mechanical properties for cardiovascular applications, J. Biomed. Mater. Res. Part A. 93A (2010) 763–775.

[4] J. Yang, J. Peng, E.A. Nyberg, F. Pan, Effect of Ca addition on the corrosion behavior of Mg–Al–Mn alloy, Appl. Surf. Sci. 369 (2016) 92–100. doi:10.1016/J.APSUSC.2016.01.283.

[5] H. Medhashree, A.N. Shetty, Electrochemical corrosion study of Mg–Al–Zn–Mn alloy in aqueous ethylene glycol containing chloride ions, J. Mater. Res. Technol. 6 (2017) 40–49. doi:10.1016/J.JMRT.2016.04.003.

[6] R. Niu, F. Yan, Y. Wang, D. Duan, X. Yang, Effect of Zr content on damping property of Mg–Zr binary alloys, Mater. Sci. Eng. A. 718 (2018) 418–426. doi:10.1016/J.MSEA.2018.01.115.

[7] B. Li, L. Hou, R. Wu, J. Zhang, X. Li, M. Zhang, A. Dong, B. Sun, Microstructure and thermal conductivity of Mg-2Zn-Zr alloy, J. Alloys Compd. 722 (2017) 772–777. doi:10.1016/J.JALLCOM.2017.06.148.

[8] N. Liu, Z. Zhang, L. Peng, W. Ding, Microstructure evolution and mechanical properties of Mg-Gd-Sm-Zr alloys, Mater. Sci. Eng. A. 627 (2015) 223–229. doi:10.1016/J.MSEA.2014.12.114.

[9] Y. Zhang, P. Gore, W. Rong, Y. Wu, Y. Yan, R. Zhang, L. Peng, J.-F. Nie, N. Birbilis, Quasi-in-situ STEM-EDS insight into the role of Ag in the corrosion behaviour of Mg-Gd-Zr alloys, Corros. Sci. 136 (2018) 106–118. doi:10.1016/J.CORSCI.2018.02.058.

[10] G. Ben-Hamu, D. Eliezer, K.S. Shin, S. Cohen, The relation between microstructure and corrosion behavior of Mg–Y–RE–Zr alloys, J. Alloys Compd. 431 (2007) 269–276. doi:10.1016/J.JALLCOM.2006.05.075.

[11] R. Ambat, N.N. Aung, W. Zhou, Evaluation of microstructural effects on corrosion behaviour of AZ91D magnesium alloy, Corros. Sci. 42 (2000) 1433–1455.

[12] P.C. Ferreira, K. de A. Piai, A.M.M. Takayanagui, S.I. Segura-Muñoz, Aluminum as a risk factor for Alzheimer's disease., Rev. Lat. Am. Enfermagem. 16 (n.d.) 151–7.

[13] Z. Li, X. Gu, S. Lou, Y. Zheng, The development of binary Mg–Ca alloys for use as

biodegradable materials within bone, Biomaterials. 29 (2008) 1329–1344. doi:10.1016/j.biomaterials.2007.12.021.

[14] I. Nakatsugawa, S. Kamado, Y. Kojima, R. Ninomiya, K. Kubota, Corrosion of magnesium alloys containing rare earth elements, Corros. Rev. 16 (1998) 139–157. doi:10.1515/CORRREV.1998.16.1-2.139.

[15] E. Emley, Principles of magnesium technology, [1st ed.]., Pergamon Press, Oxford ;New York, 1966. http://www.worldcat.org/title/principles-of-magnesium-technology/oclc/3261812 (accessed August 31, 2017).

[16] A. MM, Magnesium and Magnesium Alloys, 1999.

[17] B. Byron, Global Overview of Automotive Magnesium Requirements and Supply and Demand, (1997).

[18] E.J.K. R.W Cahn P. Haasen, Materials Science and Technology - A Comprehensive Treatment: Structure and Properties of Nonferrous Alloys, VCH Weinheim, 1996.

[19] R. Eschelbach, Taschenbuch der metallischen Werkstoffr, 1969.

[20] M.M. Avedesian, H. Baker, ASM International. Handbook Committee., Magnesium and magnesium alloys, ASM International, 1999.

[21] A. Zafari, H.M. Ghasemi, R. Mahmudi, An investigation on the tribological behavior of AZ91 and AZ91+ 3wt% RE magnesium alloys at elevated temperatures, Mater. Des. 54 (2014) 544–552.

[22] M.L. Olguín-González, D. Hernández-Silva, M.A. García-Bernal, V.M. Sauce-Rangel, Hot deformation behavior of hot-rolled AZ31 and AZ61 magnesium alloys, Mater. Sci. Eng. A. 597 (2014) 82–88. doi:10.1016/j.msea.2013.12.027.

[23] S.B. Yi, H.-G. Brokmeier, R.E. Bolmaro, K.U. Kainer, T. Lippmann, In situ measurements of texture variations during a tensile loading of Mg-alloy AM20 using synchrotron X-ray radiation, Scr. Mater. 51 (2004) 455–460.

[24] H. Ding, K. Hirai, T. Homma, S. Kamado, Numerical simulation for microstructure evolution in AM50 Mg alloy during hot rolling, Comput. Mater. Sci. 47 (2010) 919–925.

[25] X. Lin, L. Tan, Q. Zhang, K. Yang, Z. Hu, J. Qiu, Y. Cai, The in vitro degradation process and biocompatibility of a ZK60 magnesium alloy with a forsterite-containing micro-arc oxidation coating, Acta Biomater. 9 (2013) 8631–8642.

[26] I.J. Polmear, Magnesium alloys and applications, Mater. Sci. Technol. 10 (1994) 1–16. doi:10.1179/mst.1994.10.1.1.

[27] R. Stack, R. Califf, H. Phillips, D. Pryor, P. Quigley, R. Bauman, J. Tcheng, J.J. Greenfield, Interventional Cardiac Catheterization at Duke Medical Center The Duke Interventional Cardiac Catheterization Program, Am. J. Cardiol. 62 (1988) 3F–24F.

[28] H.Z. Ye, X.Y. Liu, Review of recent studies in magnesium matrix composites, J. Mater.

Sci. 9 (2004) 6153–6171. doi:10.1023/B:JMSC.0000043583.47148.31.

[29] B. Pucun, D. Taishang, H. Xiaohu, Z. Chunwang, X. Yongming, Microstructure and mechanical properties of spray-deposited Mg–12.55Al–3.33Zn–0.58Ca–1Nd alloy, Mater. Charact. 61 (2010) 756–760. doi:10.1016/j.matchar.2010.04.009.

[30] K.F. Chang, M.L.T. Guo, R.H. Kong, C.Y. a Tsao, J.C. Huang, J.S.C. Jang, Mg-Cu-Gd layered composite plate synthesized via the spray forming process, Mater. Sci. Eng. A. 477 (2008) 58–62. doi:10.1016/j.msea.2007.09.079.

[31] V. Biehl, J. Breme, Metallic Biomaterials, Materwiss. Werksttech. 32 (2001) 137–141.

[32] R.W. Murray, J.E. Hillis, Magnesium Finishing: Chemical Treatment and Coating Practices, in: SAE Tech. Pap., SAE International, 1990. doi:10.4271/900791.

[33] M.G.K. Gupta M, Insight into Designing Biocompatible Magnesium Alloys and Composites, Springer Singapore, 2015.

[34] N.E.L. Saris, E. Mervaala, H. Karppanen, J.A. Khawaja, A. Lewenstam, Magnesium: An update on physiological, clinical and analytical aspects, Clin. Chim. Acta. 294 (2000) 1–26. doi:10.1016/S0009-8981(99)00258-2.

[35] J. Vormann, Magnesium: Nutrition and metabolism, Mol. Aspects Med. 24 (2003) 27–37. doi:10.1016/S0098-2997(02)00089-4.

[36] T. Okuma, Magnesium and bone strength, Nutrition. 17 (2001) 679–680. doi:10.1016/S0899-9007(01)00551-2.

[37] B. Heublein, R. Rohde, V. Kaese, M. Niemeyer, W. Hartung, A. Haverich, Biocorrosion of magnesium alloys: a new principle in cardiovascular implant technology?, Heart. 89 (2003) 651–656. doi:10.1136/heart.89.6.651.

[38] R. Erbel, carlo Di Mario, J. Bartunek, J. Bonnier, B. de Bruyne, F. R Eberli, P. Erne, M. Haude, B. Heublein, M. Horrigan, C. Ilsley, D. Bose, J. Koolen, T. F Luescher, N. Weissman, R. Waksman, Temporary scaffolding of coronary arteries with bioabsorbable magnesium stents: a prospective, non-randomised multicentre trial, Lancet. 369 (2007) 1869–1875.

[39] N. Erdmann, N. Angrisani, J. Reifenrath, A. Lucas, F. Thorey, D. Bormann, A. Meyer-Lindenberg, Biomechanical testing and degradation analysis of MgCa0.8 alloy screws: A comparative in vivo study in rabbits, Acta Biomater. 7 (2011) 1421–1428. doi:10.1016/j.actbio.2010.10.031.

[40] H. Windhagen, K. Radtke, A. Weizbauer, J. Diekmann, Y. Noll, U. Kreimeyer, R. Schavan, C. Stukenborg-Colsman, H. Waizy, Biodegradable magnesium-based screw clinically equivalent to titanium screw in hallux valgus surgery: short term results of the first prospective, randomized, controlled clinical pilot study, Biomed. Eng. Online. 12 (2013) 62. doi:10.1186/1475-925X-12-62.

[41] L. Wolters, N. Angrisani, J. Seitz, P. Helmecke, A. Weizbauer, J. Reifenrath, Applicability

of Degradable Magnesium LAE442 Alloy Plate-Screw-Systems in a Rabbit Model, Biomed. Eng. / Biomed. Tech. (2013). doi:10.1515/bmt-2013-4059.

[42] J. Reifenrath, N. Angrisani, N. Erdmann, A. Lucas, H. Waizy, J.M. Seitz, A. Bondarenko, A. Meyer-Lindenberg, Degrading magnesium screws ZEK100: biomechanical testing, degradation analysis and soft-tissue biocompatibility in a rabbit model, Biomed. Mater. 8 (2013) 045012. doi:10.1088/1748-6041/8/4/045012.

[43] R. Glicksman, The Performance of Zinc, Magnesium and Aluminum Primary Cell Anodes. A Review, J. Electrochem. Soc. 106 (1959) 457–464.

[44] J.L. Robinson, P.F. King, No Title, Electrochem. Behav. Magnes. Anode. (1961) 36–41.

[45] K. Huber, Anodic Formation of Coatings on Magnesium, Zinc, and Cadmium, J. Electrochem. Soc. 100 (1953) 376–382.

[46] G.R. Hoey, M. Cohen, Corrosion of Anodically and Cathodically Polarized Magnesium in Aqueous Media, J. Electrochem. Soc. 105 (1958) 245–250.

[47] J.F. King, Magnesium: commodity or exotic?, Mater. Sci. Technol. 23 (2007) 1–14. doi:10.1179/174328407X154374.

[48] R.L. Petty, A.W. Davidson, J. Kleinberg, The Anodic Oxidation of Magnesium Metal: Evidence for the Existence of Unipositive Magnesium1,2, J. Am. Chem. Soc. 76 (1954) 363–366.

[49] G. Song, A. Atrens, D. Stjohn, J. Nairn, Y. Li, The electrochemical corrosion of pure magnesium in 1 N NaCl, Corros. Sci. 39 (1997) 855–875. doi:10.1016/S0010-938X(96)00172-2.

[50] G.G. Perrault, Encyclopaedia of Electrochemistry of the Elements, Marcel Dekker, New York, 1972.

[51] J.H. Hanks, R.E. Wallace, Relation of Oxygen and Temperature in the Preservation of Tissues by Refrigeration, Exp. Biol. Med. 71 (1949) 196–200. doi:10.3181/00379727-71-17131.

[52] T. Kokubo, H. Takadama, How useful is SBF in predicting in vivo bone bioactivity?, Biomaterials. 27 (2006) 2907–2915. doi:10.1016/j.biomaterials.2006.01.017.

[53] G. Song, a. Atrens, Understanding Magnesium Corrosion—A Framework for Improved Alloy Performance, Adv. Eng. Mater. 5 (2003) 837–858. doi:10.1002/adem.200310405.

[54] M. Gupta, M.O. Lai, C.Y. Soo, Processing-microstructure-mechanical properties of an Al-Cu/SiC metal matrix composite synthesized using disintegrated melt deposition technique, Mater. Res. Bull. 30 (1995) 1525–1534.

[55] G.E. Dieter, D.J. Bacon, Mechanical metallurgy, McGraw-Hill, 1988.

[56] C. DI MARIO, H.U.W. GRIFFITHS, O. GOKTEKIN, N. PEETERS, J.A.N. VERBIST, M. BOSIERS, K. DELOOSE, B. HEUBLEIN, R. ROHDE, V. KASESE, C. ILSLEY, R.

ERBEL, Drug-Eluting Bioabsorbable Magnesium Stent, J. Interv. Cardiol. 17 (2004) 391–395.

[57] F. Witte, H. Ulrich, M. Rudert, E. Willbold, Biodegradable magnesium scaffolds: Part 1: Appropriate inflammatory response, J. Biomed. Mater. Res. Part A. 81A (2007) 748–756.

[58] F. Witte, H. Ulrich, C. Palm, E. Willbold, Biodegradable magnesium scaffolds: Part II: Peri-implant bone remodeling, J. Biomed. Mater. Res. Part A. 81A (2007) 757–765.

[59] F. Witte, J. Reifenrath, P.P. Müller, H.-A. Crostack, J. Nellesen, F.W. Bach, D. Bormann, M. Rudert, Cartilage repair on magnesium scaffolds used as a subchondral bone replacement, Materwiss. Werksttech. 37 (2006) 504–508.

[60] F. Feyerabend, F. Witte, M. Kammal, W. R., Unphysiologically High Magnesium Concentrations Support Chondrocyte Proliferation and Redifferentiation, Tissue Eng. 12 (2006) 3545–3556.

[61] R. Waksman, R. Pakala, P.K. Kuchulakanti, R. Baffour, D. Hellinga, R. Seabron, F.O. Tio, E. Wittchow, S. Hartwig, C. Harder, R. Rohde, B. Heublein, A. Andreae, K.-H. Waldmann, A. Haverich, Safety and efficacy of bioabsorbable magnesium alloy stents in porcine coronary arteries, Catheter. Cardiovasc. Interv. 68 (2006) 607–617.

[62] H.R.B. Rad, M.H. Idris, M.R.A. Kadir, S. Farahany, Microstructure analysis and corrosion behavior of biodegradable Mg–Ca implant alloys, Mater. Des. 33 (2012) 88–97.

[63] Q. Peng, Y. Huang, L. Zhou, N. Hort, K.U. Kainer, Preparation and properties of high purity Mg-Y biomaterials, Biomaterials. 31 (2010) 398–403. doi:10.1016/j.biomaterials.2009.09.065.

[64] D. Vojtěch, J. Kubasek, J. Šerák, P. Novak, Mechanical and corrosion properties of newly developed biodegradable Zn-based alloys for bone fixation, Acta Biomater. 7 (2011) 3515–3522.

[65] R. Zeng, W. Qi, F. Zhang, H. Cui, Y. Zheng, In vitro corrosion of Mg-1.21Li-1.12Ca-1Y alloy, Prog. Nat. Sci. Mater. Int. 24 (2014) 492–499. doi:10.1016/j.pnsc.2014.08.005.

[66] R.C. Zeng, W.C. Qi, H.Z. Cui, F. Zhang, S.Q. Li, E.H. Han, In vitro corrosion of as-extruded Mg-Ca alloys-The influence of Ca concentration, Corros. Sci. 96 (2015) 23–31. doi:10.1016/j.corsci.2015.03.018.

[67] K.U. Kainer, Magnesium – Alloys and Technology, Wiley, 2003. doi:10.1002/3527602046.

[68] S. Zhang, X. Zhang, C. Zhao, J. Li, Y. Song, C. Xie, H. Tao, Y. Zhang, Y. He, Y. Jiang, Research on an Mg–Zn alloy as a degradable biomaterial, Acta Biomater. 6 (2010) 626–640. doi:10.1016/j.actbio.2009.06.028.

[69] F. Witte, N. Hort, C. Vogt, S. Cohen, K.U. Kainer, R. Willumeit, F. Feyerabend, Degradable biomaterials based on magnesium corrosion, 2008. doi:10.1016/j.cossms.2009.04.001.

[70] W. He, E. Zhang, K. Yang, Effect of Y on the bio-corrosion behavior of extruded Mg–Zn–Mn alloy in Hank’s solution, Mater. Sci. Eng. C. 30 (2010) 167–174.

[71] M.B. Kannan, R.K.S. Raman, In vitro degradation and mechanical integrity of calcium-containing magnesium alloys in modified-simulated body fluid, Biomaterials. 29 (2008) 2306–2314. doi:10.1016/j.biomaterials.2008.02.003.

[72] B.L. Mordike, P. Lukac, “Physical Metallurgy,” in Magnesium Technology - Metallurgy, Design Data, Applications, in: Springer-Verlag Berlin Heidelberg, 2006.

[73] The effect of calcium additions on the oxidation behavior in magnesium alloys, Scr. Mater. 42 (2000) 1089–1094. doi:10.1016/S1359-6462(00)00344-4.

[74] J.F. Nie, B.C. Muddle, Precipitation hardening of Mg-Ca(-Zn) alloys, Scr. Mater. 37 (1997) 1475–1481. doi:10.1016/S1359-6462(97)00294-7.

[75] H.S. Brar, J. Wong, M. V. Manuel, Investigation of the mechanical and degradation properties of Mg–Sr and Mg–Zn–Sr alloys for use as potential biodegradable implant materials, J. Mech. Behav. Biomed. Mater. 7 (2012) 87–95. doi:10.1016/j.jmbbm.2011.07.018.

[76] Q. Peng, X. Li, N. Ma, R. Liu, H. Zhang, Effects of backward extrusion on mechanical and degradation properties of Mg–Zn biomaterial, J. Mech. Behav. Biomed. Mater. 10 (2012) 128–137.

[77] J. Kubásek, D. Vojtěch, Structural characteristics and corrosion behavior of biodegradable Mg--Zn, Mg--Zn--Gd alloys, J. Mater. Sci. Mater. Med. 24 (2013) 1615–1626.

[78] X. Zhang, G. Yuan, L. Mao, J. Niu, W. Ding, Biocorrosion properties of as-extruded Mg–Nd–Zn–Zr alloy compared with commercial AZ31 and WE43 alloys, 2012. doi:10.1016/j.matlet.2011.08.079.

[79] L.L. Rokhlin, Magnesium alloys containing rare earth metals: structure and properties, 2003. http://books.google.com/books?id=9yKyqcqGuPMC&pgis=1.

[80] N. Birbilis, M.A. Easton, A.D. Sudholz, S.M. Zhu, M.A. Gibson, On the corrosion of binary magnesium-rare earth alloys, Corros. Sci. 51 (2009) 683–689. doi:10.1016/j.corsci.2008.12.012.

[81] N. Birbilis, B.N. Padgett, R.G. Buchheit, Limitations in microelectrochemical capillary cell testing and transformation of electrochemical transients for acquisition of microcell impedance data, Electrochim. Acta. 50 (2005) 3536–3544.

[82] G.R. Argade, S.K. Panigrahi, R.S. Mishra, Effects of grain size on the corrosion resistance of wrought magnesium alloys containing neodymium, Corros. Sci. 58 (2012) 145–151. doi:10.1016/j.corsci.2012.01.021.

[83] T. Zhang, G. Meng, Y. Shao, Z. Cui, F. Wang, Corrosion of hot extrusion AZ91 magnesium alloy. Part II: Effect of rare earth element neodymium (Nd) on the corrosion behavior of extruded alloy, Corros. Sci. 53 (2011) 2934–2942.

[84] E. Willbold, X. Gu, D. Albert, K. Kalla, K. Bobe, M. Brauneis, C. Janning, J. Nellesen, W. Czayka, W. Tillmann, Y. Zheng, F. Witte, Effect of the addition of low rare earth elements (lanthanum, neodymium, cerium) on the biodegradation and biocompatibility of magnesium, Acta Biomater. 11 (2015) 554–562. doi:10.1016/j.actbio.2014.09.041.

[85] S. Tekumalla, S. Seetharaman, N. Quy Bau, W. Leong Eugene Wong, C. Sim Goh, R. Shabadi, M. Gupta, Influence of Cerium on the Deformation and Corrosion of Magnesium, J. Eng. Mater. Technol. 138 (2016) 031011. doi:10.1115/1.4033033.

[86] Y.L. Song, Y.H. Liu, S.H. Wang, S.R. Yu, X.Y. Zhu, Effect of cerium addition on microstructure and corrosion resistance of die cast AZ91 magnesium alloy, Mater. Corros. 58 (2007) 189–192. doi:10.1002/maco.200603988.

[87] A.D. Sudholz, K. Gusieva, X.B. Chen, B.C. Muddle, M.A. Gibson, N. Birbilis, Electrochemical behaviour and corrosion of Mg–Y alloys, Corros. Sci. 53 (2011) 2277–2282. doi:10.1016/j.corsci.2011.03.010.

[88] X. Gu, Y. Zheng, Y. Cheng, S. Zhong, T. Xi, In vitro corrosion and biocompatibility of binary magnesium alloys, Biomaterials. 30 (2009) 484–498. doi:10.1016/j.biomaterials.2008.10.021.

[89] Q. Peng, Y. Huang, L. Zhou, N. Hort, K.U. Kainer, Preparation and properties of high purity Mg–Y biomaterials, Biomaterials. 31 (2010) 398–403.

[90] M. Liu, P. Schmutz, P.J. Uggowitzer, G. Song, A. Atrens, The influence of yttrium (Y) on the corrosion of Mg–Y binary alloys, Corros. Sci. 52 (2010) 3687–3701.

[91] F. Rosalbino, E. Angelini, S. De Negri, A. Saccone, S. Delfino, Electrochemical behaviour assessment of novel Mg-rich Mg–Al–RE alloys (RE=Ce, Er), Intermetallics. 14 (2006) 1487–1492.

[92] W. Zhongjun, J. Weiping, C. Jianzhong, Study on the Deformation Behavior of Mg-3.6% Er Magnesium Alloy, J. Rare Earths. 25 (2007) 744–748. doi:10.1016/S1002-0721(08)60019-8.

[93] B.L. Wu, G. Wan, X.H. Du, Y.D. Zhang, F. Wagner, C. Esling, The quasi-static mechanical properties of extruded binary Mg-Er alloys, Mater. Sci. Eng. A. 573 (2013) 205–214. doi:10.1016/j.msea.2013.02.048.

[94] E.M.M. Hiroaki Okamato Mark E. Schlesinger, ASM Handbook, Volume 3: Alloy Phase Diagrams, 2016.

[95] Y. Wan, G. Xiong, H. Luo, F. He, Y. Huang, X. Zhou, Preparation and characterization of a new biomedical magnesium–calcium alloy, Mater. Des. 29 (2008) 2034–2037.

[96] N.T. Kirkland, N. Birbilis, J. Walker, T. Woodfield, G.J. Dias, M.P. Staiger, In-vitro dissolution of magnesium–calcium binary alloys: clarifying the unique role of calcium additions in bioresorbable magnesium implant alloys, J. Biomed. Mater. Res. Part B Appl. Biomater. 95 (2010) 91–100.

[97] S.E. Harandi, M. Hasbullah Idris, H. Jafari, Effect of forging process on microstructure, mechanical and corrosion properties of biodegradable Mg–1Ca alloy, Mater. Des. 32 (2011) 2596–2603. doi:10.1016/j.matdes.2011.01.042.

[98] R.-C. Zeng, W.-C. Qi, H.-Z. Cui, F. Zhang, S.-Q. Li, E.-H. Han, In vitro corrosion of as-extruded Mg–Ca alloys—The influence of Ca concentration, Corros. Sci. 96 (2015) 23–31.

[99] Y. Murakoshi, K. Kikuchi, M. Katoh, K. Matsuzaki, Fabrication and property of degradable magnesium-calcium alloy composites with hydroxyapatite, IFMBE Proc. 31 IFMBE (2010) 1226–1229. doi:10.1007/978-3-642-14515-5_311.

[100] H.-S. Han, Y. Minghui, H.-K. Seok, J.-Y. Byun, P.-R. Cha, S.-J. Yang, Y.C. Kim, The modification of microstructure to improve the biodegradation and mechanical properties of a biodegradable Mg alloy, J. Mech. Behav. Biomed. Mater. 20 (2013) 54–60.

[101] N.T. Kirkland, J. Lespagnol, N. Birbilis, M.P. Staiger, A survey of bio-corrosion rates of magnesium alloys, Corros. Sci. 52 (2010) 287–291. doi:10.1016/j.corsci.2009.09.033.

[102] H.R.B. Rad, M.H. Idris, M.R.A. Kadir, S. Farahany, Microstructure analysis and corrosion behavior of biodegradable Mg–Ca implant alloys, Mater. Des. 33 (2012) 88–97. doi:10.1016/j.matdes.2011.06.057.

[103] J.-Y. Jung, S.-J. Kwon, H.-S. Han, J.-Y. Lee, J.-P. Ahn, S.-J. Yang, S.-Y. Cho, P.-R. Cha, Y.-C. Kim, H.-K. Seok, In vivo corrosion mechanism by elemental interdiffusion of biodegradable Mg–Ca alloy, J. Biomed. Mater. Res. Part B Appl. Biomater. 100B (2012) 2251–2260.

[104] X.N. Gu, X.L. Li, W.R. Zhou, Y. Cheng, Y.F. Zheng, Microstructure, biocorrosion and cytotoxicity evaluations of rapid solidified Mg–3Ca alloy ribbons as a biodegradable material, Biomed. Mater. 5 (2010) 35013.

[105] Y.C. Li, M.H. Li, W.Y. Hu, P.D. Hodgson, C.E. Wen, Biodegradable Mg-Ca and Mg-Ca-Y alloys for regenerative medicine, in: Mater. Sci. Forum, Trans Tech Publ, 2010: pp. 2192–2195.

[106] S.E. Harandi, M. Mirshahi, S. Koleini, M.H. Idris, H. Jafari, M.R.A. Kadir, Effect of calcium content on the microstructure, hardness and in-vitro corrosion behavior of biodegradable Mg-Ca binary alloy, Mater. Res. 16 (2013) 11–18.

[107] B. Zhang, Y. Hou, X. Wang, Y. Wang, L. Geng, Mechanical properties, degradation performance and cytotoxicity of Mg–Zn–Ca biomedical alloys with different compositions, Mater. Sci. Eng. C. 31 (2011) 1667–1673. doi:10.1016/j.msec.2011.07.015.

[108] H.R. Bakhsheshi-Rad, M.H. Idris, M.R. Abdul-Kadir, A. Ourdjini, M. Medraj, M. Daroonparvar, E. Hamzah, Mechanical and bio-corrosion properties of quaternary Mg–Ca–Mn–Zn alloys compared with binary Mg–Ca alloys, Mater. Des. 53 (2014) 283–292. doi:10.1016/j.matdes.2013.06.055.

[109] S. Cai, T. Lei, N. Li, F. Feng, Effects of Zn on microstructure, mechanical properties and corrosion behavior of Mg–Zn alloys, Mater. Sci. Eng. C. 32 (2012) 2570–2577.

[110] J. Kubasek, D. Vojtech, I. Pospisilova, Structural and corrosion characterization of biodegradable Mg-Zn alloy castings, Kov. Mater. Mater. 50 (2012) 415–424.

[111] S. Wei, T. Zhu, H. Hou, J. Kim, E. Kobayashi, T. Sato, M. Hodgson, W. Gao, Effects of Pb/Sn additions on the age-hardening behaviour of Mg–4Zn alloys, Mater. Sci. Eng. A. 597 (2014) 52–61. doi:10.1016/j.msea.2013.12.048.

[112] L.Y. Wei, G.L. Dunlop, H. Westengen, Precipitation hardening of Mg-Zn and Mg-Zn-RE alloys, Metall. Mater. Trans. A. 26 (1995) 1705–1716.

[113] X. Gao, J.F. Nie, Characterization of strengthening precipitate phases in a Mg–Zn alloy, Scr. Mater. 56 (2007) 645–648.

[114] Y. Lu, A.R. Bradshaw, Y.L. Chiu, I.P. Jones, The role of beta1 prime precipitates in the bio-corrosion performance of Mg–3Zn in simulated body fluid, J. Alloys Compd. 614 (2014) 345–352.

[115] Y. Song, E.-H. Han, D. Shan, C.D. Yim, B.S. You, The role of second phases in the corrosion behavior of Mg–5Zn alloy, Corros. Sci. 60 (2012) 238–245.

[116] C.J. Boehlert, K. Knittel, The microstructure, tensile properties, and creep behavior of Mg–Zn alloys containing 0–4.4wt.% Zn, Mater. Sci. Eng. A. 417 (2006) 315–321. doi:10.1016/j.msea.2005.11.006.

[117] G. Parande, V. Manakari, S.D.S. Kopparthy, M. Gupta, Utilizing Low-Cost Eggshell Particles to Enhance the Mechanical Response of Mg-2.5Zn Magnesium Alloy Matrix, Adv. Eng. Mater. 1700919 (2017) 1700919. doi:10.1002/adem.201700919.

[118] Y. Lu, Y.L. Chiu, I.P. Jones, Three-dimensional analysis of the microstructure and bio-corrosion of Mg–Zn and Mg–Zn–Ca alloys, Mater. Charact. 112 (2016) 113–121.

[119] A.F. Lotfabadi, H.R. Bakhsheshi-Rad, M.H. Idris, E. Hamzah, M. Kasiri-Asgarani, The role of solution heat treatment on corrosion and mechanical behaviour of Mg–Zn biodegradable alloys, Can. Metall. Q. 55 (2016) 53–64.

[120] X. LIU, D. SHAN, Y. SONG, E. HAN, Effects of heat treatment on corrosion behaviors of Mg-3Zn magnesium alloy, Trans. Nonferrous Met. Soc. China. 20 (2010) 1345–1350. doi:10.1016/S1003-6326(09)60302-2.

[121] B. Zberg, P.J. Uggowitzer, J.F. Löffler, MgZnCa glasses without clinically observable hydrogen evolution for biodegradable implants, Nat. Mater. 8 (2009) 887–891.

[122] M.K. Datta, D.-T. Chou, D. Hong, P. Saha, S.J. Chung, B. Lee, A. Sirinterlikci, M. Ramanathan, A. Roy, P.N. Kumta, Structure and thermal stability of biodegradable Mg–Zn–Ca based amorphous alloys synthesized by mechanical alloying, Mater. Sci. Eng. B. 176 (2011) 1637–1643. doi:10.1016/j.mseb.2011.08.008.

[123] Z. Xu, C. Smith, S. Chen, J. Sankar, Development and microstructural characterizations of Mg–Zn–Ca alloys for biomedical applications, Mater. Sci. Eng. B. 176 (2011) 1660–1665.

[124] P. Yin, N.F. Li, T. Lei, L. Liu, C. Ouyang, Effects of Ca on microstructure, mechanical and corrosion properties and biocompatibility of Mg-Zn-Ca alloys., J. Mater. Sci. Mater. Med. 24 (2013) 1365–73. doi:10.1007/s10856-013-4856-y.

[125] Y. Lu, A.R. Bradshaw, Y.L. Chiu, I.P. Jones, Effects of secondary phase and grain size on the corrosion of biodegradable Mg – Zn – Ca alloys, 48 (2015) 480–486. doi:10.1016/j.msec.2014.12.049.

[126] D. Zander, N.A. Zumdick, Influence of Ca and Zn on the microstructure and corrosion of biodegradable Mg–Ca–Zn alloys, Corros. Sci. 93 (2015) 222–233.

[127] H.R. Bakhsheshi-Rad, E. Hamzah, A. Fereidouni-Lotfabadi, M. Daroonparvar, M.A.M. Yajid, M. Mezbahul-Islam, M. Kasiri-Asgarani, M. Medraj, Microstructure and bio-corrosion behavior of Mg–Zn and Mg–Zn–Ca alloys for biomedical applications, Mater. Corros. 65 (2014) 1178–1187.

[128] Y. Sun, B. Zhang, Y. Wang, L. Geng, X. Jiao, Preparation and characterization of a new biomedical Mg–Zn–Ca alloy, Mater. Des. 34 (2012) 58–64. doi:10.1016/j.matdes.2011.07.058.

[129] C.C. and J.K.C. Jinshan Zhang, Jidong Xu, Weili Cheng, Corrosion Behavior of Mg–Zn–Y Alloy with Long-period Stacking Ordered Structures Jinshan, J. Mater. Sci. Technol. 28 (2012) 1157–1162. doi:10.1016/S1005-0302(12)60186-8.

[130] P. Pérez, E. Onofre, S. Cabeza, I. Llorente, J.A. Del Valle, M.C. García-Alonso, P. Adeva, M.L. Escudero, Corrosion behaviour of Mg–Zn–Y–Mischmetal alloys in phosphate buffer saline solution, Corros. Sci. 69 (2013) 226–235.

[131] Z. Wang, W. Zhao, C. Qin, Y. Cui, Fabrication and corrosion resistance of Mg-Zn-Y-based nano-quasicrystals alloys, Mater. Res. 15 (2012) 51–56. doi:10.1590/S1516-14392012005000004.

[132] A. Hanzi, A. Sologubenko, P. Uggowitzer, Design strategy for new biodegradable Mg–Y–Zn alloys for medical applications, Int. J. Mater. Res. 100 (2009) 1127–1136.

[133] X. Zhao, L.L. Shi, J. Xu, Mg-Zn-Y alloys with long-period stacking ordered structure: In vitro assessments of biodegradation behavior, Mater. Sci. Eng. C. 33 (2013) 3627–3637. doi:10.1016/j.msec.2013.04.051.

[134] D. Wang, J. Zhang, J. Xu, Z. Zhao, W. Cheng, C. Xu, Microstructure and corrosion behavior of Mg Zn Y Al alloys with long-period stacking ordered structures, J. Magnes. Alloy. 2 (2014) 78–84. doi:10.1016/j.jma.2014.01.008.

[135] Q. WANG, W. DU, K. LIU, Z. WANG, S. LI, Effect of Zn addition on microstructure and mechanical properties of as-cast Mg–2Er alloy, Trans. Nonferrous Met. Soc. China. 24 (2014) 3792–3796.

[136] H. Li, W. Du, S. Li, Z. Wang, Effect of Zn/Er weight ratio on phase formation and mechanical properties of as-cast Mg–Zn–Er alloys, Mater. Des. 35 (2012) 259–265. doi:10.1016/j.matdes.2011.10.002.

[137] X. Zhao, S. Li, Q. Wang, W. Du, K. Liu, Effects of heat treatment on microstructure and mechanical properties of Mg–5Zn–0.63Er alloy, Trans. Nonferrous Met. Soc. China. 23 (2013) 59–65. doi:10.1016/S1003-6326(13)62429-2.

[138] Z. WANG, X. WANG, Q. WANG, W. DU, Effects of ultrasonic treatment on microstructure and mechanical properties of Mg-5Zn-2Er alloy, Trans. Nonferrous Met. Soc. China. 21 (2011) 773–777. doi:10.1016/S1003-6326(11)60779-6.

[139] Z. Leng, J. Zhang, T. Yin, L. Zhang, X. Guo, Q. Peng, M. Zhang, R. Wu, Influence of biocorrosion on microstructure and mechanical properties of deformed Mg-Y-Er-Zn biomaterial containing 18R-LPSO phase, J. Mech. Behav. Biomed. Mater. 28 (2013) 332–339. doi:10.1016/j.jmbbm.2013.08.012.

[140] X.-B. Zheng, K. Liu, Z.-H. Wang, S.-B. Li, W.-B. Du, Microstructural control and hardening response of Mg--6Zn--0.5Er--0.5Ca alloy, Rare Met. 35 (2016) 526–531.

[141] K. Liu, Q.-F. Wang, W.-B. Du, Z.-H. Wang, S.-B. Li, Microstructure and mechanical properties of extruded Mgâ€“6Znâ€“xEr alloys, Trans. Nonferrous Met. Soc. China. 23 (2013) 2863–2873. doi:10.1016/S1003-6326(13)62808-3.

[142] Q. Wang, K. Liu, Z. Wang, S. Li, W. Du, Microstructure, texture and mechanical properties of as-extruded Mg–Zn–Er alloys containing W-phase, J. Alloys Compd. 602 (2014) 32–39. doi:10.1016/j.jallcom.2014.02.027.

[143] Q. Wang, W. Du, K. Liu, Z. Wang, S. Li, K. Wen, Microstructure, texture and mechanical properties of as-extruded Mg–Zn–Er alloys, Mater. Sci. Eng. A. 581 (2013) 31–38. doi:10.1016/j.msea.2013.05.055.

[144] X. Liu, J. Sun, F. Zhou, Y. Yang, R. Chang, K. Qiu, Z. Pu, L. Li, Y. Zheng, Micro-alloying with Mn in Zn-Mg alloy for future biodegradable metals application, Mater. Des. 94 (2016) 95–104. doi:10.1016/j.matdes.2015.12.128.

[145] J.H. Zhang, C. Xu, Y.B. Jing, S.H. Lv, S.J. Liu, D.Q. Fang, J.P. Zhuang, M.L. Zhang, R.Z. Wu, New horizon for high performance Mg-based biomaterial with uniform degradation behavior: Formation of stacking faults, Sci. Rep. 5 (2015) 1–16. doi:Artn 1393310.1038/Srep13933.

[146] X. Du, C. Wei, B. Wu, M. Hong, Y. Xia, W. Li, A high-performance Mg-Er-Zn-Zr alloy with low Er/Zn mass ratio, J. Cent. South Univ. 22 (2015) 4123–4127. doi:10.1007/s11771-015-2958-z.

[147] C. Xu, J. Zhang, S. Liu, Y. Jing, Y. Jiao, L. Xu, L. Zhang, F. Jiang, M. Zhang, R. Wu, Microstructure, mechanical and damping properties of Mg-Er-Gd-Zn alloy reinforced with stacking faults, Mater. Des. 79 (2015) 53–59. doi:10.1016/j.matdes.2015.04.037.

[148] J. Zhang, B. Chen, C. Liu, An investigation of dynamic recrystallization behavior of ZK60-Er magnesium alloy, Mater. Sci. Eng. A. 612 (2014) 253–266. doi:10.1016/j.msea.2014.06.058.

[149] B. Chen, J. Zhang, Microstructure and mechanical properties of ZK60-Er magnesium

alloys, Mater. Sci. Eng. A. 633 (2015) 154–160. doi:10.1016/j.msea.2015.03.009.

[150] Y. Liao, Y. Ouyang, J. Niu, J. Zhang, Y. Wang, Z. Zhu, G. Yuan, Y. He, Y. Jiang, In vitro response of chondrocytes to a biodegradable Mg–Nd–Zn–Zr alloy, Mater. Lett. 83 (2012) 206–208.

[151] L. Zhang, J. Zhang, Z. Leng, S. Liu, Q. Yang, R. Wu, M. Zhang, Microstructure and mechanical properties of high-performance Mg–Y–Er–Zn extruded alloy, Mater. Des. 54 (2014) 256–263. doi:10.1016/j.matdes.2013.08.048.

[152] F. Qi, D. Zhang, X. Zhang, X. Xu, Effect of Sn addition on the microstructure and mechanical properties of Mg-6Zn-1Mn (wt.%) alloy, J. Alloys Compd. 585 (2014) 656–666. doi:10.1016/j.jallcom.2013.09.156.

[153] W. He, E. Zhang, K. Yang, Effect of Y on the bio-corrosion behavior of extruded Mg–Zn–Mn alloy in Hank's solution, Mater. Sci. Eng. C. 30 (2010) 167–174. doi:10.1016/j.msec.2009.09.014.

[154] L. Gao, H. Yan, J. Luo, A.A. Luo, R. Chen, Microstructure and mechanical properties of a high ductility Mg–Zn–Mn–Ce magnesium alloy, J. Magnes. Alloy. 1 (2013) 283–291. doi:10.1016/j.jma.2013.11.005.

[155] T. Homma, C.L. Mendis, K. Hono, S. Kamado, Effect of Zr addition on the mechanical properties of as-extruded Mg-Zn-Ca-Zr alloys, Mater. Sci. Eng. A. 527 (2010) 2356–2362.

[156] R. Guan, I. Johnson, T. Cui, T. Zhao, Z. Zhao, X. Li, H. Liu, Electrodeposition of hydroxyapatite coating on Mg-4.0 Zn-1.0 Ca-0.6 Zr alloy and in vitro evaluation of degradation, hemolysis, and cytotoxicity, J. Biomed. Mater. Res. Part A. 100 (2012) 999–1015.

[157] M. Yang, T. Guo, H. Li, Effects of Gd addition on as-cast microstructure, tensile and creep properties of Mg–3.8 Zn–2.2 Ca (wt%) magnesium alloy, Mater. Sci. Eng. A. 587 (2013) 132–142.

[158] L. Mao, G. Yuan, S. Wang, J. Niu, G. Wu, W. Ding, A novel biodegradable Mg–Nd–Zn–Zr alloy with uniform corrosion behavior in artificial plasma, 2012. doi:10.1016/j.matlet.2012.08.012.

[159] X. Zhang, G. Yuan, J. Niu, P. Fu, W. Ding, Microstructure, mechanical properties, biocorrosion behavior, and cytotoxicity of as-extruded Mg–Nd–Zn–Zr alloy with different extrusion ratios, J. Mech. Behav. Biomed. Mater. 9 (2012) 153–162. doi:10.1016/j.jmbbm.2012.02.002.

[160] X. Zhang, G. Yuan, Z. Wang, Mechanical properties and biocorrosion resistance of Mg-Nd-Zn-Zr alloy improved by cyclic extrusion and compression, 2012. doi:10.1016/j.matlet.2012.01.086.

[161] X. Zhang, Z. Ba, Z. Wang, X. He, C. Shen, Q. Wang, Influence of silver addition on microstructure and corrosion behavior of Mg–Nd–Zn–Zr alloys for biomedical application, Mater. Lett. 100 (2013) 188–191.

[162] X. Zhang, Y. Wu, Y. Xue, Z. Wang, L. Yang, Biocorrosion behavior and cytotoxicity of a MgGdZnZr alloy with long period stacking ordered structure, Mater. Lett. 86 (2012) 42–45. doi:10.1016/j.matlet.2012.07.030.

[163] J. Zhang, C. xin, W. Cheng, L. Bian, H. Wang, C. Xu, Research on long-period-stacking-ordered phase in Mg–Zn–Dy–Zr alloy, J. Alloys Compd. 558 (2013) 195–202. doi:10.1016/j.jallcom.2012.12.165.

[164] Q. Chen, D. Shu, Z. Zhao, Z. Zhao, Y. Wang, B. Yuan, Microstructure development and tensile mechanical properties of Mg–Zn–RE–Zr magnesium alloy, Mater. Des. 40 (2012) 488–496. doi:10.1016/j.matdes.2012.03.059.

[165] J. Fan, X. Qiu, X. Niu, Z. Tian, W. Sun, X. Liu, Y. Li, W. Li, J. Meng, Microstructure, mechanical properties, in vitro degradation and cytotoxicity evaluations of Mg–1.5Y–1.2Zn–0.44Zr alloys for biodegradable metallic implants, Mater. Sci. Eng. C. 33 (2013) 2345–2352. doi:10.1016/j.msec.2013.01.063.

[166] G.-L. Song, Corrosion prevention of magnesium alloys, 2014. doi:10.1007/s13398-014-0173-7.2.

[167] J.E. Gray, B. Luan, Protective coatings on magnesium and its alloys — a critical review, J. Alloys Compd. 336 (2002) 88–113. doi:10.1016/S0925-8388(01)01899-0.

[168] R. J, Entwicklung und Anwendung von Beschictungsstoffen, 1993.

[169] G. Song, Corrosion behavior of magnesium (Mg) alloys, In: Dong H, editor. Surface engineering of light alloys, aluminum, magnesium, titanium alloys. Cambridge, UK, in: Woodhead Publishing Ltd, 2010: pp. 3–39.

[170] M. HA, Fundamentals of oxidation and tarnish. In: Uhlig HH, editor. The corrosion handbook. New York, in: John Wiley, 1948: pp. 11–20.

[171] Quantitative X-Ray Photoelectron Spectroscopy Characterization of Magnesium Oxidized in Air, J. Electrochem. Soc. 147 (2000) 1408–13.

[172] M. Santamaria, F. Di Quarto, S. Zanna, P. Marcus, Initial surface film on magnesium metal: A characterization by X-ray photoelectron spectroscopy (XPS) and photocurrent spectroscopy (PCS), Electrochim. Acta. 53 (2007) 1314–1324.

[173] A. Seyeux, M. Liu, P. Schmutz, G. Song, A. Atrens, P. Marcus, ToF-SIMS depth profile of the surface film on pure magnesium formed by immersion in pure water and the identification of magnesium hydride, Corros. Sci. 51 (2009) 1883–1886.

[174] T. Ishizaki, I. Shigematsu, N. Saito, Anticorrosive magnesium phosphate coating on AZ31 magnesium alloy, Surf. Coatings Technol. 203 (2009) 2288–2291.

[175] W. Zhou, D. Shan, E.-H. Han, W. Ke, Structure and formation mechanism of phosphate conversion coating on die-cast AZ91D magnesium alloy, Corros. Sci. 50 (2008) 329–337. doi:10.1016/j.corsci.2007.08.007.

[176] Y. CHENG, H.-I. WU, Z. CHEN, H. WANG, Z. ZHANG, Y. WU, Corrosion properties of AZ31 magnesium alloy and protective effects of chemical conversion layers and anodized coatings, Trans. Nonferrous Met. Soc. China. 17 (2007) 502–508.

[177] L.Y. Niu, Z.H. Jiang, G.Y. Li, C.D. Gu, J.S. Lian, A study and application of zinc phosphate coating on AZ91D magnesium alloy, Surf. Coatings Technol. 200 (2006) 3021–3026.

[178] Q. Li, S. Xu, J. Hu, S. Zhang, X. Zhong, X. Yang, The effects to the structure and electrochemical behavior of zinc phosphate conversion coatings with ethanolamine on magnesium alloy AZ91D, Electrochim. Acta. 55 (2010) 887–894. doi:10.1016/j.electacta.2009.06.048.

[179] E. Rocca, C. Juers, J. Steinmetz, Corrosion behaviour of chemical conversion treatments on as-cast Mg–Al alloys: Electrochemical and non-electrochemical methods, Corros. Sci. 52 (2010) 2172–2178.

[180] W. Lan, J.C. Sun, A.R. Zhou, D.F. Zhang, Structures of Zinc-Manganese Phosphate Film and Organic Coating on Magnesium Alloys, in: Mater. Res., Trans Tech Publications, 2009: pp. 880–883.

[181] M. Zhao, S. Wu, J. Luo, Y. Fukuda, H. Nakae, A chromium-free conversion coating of magnesium alloy by a phosphate–permanganate solution, Surf. Coatings Technol. 200 (2006) 5407–5412.

[182] A. Abdel Aal, Protective coating for magnesium alloy, J. Mater. Sci. 43 (2008) 2947–2954.

[183] A.S. Hamdy, M. Farahat, Chrome-free zirconia-based protective coatings for magnesium alloys, Surf. Coatings Technol. 204 (2010) 2834–2840.

[184] H. Huo, Y. Li, F. Wang, Corrosion of AZ91D magnesium alloy with a chemical conversion coating and electroless nickel layer, Corros. Sci. 46 (2004) 1467–1477.

[185] R. Rettig, S. Virtanen, Composition of corrosion layers on a magnesium rare-earth alloy in simulated body fluids, J. Biomed. Mater. Res. Part A. 88A (2009) 359–369. doi:10.1002/jbm.a.31887.

[186] R. Rettig, S. Virtanen, Time-dependent electrochemical characterization of the corrosion of a magnesium rare-earth alloy in simulated body fluids, J. Biomed. Mater. Res. Part A. 85A (2008) 167–175.

[187] L. Müller, F.A. Müller, Preparation of SBF with different HCO3- content and its influence on the composition of biomimetic apatites, Acta Biomater. 2 (2006) 181–189.

[188] R. Supplit, T. Koch, U. Schubert, Evaluation of the anti-corrosive effect of acid pickling and sol–gel coating on magnesium AZ31 alloy, Corros. Sci. 49 (2007) 3015–3023.

[189] M. Carboneras, M.C. García-Alonso, M.L. Escudero, Biodegradation kinetics of modified magnesium-based materials in cell culture medium, Corros. Sci. 53 (2011) 1433–1439.

[190] K.Y. Chiu, M.H. Wong, F.T. Cheng, H.C. Man, Characterization and corrosion studies of fluoride conversion coating on degradable Mg implants, Surf. Coatings Technol. 202 (2007) 590–598. doi:10.1016/j.surfcoat.2007.06.035.

[191] F. Witte, J. Fischer, J. Nellesen, C. Vogt, J. Vogt, T. Donath, F. Beckmann, In vivo corrosion and corrosion protection of magnesium alloy LAE442, Acta Biomater. 6 (2010) 1792–1799.

[192] J.-M. Seitz, K. Collier, E. Wulf, D. Bormann, F.-W. Bach, Comparison of the Corrosion Behavior of Coated and Uncoated Magnesium Alloys in an In Vitro Corrosion Environment, Adv. Eng. Mater. 13 (2011) B313--B323.

[193] J. zhong LI, J. gui HUANG, Y. wen TIAN, C. sheng LIU, Corrosion action and passivation mechanism of magnesium alloy in fluoride solution, Trans. Nonferrous Met. Soc. China (English Ed. 19 (2009) 50–54. doi:10.1016/S1003-6326(08)60227-7.

[194] T.F. Da Conceicao, N. Scharnagl, C. Blawert, W. Dietzel, K.U. Kainer, Surface modification of magnesium alloy AZ31 by hydrofluoric acid treatment and its effect on the corrosion behaviour, Thin Solid Films. 518 (2010) 5209–5218. doi:10.1016/j.tsf.2010.04.114.

[195] T. Yan, L. Tan, D. Xiong, X. Liu, B. Zhang, K. Yang, Fluoride treatment and in vitro corrosion behavior of an AZ31B magnesium alloy, Mater. Sci. Eng. C. 30 (2010) 740–748. doi:10.1016/j.msec.2010.03.007.

[196] T. Yan, L. Tan, B. Zhang, K. Yang, Preparation and characterization of fluoride conversion coating on biodegradable AZ31B magnesium alloy, J. Optoelectron. Adv. Mater. 16 (2014) 562–567. doi:10.1016/j.jmst.2013.12.015.

[197] M.D. Pereda, C. Alonso, L. Burgos-Asperilla, J.A. Del Valle, O.A. Ruano, P. Perez, M.A. Fernández Lorenzo De Mele, Corrosion inhibition of powder metallurgy Mg by fluoride treatments, Acta Biomater. 6 (2010) 1772–1782. doi:10.1016/j.actbio.2009.11.004.

[198] J. Zhang, N. Kong, J. Niu, Y. Shi, H. Li, Y. Zhou, G. Yuan, Influence of fluoride treatment on surface properties, biodegradation and cytocompatibility of Mg-Nd-Zn-Zr alloy, J. Mater. Sci. Mater. Med. 25 (2014) 791–799. doi:10.1007/s10856-013-5106-z.

[199] M. Thomann, C. Krause, N. Angrisani, D. Bormann, T. Hassel, H. Windhagen, A. Meyer-Lindenberg, Influence of a magnesium-fluoride coating of magnesium-based implants (MgCa0.8) on degradation in a rabbit model, J. Biomed. Mater. Res. - Part A. 93 (2010) 1609–1619. doi:10.1002/jbm.a.32639.

[200] F. Witte, J. Fischer, J. Nellesen, H.-A. Crostack, V. Kaese, A. Pisch, F. Beckmann, H. Windhagen, In vitro and in vivo corrosion measurements of magnesium alloys, Biomaterials. 27 (2006) 1013–1018. doi:10.1016/j.biomaterials.2005.07.037.

[201] M.P. Staiger, A.M. Pietak, J. Huadmai, G. Dias, Magnesium and its alloys as orthopedic biomaterials: A review, Biomaterials. 27 (2006) 1728–1734. doi:10.1016/j.biomaterials.2005.10.003.

[202] M. Gupta, M.O. Lai, D. Saravanaranganathan, Synthesis, microstructure and properties characterization of disintegrated melt deposited Mg/SiC composites, J. Mater. Sci. 35 (2000) 2155–2165. doi:10.1023/A:1004706321731.

[203] N. Bozzolo, F. Wagner, N. Dewobroto, T. Grosdidier, Recrystallization textures in some hexagonal alloys, Mater. Sci. Forum. 412 (2002) 901–906. doi:10.4028/www.scientific.net/MSF.408-412.901.

[204] J.A. Del Valle, M.T. Pérez-Prado, O.A. Ruano, Deformation mechanisms responsible for the high ductility in a Mg AZ31 alloy analyzed by electron backscattered diffraction, Metall. Mater. Trans. A Phys. Metall. Mater. Sci. 36 (2005) 1427–1438. doi:10.1007/s11661-005-0235-8.

[205] S. Seetharaman, C. Blawert, B.M. Ng, W.L.E. Wong, C.S. Goh, N. Hort, M. Gupta, Effect of erbium modification on the microstructure, mechanical and corrosion characteristics of binary Mg-Al alloys, J. Alloys Compd. 648 (2015) 759–770. doi:10.1016/j.jallcom.2015.05.284.

[206] H. Li, Q. Peng, X. Li, K. Li, Z. Han, D. Fang, Microstructures, mechanical and cytocompatibility of degradable Mg-Zn based orthopedic biomaterials, Mater. Des. 58 (2014) 43–51. doi:10.1016/j.matdes.2014.01.031.

[207] E.. Padezhnova, E.. Melnik, T.. Dobatnika, Examination of Phase Equilibrium in the Mg-Y-Zn System, Russ. Met. 4 (1982) 185.

[208] A. Niikura, A.P. Tsai, A. Inoue, T. Masumoto, New Class of Amorphous and Icosahedral Phases in Zn-Mg Rare-Earth-Metal Alloys, Jpn. J. Appl. Phys. 33 (1994) L1538–L1541. doi:10.1143/JJAP.33.L1538.

[209] A. Singh, M. Watanabe, a. Kato, a. P. Tsai, Crystallographic orientations and interfaces of icosahedral quasicrystalline phase growing on cubic W phase in Mg-Zn-Y alloys, Mater. Sci. Eng. A. 397 (2005) 22–34. doi:10.1016/j.msea.2005.02.036.

[210] A.-P. Tsai, Y. Murakami, A. Niikura, The Zn-Mg-Y phase diagram involving quasicrystals, Philos. Mag. A. 80 (2000) 1043–1054. doi:10.1080/01418610008212098.

[211] J.Y. Lee, D.H. Kim, H.K. Lim, D.H. Kim, Effects of Zn / Y ratio on microstructure and mechanical properties of Mg-Zn-Y alloys, Mater. Lett. 59 (2005) 3801–3805. doi:10.1016/J.MATLET.2005.06.052.

[212] L. Luo, Y. Liu, M. Duan, Phase Formation of Mg-Zn-Gd Alloys on the Mg-rich Corner, Materials (Basel). 11 (2018) 1351. doi:10.3390/ma11081351.

[213] H. Li, W. Du, S. Li, Z. Wang, Effect of Zn/Er weight ratio on phase formation and mechanical properties of as-cast Mg–Zn–Er alloys, Mater. Des. 35 (2012) 259–265.

[214] S.R. Agnew, M.H. Yoo, C.N. Tomé, Application of texture simulation to understanding mechanical behavior of Mg and solid solution alloys containing Li or Y, Acta Mater. 49 (2001) 4277–4289. doi:10.1016/S1359-6454(01)00297-X.

[215] H. Feng, Y. Yang, H. Chang, Influence of W-phase on mechanical properties and damping capacity of Mg-Zn-Y-Nd-Zr alloys, Mater. Sci. Eng. A. 609 (2014) 60–64. doi:10.1016/j.msea.2014.04.104.

[216] H. Xu, L.D. Xu, S.J. Zhang, Q. Han, Effect of the alloy composition on the grain refinement of aluminum alloys, Scr. Mater. 54 (2006) 2191–2196. doi:10.1016/J.SCRIPTAMAT.2006.02.035.

[217] M.. Easton, D.. StJohn, A model of grain refinement incorporating alloy constitution and potency of heterogeneous nucleant particles, Acta Mater. 49 (2001) 1867–1878. doi:10.1016/S1359-6454(00)00368-2.

[218] Y.C. Lee, A.K. Dahle, D.H. Stjohn, The role of solute in grain refinement of magnesium, Metall. Mater. Trans. A Phys. Metall. Mater. Sci. 31 (2000) 2895–2906. doi:10.1007/BF02830349.

[219] J. Zhang, Q. Ma, F. Pan, Effects of trace Er addition on the microstructure and mechanical properties of Mg-Zn-Zr alloy, Mater. Des. 31 (2010) 4043–4049. doi:10.1016/j.matdes.2010.05.008.

[220] E. Zhang, D. Yin, L. Xu, L. Yang, K. Yang, Microstructure, mechanical and corrosion properties and biocompatibility of Mg–Zn–Mn alloys for biomedical application, Mater. Sci. Eng. C. 29 (2009) 987–993. doi:10.1016/j.msec.2008.08.024.

[221] C. Ma, M. Liu, G. Wu, W. Ding, Y. Zhu, Tensile properties of extruded ZK60-RE alloys, Mater. Sci. Eng. A. 349 (2003) 207–212. doi:10.1016/S0921-5093(02)00740-2.

[222] M.R. Barnett, A. Sullivan, N. Stanford, N. Ross, A. Beer, Texture selection mechanisms in uniaxially extruded magnesium alloys, Scr. Mater. 63 (2010) 721–724. doi:10.1016/J.SCRIPTAMAT.2010.01.018.

[223] C. Xu, T. Nakata, X. Qiao, M. Zheng, K. Wu, S. Kamado, Effect of LPSO and SFs on microstructure evolution and mechanical properties of Mg-Gd-Y-Zn-Zr alloy, Sci. Rep. 7 (2017) 40846. doi:10.1038/srep40846.

[224] N. Stanford, G. Sha, J.H. Xia, S.P. Ringer, M.R. Barnett, Solute segregation and texture modification in an extruded magnesium alloy containing gadolinium, Scr. Mater. 65 (2011) 919–921. doi:10.1016/J.SCRIPTAMAT.2011.08.012.

[225] E.A. Ball, P.B. Prangnell, Tensile-compressive yield asymmetries in high strength wrought magnesium alloys, Scr. Metall. Mater. 31 (1994) 111–116. doi:10.1016/0956-716X(94)90159-7.

[226] Y. dongxia, L. xiaoyan, H. dingyong, H. hui, Effect of minor Er and Zr on microstructure and mechanical properties of Al-Mg-Mn alloy (5083) welded joints, Mater. Sci. Eng. A. 561 (2013) 226–231. doi:10.1016/j.msea.2012.11.002.

[227] H. Du, Z. Wei, X. Liu, E. Zhang, Effects of Zn on the microstructure, mechanical property and bio-corrosion property of Mg–3Ca alloys for biomedical application, Mater. Chem. Phys. 125 (2011) 568–575.

[228] H.R. Shercliff, M.F. Ashby, A process model for age hardening of aluminium alloys—I. The model, Acta Metall. Mater. 38 (1990) 1789–1802. doi:10.1016/0956-7151(90)90291-N.

[229] E. Zhang, W. He, H. Du, K. Yang, Microstructure, mechanical properties and corrosion properties of Mg–Zn–Y alloys with low Zn content, Mater. Sci. Eng. A. 488 (2008) 102–111.

[230] D.K. Xu, E.H. Han, Effects of icosahedral phase formation on the microstructure and mechanical improvement of Mg alloys: A review, Prog. Nat. Sci. Mater. Int. 22 (2012) 364–385. doi:10.1016/j.pnsc.2012.09.005.

[231] C.. Caceres, P. Lukac, Strain hardening behaviour and the Taylor factor of pure magnesium, Philos. Mag. 88 (2008) 977–989.

[232] H.. Frost, M.. Ashby, Deformation-mechanism maps, Pergamon Press, Oxford, 1982.

[233] Q. Yu, L. Qi, R.K. Mishra, J. Li, A.M. Minor, Reducing deformation anisotropy to achieve ultrahigh strength and ductility in Mg at the nanoscale., Proc. Natl. Acad. Sci. U. S. A. 110 (2013) 13289–93. doi:10.1073/pnas.1306371110.

[234] G.L. Song, Corrosion and Protection of Magnesium Alloys: An Overview of Research Undertaken by CAST, Mater. Sci. Forum. 488–489 (2005) 649–652. doi:10.4028/www.scientific.net/MSF.488-489.649.

[235] M.-C. Zhao, M. Liu, G.-L. Song, A. Atrens, Influence of pH and chloride ion concentration on the corrosion of Mg alloy ZE41, Corros. Sci. 50 (2008) 3168–3178. doi:10.1016/J.CORSCI.2008.08.023.

[236] N. Birbilis, K.D. Ralston, S. Virtanen, H.L. Fraser, C.H.J. Davies, Grain character influences on corrosion of ECAPed pure magnesium, Corros. Eng. Sci. Technol. 45 (2010) 224–230. doi:10.1179/147842209X12559428167805.

[237] Y.S. Jeong, W.J. Kim, Enhancement of mechanical properties and corrosion resistance of Mg – Ca alloys through microstructural refinement by indirect extrusion, Corros. Sci. 82 (2014) 392–403. doi:10.1016/j.corsci.2014.01.041.

[238] T. Lei, W. Tang, S.H. Cai, F.F. Feng, N.F. Li, On the corrosion behaviour of newly developed biodegradable Mg-based metal matrix composites produced by in situ reaction, Corros. Sci. 54 (2012) 270–277. doi:10.1016/j.corsci.2011.09.027.

[239] M. Alvarez-Lopez, M.D. Pereda, J. a del Valle, M. Fernandez-Lorenzo, M.C. Garcia-Alonso, O. a Ruano, M.L. Escudero, Corrosion behaviour of AZ31 magnesium alloy with different grain sizes in simulated biological fluids., Acta Biomater. 6 (2010) 1763–71. doi:10.1016/j.actbio.2009.04.041.

[240] K.D. Ralston, N. Birbilis, Effect of Grain Size on Corrosion: A Review, CORROSION. 66 (2010) 075005-075005-13. doi:10.5006/1.3462912.

[241] N.N. Aung, W. Zhou, Effect of grain size and twins on corrosion behaviour of AZ31B

magnesium alloy, Corros. Sci. 52 (2010) 589–594. doi:10.1016/j.corsci.2009.10.018.

[242] K.U. Kainer, F. von Buch, The Current State of Technology and Potential for Further Development of Magnesium Applications, in: Magnesium– Alloy. Technol., Wiley-VCH Verlag GmbH & Co. KGaA, Weinheim, FRG, n.d.: pp. 1–22. doi:10.1002/3527602046.ch1.

[243] N. Birbilis, M. Zhang, Y. Estrin, Surface grain size effects on the corrosion of magnesium, 384 (2008) 229–240. doi:10.4028/www.scientific.net/KEM.384.229.

[244] W. Zhou, T. Shen, N.N. Aung, Effect of heat treatment on corrosion behaviour of magnesium alloy AZ91D in simulated body fluid, Corros. Sci. 52 (2010) 1035–1041. doi:10.1016/j.corsci.2009.11.030.

[245] H. Okouchi, Y. Seki, T. Sekigawa, H. Hira, Y. Kawamura, Nanocrystalline LPSO Mg-Zn-Y-Al Alloys with High Mechanical Strength and Corrosion Resistance, Mater. Sci. Forum. 638–642 (2010) 1476–1481. doi:10.4028/www.scientific.net/MSF.638-642.1476.

[246] S.W. Nam, W.T. Kim, D.H. Kim, T.S. Kim, Microstructure and corrosion behavior of rapidly solidified Mg-Zn-Y alloys, Met. Mater. Int. 19 (2013) 205–209. doi:10.1007/s12540-013-2010-5.

[247] F. SHI, Y. chun YU, X. feng GUO, Z. ming ZHANG, Y. ying LI, Corrosion behavior of as-cast Mg68Zn28Y4 alloy with I-phase, Trans. Nonferrous Met. Soc. China (English Ed. 19 (2009) 1093–1097. doi:10.1016/S1003-6326(08)60412-4.

[248] J.-M. Dubois, So Useful, Those Quasicrystals, Isr. J. Chem. 51 (2011) 1168–1175. doi:10.1002/ijch.201100149.

[249] G.-L. Song, Z. Xu, Crystal orientation and electrochemical corrosion of polycrystalline Mg, Corros. Sci. 63 (2012) 100–112.

[250] G.-L. Song, R.K. Mishra, Z. Xu, Crystallographic orientation and electrochemical activity of AZ31 Mg alloy, Electrochem. Commun. 12 (2010) 1009–1012.

[251] Z. Zeng, N. Stanford, C.H.J. Davies, J.-F. Nie, N. Birbilis, Magnesium extrusion alloys: a review of developments and prospects, Int. Mater. Rev. 0 (2018) 1–36. doi:10.1080/09506608.2017.1421439.

[252] S. Keim, J.G. Brunner, B. Fabry, S. Virtanen, Control of magnesium corrosion and biocompatibility with biomimetic coatings, J. Biomed. Mater. Res. Part B Appl. Biomater. 96B (2011) 84–90. doi:10.1002/jbm.b.31742.

[253] L. Yang, N. Hort, D. Laipple, D. Höche, Y. Huang, K.U. Kainer, R. Willumeit, F. Feyerabend, Element distribution in the corrosion layer and cytotoxicity of alloy Mg–10Dy during in vitro biodegradation, Acta Biomater. 9 (2013) 8475–8487. doi:10.1016/j.actbio.2012.10.001.

[254] A.C. Hänzi, P. Gunde, M. Schinhammer, P.J. Uggowitzer, On the biodegradation performance of an Mg-Y-RE alloy with various surface conditions in simulated body fluid,

Acta Biomater. 5 (2009) 165, 170. doi:10.1016/j.actbio.2008.07.034.

[255] H.B. YAO, Y. LI, A.T.S. WEE, J.S. PAN, J.W. CHAI, EFFECT OF Y ADDITION ON THE CORROSION BEHAVIOR OF MELT-SPUN AMORPHOUS Mg–Cu RIBBONS, Surf. Rev. Lett. 08 (2001) 575–580. doi:10.1142/S0218625X01001464.

[256] S. Krishnamurthy, M. Khobaib, E. Robertson, F.H. Froes, Corrosion behavior of rapidly solidified Mg□Nd and Mg□Y alloys, Mater. Sci. Eng. 99 (1988) 507–511. doi:10.1016/0025-5416(88)90386-2.

[257] G.-L. Song, Corrosion mechanisms of magnesium alloys, 1Advanced Eng. Mater. 1 (999) 11–33.

[258] S. Zhang, J. Li, Y. Song, C. Zhao, X. Zhang, C. Xie, Y. Zhang, H. Tao, Y. He, Y. Jiang, Y. Bian, In vitro degradation, hemolysis and MC3T3-E1 cell adhesion of biodegradable Mg–Zn alloy, Mater. Sci. Eng. C. 29 (2009) 1907–1912. doi:10.1016/j.msec.2009.03.001.

[259] F. Rosalbino, E. Angelini, S. De Negri, A. Saccone, S. Delfino, Influence of the rare earth content on the electrochemical behaviour of Al-Mg-Er alloys, Intermetallics. 11 (2003) 435–441. doi:10.1016/S0966-9795(03)00016-5.

[260] F. Rosalbino, E. Angelini, S. De Negri, A. Saccone, S. Delfino, Influence of the rare earth content on the electrochemical behaviour of Al–Mg–Er alloys, Intermetallics. 11 (2003) 435–441. doi:10.1016/S0966-9795(03)00016-5.

[261] L.-H. Chiu, C.-C. Chen, C.-F. Yang, Improvement of corrosion properties in an aluminum-sprayed AZ31 magnesium alloy by a post-hot pressing and anodizing treatment, Surf. Coatings Technol. 191 (2005) 181–187. doi:10.1016/J.SURFCOAT.2004.02.035.

[262] E. Zhang, L. Xu, K. Yang, Formation by ion plating of Ti-coating on pure Mg for biomedical applications, Scr. Mater. 53 (2005) 523–527. doi:10.1016/J.SCRIPTAMAT.2005.05.009.

[263] A. Duncanson, R.W.H. Stevenson, Some Properties of Magnesium Fluoride crystallized from the Melt, Proc. Phys. Socirty. 72 (1958) 1001.

[264] HANDBOOK OF MATERIALS FOR MEDICAL DEVICES, 2003. www.asminternational.orgwww.asminternational.org (accessed October 22, 2018).

[265] S.S. Abd El-Rahman, Neuropathology of aluminum toxicity in rats (glutamate and GABA impairment), Pharmacol. Res. 47 (2003) 189–194. doi:10.1016/S1043-6618(02)00336-5.

[266] H. Tapiero, K.D. Tew, Trace elements in human physiology and pathology: Zinc and metallothioneins, Biomed. Pharmacother. 57 (2003) 399–411. doi:10.1016/S0753-3322(03)00081-7.

[267] J.H. Zhang, C. Xu, Y.B. Jing, S.H. Lv, S.J. Liu, D.Q. Fang, J.P. Zhuang, M.L. Zhang, R.Z. Wu, New horizon for high performance Mg-based biomaterial with uniform degradation behavior: Formation of stacking faults, Sci. Rep. 5 (2015) 1–16. doi:Artn 1393310.1038/Srep13933.

[268] S. Zhang, J. Li, Y. Song, C. Zhao, X. Zhang, C. Xie, Y. Zhang, H. Tao, Y. He, Y. Jiang, Y. Bian, In vitro degradation, hemolysis and MC3T3-E1 cell adhesion of biodegradable Mg-Zn alloy, Mater. Sci. Eng. C. 29 (2009) 1907–1912. doi:10.1016/j.msec.2009.03.001.

[269] T. Yan, L. Tan, D. Xiong, X. Liu, B. Zhang, K. Yang, Fluoride treatment and in vitro corrosion behavior of an AZ31B magnesium alloy, Mater. Sci. Eng. C. 30 (2010) 740–748. doi:10.1016/j.msec.2010.03.007.

[270] ISO 10993-5:2009 - Biological evaluation of medical devices -- Part 5: Tests for in vitro cytotoxicity, (n.d.). https://www.iso.org/standard/36406.html (accessed October 22, 2018).

[271] Y. Zhang, M. Forsyth, B.R.W. Hinton, The Effect of Treatment Temperature on Corrosion Resistance and Hydrophilicity of an Ionic Liquid Coating for Mg-Based Stents, ACS Appl. Mater. Interfaces. 6 (2014) 18989–18997. doi:10.1021/am506825d.

[272] G. Subbiahdoss, D.W. Grijpma, H.C. van der Mei, H.J. Busscher, R. Kuijer, Microbial biofilm growth versus tissue integration on biomaterials with different wettabilities and a polymer-brush coating, J. Biomed. Mater. Res. Part A. 9999A (2010) NA-NA. doi:10.1002/jbm.a.32731.

[273] N.P. Lang, G.E. Salvi, G. Huynh-Ba, S. Ivanovski, N. Donos, D.D. Bosshardt, Early osseointegration to hydrophilic and hydrophobic implant surfaces in humans, Clin. Oral Implants Res. 22 (2011) 349–356. doi:10.1111/j.1600-0501.2011.02172.x.

[274] J. Rosina, E. Kvašňák, D. Šuta, H. Kolářová, J. Málek, L. Krajči, Temperature dependence of blood surface tension, Physiol. Res. 56 (2007). doi:1306 [pii].

[275] P. Makkar, H.J. Kang, A.R. Padalhin, I. Park, B.-G. Moon, B.T. Lee, Development and properties of duplex MgF2/PCL coatings on biodegradable magnesium alloy for biomedical applications., PLoS One. 13 (2018) e0193927. doi:10.1371/journal.pone.0193927.

[276] S.P. Khan, G.G. Auner, G.M. Newaz, Influence of nanoscale surface roughness on neural cell attachment on silicon, Nanomedicine Nanotechnology, Biol. Med. 1 (2005) 125–129. doi:10.1016/j.nano.2005.03.007.

[277] R.S. Krishnan, J.P. Russell, The first-order Raman spectrum of magnesium fluoride, Br. J. Appl. Phys. 17 (1966) 501–503. doi:10.1088/0508-3443/17/4/308.

[278] B.R. Sunil, A.A. Kumar, T.S. Sampath Kumar, U. Chakkingal, Role of biomineralization on the degradation of fine grained AZ31 magnesium alloy processed by groove pressing, Mater. Sci. Eng. C. 33 (2013) 1607–1615. doi:10.1016/J.MSEC.2012.12.095.

[279] D.A. Puleo, A. Nanci, Understanding and controlling the bone-implant interface., Biomaterials. 20 (1999) 2311–21.

[280] T. Yan, L. Tan, B. Zhang, K. Yang, Preparation and characterization of fluoride conversion coating on biodegradable AZ31B magnesium alloy, J. Optoelectron. Adv. Mater. 16 (2014) 562–567. doi:10.1016/j.jmst.2013.12.015.

[281] J. Lellouche, A. Friedman, J.-P. Lellouche, A. Gedanken, E. Banin, Improved antibacterial and antibiofilm activity of magnesium fluoride nanoparticles obtained by water-based ultrasound chemistry, Nanomedicine Nanotechnology, Biol. Med. 8 (2012) 702–711. doi:10.1016/J.NANO.2011.09.002.

Abstract: With the ability to bio-degrade and thereby reducing the stress-shielding effect, biodegradable implants are of great importance in medical research. Among all the materials, magnesium is the one which shows promising results being bio-degradable and with the properties comparable with its young's modulus to that of bones. In the present study, the approaches adopted to improve the mechanical and corrosion behaviors of pure magnesium using carefully chosen: (a) Alloying elements like zinc, calcium and erbium (Mg-2Zn-2Er, Mg-2Zn-0.6Ca-1Er, etc.) to control the degradation behavior (b) Secondary processes like extrusion to alter and improve the microstructure (c) Surface treatments like fluoride coatings to further protect the surface to resist the rapid dissolution. The first part of this thesis focuses on the microstructural characterization of as-DMDed and as-extruded alloys. The microstructural characterization (XRD and TEM) reveals the presence of $MgZn_2$, W-phase ($Mg_3Zn_3Er_2$) and i-phases (Mg_3Zn_6Er) in different alloys. The mechanical property assessment revealed an increment in the tensile and compressive properties of ternary and quaternary alloys as compared to pure Mg and Mg-2Zn binary alloy. These values are attributed to a reduction in grain size, presence of solute atoms and secondary phases. Mg-2Zn-2Er and Mg-3Zn-0.5Er showed enhanced corrosion resistance due to the fine grain sized microstructure and a uniform distribution of secondary phases. The cell viability values were enhanced with increased coating time and it was found that these alloys could serve as potential candidates for further in-vivo tests to establish their applicability.

Keywords: Magnesium, biocompatibility, cell-toxicity, surface treatment, orthopedic implants, biodegradation

Résumé: Étant donné leur capacité à se dégrader à l'intérieur du corps, les implants biodégradables ont fait l'objet de nombreuses recherches médicales. Parmi tous les matériaux, c'est le magnésium, un élément indispensable du corps humain, qui conduit aux résultats les plus favorables car son module d'Young est similaire à celui de l'os. De ce fait, les méthodes adoptées afin d'améliorer le comportement du magnésium pur vis-à-vis de la corrosion sont les suivantes: a) Ajout d'éléments d'alliage comme le zinc, le calcium et l'erbium (Mg-2Zn-2Er, Mg-2Zn-0.6Ca-1Er, etc.) pour contrôler le comportement de dégradation b) Procédés secondaires tels que l'extrusion pour modifier sa microstructure c)Revêtements de surface à base de fluorure pour mieux protéger la surface. La première partie de cette thèse porte sur la caractérisation microstructurale d'alliages. La caractérisation microstructurale révèle la présence de $MgZn_2$, de phases W ($Mg_3Zn_3Er_2$) et i (Mg_3Zn_6Er) dans différents alliages. L'évaluation des propriétés mécaniques a révélé une augmentation des propriétés de traction et de compression des alliages ternaires et quaternaires par rapport aux alliages de Mg et de Mg-2Zn. Ces propriétés mécaniques améliorées sont attribuées à une réduction de la taille des grains, à la présence d'atomes de soluté et à des phases secondaires. Mg-2Zn-2Er et Mg-3Zn-0.5Er présentaient une résistance à la corrosion améliorée en raison de la microstructure à granulométrie fine et d'une répartition uniforme des phases secondaires. La viabilité cellulaire a été améliorée avec l'épaisseur du temps de revêtement et ces alliages pourraient servir de candidats potentiels pour d'autres tests in vivo.

Mot clés : magnésium, biocompatibilité, toxicologie cellulaire, revêtement de surface, implants orthopédiques, biodégradation